

Tailor-Made Light Management Textures for  
Liquid Phase Crystallized Silicon Solar Cells  
– Technological and device considerations –

vorgelegt von  
M. Sc.  
David Eisenhauer  
geb. in Weinheim/Bergstr.

von der Fakultät IV - Elektrotechnik und Informatik  
der Technischen Universität Berlin  
zur Erlangung des akademischen Grades

Doktor der Naturwissenschaften  
– Dr. rer. nat. –

genehmigte Dissertation

Promotionsausschuss:

Vorsitzender: Prof. Dr. Roland Thewes  
Gutachter: Prof. Dr. Bernd Rech  
Gutachterin: Prof. Dr. Christiane Becker  
Gutachter: Assoc. Prof. Dr. Olindo Isabella  
Gutachter: RNDr. Antonín Fejfar, CSc.

Tag der wissenschaftlichen Aussprache: 18. Juli 2018

Berlin 2018



*Ah, there's nothing more exciting than science.  
You get all the fun of  
sitting still, being quiet, writing down numbers, paying attention.  
Science has it all.*

Principal Seymour Skinner  
in „The Simpsons“



# Contents

<b>1</b>	<b>Introduction</b>	<b>1</b>
<b>2</b>	<b>Theoretical background</b>	<b>9</b>
2.1	Optical properties of silicon . . . . .	9
2.1.1	Light-matter interaction . . . . .	12
2.1.2	Light management . . . . .	15
2.2	Electronic properties of silicon . . . . .	18
2.2.1	Electronic loss mechanisms . . . . .	19
2.3	Solar cell characteristics . . . . .	22
<b>3</b>	<b>Experimental and numerical methods</b>	<b>27</b>
3.1	Substrate preparation . . . . .	27
3.1.1	Nano-imprint lithography . . . . .	27
3.1.2	Texturing of silicon oxide layers . . . . .	32
3.1.3	SMART texture production . . . . .	34
3.2	Solar cell precursor stack production . . . . .	35
3.2.1	Absorber texturization . . . . .	37
3.3	Solar cell production . . . . .	38
3.4	Characterization techniques . . . . .	39
3.4.1	Structural properties . . . . .	40
3.4.2	Optical properties . . . . .	43
3.4.3	Opto-electronic properties . . . . .	45
3.5	Numerical methods . . . . .	47
3.5.1	One-dimensional simulations . . . . .	48
3.5.2	Three-dimensional simulations . . . . .	49
<b>4</b>	<b>Sinusoidal nano-structures</b>	<b>51</b>
4.1	Previous work . . . . .	51
4.2	Process development . . . . .	53
4.2.1	Optimization of the reactive ion etching process . . . . .	53
4.2.2	Structural analysis of sinusoidal structures . . . . .	56
4.3	Optical analysis . . . . .	57
4.3.1	Optical properties of different interlayer stacks . . . . .	58
4.3.2	Optical properties of sinusoidal nano-textures . . . . .	60
4.4	Solar cell results . . . . .	61
4.5	Conclusion . . . . .	64
<b>5</b>	<b>Smooth anti-reflective three-dimensional textures</b>	<b>67</b>
5.1	Previous work . . . . .	67
5.2	SMART texture production . . . . .	69
5.3	Optical analysis . . . . .	72

5.3.1	Simulations . . . . .	72
5.3.2	Comparison of experiment and simulations . . . . .	74
5.4	Proof-of-concept solar cells . . . . .	76
5.5	SMART texture optimization . . . . .	82
5.5.1	Titanium oxide sol-gel annealing . . . . .	82
5.5.2	Combination with light-trapping measures . . . . .	85
5.5.3	Implementation of novel interlayer developments . . . . .	88
5.6	Towards solar cells on optimized SMART texture . . . . .	92
5.7	Conclusion . . . . .	94
<b>6</b>	<b>Tailor-made micro-textures for light trapping</b>	<b>97</b>
6.1	Process development and optimization . . . . .	97
6.1.1	Variation of the gas composition . . . . .	98
6.1.2	Process parameter optimization . . . . .	100
6.2	Structural analysis . . . . .	102
6.2.1	Grain orientation dependency . . . . .	102
6.2.2	Surface analysis . . . . .	105
6.3	Optical analysis . . . . .	109
6.4	Solar cell results . . . . .	114
6.5	Conclusion . . . . .	117
<b>7</b>	<b>Discussion</b>	<b>119</b>
7.1	Optical loss analysis . . . . .	119
7.1.1	The Tiedje-Yablonovitch limit for silicon thin-film solar cells . . . . .	119
7.1.2	Losses in state-of-the-art planar devices . . . . .	121
7.1.3	Loss analysis for textured LPC silicon thin-film solar cells . . . . .	124
7.1.4	Conclusion . . . . .	127
7.2	Potential applications for other solar cell types . . . . .	130
<b>8</b>	<b>Summary and Outlook</b>	<b>133</b>
	<b>List of Figures</b>	<b>139</b>
	<b>List of Tables</b>	<b>140</b>
	<b>Bibliography</b>	<b>141</b>
	<b>Appendices</b>	
<b>A</b>	<b>Scientific Contributions</b>	<b>ix</b>
<b>B</b>	<b>Acknowledgement</b>	<b>xiii</b>
<b>C</b>	<b>Declaration</b>	<b>xv</b>

# 1 Introduction

The year 2017 was the first year in which renewable electricity generation including wind, solar, and biomass surpassed that from coal in the European Union, proving the competitiveness of renewable technologies with conventional concepts relying on fossil fuels. Of these renewable energy technologies, photovoltaics contributes about 20 % to power generation [1].

The photovoltaic market is dominated by silicon wafer-based technologies with a market share over 90 % [2], including both mono-crystalline and multi-crystalline silicon solar cells and modules. Record devices, with power conversion efficiencies of 26.6 % [3, 4] and 22.3 % [4, 5], respectively, operate close to the physical limit of 29.4 % for a silicon solar cell [6, 7]. Hence, cost reduction should not only be driven by efficiency improvement and approaches to reduce manufacturing costs should be investigated. One possibility to achieve this is the reduction of material consumption. In the current technology, however, the potential for thinner silicon wafers is limited by sawing losses and handling issues [2].

Several approaches to overcome these challenges were studied [8, 9], including kerfless wafers [10–13], epitaxial silicon growth with substrate transfer [14–16] and thin-film solar cells [17, 18]. Potential benefits of thin-film solar cells include material reduction, large-scale and high throughput production, and a monolithic module integration. An excellent material quality comparable to wafer-based devices on low-cost substrates is required to realize potential cost benefits.

Due to their reduced absorber thickness, all of these approaches depend on efficient light management schemes [19, 20], which aim at reducing reflection losses (light in-coupling) or increasing the light path in the absorber (light trapping) in order to maximize the amount of incident photons absorbed in the solar cell. The implementation of surface textures constitutes an efficient measure for improved light management in thin-film silicon solar cells. Light management textures have been studied in experiment and simulations. Generally, the texture needs to be tailored for the respective solar cell type. Studied structures include dielectric random [21, 22] and periodic [20, 22–24] textures, as well as approaches based on plasmonic effects of metallic nano-structures [25, 26]. Furthermore, concepts where the absorber

layer itself is three-dimensionally textured were investigated, including nano-wires [27, 28], nano-holes [29–31], nano-cones [32] and nano-domes [33].

One promising approach to realize efficient thin-film silicon solar cells is the direct growth and crystallization of 10  $\mu\text{m}$  to 20  $\mu\text{m}$  thick silicon layers on glass substrates. Material quality of this concept could significantly be enhanced by substituting solid phase crystallization (SPC) [17, 34] by liquid phase crystallization (LPC) [35–38]. During LPC the sample is scanned under a line-shaped energy source, shortly heating the underlying silicon layer over its melting temperature. On solidifying, already crystallized areas act as seed layers, resulting in a crystalline silicon layer with grains of several millimeter in width and centimeters in length [39].

LPC silicon solar cells on glass demonstrated increasing solar cell efficiencies in recent years, rising from initially less than 5% in 2011 to 14.2% in February 2018 [40–43]. The main developments were based on optimized interlayers between the glass substrate and silicon absorber layer and the solar cell contacting scheme. Despite this rapid development in solar cell efficiency, the record efficiency of LPC thin-film silicon solar cells on glass is still significantly below that of cells on multi-crystalline silicon wafers. Solar cell parameters of this LPC silicon record cell are compared to the record device produced on high performance multi-crystalline wafers in Table 1.1, revealing that both the open-circuit voltage  $V_{\text{oc}}$  and fill factor  $FF$  are approaching values close to those reached for record wafer-based devices. The main difference in efficiency arises from the short-circuit current density  $j_{\text{sc}}$ , which is about 30% lower for LPC silicon solar cells. In consequence, implementing efficient light management measures is required to close this gap.

**Table 1.1:** Solar cell parameters short-circuit current density  $j_{\text{sc}}$ , open-circuit voltage  $V_{\text{oc}}$ , fill factor  $FF$  and power conversion efficiency  $\eta$  of the record cells for LPC silicon [43] compared to high performance multi-crystalline (mc-Si) wafer-based devices [5].

Cell type	thickness $\mu\text{m}$	$j_{\text{sc}}$ $\text{mA cm}^{-2}$	$V_{\text{oc}}$ $\text{mV}$	$FF$ $\%$	$\eta$ $\%$
LPC silicon	15	29.0	654	74.9	14.2
mc-Si wafer	195	41.1	674	80.5	22.3

Figure 1.1(a) illustrates the schematic stack of the basic optical structure of a LPC silicon thin-film solar cell. It exhibits a planar glass-silicon interface with a three-layer interlayer stack. These serve as diffusion barrier against glass impurities during high-temperature processes, anti-reflective coating, and wetting and passivation layer. At the back-side of the 15  $\mu\text{m}$  thick absorber, a random pyramid texture is produced by wet-chemical etching in potassium hydroxide. Finally, a rear reflector is employed to reduce transmission losses.

An absorption spectrum of a typical LPC silicon thin-film solar cell (solid) is depicted in Fig. 1.1(b), compared to the Tiedje-Yablonovitch limit (dashed) constituting the maximum absorptance in 15  $\mu\text{m}$  thick silicon (cf. section 2.1.2 and [44]). The maximum achievable short-circuit current density  $j_{\text{sc,max}}$  of a silicon solar cell with a thickness of 15  $\mu\text{m}$  is already reduced from 43.9  $\text{mA cm}^{-2}$  to 40.5  $\text{mA cm}^{-2}$  due to low absorptance in the near infrared. For a LPC silicon solar cell on glass, additional losses from reflection at the interfaces from air to glass and glass to silicon and from non-absorption (shaded area) reduce the maximum achievable short-circuit current density to 33.8  $\text{mA cm}^{-2}$ . Hence, the current device design exhibiting planar interlayers at the glass-silicon interface causes a  $j_{\text{sc,max}}$  loss of 6.7  $\text{mA cm}^{-2}$ .

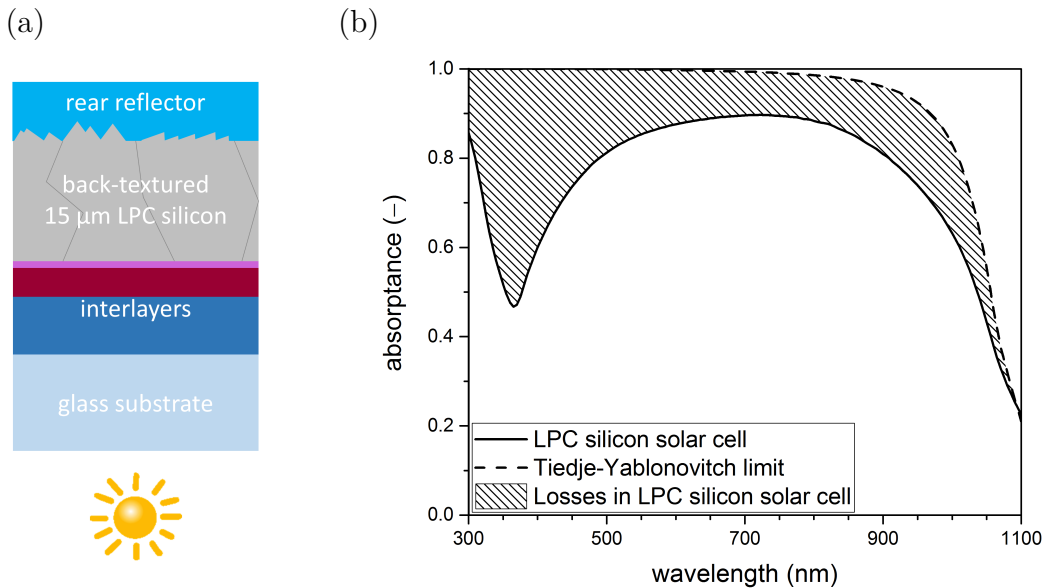


**Figure 1.1:** (a) Schematic of the optical structure of a LPC silicon thin-film solar cell. (b) Absorptance of a 15  $\mu\text{m}$  thick LPC silicon thin-film absorber with a random pyramid texture and reflector at the back-side (solid) and the corresponding Tiedje-Yablonovitch limit (dashed) constituting the upper limit of absorptance [44]. Losses due to reflection at the sun-facing interfaces and non-absorptance are highlighted (shaded area).

Nano- and micro-textures were implemented in liquid phase crystallized silicon thin-film solar cells on glass, aiming at reducing the  $j_{\text{sc,max}}$  loss by improved light management. Several textures were previously studied [45–52], either by periodic structures using nano-imprint lithography (NIL) [45–49] or by directly texturing the glass substrate [50–52]. Textured glass substrates with a random structure could be produced by mechanical abrasion using sand-blasting [51, 52], by wet-chemical etching using sacrificial layers [50] and by nano-imprinting of an etched zinc oxide surface [45]. Periodic structures that were investigated contain a square lattice of U-shaped micro-textures [45–47], and hexagonal nano-pillars and sinusoidal textures [48, 49]. By developing a method to preserve the texture at the back-side of the silicon absorber, double-sided structured LPC silicon layers could be established [45]. In addition to

the anti-reflective effect, the structures enhanced back-scattering at the back-side of the silicon absorbers, thus increasing the light path and absorptance also for long wavelength light.

However, all investigated approaches did not lead to an increase in short-circuit current density compared to state-of-the-art planar devices. For higher textures, this could be explained by electronic losses that were caused by additional defects introduced by the textures [45, 48]. The U-shaped micro-texture lead to dislocations that caused recombination of charge carriers at the interface and in the bulk [45]. These losses were less severe for sinusoidally textured substrates, but recombination was still higher than for solar cells with planar substrates [48]. For randomly textured substrates with small feature sizes, the structures did not cause additional defects and the material quality was found to be equivalent to planar devices. Yet, the anti-reflective effect of these textures was not very pronounced and, therefore, short-circuit current density did not exceed that of state-of-the-art devices.

This trade-off between optical properties and material quality of textured solar cells has been well-known for other silicon thin-film technologies, e.g. poly-crystalline [53, 54] and micro-crystalline silicon thin-film solar cells [55–58]. One successful approach to overcome this trade-off for light trapping at the back-side of micro-crystalline silicon thin-film solar cells was the flat light scattering substrate (FLiSS) [59–62]. In this FLiSS approach, a periodic [59] or random [60, 61] zinc oxide texture was smoothed by an amorphous silicon deposition and subsequent polishing. This allowed material growth with high material quality while exploiting the scattering of the optically rough texture.

Another technique employed in amorphous silicon solar cells used imprinting of random nano- and micro-pyramids and spin-coating of zinc oxide nanoparticles for anti-reflection, allowing a power conversion efficiency increase of 18% (relative) [63].

In this thesis, several approaches to reduce the main optical losses described above are investigated with respect to their potential to increase the short-circuit current density of state-of-the-art LPC silicon thin-film solar cells on glass while preserving the electronic material quality of the solar cell, as schematically illustrated in Fig. 1.2. The focus hereby lies on the development of tailored nano- and micro-structures that combine both, enhanced optical properties and a material quality equivalent to state-of-the-art LPC silicon thin-film solar cells. In particular, nano-structures at the buried glass-silicon interface, namely sinusoidal textures and smooth anti-reflective three dimensional textures, are examined with respect to their ability to enhance light in-coupling while fulfilling the requirements posed for interlayers during LPC processing. A method for the production of tailor-made micro-textures independent

of silicon crystal grain orientation at the silicon back-side is introduced and micro-textures produced using this approach are investigated with respect to their light trapping properties.

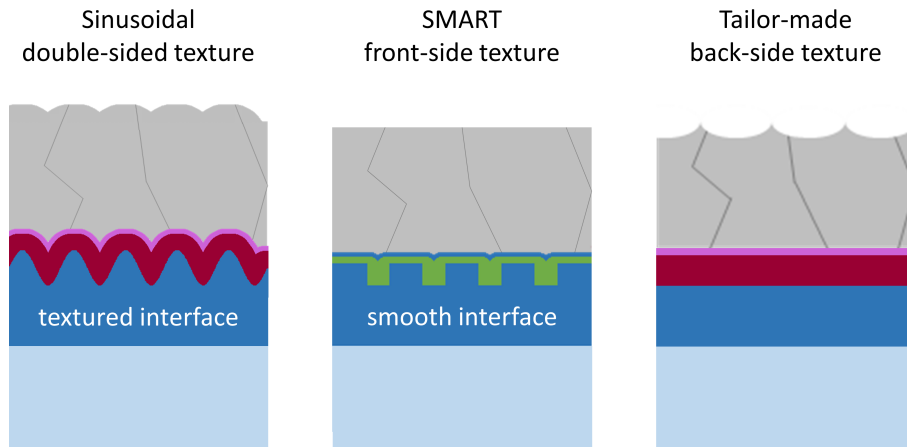


**Figure 1.2:** Schematic stacks of the light management textures investigated in this thesis, including double-sided sinusoidal textures, front-side smooth anti-reflective three-dimensional (SMART) textures and tailor-made back-side textures.

Firstly, a novel method for nano-structure production using a combination of nano-imprint lithography and reactive ion etching is applied to the sinusoidal texture. That way, height-to-period ratios of 0.5 were reached, whereas the previously employed method limited height-to-period ratios to 0.3. In consequence, light in-coupling properties of LPC silicon absorbers on sinusoidally textured substrates could be improved. Interlayers that were found to enhance the interface quality for planar LPC silicon solar cells are implemented in the process for solar cells exhibiting a sinusoidal texture to analyze the influence of interlayers on the optical properties and material and interface quality of textured LPC silicon thin-film solar cells.

A second texture at the glass-silicon interface that was developed in the scope of the thesis is an optically rough texture with a smooth surface, inspired by the FLiSS approach. This “smooth anti-reflective three-dimensional” (SMART) texture aims at combining the advantages of textured interfaces of enhanced light in-coupling with that of planar interfaces, namely optimal passivation properties. The SMART texture could be realized by combining a silicon oxide nano-pillar texture produced by nano-imprint lithography with spin-coating of titanium oxide. The spin-coating leads to a preferential material deposition in the areas between the nano-pillars, leaving a smooth surface that is optically rough due to the contrast in refractive indices between silicon oxide, titanium oxide and silicon.

The third approach deals with the challenges posed for light trapping at the back-side of LPC silicon thin-film absorbers. Using a combination of nano imprint lithography and reactive ion etching, tailored micro-textures can be produced independent

of the silicon crystal grain orientation, in contrast to the state-of-the-art method of wet-chemical etching using potassium hydroxide. Honeycomb textures of different periods and height-to-period ratios were produced in LPC silicon employing this technique. The optical properties of these textures are analyzed and compared to several textures known from literature.

Finally, optical losses in state-of-the-art device designs for LPC silicon thin-film solar cells on glass are investigated in experiment and simulation. The potential of the texturing methods and textures developed in the scope of this thesis to mitigate these losses are presented. Additionally, first experiments for the application of the back-side texturing method for monolithic perovskite/silicon tandem solar cells are presented.

The thesis is structured as follows:

**Chapter 2** summarizes the theoretical backgrounds underlying the topics presented in the thesis. In particular, optical and electronic properties of silicon, the basic working principles of (silicon) solar cells and main loss mechanisms are discussed.

**Chapter 3** gives an overview of experimental and numerical methods employed in the thesis. Experimental methods include the processes for the production of nano-textured liquid phase crystallized silicon thin-film solar cells that were applied or developed in the scope of this thesis. In addition, characterization and simulation techniques used are presented.

**Chapter 4** establishes the nano-structure production process using a combination of nano-imprint lithography and reactive ion etching for sinusoidal textures with a higher height-to-period ratio compared to previous work. In addition, novel interlayer deposition techniques developed for state-of-the-art LPC silicon solar cells with a planar glass-silicon interface are applied to sinusoidally textured substrates. The properties of high height-to-period ratio sinusoidally textured glass substrates in combination with these novel interlayers with respect to light in-coupling and solar cell characteristics are analyzed.

**Chapter 5** describes the production of the smooth anti-reflective three-dimensional texture and its implementation in the liquid phase crystallization solar cell process. The SMART texture is established using experimental and numerical methods, and an experimental proof of outperforming a state-of-the-art LPC silicon thin-film solar cell on glass is presented. Further optimization of the titanium oxide layer and combination of the SMART texture with back-side textures is investigated and implemented in LPC silicon thin-film solar cells.

**Chapter 6** comprises the method of tailor-made silicon back-side texturing using nano-imprint lithography and reactive ion etching. Optimized parameters for nano-structure etching are presented and applied to a wide range of honeycomb textures,

revealing a texturing independent of silicon crystal grain orientation. The optical properties of LPC silicon thin-film solar cells on glass exhibiting these textures are investigated and compared to the established method of wet-chemical etching using potassium hydroxide.

**Chapter 7** addresses optical losses of state-of-the-art LPC silicon thin-film solar cells on glass from experiment and simulations. The approaches presented in the previous chapters are analyzed with respect to their potential to mitigate these losses in state-of-the-art LPC silicon thin-film silicon solar cells on glass. In addition, ways to utilize the presented methods for monolithic perovskite/silicon tandem solar cells are discussed.

**Chapter 8** summarizes the thesis and gives an outlook to future work.



## 2 Theoretical background

This chapter gives a concise overview of the physical background of the experiments conducted in this thesis. Section 2.1 introduces the solar spectrum used for solar energy conversion and its interaction with matter. In this light, optical loss mechanisms in silicon solar cells are discussed. Subsequently, the basics of light management employed to reduce these losses are described. Another loss mechanism of solar cells are electronic losses. An overview of electronic properties of silicon and its defects is given in section 2.2. Finally, the basic working principles of solar cells are presented in section 2.3.

### 2.1 Optical properties of silicon

Solar cells convert sunlight to electrical energy. Hence, their optical properties need to be optimized to fit the spectral irradiance of the sun at the earth's surface. Figure 2.1(a) depicts the solar AM1.5g irradiance spectrum [64] representing the mean solar irradiance during the year for both direct and diffuse light.

Silicon is a semiconductor with an indirect bandgap of 1.12 eV, corresponding to a wavelength of around 1100 nm (highlighted in grey in Fig. 2.1(a)). The spectral (grey) and cumulative (black) photon flux corresponding to the spectral irradiance is calculated and illustrated up to a wavelength of 1100 nm in Fig. 2.1(b). Light with a wavelength longer than the silicon band gap is only weakly absorbed. In silicon wafer-based solar cells, the wavelength range from 1100 nm to 1200 nm still contributes to current generation, but is negligible for thin-film silicon devices. It is found that while irradiation is highest for a wavelength of 550 nm, the maximum photon flux is observed at  $\approx 670$  nm. The cumulative photon flux at 1100 nm of  $43.9 \text{ mA cm}^{-2}$  represents the maximum achievable photon flux that a silicon solar cell can convert into electrical energy. In reality, the current generated by the solar cell will be lowered by optical losses, e.g. reflection and non-absorption, and electrical losses, which will be discussed in the following sections.

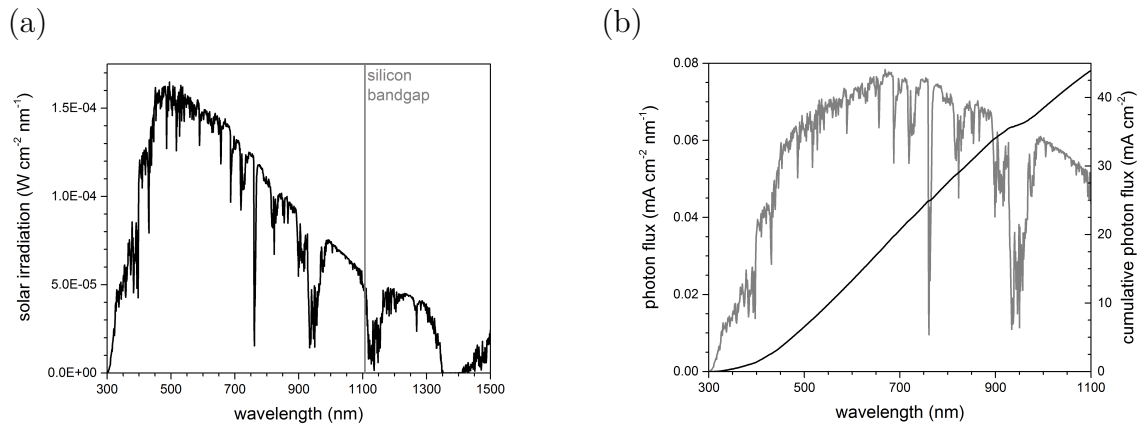


**Figure 2.1:** (a) Solar AM1.5g irradiance spectrum (data taken from [64]). The wavelength corresponding to the bandgap of silicon is highlighted in grey. (b) Spectral (grey) and cumulative (black) photon flux calculated from the solar irradiance spectrum in (a). The cumulative photon flux at 1100 nm represents the maximum achievable short-circuit current density of a silicon solar cell (cf. section 2.3).

Due to its indirect bandgap, light absorption in silicon for a photon energy  $< 3.4$  eV requires a process with a phonon to allow for energy as well as momentum conservation [65–67]. The absorption coefficient  $\alpha(E_{\text{ph}})$  of an indirect band gap semiconductor at a photon energy of  $E_{\text{ph}}$  can therefore be written as [65, 68, 69]

$$\alpha(E_{\text{ph}}) = \alpha_e(E_{\text{ph}}) + \alpha_a(E_{\text{ph}}), \quad (2.1)$$

where

$$\alpha_e(E_{\text{ph}}) = \frac{c(E_{\text{ph}} - E_g + E_{\text{phonon}})^2}{\exp\left(\frac{E_{\text{phonon}}}{kT}\right) - 1}, \quad (2.2)$$

represents light absorption under the emission of a phonon (index e) and

$$\alpha_a(E_{\text{ph}}) = \frac{c(E_{\text{ph}} - E_g - E_{\text{phonon}})^2}{1 - \exp\left(\frac{-E_{\text{phonon}}}{kT}\right)}, \quad (2.3)$$

describes light absorption if a phonon is absorbed (index a), with  $E_g$  and  $E_{\text{phonon}}$  being the bandgap and phonon energy, respectively.  $c$  is a material specific constant,  $k$  the Boltzmann constant and  $T$  the temperature. The absorption coefficient is frequently expressed as a function of wavelength  $\lambda = hc/E_{\text{ph}}$  rather than energy  $E_{\text{ph}}$ .

According to Lambert-Beer's law [66, 70], the light intensity  $I$  in a medium decreases as

$$I(z, \lambda) = I(z = 0, \lambda) \exp(-\alpha(\lambda) \cdot z). \quad (2.4)$$

For a semiconductor layer of thickness  $t$ , the absorptance  $A(\lambda)$  is then defined by

$$A(\lambda) = \frac{I(z = 0, \lambda) - I(z = t, \lambda)}{I(z = 0, \lambda)} = 1 - \exp(-\alpha(\lambda) \cdot t). \quad (2.5)$$

An intuitive measure to evaluate absorptance in semiconductors is the inverse of the absorption coefficient, the so-called penetration depth  $\alpha(\lambda)^{-1}$ . The penetration depth represents the thickness at which the light intensity is reduced to  $1/e$  of its initial intensity. Figure 2.2 demonstrates the penetration depth in crystalline silicon in the wavelength range of interest for silicon solar cells. For reference, the typical thicknesses of a wafer-based (grey) and liquid phase crystallized (red) silicon solar cell,  $180 \mu\text{m}$  and  $15 \mu\text{m}$ , respectively, are highlighted by horizontal lines.

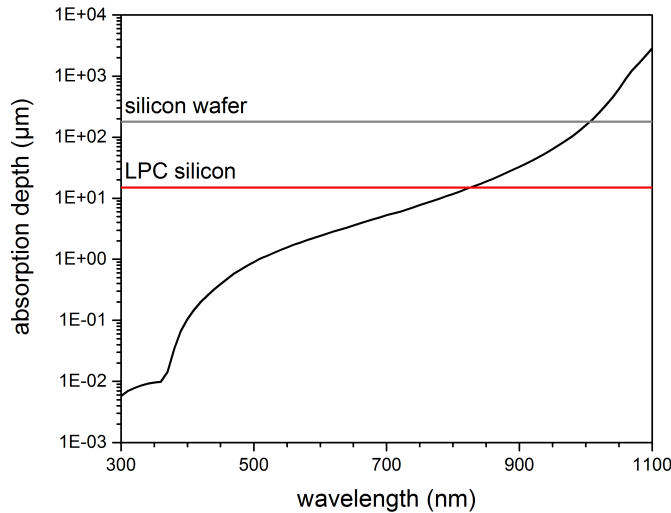


**Figure 2.2:** Spectral absorption depth in crystalline silicon. The typical thicknesses of a wafer-based (grey) and liquid phase crystallized (red) silicon solar cell,  $180 \mu\text{m}$  and  $15 \mu\text{m}$ , respectively, are highlighted for reference.

The penetration depth can be employed to estimate an appropriate thickness of a solar cell. For silicon, a minimum absorber layer of several hundred micrometer is required to absorb the entire usable spectrum up to the band gap energy [19, 66, 71]. For a thinner absorber, in particular a liquid phase crystallized silicon absorber with a thickness of only  $15 \mu\text{m}$ , the penetration depth becomes larger than the absorber thickness at a wavelength of around  $800 \text{ nm}$  (see Fig. 2.2). Thus, additional light

management measures need to be employed (see section 2.1.2) to still absorb a substantial fraction of the incoming light.

### 2.1.1 Light-matter interaction

The optical properties of a solar cell are not only influenced by absorption events, but also by light propagation through the media constituting the solar cell. Light propagation in a medium can be described by its (complex) refractive index

$$n(\lambda) = n'(\lambda) + i k(\lambda), \quad (2.6)$$

where its real part

$$n'(\lambda) = \frac{c_{\text{vacuum}}}{c_{\text{medium}}} \quad (2.7)$$

is referred to as (real) refractive index and its imaginary part

$$k(\lambda) = \frac{\alpha(\lambda) \cdot \lambda}{4\pi} \quad (2.8)$$

is the extinction coefficient describing the attenuation of an electro-magnetic wave propagating through a medium [72]. If two media with refractive indices  $n_1$  and  $n_2$  are brought together, an interface with an abrupt change in refractive index is formed, as sketched in Fig. 2.3.

If light travelling in medium 1 encounters this interface under an angle  $\theta_1$ , it is partly reflected and partly enters medium 2. The angle of propagation in medium 2 is given by Snell's law [69]

$$n_1 \sin \theta_1 = n_2 \sin \theta_2 \quad (2.9)$$

One consequence of Snell's law is the occurrence of total internal reflection. This can take place for  $n_1 > n_2$  under the condition that  $\theta_2 \geq 90^\circ$ . The so-called total internal reflection angle  $\theta_{\text{crit}}$  is determined to

$$\theta_{\text{crit}} = \arcsin\left(\frac{n_2}{n_1}\right). \quad (2.10)$$

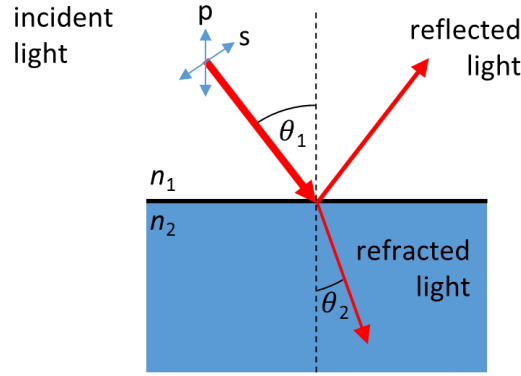


**Figure 2.3:** Sketch of incident light travelling through a medium with refractive index  $n_1$ , approaching an interface to a medium with  $n_2$  under an incident angle  $\theta_1$ . Light is partly reflected back into medium 1 or transmitted into medium 2 while being refracted into an angle of  $\theta_2$ . The polarization states of the incoming light, namely perpendicular (s) and parallel (p) to the plane of incidence, are depicted as blue arrows.

The electro-magnetic light wave can be factored in two components, whereby as a convention, the direction of the electric light parallel (so-called *s*-polarization) and perpendicular (*p*-polarization) to the plane of incidence [69] is taken as reference. The polarization directions are sketched for the incident light in Fig. 2.3 (blue arrows).

The proportion of light being reflected or transmitted at the interface between medium 1 and medium 2 is given by the Fresnel equations [69]

$$r_s(\theta_1) = \frac{n_1 \cos \theta_1 - n_2 \cos \theta_2}{n_1 \cos \theta_1 + n_2 \cos \theta_2} \quad (2.11)$$

$$t_s(\theta_1) = \frac{2 n_1 \cos \theta_1}{n_1 \cos \theta_1 + n_2 \cos \theta_2} \quad (2.12)$$

for *s*-polarized light and

$$r_p(\theta_1) = \frac{n_1 \cos \theta_2 - n_2 \cos \theta_1}{n_1 \cos \theta_2 + n_2 \cos \theta_1} \quad (2.13)$$

$$t_p(\theta_1) = \frac{2 n_1 \cos \theta_1}{n_1 \cos \theta_2 + n_2 \cos \theta_1} \quad (2.14)$$

for *p*-polarization. The total intensity reflected at the interface under the assumption

of unpolarized light is calculated as

$$R(\theta_1) = \frac{1}{2} (r_s(\theta_1)^2 + r_p(\theta_1)^2) . \quad (2.15)$$

For perpendicular incidence,  $\theta_1 = 0$ , this can be simplified to [65, 73, 74]

$$R(\theta_1 = 0) = \left( \frac{n_1 - n_2}{n_1 + n_2} \right)^2 . \quad (2.16)$$

The solar cell type investigated in this thesis employs silicon as absorber material on glass substrates. Hence, the basic structure is a stack of three media consisting of air (medium 1), glass (medium 2) and silicon (medium 3), as sketched in Fig. 2.4. In this structure, reflection and transmission occur at all interfaces. In consequence, light can be reflected back into medium 1 by reflectance at every interface of the device (orange arrows in Fig. 2.4). For the first interface formed by air and glass with  $n_1 = 1.0$  and  $n_2 = 1.5 - 1.52$  [75], a reflectance for normal incidence of 4% is calculated from Eq. (2.16). As the refractive index of silicon varies with the light wavelength, reflection at the glass-silicon interface varies between 50% at 300 nm and 17% at 1200 nm with a mean value of 21.3% [76].

Only the fraction of light transmitted through these interfaces can be absorbed in the silicon absorber (red arrows). For a penetration depth of the light in the absorber material smaller than the absorber thickness, light is absorbed during a first pass through the silicon layer. If light is not absorbed in the first pass, it is, again, either reflected or transmitted at the silicon back-side. If light is transmitted, it leaves the solar cell (purple arrow) and can not be used for current generation. Back-reflected light passes the absorber a second time and may be absorbed during this pass. Evidently, all of the events may take place multiple times, which were omitted in the figure and description for clarity.

To cut a long story short, light incident on a solar cell can either be absorbed in the device or be reflected and transmitted at single or multiple interfaces. This can be described by the relation

$$A(\lambda) = 1 - R(\lambda) - T(\lambda) , \quad (2.17)$$

as visualized in Fig. 3.12(b) in the next chapter.

To maximize absorption  $A(\lambda)$  in a solar cell, both reflectance  $R(\lambda)$  and transmittance  $T(\lambda)$  need to be minimized. This can be achieved by implementing light management measures which will be discussed in the following section.

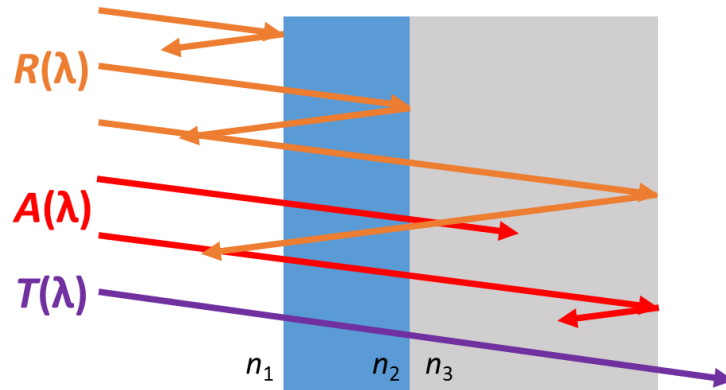


**Figure 2.4:** Sketch of light paths representing reflection ( $R(\lambda)$ , orange), absorption ( $A(\lambda)$ , red), and transmission ( $T(\lambda)$ , purple) in a basic solar cell with a sun-facing layer of refractive index  $n_2$  and an absorber layer with refractive index  $n_3$ . Those paths with multiple passes through the layers were omitted for clarity.

## 2.1.2 Light management

As described previously, about one in four photons is reflected back before reaching the silicon absorber in the basic device design. Depending on the wavelength of the incoming light and the resulting penetration depth in silicon (see Fig. 2.2), a large fraction of light is transmitted after passing the silicon absorber (cf. Fig. 3.12(b)) or even leaves the absorber after multiple passes. These losses are addressed by implementing light management measures in the solar cell devices aiming at reducing reflection (light in-coupling) and non-absorption (light trapping).

### Light in-coupling

Light in-coupling aims at reducing reflection losses before the incoming light first encounters the silicon absorber. In the device design discussed in this thesis, light in-coupling measures are implemented at the glass-silicon interface. Three main approaches for light in-coupling are discussed in the following, which can also be combined for additional benefits [19, 66, 77].

- The first approach relies on the implementation of additional layers [72, 78–80]. Introducing a third material at the interface between materials with refractive indices of  $n_1$  and  $n_2$  can lead to a reduction of reflection. This so-called **graded index effect** can be achieved if the refractive index  $n_3$  of the additional layer fulfills the requirement  $n_1 < n_3 < n_2$  [72]. More specifically, an optimum refractive index of  $n_{3,opt} = \sqrt{n_1 \cdot n_2}$  can be derived from Eq. (2.15). As an

example, anti-reflection at the glass-silicon interface is optimized for a material with a refractive index of  $n_3 = \sqrt{n_{\text{glass}} \cdot n_{\text{silicon}}} \approx 2.4$  (cf. magenta curve in Fig. 5.3).

- Secondly, **anti-reflective coatings** can affect the light in-coupling into solar cells [80–83]. In contrast to the first approach, they are usually tailored to one specific wavelength  $\lambda_{AR}$ , e.g. 550 nm matching the solar spectrum. Anti-reflection coatings with a thickness of  $\lambda_{AR}/4$  reduce the reflectivity due to destructive interference, caused by the incoming light being out of phase with the reflected beam [72, 83]. Generally, the materials for anti-reflective coatings are chosen such that their refractive index gives an additional graded-index effect (see above). As an example, a  $\approx 70$  nm thick  $\text{SiN}_x$  layer with  $n_{\text{SiN}_x} \approx 2.0$  is usually employed at the glass-silicon interface in LPC silicon solar cells, combining the graded index effect of an intermediate refractive index medium with anti-reflective interference effects at wavelengths close to 550 nm.
- Last, **surface and interface textures** are used to minimize reflection losses at interfaces. Surface roughness with both a random or deterministic texture are employed in solar cells. Interface texturing facilitates several anti-reflective effects. For one thing, a surface texture with features smaller than the wavelength may lead to a gradual change of intermixing media and their effective refractive index, corresponding to a graded index effect of multiple layers [80, 82, 84–86]. Secondly, surface textures much larger than the wavelength may lead to multiple reflections at the interface prior to back-reflection [87–89]. If the surface texture feature size and wavelength is comparable, both aforementioned effects as well as wave optical phenomena influence the anti-reflective properties [90, 91], lacking a vivid description.

Summarizing, light in-coupling over an interface can be improved by implementing intermediate layers with a refractive index between the media forming the interface to create a graded index effect. If the intermediate layers exhibit an appropriate optical thickness of  $\lambda/4$ , an additional anti-reflective coating effect due to destructive interference is achieved. Thirdly, interface textures improve light in-coupling, whereby the mechanisms dominating light in-coupling effects depend on the relation of light wavelength and typical texture feature dimensions.

### Light trapping

Light in-coupling efficiently reduces front reflection in solar cells. However, apart from some interface textures, they do not scatter the incoming light. Hence, in-

cident light with normal incidence travels through the absorber perpendicular to the (planar) interfaces. For a small absorption coefficient as is the case for long wavelength light in silicon (see Fig. 2.2), this leads to substantial losses [92–95]. Light trapping measures aim at increasing the light path in the solar cell to increase absorptance for light which is weakly absorbed. A commonly used figure of merit hereby is the light path enhancement factor [77], quantifying the light path in a textured device compared to a given reference, most common a comparable structure with planar interfaces. Two different methods for light trapping are introduced in the following:

- The first light trapping measure is a **back reflector** that reflects a large fraction of light back into the absorber. This leads to a light path enhancement factor of 2. Materials that are frequently employed as back reflectors in solar cells are dielectric layers [96, 97], metallic mirrors [98–100] or white paint back reflectors [54, 96].
- As a second measure, **back-side textures** are implemented to scatter light into large angles. This not only enhances the light path in the absorber by changing the propagation direction, but also increases the probability of being reflected back at the front-side of the device or even exceeding the critical angle for total internal reflection described in Eq. (2.10) [101, 102]. As already stated for front-side textures, both statistical and deterministic surface textures are employed in solar cells. For light trapping, texture periods typically are chosen to be much larger than the light wavelength, such that geometrical optics dominate optical properties. As an example, the most common back-side texture for crystalline silicon solar cells are random pyramids produced by wet-chemical etching in potassium hydroxide [103–105].

A widely used benchmark for light management is the **Lambertian scatterer**. This structure consists of a semiconductor of thickness  $t$  and a texture with following properties: Firstly, a front-side reflection of zero is assumed. Secondly, the light propagation direction is perfectly randomized by the texture, corresponding to an angular intensity distribution of  $\cos(\theta)$ . A perfect back reflector at the rear side completes the structure. For this stack, Yablonovitch et al. derived a theoretically maximum achievable light path of  $4n^2t$  [101], which is often referred to as **Yablonovitch limit**.

Absorptance  $A(\lambda)$  in a semiconductor slab of thickness  $t$  exhibiting a non-reflecting front surface and a perfect Lambertian back reflector at the back-side was calculated

to [44]

$$A(\lambda) = \frac{\alpha(\lambda)}{\alpha(\lambda) + \frac{1}{4n^2t}}. \quad (2.18)$$

This **Tiedje-Yablonovitch absorption limit** constitutes the benchmark for optimal light trapping in thin-film solar cells. While being physically valid only in the weak absorption limit ( $t \times \alpha \ll 1$ ), the Tiedje-Yablonovitch limit is widely used in literature for textured solar cells and is therefore employed as benchmark in this thesis.

For periodic structures with a period in the range of the wavelength of the incident light, the Yablonovitch limit could be surpassed. If the texture period is comparable to the light wavelength, it is rather diffracted than scattered, thus coupling into modes in the absorber material [106–108]. As these modes exhibit sharp resonances, overcoming of the Yablonovitch limit was only achieved for narrow wavelength and incident angle ranges [20, 106, 109]. In consequence, the Lambertian scatterer is a suitable benchmark for light trapping in solar cells.

The samples featured in this thesis make use of all the above light management techniques. Reference samples exhibit a 70 nm thick silicon nitride layer with a refractive index of 2.0, serving as both graded index layer and anti-reflective coating. Interface textures are investigated in light of their potential to improve light in-coupling in liquid phase crystallized silicon thin-film solar cells. At the back-side of the silicon layers, the state-of-the-art random pyramid texture produced by wet-chemical etching and white-paint rear reflector are employed for reference samples and devices with front-side texture. Additionally, periodic micro-textures for light trapping are investigated.

## 2.2 Electronic properties of silicon

Realistic silicon crystals exhibit defects, limiting the lifetime of charge carriers in the material [67, 74, 110–112]. As liquid phase crystallized silicon is a multi-crystalline material, additional defects at grain boundaries, so-called intra-grain defects, occur. Grain boundaries with a high number of dangling bonds, stacking faults, point defects, and dislocations were identified as most important defects in this material [113–116]. These defects introduce energy states in the bandgap of the material. The degree of recombination hereby depends on the position of a specific defect [67, 117]. The most effective recombination centers are found in the middle of the bandgap.

Shallow defects can be used to provide additional charge carriers in the semiconductor material, thus causing a doping effect. This is done by introducing suitable foreign atoms into the semiconductor crystal. If the energy difference to the valence or conduction band is in the order of the thermal energy  $k_B T \approx 25$  meV at room temperature [67, 69], one electron (n-type doping) or hole (p-type doping) of the foreign atom is transferred to the host crystal and contributes to an enhanced conductivity. For silicon, phosphorus and boron are the most common dopants for n-type and p-type silicon, respectively.

Illumination or current injection leads to excess electron-hole pairs that cause a disturbance of the thermal equilibrium, in which the semiconductor evinces carrier concentrations of  $n_0$  and  $p_0$ , whereby  $n_0 \times p_0 = n_i^2$  holds, with the intrinsic carrier concentration  $n_i$  being a material constant. Excess carriers  $\Delta n$  and  $\Delta p$  are calculated by

$$n = n_0 + \Delta n = N_C \exp\left(-\frac{1}{k_B T}(E_C - E_{F,n})\right) \quad (2.19)$$

$$p = p_0 + \Delta p = N_V \exp\left(\frac{1}{k_B T}(E_V - E_{F,p})\right), \quad (2.20)$$

where  $N_C$  and  $N_V$  denote, respectively, the effective density of states at the conduction and valence band edge energies  $E_C$  and  $E_V$ . The quasi Fermi energy  $E_F$  is separately defined for electrons and holes [118, 119].

### 2.2.1 Electronic loss mechanisms

As additional charge carriers disturb the thermal equilibrium in the semiconductor, excess electrons and holes tend to restore the equilibrium by recombining with a recombination rate  $U$  of

$$U(\Delta n) = -\frac{\delta \Delta n}{\delta t}. \quad (2.21)$$

The three most common recombination mechanisms will briefly be discussed in the following. Band-to-band and Auger recombination are characteristic for the absorber material and unavoidable. Shockley-Read-Hall (SRH) recombination, in contrast, involves a defect state and depends on the defect density [69, 117, 120].

- **Band-to-band recombination** is a radiative process in which the energy of the recombining electron-hole pair is transferred to a photon and, in case of an indirect semiconductor, an additional phonon. This radiative recombination constitutes the inverse process to the generation of an electron-hole pair after absorption. Band-to-band recombination rates are rather low in indirect semiconductors like silicon as a phonon needs to be involved.
- **Auger recombination** is a three-particle process involving an electron-hole pair and an additional charge carrier. The excess energy of the recombining electron-hole pair is transferred to an additional charge carrier, which subsequently relaxates back to its initial state by transferring its extra energy and momentum to phonons. Due to the Auger recombination involving three particles, its recombination rate quadratically depends on carrier concentration [121]. Auger recombination limits the maximum solar cell efficiency of silicon solar cells to 29.4% [7], compared to the Shockley-Queisser limit of 32.3%. It is crucial for high excess carrier density conditions like high-injection and highly doped semiconductors with doping concentrations around  $10^{18}$ . For LPC silicon thin-film solar cells, the influence of Auger recombination can be neglected [122].
- Recombination involving a defect state is referred to as **Shockley-Read-Hall (SRH)** recombination. In SRH recombination, the charge carrier is trapped in a defect with a trap energy within the band gap. This energy is characteristic for the type of defect, e.g. impurity atoms or crystallographic defects. Defects causing a trap energy close to the band edges, like those introduced by doping atoms, are less harmful as the trapped charge carriers can be re-emitted with a high probability. In consequence, defects in the middle of the band gap are the most effective recombination centers [67, 69, 117, 120]. SRH recombination is the dominant recombination mechanism in indirect semiconductors. For LPC silicon, in particular, grain-boundary recombination and regions with a high concentration of stacking faults were identified as the dominant recombination processes [123].

As all of the above processes occur in parallel, the total recombination rate in the absorber is given by the sum of the individual contributions

$$U_{\text{total}} = U_{\text{rad}} + U_{\text{Auger}} + \sum_i U_{\text{SRH},i}, \quad (2.22)$$

whereby multiple defect types  $i$  contribute to SRH recombination.

The **bulk carrier lifetime** defined as

$$\tau_{\text{bulk}} = \frac{\Delta n}{U_{\text{total}}} \quad (2.23)$$

can therefore be calculated from

$$\frac{1}{\tau_{\text{bulk}}} = \frac{1}{\tau_{\text{rad}}} + \frac{1}{\tau_{\text{Auger}}} + \frac{1}{\tau_{\text{SRH}}} . \quad (2.24)$$

In addition to bulk recombination, interfaces at the front and back-side of the absorber layer exhibit a high amount of defects due to the termination of the crystal lattice. The recombination rate at interfaces is calculated similarly to SRH recombination. As the number of defects is so high, the trap states can be treated as a continuum of states in the bandgap and a single surface recombination rate  $U_s$  is given by integrating over the energy range from the valence to the conduction band edge. From this, the **surface recombination velocity**

$$S(n_s, p_s) = \frac{U_s(n_s, p_s)}{\Delta n_s} \quad (2.25)$$

is calculated for surface carrier concentrations of  $n_s$  and  $p_s$  and an excess carrier concentration  $\Delta n_s$  at the surface.

Finally, the **total effective carrier lifetime**  $\tau_{\text{eff}}$  in an absorber layer of thickness  $t$  taking both bulk and interface recombination into account is given by [65, 67, 124, 125]

$$\frac{1}{\tau_{\text{eff}}} = \frac{1}{\tau_{\text{bulk}}} + \frac{S_{\text{front}} + S_{\text{back}}}{t} := \frac{1}{\tau_{\text{bulk}}} + \frac{1}{\tau_s} . \quad (2.26)$$

While bulk recombination takes place in the volume, surface recombination is calculated per unit area [126]. Hence, an increased surface recombination is expected if textures that increase the surface area are introduced in the solar cell.

To reduce recombination in a silicon absorber bulk, hydrogen passivation can be employed [127–130]. In this method, hydrogen ions diffuse into the silicon layer, where they saturate dangling bonds to form a Si–H bond which gives rise to a defect state out of the band gap. A similar chemical passivation can be used to saturate surface defects, e.g. by growing a silicon oxide on the surface that terminates the absorber with Si–O bonds [19]. Recombination at a surface can further be reduced

by implementing a material causing fixed charges at the interface. This so-called field effect passivation effect repels similarly charged carriers in the absorber from the interface, thus slowing recombination. Several materials [131–138], including silicon nitride [131, 138] and silicon oxide [130, 132], provide suitable fixed charges to exploit a field effect passivation in silicon.

Solar cells investigated in this thesis typically exhibit a silicon oxide or silicon oxynitride layer followed by a silicon nitride layer for passivation. For LPC silicon thin-film solar cells, n-type doping was found to be beneficial [139], stemming from a lower surface recombination velocity for n-type compared to p-type silicon [140]. Hence, all absorber layers in this thesis exhibit n-type doping.

## 2.3 Solar cell characteristics

Solar cells utilize the electron-hole pairs generated by light absorption (section 2.1.1) for electrical power generation. To do this, the electron-hole pairs need to be transferred to an external circuit via contact layers before they recombine (section 2.2.1). Under ideal conditions, a solar cell can be described using an equivalent circuit of a diode characterized by the dark saturation current  $j_0$  [65, 67, 69, 141] given by

$$j_0 = e n_i^2 \left( \frac{D_n}{L_n N_A} + \frac{D_p}{L_p N_D} \right), \quad (2.27)$$

where  $e$  is the elementary electron charge,  $n_i$  the intrinsic charge carrier density,  $D_n$  and  $D_p$  the electron and hole diffusion constants, respectively,  $L = \sqrt{D \cdot \tau}$  the diffusion length, and  $N_A$  and  $N_D$  the concentration of acceptor and donor atoms, respectively.

Under illumination, the solar cell is described as a diode in parallel to a current source providing a photo current  $j_{\text{ph}}$ . In this case, the relation between applied voltage and current becomes

$$j_{\text{illum,ideal}}(U) = j_0 \left[ \exp\left(\frac{eV}{k_B T}\right) - 1 \right] - j_{\text{ph}}. \quad (2.28)$$

For a realistic solar cell, recombination losses and losses in contact layers require a more complex equivalent circuit as idealized model, as sketched in Fig. 2.5(a). In comparison to an ideal solar cell, a second diode is introduced that takes recombination processes into account. This second diode has an ideality factor  $n_2 > 1$  [69,

142, 143]. Resistive losses in the contact layers are represented by series resistance  $R_s$  and parallel resistance  $R_p$ .

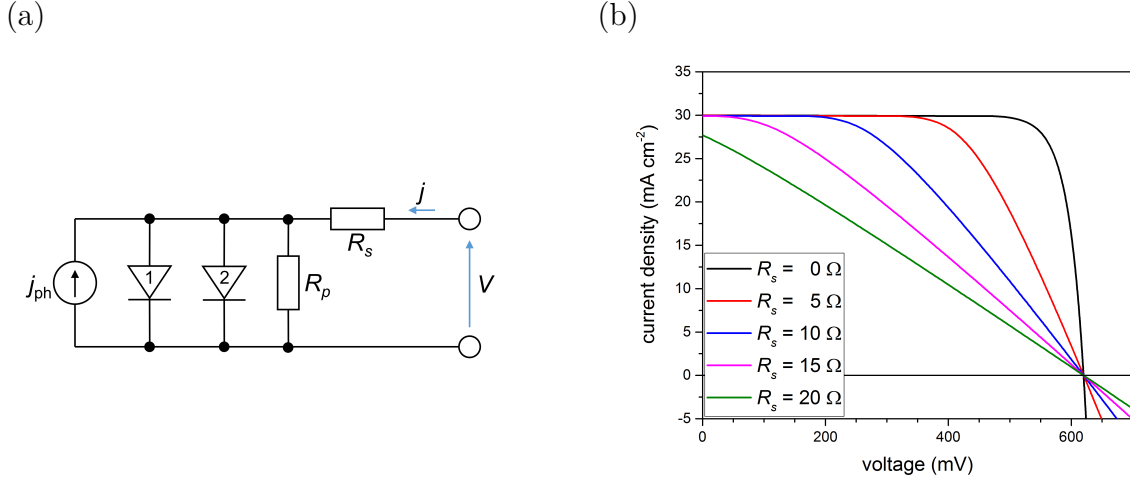


**Figure 2.5:** (a) Equivalent circuit of a solar cell with a two diode model. The second, non-ideal diode takes recombination processes into account, while the series and parallel resistances  $R_s$  and  $R_p$  represent resistive losses in the contact layers. (b) Influence of series resistance on the current-voltage characteristics of a solar cell.

The  $j - V$  characteristics of a solar cell represented by this approximated equivalent circuit is given by [69]

$$j(V) = j_{0,1} \left[ \exp \left( \frac{e(V - AjR_s)}{k_B T} \right) - 1 \right] + j_{0,2} \left[ \exp \left( \frac{e(V - AjR_s)}{n_2 k_B T} \right) - 1 \right] + \frac{V - AjR_s}{R_p} - j_{ph}, \quad (2.29)$$

where  $A$  is the area of the solar cell.

Both series and parallel resistances influence the  $j - V$  characteristics compared to an ideal solar cell. Figure 2.5(b) illustrates the influence of series resistance under the assumption of  $j_0 = 1 \times 10^{-9}$  mA cm<sup>-2</sup>,  $A = 1$  cm<sup>2</sup> and  $j_{ph} = 30$  mA cm<sup>-2</sup>. To focus on the effect of  $R_s$ , the second photo-diode and influence of parallel resistance was omitted in the calculations based on Fig. 2.5(b).

A typical  $j - V$  curve of a solar cell is depicted in Fig. 2.6. The  $j - V$  curve can be used to determine all vital solar cell parameters as illustrated in Fig. 2.6. These parameters are [69, 119, 126, 141]:

- The **short-circuit current density**  $j_{sc}$  is defined as the current flowing through the solar cell if the contact layers are short-circuited, corresponding to  $V = 0$ . Under ideal conditions, the short-circuit current density equals  $-j_{ph}$ , as is easily derived from Eq. (2.28). In a real device, recombination

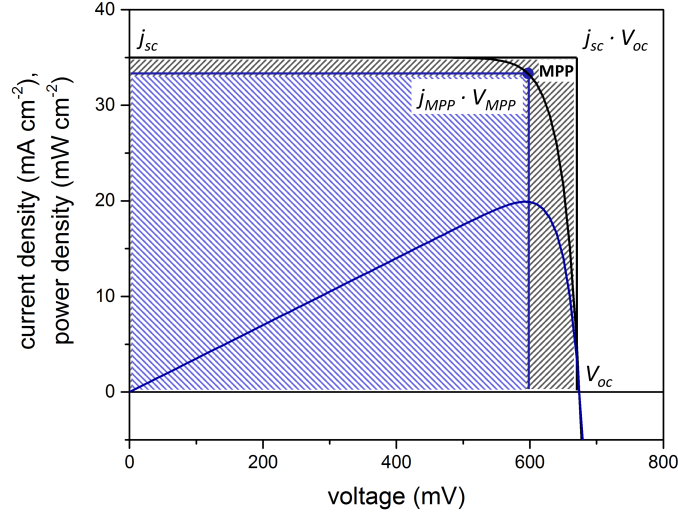


**Figure 2.6:** Typical  $j - V$  curve (black) and corresponding  $P - V$  curve (blue) of a solar cell. The maximum power point (MPP) and the solar cell parameters  $j_{sc}$  and  $V_{oc}$  are denoted. The areas  $j_{MPP} \cdot V_{MPP}$  and  $j_{sc} \cdot V_{oc}$  determining the fill factor  $FF$  are highlighted by blue and grey shading, respectively.

and contact resistances lead to a difference, which is, under the assumption  $R_p \gg R_s$ , calculated to

$$j_{sc} = -j_{ph} + j_{0,1} \left[ \exp \left( \frac{eA j_{sc} R_s}{k_B T} \right) - 1 \right] + j_{0,2} \left[ \exp \left( \frac{eA j_{sc} R_s}{n_2 k_B T} \right) - 1 \right]. \quad (2.30)$$

- The **open-circuit voltage**  $V_{oc}$  is the maximum voltage under which no current is extracted from the device,  $j = 0$ . It constitutes the maximum voltage a solar cell can deliver.  $V_{oc}$  is calculated from Eq. (2.28) to

$$V_{oc} = \frac{k_B T}{e} \ln \left( \frac{j_{ph}}{j_0} + 1 \right) \approx \frac{k_B T}{e} \ln \left( \frac{j_{ph}}{j_0} \right), \quad (2.31)$$

whereby the approximation is justified as  $j_{ph} \gg j_0$ .

Eq. (2.31) reveals that  $V_{oc}$  is linked to  $j_0$ , which in turn depends on recombination in the solar cell (cf. Eq. (2.27)).  $V_{oc}$  can therefore be used as a measure of recombination in solar cells.

- The **fill factor**  $FF$  is defined as the ratio between the maximum power generated by the solar cell,  $P_{MPP} = j_{MPP} V_{MPP}$ , and the product of  $j_{sc}$  and  $V_{oc}$

$$FF = \frac{j_{MPP} \cdot V_{MPP}}{j_{sc} \cdot V_{oc}}. \quad (2.32)$$

The fill factor is graphically depicted in Fig. 2.6 as the ratio of the areas shaded in blue and black.

- The **power conversion efficiency**  $\eta$  is the most important solar cell parameter. It is calculated as the ratio of the maximum power generated by a solar cell and the incident power of the irradiation  $I_{in}$ ,

$$\eta = \frac{P_{MPP}}{I_{in}} = \frac{j_{MPP} \cdot V_{MPP}}{I_{in}} = \frac{j_{sc} V_{oc} FF}{I_{in}}. \quad (2.33)$$

Under standard testing conditions ( $T = 25\text{ }^{\circ}\text{C}$ , irradiation under AM1.5g spectrum), the incident power is set to  $I_{in} = 100\text{ mW cm}^{-2}$ .



# 3 Experimental and numerical methods

This chapter introduces the methods employed for the production of nano-textured substrates (section 3.1), silicon absorbers (section 3.2), back-side textures on these absorbers (section 3.2.1), and solar cells (section 3.3). Tools for the characterization of the produced samples (section 3.4) are presented as well as numerical methods for one-dimensional and three-dimensional simulations (section 3.5).

The smooth anti-reflective three-dimensional texture and its production method described in section 3.1.3 was filed as a patent [144].

## 3.1 Substrate preparation

### 3.1.1 Nano-imprint lithography

Nano-imprint lithography (NIL) is a lithographic technique that allows to produce nano-structures with high throughput at high resolution and low costs [145]. It relies on a two-step replication of a master structure in resist materials using molds. In a first step, an inverse master structure is produced in a mold material, which is subsequently pressed into a liquid resist. The resist is then cured, usually by thermal treatment or UV light, and the mold removed from the hardened resist containing the replicated master structure.

In this section, the production of master structures with a honeycomb pattern and their inversion is described before giving a detailed overview over the nano-imprint lithography process as it is applied in this thesis.

#### Honeycomb master production

Honeycomb masters were fabricated in the Nano-Processing facility at the National Institute of Advanced Industrial Science and Technology (AIST) in Tsukuba, Japan.

The fabrication process, which is sketched in Fig. 3.1, was established by Sai et al. [146–148]. There, the honeycomb pattern serves as a textured substrate in the production of high-efficiency micro-crystalline silicon thin-film solar cells [146–150]. Silicon wafers with a thermal silicon oxide layer with a thickness of 1000 nm or 1800 nm were coated with a UV-curable negative-tone resist (step 1 in Fig. 3.1). Using a photolithography i-line stepper set-up, hexagonal hole arrays with periods of 1.5  $\mu\text{m}$ , 3.0  $\mu\text{m}$  and 6.0  $\mu\text{m}$  were scribed from a photo mask previously produced at AIST and subsequently opened in the resist layer by developing the resist (step 2). Different diameters of the openings allow varying height-to-period ratios in the later honeycomb master structures.

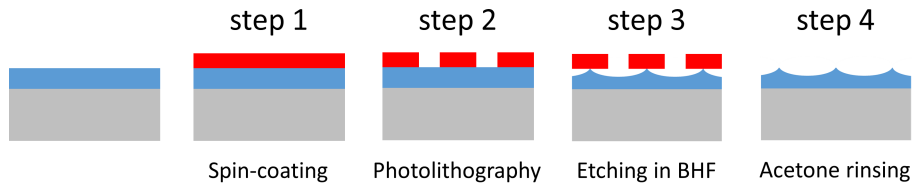


**Figure 3.1:** Schematic production process for master structures with a honeycomb pattern relying on photolithography (step 2) and wet-chemical etching in buffered hydrofluoric acid (BHF, step 3).

The wafers with the patterned resist layers were subsequently etched in a mixture of buffered hydrofluoric acid (BHF) of 7 : 1  $\text{NH}_4\text{F}:\text{HF}$  and de-ionized water (step 3). The resist hereby serves as an etching mask, and the underlying oxide is etched only where the resist was opened in the previous patterning step. The wet-chemical etching leads to under-etching of the resist layer, whereby bowl-shaped trenches emerge. By changing the dilution of BHF in de-ionized water, the depth of these trenches can be varied. Once the trenches from adjoining holes overlap, the resist layer starts peeling from the surface and the wafer is pulled from the etching solution. Resist residues are removed by rinsing the sample in acetone (step 4).

The surfaces of honeycomb masters were analyzed using an atomic force microscope to extract the heights of varying etching conditions. The texture height was determined measuring from the highest point to the bottom of the bowl-shaped trench. Using the technique described above, honeycomb textures with height-to-period ratios ranging from 0.1 to 0.3 were manufactured for the periods of 1.5  $\mu\text{m}$ , 3.0  $\mu\text{m}$  and 6.0  $\mu\text{m}$ . Table 3.1 summarizes the parameters of hole diameter and etchant dilution for the produced master structures.

Before using the masters in nano-imprint lithography, an anti-sticking layer was deposited on the surface of the honeycomb patterned masters. For this, the surface of the wafer was activated in an oxygen plasma. Subsequently, an anti-sticking layer

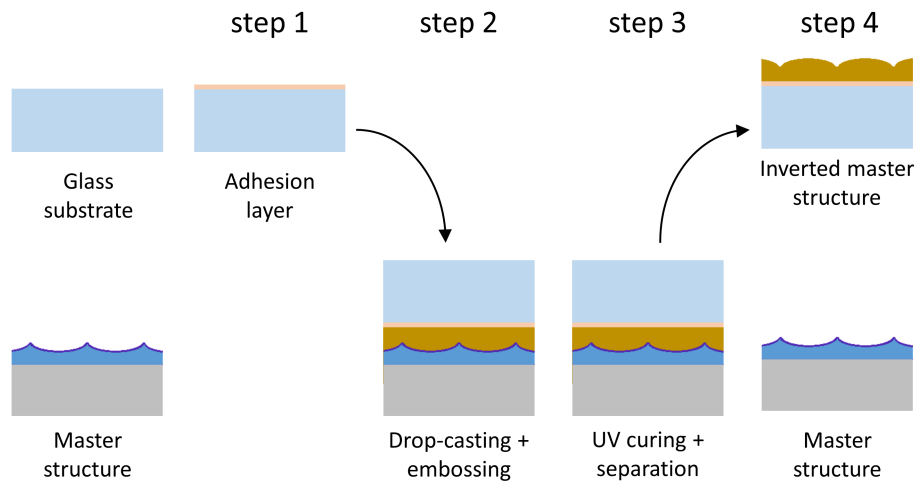
**Table 3.1:** Hole diameter in photolithography and etchant dilution in de-ionized water used in honeycomb master production.

hole diameter (nm) etchant dilution (%)		height-to-period ratio			
		0.1	0.2	0.25	0.3
period ( $\mu\text{m}$ )	1.5	750 nm	500 nm	500 nm	
		70%	60%	10%	
	3.0	600 nm	600 nm	600 nm	600 nm
		90%	60%	20%	10%
	6.0	1200 nm	1200 nm	1200 nm	
		80%	60%	30%	

of 1H,1H,2H,2H-perfluorodecyl-trichlorosilane was applied by vacuum evaporation deposition [145].

### Master inversion

The honeycomb masters were originally developed as light trapping textures for micro-crystalline silicon thin-film solar cells in substrate configuration. Liquid phase crystallized silicon thin-film solar cells, in contrast, are superstrate devices, e.g. the light impinges through the glass. Hence, light encounters the texture from the opposite direction compared to the multi-crystalline silicon thin-film solar cell. To investigate the influence of this difference, the produced honeycomb masters were inverted as described in refs. [151, 152]. This method, as sketched in Fig. 3.2, relies on a commercial working stamp material (OrmoStamp from micro resist technology GmbH) as inverting layer.

**Figure 3.2:** Schematic production process of inverted honeycomb patterns using OrmoStamp (brown color) as master structure in UV-NIL.

A glass sheet is used as substrate for the inverted pattern structure. An adhesion promoting layer (OrmoPrime 08 from micro resist technology GmbH) is spin-coated on the glass (step 1 in Fig. 3.2) to facilitate a facile separation of the inverted structure in the latter processing. The working stamp material is drop-cast on the master structure and the glass substrate is embossed onto the master by applying gentle pressure (step 2). After UV curing, the hardened layer is separated from the master structure (step 3), comprising the inverted master structure on its surface (step 4). In a final step, an anti-sticking layer of 1H,1H,2H,2H-perfluorodecyltrichlorosilane is applied on the inverted master structure by vacuum evaporation deposition [145].

### UV-NIL texturing

Master production is generally the most time- and cost-intensive step. Consequently, nano-imprint lithography (NIL) was developed to facilitate a reproduction of this master structure in a low cost, high throughput procedure [145, 153–155]. Fig. 3.3 depicts the schematic nano-imprint lithography process, which is divided in two main processes. In a first step (Fig. 3.3(a)), a mold with the inverse of the master structure is produced in the polymer poly(dimethylsiloxane) (PDMS). For this, a commercially available PDMS precursor and suitable catalyst are mixed in a 9 : 1 ratio and degassed in a desiccator to prevent gas bubbles in the later mold. After degassing, the viscous PDMS is poured on the master structure (step 1) and thermally annealed at 70 °C for 20 min (step 2). The thermal treatment hardens the PDMS layer and facilitates a residue-free removal (step 3), thereby ensuring a non-destructive process that allows re-using the master structure repeatedly.

In the second processing sequence (Fig. 3.3(b)), the PDMS mold is employed to reproduce the master structure in a UV-curable resist. As substrates, Corning Eagle XG<sup>®</sup> glass sheets with a size of 5 × 5 cm<sup>2</sup> and a silicon oxide diffusion barrier were utilized. Details about the diffusion barrier processing can be found in section 3.2. In the scope of this thesis, two types of resist materials were used, namely a high-temperature stable sol-gel produced by Philips [156], and organic and hybrid polymers developed and produced by micro resist technology GmbH [157, 158]. The Philips sol-gel is based on a composition of methyl-tri-methoxy-silane and tetramethoxy-ortho-silicate, which forms a silicon-oxygen network after curing [156]. The hybrid polymer OrmoComp<sup>®</sup> consists of an unsaturated anorganic-organic hybrid polymer that exhibits glass-like properties after curing, and provides a short-term temperature stability up to 270 °C [158]. UVcur06 is a purely organic, silicon-free polymer and can therefore be removed residue-free in an oxygen plasma [157]. The high-temperature stable sol-gel is spin-coated onto the substrate first for 10 s at

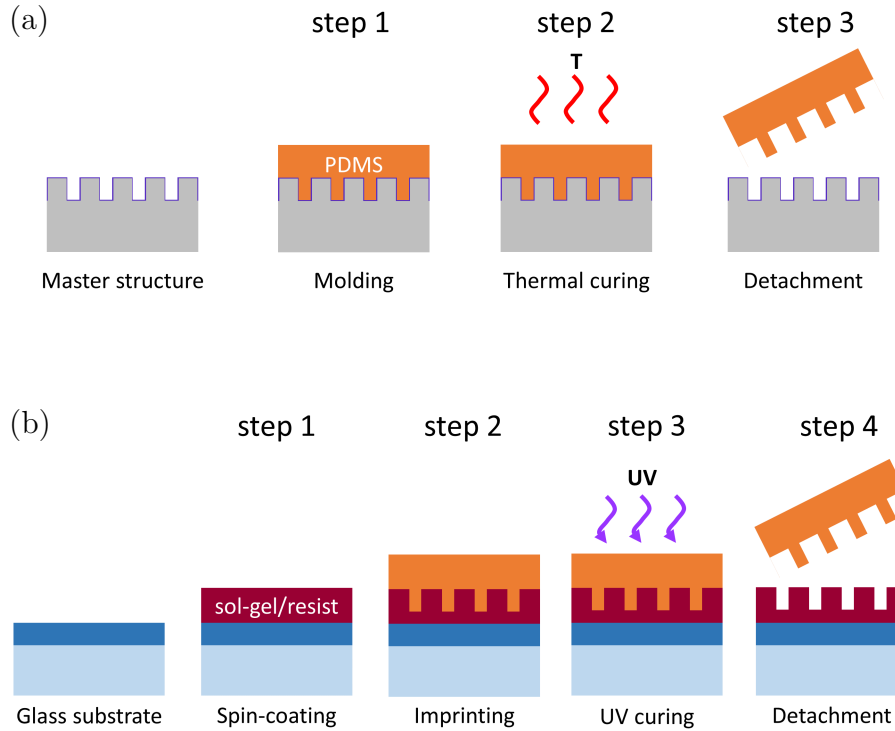


**Figure 3.3:** Schematic of (a) poly(dimethylsiloxane) (PDMS) mold production by molding (step 1) and thermal hardening (step 2) and (b) the imprinting process in a UV-curable sol-gel or resist layer (UV-NIL) by pressing the mold onto a spin-coated resist (step 1 and 2). The resist is then hardened by UV curing through the PDMS mold (step 3).

1000 rpm to form an adhesion layer on the substrate, then for 30 s at 500 rpm to form the bulk of the sol-gel. The two-step spin-coating results in a layer thickness of  $\approx 600$  nm (step 1 in Fig. 3.3(b)). For the organic and hybrid polymer resists, a single spin-coating process is employed, where the spin speed can be varied between 500 rpm and 3000 rpm depending on the desired layer thickness. The resists require a pre-bake for 2 minute at  $80^\circ\text{C}$  prior to imprinting. During imprinting, the PDMS mold is gently rolled onto the coated substrate with the aid of a metal cylinder (step 2). The sol-gel and resists are hardened under a commercial broadband UV light source (step 3) for 5 min, 4 min, and 2 min for the sol-gel, hybrid and organic resist, respectively. Subsequently, the mold is detached from the cured resist (step 4) and may be re-used multiple times. The cured layers are post-baked for 8 min at  $100^\circ\text{C}$  (sol-gel) or 10 min at  $130^\circ\text{C}$  (organic and hybrid resists).

During liquid phase crystallization of silicon, the substrate is heated to temperatures above  $700^\circ\text{C}$ . In addition, the textured substrates come into direct contact with the molten silicon during LPC for several seconds, heating the substrate further. The textured substrates need to withstand these temperatures and processing peculiarities, which requires additional processing steps to ensure stability at these temperatures (Fig. 3.4). For the high-temperature stable sol-gel, a thermal anneal-

ing for 1 h at 600 °C (step 2) is performed to drive out all organic residues. Over the course of this, the sol-gel volume shrinks by about 30 – 50%, in particular also reducing the structure height.

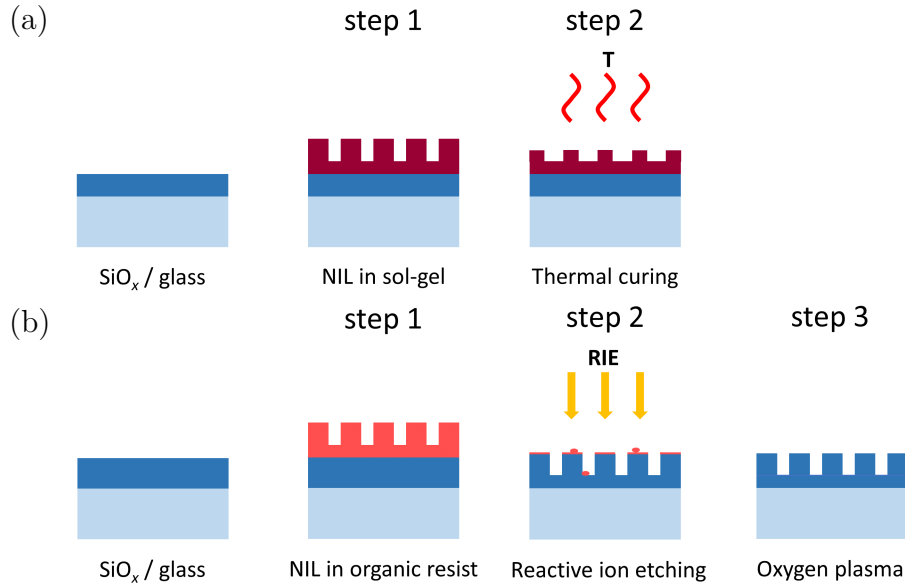


**Figure 3.4:** Comparison of further processing after nano-imprinting to ensure high-temperature stability, for (a) a high-temperature stable sol-gel using thermal annealing and (b) a resist layer transferred to silicon oxide by reactive ion etching.

The organic and hybrid resists are not directly suitable for high-temperature processing. They can, however, be used for pattern replication by reactive ion etching, which will be discussed in more detail in the following section.

### 3.1.2 Texturing of silicon oxide layers

Reactive ion etching (RIE) allows to replicate nano-imprinted textures in the underlying silicon oxide diffusion barrier without shrinkage, in contrast to the previously employed method using high-temperature stable sol-gels. To comprehend the procedure of texture replication using NIL and RIE, reactive ion etching is firstly introduced before discussing the particularities of the NIL+RIE method which was developed in the scope of this thesis.

#### Reactive ion etching

In reactive ion etching, as sketched in Fig. 3.5, etching gases (red color) are injected in an evacuated chamber, where they are ionized in a plasma (purple) and accel-

erated towards the sample (blue). The choice of etch gases determines the etching mechanism. Inert gases like Argon result in a purely physical etching, while suitable reactive species for the target material additionally give rise to a chemical etch rate. The chamber pressure during the process is controlled by changing the position of a butterfly valve towards the vacuum pump. The plasma is generated using either a capacitive-coupled radio frequency (RF, orange) or inductively-coupled plasma (ICP, green) power source. Generally, an inductively-coupled plasma is characterized by a high plasma density, leading to high etch rates and isotropic etch profiles. The capacitive-coupled power provides directional electric fields and therefore typically results in anisotropic etching profiles [67, 159–161]. In this thesis, an Oxford 80 ICP etcher was employed. By utilizing both, RF and ICP powers, their advantages of directional etching and high etch rate, respectively, can be combined.

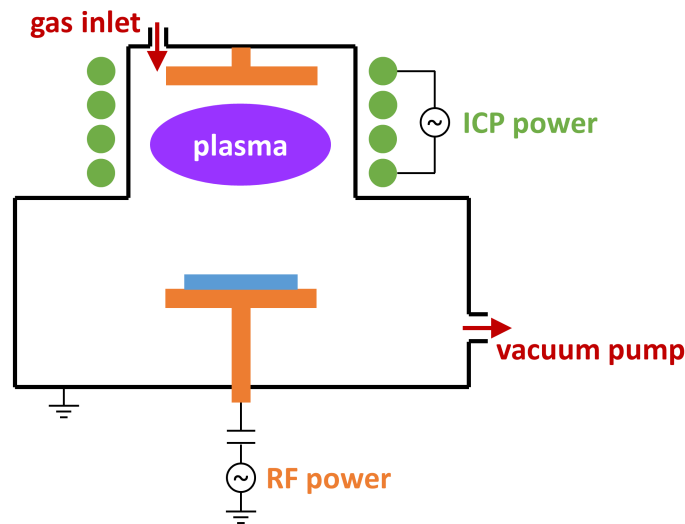


**Figure 3.5:** Schematic structure of a reactive ion etching chamber with a radio frequency (RF, orange) and inductively-coupled plasma (ICP, green) power source. Etching gases (red) are ionized in a plasma (purple) and accelerated towards the sample (blue).

### Reactive ion etching of silicon oxide

Reactive ion etching is applied to produce textured glass substrates as light in-coupling structures in LPC silicon solar cells. This process relies on a combination of nano-imprint lithography (NIL) and reactive ion etching (RIE), whereby a nano-imprinted textured resist serves as three-dimensional soft etching mask during subsequent reactive ion etching. Figure 3.4(b) illustrates a sketch of this texture replication process. The texture is to be replicated in the silicon oxide diffusion barrier. Hence, its thickness is increased by the intended texture height to ensure a sufficient residual thickness of at least 200 nm after texturing. A resist layer is

spin-coated onto the coated glass substrate and subsequently textured by NIL (Fig. 3.4(b), step 1). Subsequently, the texture imprinted into the resist is transferred into the underlying silicon oxide layer by reactive ion etching (step 2). Optimized process parameters for the etching of the organic UV-NIL resist UVcur06 into silicon oxide were identified, namely a gas composition of 25 sccm Ar and 25 sccm  $\text{CHF}_3$ , a chamber pressure of  $p = 20$  mTorr, and an RF plasma power of  $P_{\text{RF}} = 200$  W. The reader is referred to section 6.1 for a discussion of parameter optimization. Possible residues of the organic resist can be removed from the sample by an oxygen plasma treatment (step 3), ensuring high-temperature stability in the ensuing high-temperature processes, in particular liquid phase crystallization.

### 3.1.3 SMART texture production

The smooth anti-reflective three-dimensional (SMART) texture relies on a combination of nano-imprint lithography and spin-coating of titanium oxide to produce a texture that is optically rough but, at the same time, features a smooth surface. Figure 3.6 exhibits the schematic production process of a SMART texture that was developed in this thesis. Using UV-NIL, a glass substrate with a nano-pillar texture is produced. Both high-temperature stable sol-gel layers as well as nano-textures produced by reactive ion etching of organic resists may be used for this purpose. A liquid precursor solution consisting of a mildly acidic solution of titanium isopropoxide in anhydrous ethanol [162, 163] is cast on the nano-pillar array and spin-coated for 30 s (Fig. 3.6, step 1). Varying the spin speed between 500 rpm and 3000 rpm leads to varied film thicknesses. Solvents are removed from the layer by heating the sample for 30 min at 150 °C. Subsequently, a compact titanium oxide layer is formed by a second annealing step for 30 min at temperatures between 500 °C and 800 °C (step 2). The spin-coating results in a preferential material deposition in the areas between the nano-pillars, leaving a smooth surface which is “optically rough” due to the refractive index contrast of the employed materials. Finally, a 10 nm thin passivation layer of silicon oxide or silicon oxy-nitride is deposited on the silicon oxide nano-pillar array with the voids filled by titanium oxide to constitute the SMART texture (step 3).

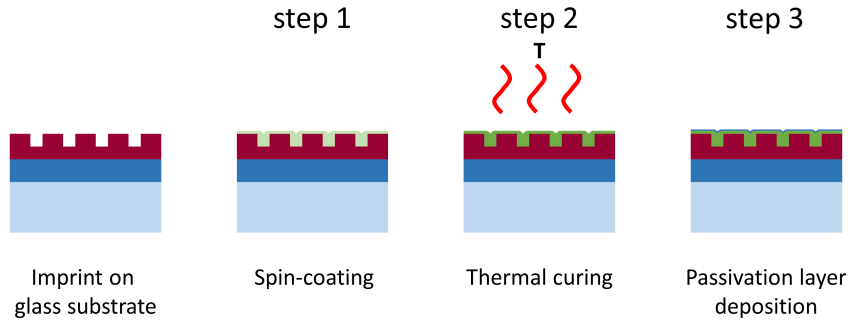


**Figure 3.6:** Schematic production process of a SMART texture by spin-coating a titanium oxide ( $\text{TiO}_x$ ) precursor solution (step 1) on a nano-imprinted nano-pillar array, preferably filling the voids between the pillars. Organic solvents are removed by thermal curing (step 2), resulting in a compact  $\text{TiO}_x$  layer. Finally, a 10 nm thin passivation layer of silicon oxide or silicon oxy-nitride is deposited to constitute the SMART texture (step 3).

## 3.2 Solar cell precursor stack production

High-quality liquid phase crystallized silicon requires the deposition of interlayers that serve as diffusion barrier, anti-reflective coating, and wetting and passivation layers [35–37, 40, 136–138, 164, 165]. The texturing process is implemented in the established process for LPC solar cells exhibiting a planar glass substrate as described in the following.

All glass sheets were firstly coated with a silicon oxide diffusion barrier deposited by plasma-enhanced chemical vapor deposition (PECVD). The diffusion barrier prevents metal impurities from the glass to penetrate into the silicon absorber during high temperature processing. The standard thickness of this diffusion barrier layer is 200 nm. Thicker layers were utilized for textures replicated in the silicon oxide layer to ensure a residual thickness of 200 nm after patterning. A 70 nm thick anti-reflective silicon nitride layer is deposited by PECVD on both textured and planar substrates. This step is omitted for the SMART texture, where the spin-coated titanium oxide layer acts as anti-reflective coating. Finally, a wetting and passivation layer is deposited by PECVD, whereby a 10 nm thin silicon oxide layer [42, 136, 164] or a plasma-oxidized silicon nitride layer [43, 138, 166] is employed. Table 3.2 summarizes the deposition steps for different sample systems discussed in this thesis.

The silicon absorber is deposited on the coated substrates by high-rate electron beam evaporation [38, 53, 167] with a deposition rate of up to  $600 \text{ nm min}^{-1}$  at a heater temperature between  $600^\circ\text{C}$  and  $640^\circ\text{C}$ . Substrate temperature was measured to  $\approx 540^\circ\text{C}$  prior to deposition, during which the temperature drops during the first 100 s of deposition before stabilizing at  $\approx 440^\circ\text{C}$ . Absorber doping is achieved us-

**Table 3.2:** Overview of layer stacks and production processes for different sample types manufactured in this thesis.

substrate	Diffusion barrier	Texture type	Anti-reflective layer	Passivation layer
reference sample	250 nm SiO <sub>x</sub>	–	70 nm SiN <sub>x</sub>	10 nm SiO <sub>x</sub> 10 nm Si(ON)
sol-gel texture	250 nm SiO <sub>x</sub>	Philips sol-gel	70 nm SiN <sub>x</sub>	10 nm SiO <sub>x</sub> 10 nm Si(ON)
SMART texture	250 nm SiO <sub>x</sub>	Philips sol-gel NIL+RIE	≈ 50 nm TiO <sub>x</sub>	10 nm SiO <sub>x</sub> 10 nm Si(ON)
NIL+RIE texture	(250 nm + h <sub>texture</sub> ) SiO <sub>x</sub>	Resist + RIE	70 nm SiN <sub>x</sub>	10 nm SiO <sub>x</sub> 10 nm Si(ON)

ing a thin highly-doped amorphous silicon layer which is deposited by PECVD on top of the electron-beam evaporated silicon. During LPC, doping atoms are evenly distributed in the whole absorber layer [40]. In a final step, a 100 nm thick silicon oxide capping layer is deposited via PECVD. For textured substrates, this capping layer leads to double-sided textured LPC silicon layers [46–48].

Liquid phase crystallization is performed by scanning the sample under a line-shaped laser with a wavelength of 808 nm with a scanning speed of 3 mm s<sup>-1</sup>. Two laser sources were used in this thesis, one with a line width of 3.3 cm and one with 5.0 cm, for which crystallization takes place under vacuum conditions. Crystallization results for both laser sources are equivalent [40]. The crystallization process is followed by a rapid thermal annealing for 1 min at 950 °C to reduce glass deformations resulting from thermal stress induced by the crystallization process.

The silicon oxide capping layer is removed by wet-chemical etching in hydrofluoric acid. Absorbers for electronic characterization undergo a hydrogen plasma treatment for 15 min at a heater temperature of 600 °C to saturate defects in the silicon layer and thereby enhancing material quality [130, 168].

Absorbers for optical characterization were partly produced using solid phase crystallization (SPC) instead of LPC. For SPC silicon absorbers, the deposition temperature during electron beam evaporation is reduced to 300 °C, doping and capping layer deposition is omitted. Solid phase crystallization is performed in a furnace for 20 h at 600 °C. While electronic material quality is limited for SPC silicon [38], optical properties are equivalent to LPC silicon up to a wavelength of 900 nm, allowing to compare light in-coupling properties of SPC and LPC samples up to this wavelength [169].

### 3.2.1 Absorber texturization

The back-side of the silicon absorber can be textured to improve light trapping in the silicon absorber. Two approaches for this were investigated in this thesis, as sketched in Fig. 3.7. For both approaches, the top 300 – 500 nm of the LPC silicon absorber was etched away to remove potential surface damages induced by hydrogen plasma treatment in a silicon etch solution consisting of hydrofluoric acid, nitric acid and phosphorous acid diluted in de-ionized water for 1 min prior to the texturing.

#### Wet-chemical etching

State-of-the-art LPC silicon solar cells rely on a random pyramid texture derived from wet-chemical etching in a solution of potassium hydroxide [42, 43, 51, 52]. Wet-chemical etching is performed at 80 °C in a hydrous solution containing potassium hydroxide (KOH) and an organic etching agent which is provided by GP solar [170]. KOH etching of silicon relies on a silicon crystal grain orientation dependent etch rate [88, 171]. The close-packed {111} direction hereby exhibits the lowest etch rate. In consequence, etching in KOH leads to a silicon surface with bared {111} facets. For a silicon layer with {100} surface orientation, KOH texturing results in a random pyramid texture [171]. For LPC silicon, an etching time of 3 min leads to pyramids with a height up to 2  $\mu\text{m}$ , whereby pyramids are tilted on grains with a crystal grain orientation differing from a {100} surface (see Fig. 3.10 and [88]). Current LPC silicon thin-film solar cells exhibit a random distribution of grain orientations with a tendency towards a {100} surface [123, 172].

#### Reactive ion etching of silicon absorbers

The second texturization method was developed in the scope of this thesis. It relies on a combination of nano-imprint lithography and reactive ion etching to produce tailor-made textures independent of the silicon crystal grain orientation. In a first step, an organic or hybrid resist layer is spin-coated on the liquid phase crystallized silicon absorber and subsequently textured using UV-NIL (Fig. 3.7(b), step 1). In a process similar to the pattern replication in silicon oxide described in section 3.1.2, the texture is transferred into the LPC silicon absorber (step 2). Optimized parameters for pattern replication were identified, namely gas flows of 35.7 sccm  $\text{CHF}_3$  and 14.3 sccm  $\text{SF}_6$  with a chamber pressure of 20 mTorr, an RF power of  $P_{\text{RF}} = 100 \text{ W}$ , and an ICP power of  $P_{\text{ICP}} = 50 \text{ W}$ . A discussion of process optimization is found in section 6.1.2.

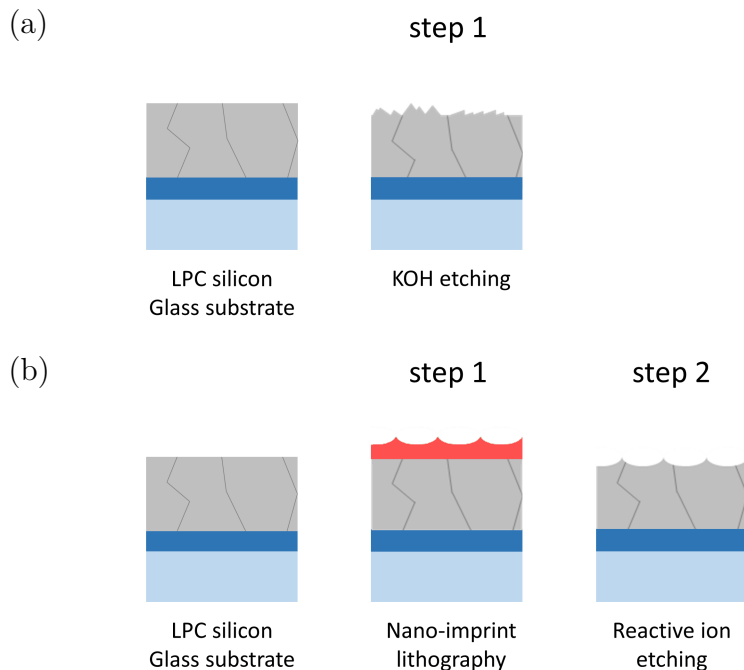


**Figure 3.7:** Schematic production process of back-side textures in liquid phase crystallized (LPC) silicon absorbers using (a) wet-chemical etching in potassium hydroxide (KOH) and (b) a combination of nano-imprint lithography in organic resists and reactive ion etching to replicate the texture in LPC silicon.

### 3.3 Solar cell production

Solar cells were produced using a lithography-free cell design developed by Haschke et al. [39], therein denoted as test structure. While these cells typically exhibit a low fill factor, they still allow a reliable evaluation of the essential solar cell parameters, namely the open-circuit voltage  $V_{oc}$  and short-circuit current density  $j_{sc}$  (cf. section 2.3). The steps involved in the production of these solar cells are schematically depicted in Fig. 3.8. The top 300 – 500 nm of the n-doped absorber are etched away in a silicon etching solution to remove potential surface damage from hydrogen plasma treatment. This step is omitted for devices with a rear-side texture as the damaged surface was already etched away prior to texturization (see section 3.2.1). After an RCA cleaning step, a standard procedure for silicon surface cleaning [173], the full substrate area is covered with a hetero-emitter of 5 nm intrinsic and 10 nm p-doped hydrogenated amorphous silicon (a-Si:H) by PECVD (step 1 in Fig. 3.8). Subsequently, an 80 nm thick indium-doped tin oxide (ITO) layer is deposited on the whole substrate via sputtering. Solar cells are defined by the attachment of sticky polyimide dots with a diameter of 8 mm (step 3), corresponding to a cell area of 0.503 cm<sup>2</sup> in the finished devices.

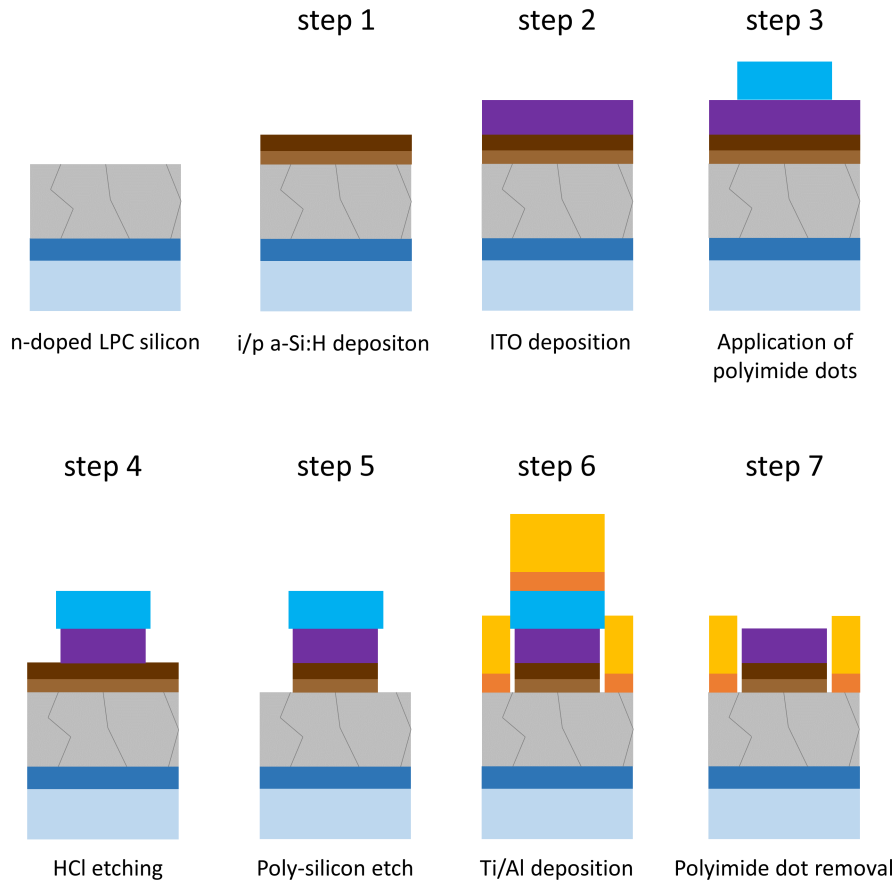


**Figure 3.8:** Schematic production process of the lithography-free solar cell processing employed in the thesis. It exhibits a hetero-emitter and relies on polyimide dots as etching and deposition mask to form the contacts of the solar cell.

Using a mixture of 1 : 1 concentrated hydrochloric acid and de-ionized water, the ITO layer is partly etched away, whereby the polyimide dots act as an etching mask (step 4). Likewise, the a-Si:H layers are removed in a silicon etching solution (step 5). The wet-chemical etching processes result in an under-etching of the polyimide dots, as indicated in step 5 of Fig. 3.8. A metallization of 30 nm titanium and 1  $\mu$ m aluminum is thermally evaporated on the samples (step 6) with the polyimide dots serving as deposition mask. Finally, the polyimide dots are peeled from the samples (step 7). Due to the under-etching during wet-chemical etching, the metal and ITO surfaces form separate contacts of the solar cell.

### 3.4 Characterization techniques

Multiple characterization techniques were employed to analyze the structure of the textures produced in the scope of the thesis (section 3.4.1). The impact of textures

on the optical (section 3.4.2) and electronic (section 3.4.3) properties of liquid phase crystallized silicon thin-film solar cells was investigated.

### 3.4.1 Structural properties

#### Atomic force microscopy

Atomic force microscopy (AFM) measurements were performed using a Park Systems XE-70 equipped with high-aspect ratio tips to investigate surface textures with precision in the nanometer range. During AFM, a cantilever with a sharp tip is scanned over the sample while adapting its height as a result of interactions with the sample. The changing height of the tip is transferred to a topography map of the sample surface [174, 175]. All measurements in the scope of this thesis were performed in the non-contact mode, for which attractive van-der-Waals forces dominate the tip-sample interaction [176]. AFM measurements are therefore a suitable method to investigate textured surfaces for all materials and textures employed in this thesis. As an example for a typical measurement, the surface topography of a nano-imprinted hexagonal nano-pillar array with a nominal period of 1000 nm is depicted in Fig. 3.9.

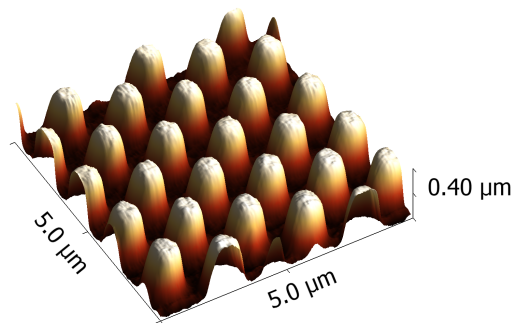


**Figure 3.9:** Example of an atomic force microscope surface image of a nano-imprinted hexagonal nano-pillar array with a nominal period of 1000 nm.

AFM images were used to determine the sample period  $P$  and height  $h$  to derive the height-to-period ratio  $h/P$ . In the presented example, a period of  $P = 1050$  nm and height of  $h = 350$  nm was measured, corresponding to a height-to-period ratio of  $h/P = 0.33$ . The difference between measured to designed period indicates an uncertainty of 5% due to processing and measurement inaccuracies.

Measurements of the sample surfaces using AFM are restricted to a maximum size of  $40 \times 40 \mu\text{m}^2$ . If larger areas are to be investigated, laser scanning confocal microscopy can be employed as an alternative approach.

### Laser scanning confocal microscopy

Laser scanning confocal microscopy (LSCM) is a special kind of light microscope, in which a point source is scanned over the sample surface instead of a large area illumination. For this, a laser beam is focused at a specific height and scanned over the designated surface area. Using a pinhole further reduces the size of the light beam and, as a consequence, enhanced optical resolution and a very low depth of focus. By varying the focus height and stacking multiple surface images, three-dimensional profiles can be extracted from the LSCM measurements.

The measurements presented in this thesis were taken with a KEYENCE VK-X laser scanning confocal microscope. While the resolution of LSCM is lower than that of an atomic force microscope, it allows to measure larger surface areas and larger height differences. Figure 3.10 exhibits an example for a LSCM surface image of a LPC silicon absorber with a random pyramid texture produced by wet-chemical etching in potassium hydroxide with an area of approximately  $70 \times 95 \mu\text{m}^2$ .

LSCM surface imaging was mainly employed for sample surface analysis of larger structures and large areas, e.g. texture variations over the sample.

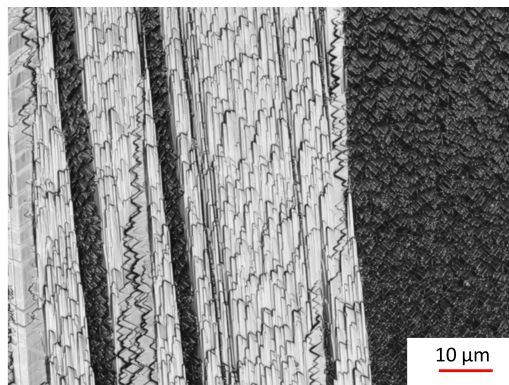


**Figure 3.10:** Example of a laser scanning confocal microscope image of a liquid phase crystallized silicon surface after wet-chemical etching in potassium hydroxide (cf. section 3.2.1).

### Scanning electron microscopy

In scanning electron microscopy (SEM), a focused electron beam is scanned over the sample to measure its surface topography. SEM images were recorded with a HITACHI S-4100 SEM with a cold field emission gun generating electron beams with an acceleration voltage between 5 kV and 30 kV. Electron beam imaging requires measuring in high vacuum. Non-conductive materials potentially lead to charging effects, which inhibit the focusing of the electron beam and cause a blurry

appearance of the respective layers. Hence, the capability of SEM in imaging these materials can be limited.

Incident electrons cause the release of secondary electrons due to elastic and inelastic scattering at atoms near the surface. These secondary electrons are detected together with back-scattered electrons in a suitable detector. The amount of secondary electrons depends on various parameters, in particular the surface topography and materials, and can therefore be used as a parameter for imaging contrast [177, 178]. Tilting the sample holder allows to measure the surface at an angle, notably also in cross section to analyze layered materials. As an example for SEM imaging, Fig. 3.11 illustrates an inverted pyramid texture nano-imprinted into an organic resist partially etched into silicon using reactive ion etching. The image was taken in cross-section with a tilting angle of  $30^\circ$ . The image exhibits two kinds of contrast. Firstly, a material contrast – the resist layer appears darker than silicon. Secondly, a topography contrast is found, in particular an edge contrast at the cleaving edge of the silicon wafer and around the edges of the micro-texture. Remarkably, the non-conductive organic resist layer does not exhibit charging effects in this image.

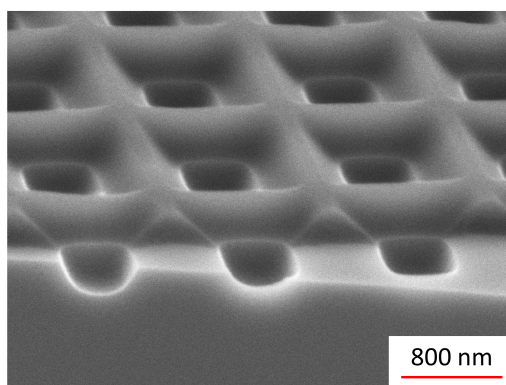


**Figure 3.11:** Example of a scanning electron microscope image of a nano-imprinted texture in an organic resist partially replicated in silicon, in cross-section tilted by  $30^\circ$ .

### Raman spectroscopy

Raman spectroscopy was employed to analyze the crystalline structure of materials used for substrate textures [179], in particular titanium oxide layers derived from sol-gel on silicon substrate. The method relies on inelastic scattering of incoming laser irradiation, in the set-up employed in this thesis with a wavelength of 633 nm. Inelastic scattering by absorption or emission of a phonon give rise to characteristic modes for a material and their crystalline phases. This allows to analyze changes in the structural properties due to processing changes.

### Spectroscopic ellipsometry

Ellipsometry is a suitable method to measure the (complex) refractive index and film thicknesses in planar layer stacks [180]. The measurement principle is based on the polarization change of a light beam reflected at the surface of a specimen. The amplitude ratio  $\Phi$  and phase difference  $\Delta$  depend on both thickness and material properties of the investigated sample. A SENTECH SE-850 spectroscopic ellipsometer was employed to analyze the refractive indices and thicknesses of studied materials. The UV/Vis range with wavelengths between 380 nm and 850 nm was chosen for the optical analysis. Using the producer's SpectraRay software [181], a model of the measured stack was set up using tabulated values for the substrate and Tauc-Lorentz models for the films under investigation [182, 183]. Material parameters were determined by fitting the measured ellipsometry data to the model.

### 3.4.2 Optical properties

#### Optical UV/Vis/NIR spectroscopy

Optical measurements were conducted using a Perkin Elmer UV/Vis/NIR Lambda 1050 photo spectrometer in a wavelength range from 300 nm up to 1200 nm with a step size of 5 nm. Two light sources are used to provide an adequate light intensity over the whole wavelength range. Up to 320 nm, a deuterium lamp is used, while a tungsten lamp provides light for longer wavelengths. The light is monochromatized using a grating monochromator. The part of the measurement set-up used for detection is sketched in Fig. 3.12(a). The monochromatic light is split to generate a reference beam (dashed green in Fig. 3.12(a)) and a probe beam (solid green). The reference beam enters the integrating sphere (blue outline) without hitting the sample and is used to determine the light intensity. The probe beam hits the sample (grey) which is tilted under an angle of  $8^\circ$  to prevent the specular reflection from escaping the integrating sphere through the opening for the probe beam. The integrating sphere is designed to generate a homogenous intensity distribution by diffuse scattering at the sphere's inner surface [184], in particular at the detection area in the bottom of the sphere (black area in Fig. 3.12(a)). Optical measurements presented in this thesis were measured in the center of the integrating sphere instead of measuring in front of (transmittance) or behind (reflectance) the sphere. This allows to correctly measure samples exhibiting pronounced scattering, for which light may be scattered out of the opening of the integrating sphere if measured outside of the sphere. Two detectors are used in the measurements, namely a photomultiplier

up to a wavelength of 820 nm and an indium gallium arsenide detector for longer wavelengths.

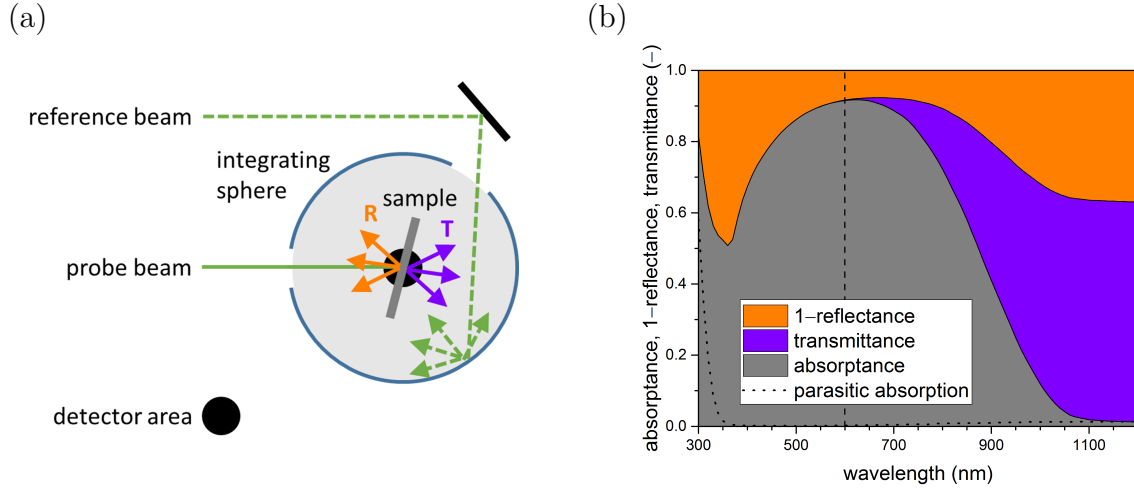


**Figure 3.12:** (a) Schematic measurement set-up of the UV/Vis/NIR spectrometer. (b) Example of an optical spectrum of a 15  $\mu\text{m}$  thick LPC silicon absorber on glass with a 250 nm silicon oxide/70 nm silicon nitride/10 nm silicon oxide interlayer stack. Parasitic absorption in the glass substrate and interlayers is included as a dotted line. The area of interest for anti-reflective properties without an influence of the silicon back-side (defined by a negligible transmittance) is highlighted by a dashed line, up to 600 nm in this case.

Figure 12(b) illustrates a typical optical spectrum for a 15  $\mu\text{m}$  thick LPC silicon absorber with a planar interlayer stack of 250 nm silicon oxide/70 nm silicon nitride/10 nm silicon oxide. As discussed in section 2.1.1, incident light is either reflected (orange, plotted as 1-reflectance), absorbed (grey) or transmitted (purple) after passing through the sample. If the penetration depth of the incident light is smaller than the absorber thickness, no light reaches the back-side and transmittance is negligible. For a 15  $\mu\text{m}$  thick LPC silicon absorber, this is the case at a wavelength of 600 nm, as indicated by a dashed line in Fig. 3.12(b). In the short wavelength range up to 400 nm, the glass substrate and interlayers contribute to absorbance in the sample (dotted line) and therefore need to be taken into account in the analysis. Hence, anti-reflective properties of the investigated solar cells are evaluated in the wavelength range between 400 nm and 600 nm, where parasitic absorption and light trapping at the silicon back-side are negligible.

The light management structures implemented in this thesis aim at an absorption enhancement by reducing reflectance (orange area in Fig. 3.12(b)) and transmission losses (purple area) in the silicon absorbers. To evaluate their potential to improve light absorption in LPC silicon solar-cells, mean absorbance and the so-called maximum achievable short-circuit current density are employed as figures of merit. The maximum achievable short-circuit current density  $j_{sc,max}$  represents the upper bound

for the short-circuit current density of a solar cell, as it assumes that every absorbed photon contributes one electron-hole pair to current generation. It is calculated by

$$j_{sc,max} = e \int_{300\text{nm}}^{1100\text{nm}} \frac{\Phi(\lambda)}{h\nu} A(\lambda) d\lambda, \quad (3.1)$$

where  $e$  is the elementary charge of an electron,  $h\nu$  the photon energy,  $\Phi(\lambda)$  the spectral photon flux under AM1.5g illumination and  $A(\lambda)$  the absorptance at wavelength  $\lambda$  derived from UV/Vis/NIR measurements.

### 3.4.3 Opto-electronic properties

#### Quantum efficiency

Quantum efficiency measurements are a commonly used characterization technique for solar cells. External quantum efficiency (EQE) relates the current generated in the solar cell to the incoming photon flux for a specific wavelength. A custom-made setup with a probing beam size of  $3\text{ mm} \times 2\text{ mm}$  generated using Xenon and Halogen lamps and a grating to provide monochromatic light is used. A broadband halogen lamp bias light allows to measure under light intensities close to the solar spectrum intensity of  $100\text{ mW cm}^{-2}$ . By chopping the probe beam and using a lock-in technique, the continuous bias light does not alter the results of the EQE measurement. For an ideal solar cell, every incident photon generates an electron-hole pair which contributes to current generation up to the wavelength corresponding to the absorber material band gap, leading to an EQE of unity. For longer wavelengths, light is not absorbed in the solar cell and EQE becomes zero. For a realistic solar cell, EQE is reduced due to both optical and electronic losses. For LPC silicon, optical losses in the short-wavelength range are parasitic absorption in the glass substrate and interlayers, and non-absorption due to reflection. In the long wavelength range, where the penetration depth becomes larger than the absorber thickness, non-absorption becomes the largest loss factor. Electronic losses arise due to defects in the material, either at interfaces or in the bulk. Defects at the front glass-silicon interface mainly reduce EQE in the short-wavelength range, where most of the light is absorbed close to this interface. Bulk defects, e.g. at grain boundaries, cause recombination of charge carriers and are therefore independent of the wavelength of absorbed light. If the absorptance  $A$  of the solar cell is known, internal quantum efficiency (IQE)

can be calculated from  $\text{IQE} = \text{EQE}/A$ . IQE relates current generation to every absorbed photon and is a measure of electronic losses in the solar cell. Hereby, parasitic absorption needs to be taken into account as it contributes to absorptance but not current generation.

External quantum efficiency measurements allow to calculate the short-circuit current density provided by the solar cell via

$$j_{\text{sc,EQE}} = e \int_{300\text{nm}}^{1100\text{nm}} \Theta(\lambda)\text{EQE}(\lambda) d\lambda, \quad (3.2)$$

where  $e$  is the electron elementary charge,  $\Theta(\lambda)$  the incident photon flux corresponding to the solar spectrum (see Fig. 2.1(b)) and  $\text{EQE}(\lambda)$  the external quantum efficiency at wavelength  $\lambda$ .

In summary, quantum efficiency measurements are a suitable method to characterize how efficiently the investigated solar cells convert incoming light to current at a given wavelength. In doing so, both optical and electronic loss mechanisms are taken into account. In combination with absorption measurements, it allows to distinguish between optical and electronic losses. If parasitic absorption losses are accounted for, electronic losses can be expressed by the internal quantum efficiency [19, 66, 67].

### Current-voltage characteristics

Current-voltage characteristics were measured with a WXS-156S-L2 solar simulator of WACOM ELECTRONIC CO. The solar simulator is equipped with a dual light source with a Xenon and Halogen lamp mimicking the solar AM1.5g spectrum, with a classification class AAA after DIN norm 60904-9:2007. Current-voltage characteristics are measured under standard testing conditions, corresponding to an illumination intensity of  $100\text{ mW cm}^{-2}$  at  $25\text{ }^\circ\text{C}$ . Solar cell parameters, namely open-circuit voltage, short-circuit current density, fill factor and power conversion efficiency are calculated from the measured data employing a two-diode fitting model (cf. section 2.3). Current-voltage characteristics are the standard measurement technique to determine a solar cell's power conversion efficiency [4, 186, 187].

### Suns- $V_{\text{oc}}$ method

The Suns- $V_{\text{oc}}$  method allows to measure open-circuit voltages of the lithography-free processed solar cells used in this thesis (section 3.3). Measurements were performed

with a Suns- $V_{oc}$  unit of a WCT-100 photo-conductance lifetime tool by Sinton Instruments. The Suns- $V_{oc}$  method relies on tracking the open-circuit voltage as a function of light intensity. A flash lamp with slow decay is used as a light source, providing light intensities up to a few suns. The intensity decay is decisively slower than the carrier lifetime in the device, ensuring quasi-steady state conditions during the measurements. In contrast to current-voltage characteristics measurements described above, the current is measured with a separate calibrated photodiode, allowing to determine the illumination density independent of the measured sample. These aspects facilitate a quick determination of open-circuit voltages as well as measurements with high throughput [188, 189]. Another peculiarity of the Suns- $V_{oc}$  method is that measurements are performed under open-circuit conditions. Accordingly, series resistance does not alter the measurements (see section 2.3) and requirements for the contacting scheme are reduced. In combination with the short-circuit current density, which may be calculated from EQE measurements described above, an idealized current-voltage curve can be calculated under the assumption of the short-circuit current density being a linear function of illumination intensity [190, 191]. An idealized fill factor can be calculated from this  $j - V$  characteristics, which constitutes the limit of  $FF$  for a perfect contacting scheme. The resulting fill factor is also referred to as pseudo fill factor (pseudo- $FF$ ), from which the pseudo-efficiency might be calculated using Eq. (2.32).

### 3.5 Numerical methods

Simulations allow to calculate solutions for Maxwell's equations based on numerical assumptions. From these, optical properties of a solar cell can be calculated in a fast and controllable way. Parameters like layer thicknesses and texture geometry can be varied easily and cost-effective. In this way, simulations may assist to guideline the experiment to identify optimized parameters and, in consequence, optical properties in real solar cells.

In this thesis, one-dimensional and three-dimensional simulations were employed and will be introduced in the next sections. Three-dimensional simulations using the finite element method solve Maxwell's equations for a three-dimensional texture that is discretized in the trial space [192]. While the simulations are time- and resource-consuming, they allow precise approximations of the solutions to Maxwell's equation. In consequence, a complete layer stack including the silicon back-side of LPC silicon thin-film solar cells can not be treated in three-dimensional simulations and one-dimensional simulations were employed for these cases. For one-dimensional

simulations, a net radiation approach is used, relying on the continuity conditions of the electric field in Maxwell’s equations [192].

### 3.5.1 One-dimensional simulations

One-dimensional simulations were performed using the optical simulation software “GenPro4” developed at Delft University of Technology [193, 194]. The software code numerically calculates the absorptance in both coherent and incoherent layers based on an extended net radiation approach and gives reflectance and transmittance of the investigated layer stack. Input parameters for the layers are their complex refractive indices and layer thicknesses. While interference is taken into account in coherent layers, it is neglected for incoherent layers by assuming that incident and reflected beam do not exhibit a correlated phase [194]. Despite the one-dimensional simulation approach, textured interface can be approximated in GenPro4. For this, scatter matrices describing the reflectance and transmittance at an interface are distributed in multiple angular intervals relative to the interface [193]. Two models can be employed to calculate the light intensity in the angular intervals, namely a ray-optics model using a ray tracing technique [195, 196] and a wave-optics model based on the scalar scattering theory developed by Jäger et al. [197, 198]. The ray-optics model is most suitable for textures with features much larger than the wavelength range investigated, whereas the wave-optics model is used for textures with typical feature sizes comparable to the wavelength. Surface topographies measured by atomic force microscopy (section 3.4.1) were used as input for the calculation models. The LPC silicon thin-film solar cells modelled in this thesis, as sketched in Fig. 3.13(a), exhibit a SMART texture (see section 3.1.3) with a period of 750 nm at the front-side and random pyramids at the back-side. The pyramid texture was produced by wet-chemical etching in potassium hydroxide (see section 3.2.1) with a typical size of 2  $\mu\text{m}$  at the back-side of the silicon absorber. The modelled structure of these stacks is sketched in Fig. 3.13(b). The SMART texture was represented as an effective medium with an effective dielectric constant  $\varepsilon_{\text{eff}}$  calculated using the Maxwell-Garnett equation [84, 199]

$$\varepsilon_{\text{eff}} = \varepsilon_{\text{SiO}_x} \frac{2 \cdot (1 - ff) \cdot (\varepsilon_{\text{TiO}_x} - \varepsilon_{\text{SiO}_x}) + \varepsilon_{\text{TiO}_x} + 2 \cdot \varepsilon_{\text{SiO}_x}}{2 \cdot \varepsilon_{\text{SiO}_x} + 2 \cdot \varepsilon_{\text{TiO}_x} + (1 - ff) \cdot (\varepsilon_{\text{TiO}_x} - \varepsilon_{\text{SiO}_x})}, \quad (3.3)$$

where  $ff$  denotes the filling fraction of the hexagonal array of  $\text{SiO}_x$  nano-pillars. The effective refractive index  $n_{\text{eff}} = \sqrt{\varepsilon_{\text{eff}}}$  may be calculated from the dielectric constant.

Scattering due to textures at the front and back-side are taken into account by wave-optical and ray-optical models, respectively.

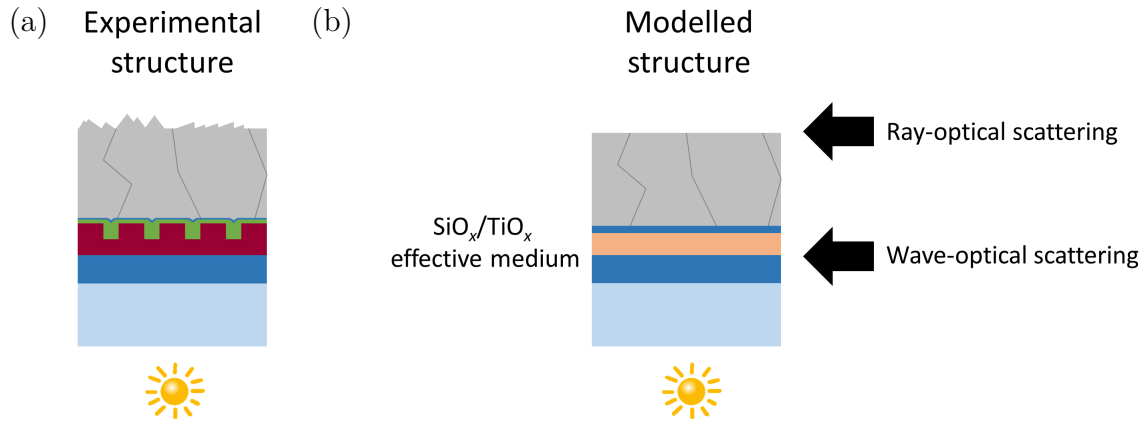


**Figure 3.13:** Schematic of (a) the experimental structure of a LPC silicon absorber with a SMART texture at the front-side and random pyramid texture at the back-side and (b) the adapted structure for one-dimensional simulations with planar interfaces and scattering models.

### 3.5.2 Three-dimensional simulations

The finite-element solver “JCMsuite” was used for three-dimensional simulations [200, 201]. JCMsuite calculates rigorous solutions to Maxwell’s equation for a given structure in three dimensions. For this, a unit cell of the periodic structure is meshed into tetrahedra and prisms. Solutions to Maxwell’s equations are approximated by a polynomial on every finite element, whereby periodic boundary conditions at the side of the unit cell are applied. In this thesis, a relative error of the field energy of  $10^{-3}$  is chosen, which is ensured by constraining the typical side lengths of the elements and adapting the polynomial degree during simulations.

As the simulation is limited by memory and time, the computational domain is enclosed by artificial absorbing layers at the top and bottom, so-called perfectly matched layers. This ensures a computational domain limited to finite thickness for scattering problems [192]. In the perfectly-matched layer, it is assumed that every photon reaching its interface is absorbed, corresponding to an infinitely thick layer. The simulated SMART structures consist of hexagonal arrays of nano-pillars with titanium oxide filling the voids between nano-pillars (see section 3.1.3). The simulation assumes a perfectly flat surface of the silicon oxide/titanium oxide inter-mixed layer. A 10 nm thin silicon oxide layer on top of this inter-mixed layer terminates the texture. The geometrical parameters describing the SMART texture are the period  $p$  of the unit cell and the height  $h$  and the diameter  $d$  of the-nano-pillar, as

indicated in Fig. 3.14.

The area filling fraction  $ff$  corresponding to the relative areas of the nano-pillar and the unit cell is given by

$$ff = 2\pi\sqrt{3}(d \cdot p). \quad (3.4)$$

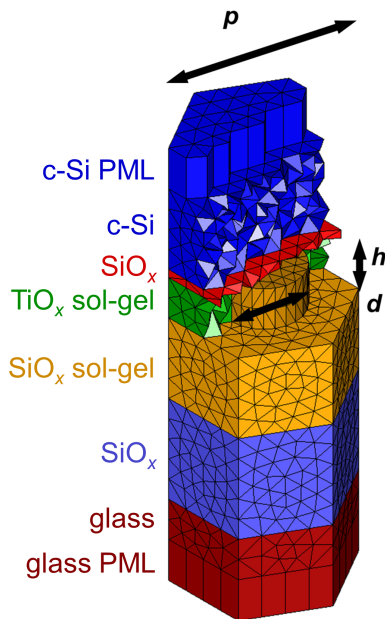


**Figure 3.14:** Unit cell of the simulated SMART texture, indicating the geometrical parameters varied in the simulations, namely the period  $p$  of the unit cell and the height  $h$  and diameter  $d$  of the silicon oxide nano-pillars. The top and bottom of the simulation domain are enclosed by perfectly-matched layers (PML).

## 4 Sinusoidal nano-structures

Sinusoidally textured glass substrates were extensively studied as light management textures in LPC silicon thin-film solar cells by Köppel [49]. In this study, high electronic material quality with open-circuit voltages above 600 mV was demonstrated. The method employed limited the height-to-period ratio of sinusoidal textures to 0.3, while simulations by Jäger et al. [202] revealed improved light in-coupling for higher height-to-period ratios up to 0.5. The method introduced in section 3.1.2 using a combination of nano-imprint lithography (NIL) of commercially available resists and subsequent reactive-ion etching (RIE) is applied to sinusoidal nano-textures with height-to-period ratios of 0.5. Additionally, newly developed interlayers that demonstrated to improve the glass-silicon interface in planar devices [43, 138] are applied to these textures and their influence on optical properties and interface quality is studied. The surfaces of sinusoidal textures produced using this NIL+RIE method are analyzed, and their optical properties in LPC silicon solar cells is investigated. Finally, solar cell results on these textured substrates are presented. Parts of the results presented in this chapter were previously published in [203].

### 4.1 Previous work

Sinusoidal textures were investigated as light management structures in LPC silicon thin-film solar cells in [48, 49]. After steep textures were found to cause dislocations in the silicon absorber after crystallization [45, 46], the sinusoidal texture was developed as an alternative texture without edges and steep flanks, aiming at optimizing interface quality. The sinusoidal textures studied in [49] had periods of 500 nm and 750 nm based on simulations predicting these to be close to the optimal period for light in-coupling in liquid phase crystallized silicon thin-film solar cells on glass [204, 205]. Master structures with a hexagonal sinusoidal texture with a height-to-period ratio of 0.5 were produced by laser interference lithography [206]. The structures were replicated into high-temperature stable sol-gel layers [156] using UV-NIL. To ensure process compatibility with the high temperatures during LPC,

these sol-gels require a thermal annealing step at 600 °C. This process leads to a substantial shrinkage of the nano-structures, thereby limiting the height-to-period ratio to 0.3. Simulations by Jäger et al. [202] revealed that light in-coupling into the silicon absorber is enhanced by higher aspect ratios up to around 0.5, as depicted in Fig. 4.1. Therefore, fully exploiting the optical potential of the sinusoidal texture requires a fabrication method that allows to replicate the nano-structures without shrinkage, while still providing the necessary stability at high temperatures.

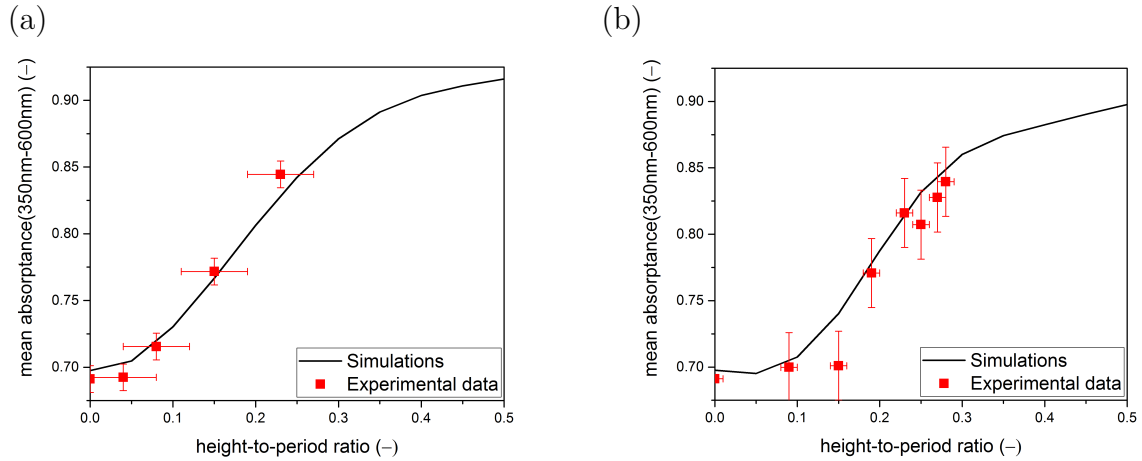


**Figure 4.1:** Simulated (lines) and experimental (dots) mean absorptance at the sinusoidally textured glass-silicon interface for a period of (a) 500 nm and (b) 750 nm, adapted from [202].

Sinusoidal textures with height-to-period ratios below 0.3 produced using the Philips sol-gel with high-temperature stability have experimentally demonstrated efficient anti-reflection at the interface between glass substrate and LPC silicon. However, absorption enhancement only leads to an increased solar cell efficiency if the implementation of the texture does not reduce carrier extraction by inducing defects in the absorber material or its interfaces. While bulk material quality could be shown to be close to that of comparable planar reference devices, providing open-circuit voltages above 600 mV [48, 49], characteristics of the external quantum efficiency revealed that surface recombination at the textured interface is still higher than for planar devices, indicating texture-induced defects at this interface.

The sinusoidal nano-textures presented in this chapter exhibit a height-to-period ratio of 0.5 reached by the newly developed texture production method based on a combination of nano-imprint lithography and reactive ion etching (cf. section 3.1.2). Additionally, novel interlayers between textured glass substrate and LPC silicon absorber are investigated with respect to their influence on optical properties and interface and material quality of solar cells exhibiting a sinusoidal texture.

## 4.2 Process development

### 4.2.1 Optimization of the reactive ion etching process

In the method presented here, nano-imprinted resist layers act as three-dimensional soft etching masks in a subsequent reactive ion etching (RIE) process. The following prerequisites should be fulfilled in order to replicate nano-structures with high structural fidelity. First, a reactive ion etching process that facilitates the same etch rates for the resist mask layer and the underlying material needs to be identified. If the etch rate of the materials differs, the resulting texture is compressed or stretched accordingly. Secondly, the etching process should be anisotropic, e.g. directional, to prevent pattern distortions. For the implementation of sinusoidal textures produced by this method into liquid phase crystallized silicon thin-film solar cells on glass, two commercially available UV-curable resists (OrmoComp and UVcur06 from microresist technology GmbH) were analyzed as mask materials. The silicon oxide ( $\text{SiO}_x$ ) diffusion barrier produced by plasma-enhanced chemical vapor deposition (PECVD) was identified as a suitable target material.

Etch rates of these three materials were examined for different gas compositions frequently employed for silicon oxide etching [207]. Gas compositions include a mixture of 25 sccm Ar and 25 sccm  $\text{CHF}_3$  (process (I)), these gases with an additional 2 sccm  $\text{O}_2$  (process (II)), 40 sccm  $\text{CHF}_3$  and 2 sccm  $\text{O}_2$  (process (III)), and a mixture of 35 sccm  $\text{CHF}_3$  and 14 sccm  $\text{SF}_6$  (process (IV)). Figure 4.2 illustrates the measured etch rates for PECVD silicon oxide (black squares), OrmoComp (blue triangles) and UVcur06 (green circles). As the resists contain organic constituents, the inclusion of oxygen, process (II) compared to process (I), increases the etch rate for the resists by a factor of two, whereby the etch rate for  $\text{SiO}_x$  is unchanged. For process (III), without Argon as dilution gas, the etch rate of the resists is lower despite a higher relative oxygen content in the chamber. Further, the etch rate for  $\text{SiO}_x$  rises due to a higher concentration of  $\text{CHF}_3$  as etching agent. Process (IV) is found not to be suitable for pattern replication as the resists are etched more than twice as fast as the silicon oxide.

Similar etch rates for the resists and PECVD silicon oxide, a requirement for pattern replication without structural distortions, is given for process (I) and, additionally, for UVcur06 in combination with process (III).

Consequently, these combinations were further analyzed in regards to the anisotropy of the process. For that purpose, hexagonal nano-pillar arrays with a period of 750 nm and a height of 100 nm were nano-imprinted on top of and subsequently replicated in PECVD  $\text{SiO}_x$  using the aforementioned processes (I) and (III). The

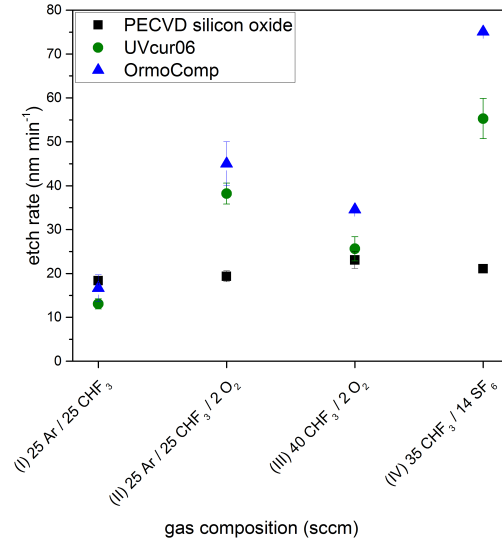
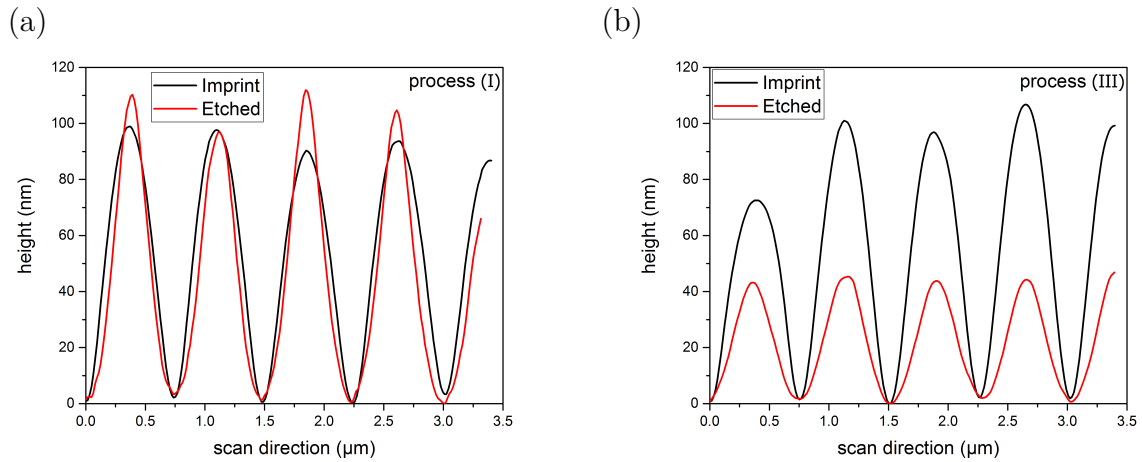


**Figure 4.2:** Etch rates for different gas compositions for silicon oxide produced by chemical vapor deposition (black squares) and two commercially available resists, OrmoComp (blue triangles) and UVcur06 (green circles).

vertical sidewalls of the nano-pillars allow to evaluate the anisotropy of the etching processes.

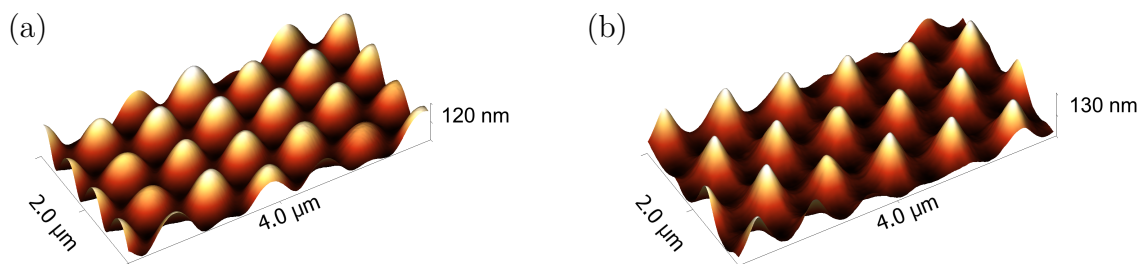
For the method to be compatible with subsequent high temperature processes, in particular liquid phase crystallization with temperatures above 700 °C, potential resist residues need to be removed without altering the replicated pattern. For UVcur06, it was found that a residue-free removal is ensured by an oxygen plasma treatment [157], which does not affect the replicated pattern in the silicon oxide layer. For OrmoComp, on the contrary, no process could be identified that provided a residue-free removal while preserving the replicated texture as it exhibits glass-like properties after UV curing [158]. Hence, OrmoComp was discarded as a suitable masking material and further experiments were limited to UVcur06.

Figure 4.3 depicts surface profiles measured using atomic force microscopy for etching processes (I) (Fig. 4.3(a)) and process (III) (Fig. 4.3(b)). The imprinted structure in UVcur06 (black) and the replicated pattern after etching (red) are compared. Due to the AFM surface profile constituting a convolution of tip geometry and surface topography, the flanks of the nano-pillar appear to be inclined. Pattern replication was successful for both processes, the nano-pillar array is clearly recognizable. For process (III), however, the height of the nano-structure is reduced to about half of the imprinted structure as a result of partly isotropic etching. Isotropic etching leads to a removal of material on the sides of the nano-pillar. If the thickness of material etched horizontally becomes larger than the pillar diameter, the height of the texture is reduced.



**Figure 4.3:** Atomic force microscope profiles for (a) etching process (I) and (b) etching process (III), for a hexagonal nano-pillar array imprinted into UVcur06 (black) and etched into silicon oxide (red).

The sample etched by process (I), on the contrary, exhibits an increase in mean pillar height by about 10 nm, which is in line with variations over one sample and the accuracy of AFM measurement (see section 3.4.1). Side-walls of the structure etched in  $\text{SiO}_x$  are streamlined due to partly isotropic etching, but the effect is considerably smaller than for process (III). Surface topography images of the imprinted and replicated texture employing process (I) measured by AFM, disclosed in Fig. 4.4, illustrate this further. While the nano-pillars are clearly replicated, material removal at the tips of the nano-pillars is evident. As a consequence, the conicity of the etched nano-pillars is greater than that of the imprinted structure. Still, the pattern is transferred with sufficient structural fidelity. Hence, using UVcur06 as mask material and a reactive ion etching process with a gas composition of 25 sccm Ar and 25 sccm  $\text{CHF}_3$ , chamber pressure of 20 mTorr, and plasma power of  $P_{\text{RF}} = 200 \text{ W}$  constitute a process for pattern replication into the silicon oxide diffusion barrier.



**Figure 4.4:** Atomic force microscope images of a nano-pillar array with a period of 750 nm and a height of around 100 nm (a) imprinted into UVcur06 and (b) replicated in silicon oxide using etching process (I).

## 4.2.2 Structural analysis of sinusoidal structures

Having established a suitable RIE process for pattern replication from UVcur06 to the silicon oxide diffusion barrier, sinusoidal nano-textures with a period of 750 nm and a height-to-period ratio of 0.5 were produced using the NIL+RIE approach. Fig. 4.5 depicts AFM surface profiles of the sinusoidal texture nano-imprinted into UVcur06 (black) and the same texture after etching into silicon oxide (red). For comparison, the sinusoidal texture imprinted into the previously used high-temperature stable sol-gel (green) [48] after thermal annealing is included.

As already stated in the previous section, the reactive ion etching process preserves the surface topography and height of the master structure. The influence of partly isotropic etching on texture deformation is less pronounced as for the sharp-edged nano-pillar texture. The structure imprinted into the organic resist UVcur06, which constitutes a duplicate of the master structure, has a height-to-period ratio of 0.5 and exhibits a characteristic feature of the valley being steeper than the top of the structure [49]. For the replicated structure, the steep valley is smoothed out by the reactive ion etching process, and appears more symmetrical than the imprinted structure. Texture height, however, stays constant after pattern replication, and the height-to-period ratio of 0.5 is conserved.

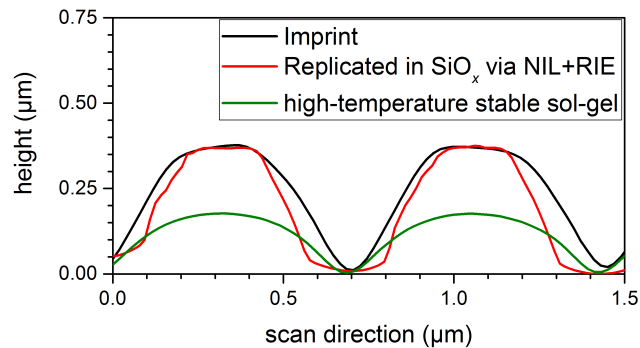


**Figure 4.5:** Atomic force microscope profiles of a hexagonal sinusoidal texture with a period of 750 nm and a height-to-period ratio of 0.5, nano-imprinted in the organic resist UVcur06 (black) constituting a duplicate of the master structure, replicated in silicon oxide by means of reactive ion etching (red), and nano-imprinted in a high-temperature stable sol-gel after thermal annealing (green).

For the texture imprinted into the high-temperature stable sol-gel, the shrinkage during thermal annealing is clearly observed. The height of the structure is reduced by 50% due to the driving out of organic constituents. The steep valley of the texture is preserved after annealing.

Surface topography of the sinusoidal textures disclosed in Fig. 4.6 was measured by atomic force microscopy. Again, the lower height of the texture produced by

the method relying on the high-temperature stable sol-gel (green outline) is clearly identified. The texture imprinted into UVcur06 (black) and the texture replicated in  $\text{SiO}_x$  by means of RIE (red) exhibit a close resemblance, emphasizing the high degree of structural fidelity achievable with the NIL+RIE method. The surface of the sinusoidally textured high-temperature stable sol-gel layer is rounded compared to the master structure represented by the duplicated texture imprinted in UVcur06, which reveals contours at the top of the texture.

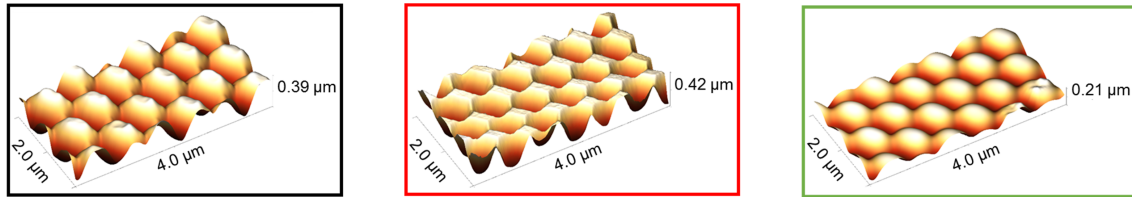


**Figure 4.6:** Atomic force microscope images of a hexagonal sinusoidal texture with a period of 750 nm and a height-to-period ratio of 0.5, nano-imprinted into the organic resist UVcur06 (black), replicated into silicon oxide by NIL+RIE (red), and nano-imprinted in a high-temperature stable sol-gel after thermal annealing (green).

In summary, a method for the replication of textures nano-imprinted into an organic resist to the silicon oxide diffusion barrier was developed and optimized for high structural fidelity. Optimized process parameters during reactive ion etching allowed to reproduce a sinusoidal nano-texture with a period of 750 nm and a height-to-period ratio of 0.5 in the silicon oxide diffusion barrier without shrinkage and pattern distortion, compared to only 0.25 in the previously employed nano-imprinting into a high-temperature stable sol-gel that suffers from shrinkage during thermal annealing.

### 4.3 Optical analysis

In the time this thesis was conducted, novel interlayer deposition methods were developed for liquid phase crystallized silicon thin-film solar cells on glass with planar glass-silicon interface [42, 43, 136–138, 166]. Changing from interlayers deposited by physical vapor deposition (PVD) to plasma-enhanced chemical vapor deposition (PECVD) facilitated improved solar cell efficiencies due to a lower interface recombination [137, 166]. A three-layer interlayer stack of 250 nm silicon oxide ( $\text{SiO}_x$ )/70 nm silicon nitride ( $\text{SiN}_x$ )/10 nm  $\text{SiO}_x$  was implemented, serving as diffusion barrier against glass impurities, anti-reflective coating, and wetting and passivation layer, respectively. Interface quality could further be improved by changing the interlayer stack from the  $\text{SiO}_x/\text{SiN}_x/\text{SiO}_x$  stack to 250 nm  $\text{SiO}_x$ /70 nm  $\text{SiN}_x$

with a subsequent plasma oxidation of the top  $\approx 10$  nm of the  $\text{SiN}_x$  layer. The plasma oxidation results in an oxygen-rich silicon oxy-nitride ( $\text{Si}(\text{ON})$ ) layer and, consequently, reduces the  $\text{SiN}_x$  layer thickness to about 60 nm.

These interlayer deposition techniques were applied to sinusoidally textured glass substrates with a height-to-period ratio of 0.5 produced by the NIL+RIE method. The following section discusses the influence of interlayer types (section 4.3.1), and presents a comparison of optical properties of sinusoidal textures with varied height-to-period ratio resulting from the texturing technique (section 4.3.2).

### 4.3.1 Optical properties of different interlayer stacks

The light in-coupling properties of LPC silicon absorbers with different interlayers are analyzed by absorption measurements to identify an interlayer stack that facilitates optimized light in-coupling properties in combination with sinusoidal nano-textures with a height-to-period ratio of 0.5 produced by the NIL+RIE approach. For reference, an analysis of light in-coupling for planar interlayer stacks is included. The investigated wavelength range was limited between 300 nm and 600 nm. In this wavelength range, an influence of the silicon back-side by varying absorber thickness and, in the case of sinusoidally textured absorbers, double-sided texturing, can be excluded. As a first step, the absorptance of LPC silicon absorbers with planar glass-silicon interface was investigated for different interlayer deposition techniques, as illustrated in Fig. 4.7(a).

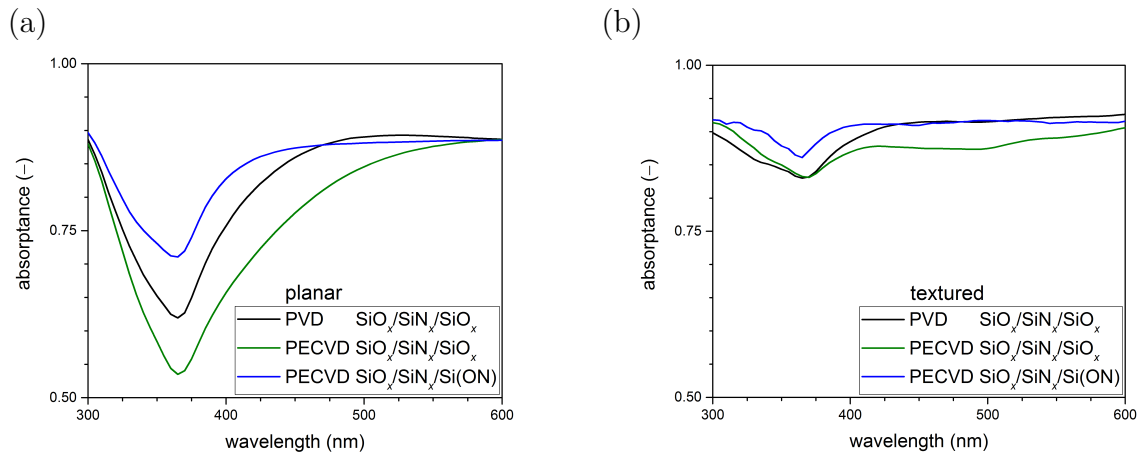


**Figure 4.7:** Absorptance of LPC silicon absorbers with different interlayers on (a) planar substrates and (b) substrates with sinusoidal textures with a period of 750 nm and height-to-period ratio of 0.25.

Comparing the silicon oxide/silicon nitride/silicon oxide stacks between the deposition methods of PVD (black curve in Fig. 4.7) and PECVD (green), a lower

absorptance and thus, higher reflectance, is found for the sample with PECVD interface. This indicates a higher refractive index of the  $\text{SiN}_x$  layer for the PVD deposition, which could be explained by a more compact layer growth. If the  $\text{SiO}_x$  passivation layer (green) is replaced by a  $\text{Si}(\text{ON})$  layer by oxidizing the top  $\approx 10$  nm of the  $\text{SiN}_x$  layer (blue), reflectance in the short wavelength range between 300 nm and 550 nm can be reduced. The anti-reflective properties are hence enhanced for shorter wavelengths. This is attributed to an increased refractive index of the silicon oxy-nitride passivation layer compared to the silicon oxide layer.

For sinusoidally textured LPC silicon absorbers with a height-to-period ratio of 0.25 (Fig. 4.7(b)), overall absorption is higher compared to the planar interlayer stacks. In particular, reflectance in the wavelength range from 300 nm and 450 nm is reduced. Comparing interlayer deposition techniques for sinusoidally textured glass substrates reveals the same trend as for absorbers grown on planar glass substrates. The PECVD  $\text{SiO}_x/\text{SiN}_x/\text{SiO}_x$  stack exhibits a higher reflectance, possibly due to a lower refractive index of the silicon nitride layer compared to its counterpart produced by PVD. For the  $\text{SiO}_x/\text{SiN}_x/\text{Si}(\text{ON})$  stack, reflectance is lower than for the  $\text{SiO}_x/\text{SiN}_x/\text{SiO}_x$  stack produced by PECVD and comparable to the PVD interlayers. In the short wavelength range  $< 450$  nm, the  $\text{Si}(\text{ON})$  passivation layer decreases reflectance compared to the PVD interlayer stack. Mean absorptance was calculated in the wavelength range from 400 nm to 600 nm to exclude the parasitic absorption in the glass occurring for wavelengths  $< 400$  nm. Mean absorptance values for planar (black) and sinusoidally textured (blue) LPC silicon absorbers with different interlayers are summarized in Fig. 4.8. Independent of interlayer deposition technique, absorption is higher for LPC silicon layers with a sinusoidal texture at the glass-silicon interface by more than 3% (absolute). Using a PECVD  $\text{SiO}_x/\text{SiN}_x/\text{Si}(\text{ON})$  interlayer stack in combination with a sinusoidal nano-texture allows to absorb more than 91% of the incoming light, whereby around 4% are already reflected at the air-glass interface.

In conclusion, the implementation of an  $\text{SiO}_x/\text{SiN}_x/\text{Si}(\text{ON})$  interlayer stack deposited by plasma-enhanced chemical vapor deposition not only gives rise to optimized electronic interface quality [43, 138], but also improves light in-coupling at the glass-silicon interface. An additional absorption gain over the state-of-the-art interlayer stack employed in LPC silicon record solar cell devices can be achieved by a sinusoidal texture at the glass-silicon interface. Further optimizing the light in-coupling at the glass-silicon interface requires sinusoidal nano-textures with a higher height-to-period ratio [202] as described in the following section.

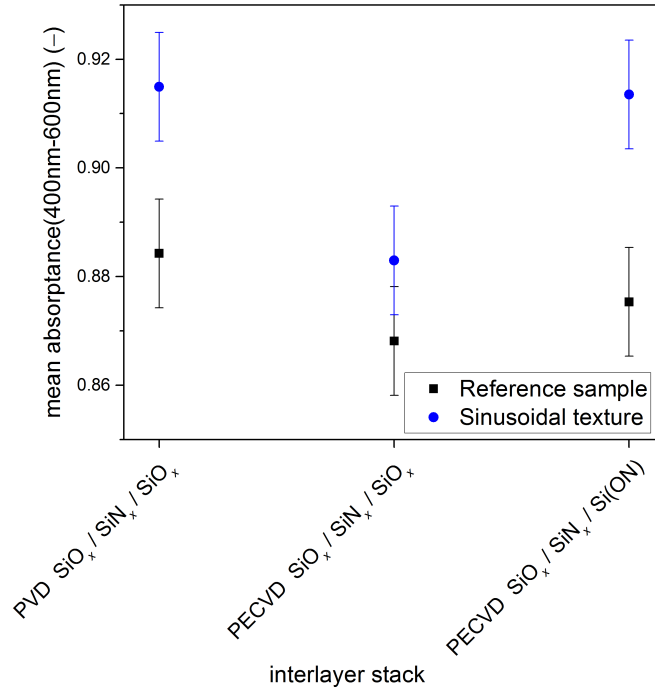


**Figure 4.8:** Mean absorbance from 400 nm to 600 nm for LPC silicon thin-film absorbers with different interlayer stacks on planar substrates (black squares) and substrates with a sinusoidal texture with a period 750 nm and a height-to-period ratio of 0.25 (blue circles).

### 4.3.2 Optical properties of sinusoidal nano-textures

To further optimize the light in-coupling at the glass-silicon interface, the NIL+RIE method was employed for producing glass substrates for liquid phase crystallized silicon solar cells with a sinusoidal nano-texture with a height-to-period ratio of 0.5. The sinusoidal textures produced by the high-temperature stable sol-gel method are only half as high as those from the NIL+RIE method due to technological restrictions, giving a height-to-period ratio of 0.25. Figure 4.9 depicts the absorbance of LPC silicon absorber layers with a SiO<sub>x</sub>/SiN<sub>x</sub>/Si(ON) interlayer stack and a sinusoidal nano-texture produced by nano-imprinting into a high-temperature stable sol-gel (blue) and via the NIL+RIE method (red). Absorbance curves exhibit variations in the range of about 0.5% (absolute), which are attributed to the 5 × 5 cm<sup>2</sup> large samples causing an irregular intensity distribution in the integrating sphere. The sample with the sinusoidal texture produced by the NIL+RIE method exhibits higher absorbance values for wavelengths > 400 nm. Mean absorption between 400 nm and 600 nm could be increased from 91.4% to 93.0% by the implementation of the sinusoidal texture with a height-to-period ratio of 0.5 produced by NIL+RIE. Considering the 4% reflection loss at the air-glass interface (dashed curve in Fig. 4.9), less than 3% of the incoming light is reflected at the textured interface coated

with silicon nitride/silicon oxy-nitride anti-reflective and passivation layers, allowing to efficiently absorb the solar irradiation in this wavelength regime.

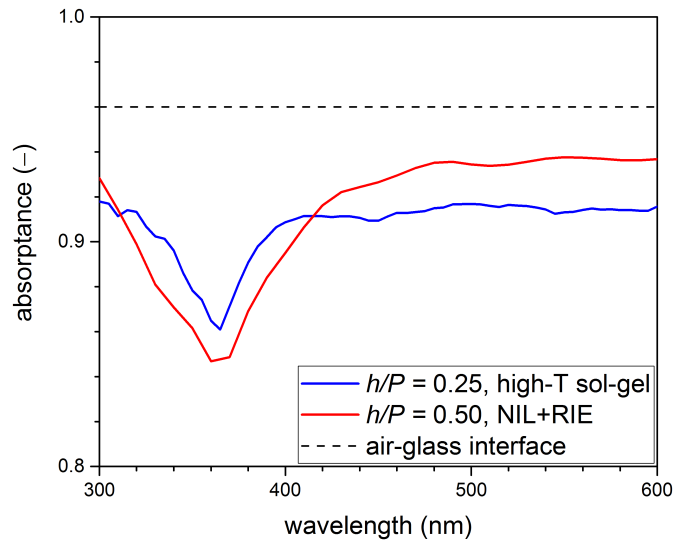


**Figure 4.9:** Absorptance of LPC silicon absorber layers on glass substrates with a sinusoidal texture with a period of 750 nm and a height-to-period ratio  $h/P$  of 0.25 produced by nano-imprinting into a high-temperature stable sol-gel layer (blue) and with  $h/P = 0.5$  reached by employing the NIL+RIE method (red). Reflectance at the air-glass interface (dashed), represented as  $1 - R$  is included for reference.

In a nutshell, the influence of the interlayer stack and the deposition method on the optical properties of LPC silicon absorbers with planar and sinusoidally textured glass-silicon interface was investigated. It was found that the change from PVD to PECVD interlayers – which was motivated by in-line processing and advances in interface passivation – reduced light in-coupling if the same  $\text{SiO}_x/\text{SiN}_x/\text{SiO}_x$  interlayer stack was applied. The PECVD process, however, allowed to implement a novel process based on plasma oxidation of the silicon nitride anti-reflective layer, which enhanced absorption back to the level for PVD interlayers.

Implementing sinusoidal nano-textures with a height-to-period ratio of 0.5 produced by NIL+RIE into LPC silicon absorbers on glass allowed to further increase light in-coupling, and mean absorptance values between 400 nm and 600 nm of more than 93% could be reached, of which 4% are already reflected at the air-glass interface.

## 4.4 Solar cell results

Solar cells were manufactured on glass substrates exhibiting a sinusoidal texture produced by NIL+RIE. The state-of-the-art interlayer stack consisting of a silicon nitride layer in combination with plasma-oxidation of the first 10 nm was deposited

on the sinusoidally textured silicon oxide diffusion barrier with a height-to-period ratio of 0.5. Figure 4.10 exhibits the external quantum efficiency and absorption characteristics of solar cells with 15  $\mu\text{m}$  thick LPC silicon absorber on a sinusoidal texture (red) and a parallel-processed reference sample with a planar glass-silicon interface and a KOH pyramid back-side texture (light red). As a reference, a solar cell with a sinusoidal texture produced by imprinting in high-temperature stable sol-gel and PVD interlayers (black) and its planar counterpart (grey) is illustrated [48]. The EQE of the planar samples is equivalent up to a wavelength of 700 nm. For longer wavelengths, the higher absorption due to the KOH back-side texture results in a higher EQE. Among the samples with a sinusoidal texture, no significant difference in EQE is found for wavelengths up to 750 nm. For longer wavelengths, EQE is higher for the texture produced by NIL+RIE. The EQE gain is based on a higher absorptance of the sample with a high height-to-period ratio sinusoidal texture (dashed lines in Fig. 4.10).

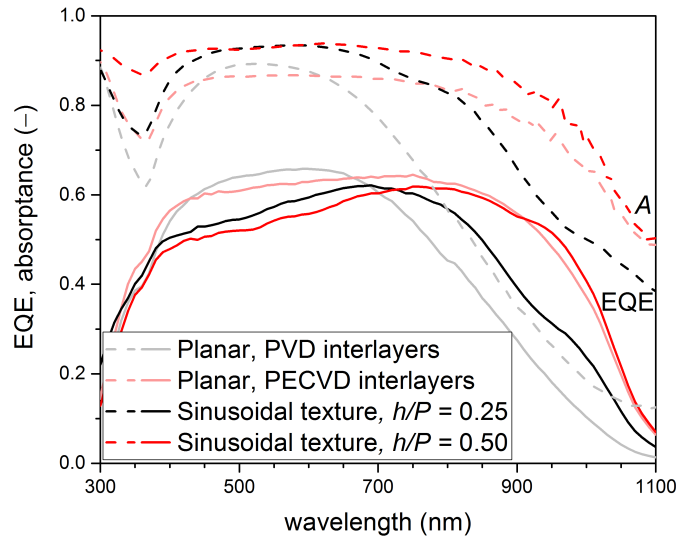


**Figure 4.10:** External quantum efficiency (EQE, solid) and absorptance ( $A$ , dashed) of LPC silicon solar cells with planar (grey, light red) and sinusoidally textured (black, red) glass-silicon interfaces. The sinusoidal textures differ in their height-to-period ratio  $h/P$  due to the employed production method, namely high-temperature stable sol-gels leading to an  $h/P$  of 0.25 (black), and  $h/P = 0.5$  for the NIL+RIE method (red). The cells exhibit different interlayer stacks, namely a  $\text{SiO}_x/\text{SiN}_x/\text{SiO}_x$  stack deposited by PVD (grey, black) and  $\text{SiO}_x/\text{SiN}_x/\text{Si(ON)}$  deposited by PECVD (light red, red).

This is attributed to the sinusoidal texture produced by NIL+RIE being replicated at the back-side of the device [46, 47] with larger height, where higher textures increase light trapping and, hence, absorptance.

Comparing the solar cells with sinusoidal textures to the reference samples reveals that the sinusoidal texture reduces EQE independent of nano-texture height and interlayer deposition technique. Despite the higher absorptance, EQE is reduced in

the short wavelength range, where most of the light is absorbed close to the front glass-silicon interface, indicating higher surface recombination.

To further investigate the interface and bulk properties of the LPC silicon solar cells on sinusoidal textures and planar glass substrates, internal quantum efficiency (IQE) was calculated from EQE and absorptance. This allows assessing material quality independent of optical properties of the solar cell. IQE was calculated for illumination through the glass (superstrate configuration) and from the back-side of the device (substrate configuration), as indicated in the schematic measurement setup disclosed in Fig. 4.11(a).

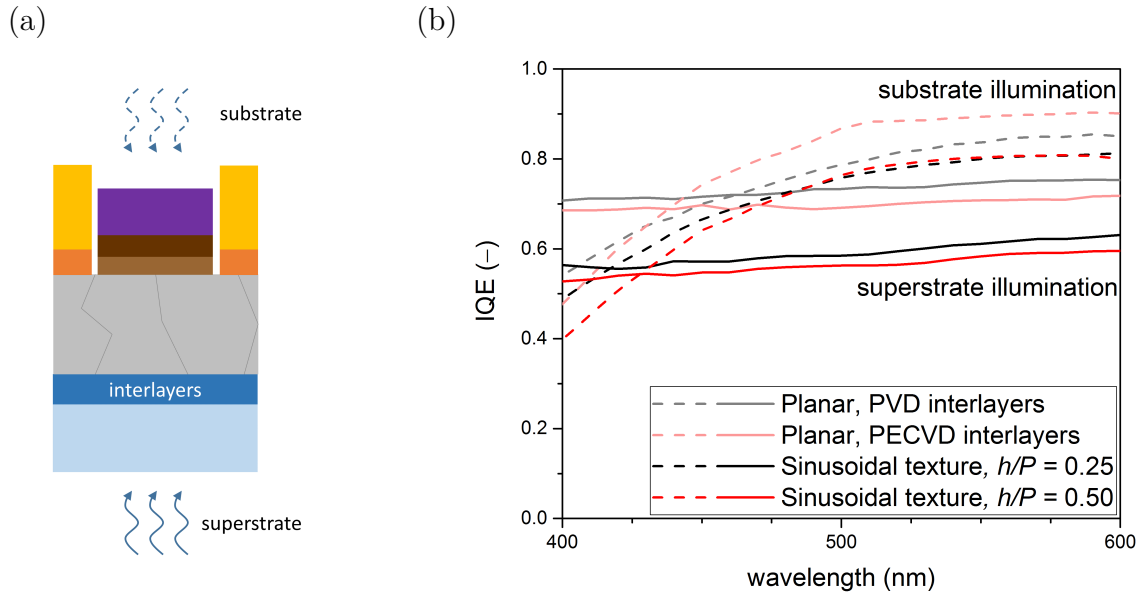


**Figure 4.11:** (a) Schematic of the measured solar cells. The illumination direction of measurements in substrate and superstrate configuration is depicted for reference. (b) Internal quantum efficiency (IQE) of LPC silicon solar cells with planar (grey, light red) and sinusoidally textured (black, red) glass-silicon interfaces, measured for substrate (dashed) and superstrate (solid) illumination. The sinusoidal textures differ in their height-to-period ratio  $h/P$  due to the employed production method, namely high-temperature stable sol-gels [48] leading to an  $h/P$  of 0.25 (black), and  $h/P = 0.5$  for the NIL+RIE method (red). The cells exhibit different interlayer stacks, namely a  $\text{SiO}_x/\text{SiN}_x/\text{SiO}_x$  stack deposited by PVD (grey, black) and  $\text{SiO}_x/\text{SiN}_x/\text{Si}(\text{ON})$  deposited by PECVD (light red, red).

Both interface and bulk material quality affect the IQE. The IQE analysis is restricted to a wavelength range from 400 nm to 600 nm. In this range, the penetration depth of the incoming light is smaller than the absorber thickness, and therefore an influence of the opposite interface can be excluded. Additionally, parasitic absorption in the glass substrate is negligible for wavelengths  $> 400$  nm. In consequence, IQE in this wavelength range reflects bulk properties and interface quality of the interface facing the illumination. Under the assumption that interface quality of the silicon back-side is unchanged for the sinusoidally textured samples, it can be

assumed that differences in IQE under substrate illumination are solely caused by a varying amount of bulk defects. Fig. 4.11(b) exhibits IQE for illumination through the glass (solid lines) and from the back-side (dashed).

As discussed for the EQE of the solar cells, sinusoidally textured devices induce defects in the LPC silicon layer, reflected in an IQE in superstrate configuration that is lower than that of planar cells by about 10 – 15% (absolute).

For illumination from the back-side of the device (substrate configuration), differences in IQE are considered to be solely caused by bulk defects. A clear difference in IQE from the textured devices to the planar reference is found, amounting to about 5 – 10% (absolute). Thus, the sinusoidal textures appear to not only cause defects at the glass-silicon interface, but also bulk defects that reduce IQE for illumination from the back-side of the cell.

To summarize, LPC silicon thin-film solar cells on sinusoidally textured glass substrates with distinct height-to-period ratio due to their production method were combined with different interlayer deposition techniques to analyze their impact on bulk material and interface quality. It was found that the sinusoidal texture induces both bulk and interface defects, independent of height-to-period ratio and interlayer deposition technique.

## 4.5 Conclusion

The influence of increased height-to-period ratios resulting from a novel nano-texture production method on the optical and opto-electronic properties of LPC silicon manufactured on these textured substrates was investigated. In addition, optical properties of different interlayers at the planar or sinusoidally textured glass-silicon interface of LPC silicon absorbers were compared. A newly developed technology based on nanoimprint lithography and reactive ion etching was applied to produce silicon oxide layers with sinusoidal textures with a height-to-period ratio of 0.5. The method applied before, nano-imprinting of high-temperature stable sol-gels, facilitated a maximum height-to-period ratio of only 0.3. The optical properties of LPC silicon absorbers with a sinusoidal nano-texture and different interlayer stacks were investigated. Using a PECVD interlayer stack with a plasma-oxidized silicon nitride layer in combination with a sinusoidal texture with a height-to-period ratio of 0.5, mean absorptance values between 400 nm and 600 nm of 93.0% could be reached, of which 4% can be attributed to reflectance at the sun-facing air-glass interface. For LPC silicon thin-film solar cells with a planar glass-silicon interface, this interlayer stack also exhibited optimized interface passivation properties [43, 138].

LPC silicon thin-film solar cells were produced on sinusoidally textured glass substrates produced by nano-imprinting into high-temperature stable sol-gels and by the NIL+RIE method. Analysis of the external quantum efficiency and internal quantum efficiency for illumination from the front and back-side of the device yielded that textured samples reduce the interface and bulk material quality independent of interlayer deposition technique for both height-to-period ratios of 0.25 and 0.5. On the other hand, previous studies on the optical properties of sinusoidal nano-textures demonstrated that a minimum height-to-period ratio of 0.19 is required to efficiently reduce reflection at the glass-silicon interface [48].

Solar cell results on sinusoidally textured glass substrates indicate that the nano-texture induces defects in the LPC silicon absorber and the textured glass-silicon interface. It is therefore assumed that EQE losses are unavoidable for sinusoidal textures high enough for increased light in-coupling. A detailed analysis of structural properties, e.g. by transmission electron microscopy [45, 58], might support this hypothesis further.



# 5 Smooth anti-reflective three-dimensional textures

As the sinusoidal texture was shown to not be ideally suited as anti-reflective texture at the glass-silicon interface of liquid phase crystallized silicon thin-film solar cells due to texture-induced defects, a second approach was investigated, namely the smooth anti-reflective three-dimensional (SMART) texture. This structure aimed at combining the optical benefits of nano-texturing with the interface quality of planar interfaces. To do this, an optically rough texture with smooth surface was designed and subsequently realized.

This chapter introduces the smooth anti-reflective three-dimensional texture by describing its production (section 5.2) and analyzing its suitability for light in-coupling in LPC silicon thin-film solar cells by measurements and simulations of optical (section 5.3) as well as electronic (section 5.4) properties. Further optimizations are discussed (section 5.5) and the route towards high efficiency devices employing a SMART texture is pointed out (section 5.6).

Parts of the results presented in this chapter were previously published in [208–210].

## 5.1 Previous work

Several nano- and micro-textures for light in-coupling at the glass-silicon interface of liquid phase crystallized silicon thin-film solar cells on glass were investigated prior to this thesis, including a square lattice with a period of  $2\ \mu\text{m}$  [46, 47], a hexagonal nano-pillar texture with a period of  $750\ \text{nm}$  [48], random textures derived from nano-imprinted zinc oxide textures [45, 46] and glass texturing [50, 52, 211], and a sinusoidal texture [48, 49]. The latter has already been discussed in the previous chapter. It was concluded that sinusoidal textures cause defects at the glass-silicon interface and thereby reduce carrier extraction and short-circuit current density despite the increased absorptance values. This is demonstrated by changes due to

the texture in the maximum achievable short-circuit current density  $j_{sc,max}$  derived from absorptance and short-circuit current density  $j_{sc,EQE}$  calculated from external quantum efficiency disclosed in Table 5.1 for several textures. Textures that did not reduce the interface and bulk quality of the LPC silicon solar cells include a nano-imprinted zinc oxide texture [45, 46] and glass substrates with a modulated surface texture [50]. However, the dimensions of these textures were not suited to increase light in-coupling into the LPC silicon absorber layers with thicknesses between 10  $\mu\text{m}$  and 15  $\mu\text{m}$ . Thus, no significant gain in EQE could be observed for nano-textured devices compared to their planar counterparts.

**Table 5.1:** Comparison of changes in maximum achievable short-circuit current density  $j_{sc,max}$  derived from absorptance and short-circuit current density  $j_{sc,EQE}$  calculated from external quantum efficiency (EQE) for LPC silicon thin-film solar cells with different textures at the glass-silicon interface, compared to their respective reference samples with planar glass-silicon interface.

Texture	$j_{sc,max}$ gain $\text{mA cm}^{-2}$	$j_{sc,EQE}$ gain $\text{mA cm}^{-2}$
Sinusoidal texture [48]	+0.7	-1.0
Nano-pillar array [48]	+0.6	-4.8
Zinc oxide texture [45]	-0.2	-0.1
Randomly textured glass [50]	+0.3	+0.2

This chapter presents a texture that was developed to overcome this trade-off between enhanced light in-coupling and deteriorated material quality, the smooth anti-reflective three-dimensional (SMART) texture. The SMART texture relies on nano-imprint lithography of hexagonal silicon oxide nano-pillar arrays and spin-coating of titanium oxide, leading to a texture that is optically rough, but exhibits a smooth substrate-to-silicon interface (cf. section 3.1.3). This feature allows to provide both, improved anti-reflective properties and equivalent interface passivation properties compared to planar interlayer stacks. The chapter comprises design considerations for light in-coupling by three-dimensional simulations and in experiment, the optical properties of the SMART texture with optimized design parameters and results of a proof-of-concept solar cell with a SMART texture. Optical properties are further optimized by advanced processing and double-interlayer systems using a SMART texture / silicon nitride stack. Finally, preliminary solar cell results on these optimized SMART textures are presented.

## 5.2 SMART texture production

The SMART texture developed in the scope of this thesis combines nano-imprinted nano-pillar arrays with a spin-coating process to fill the areas between the pillars (see Fig. 5.1). While the NIL technology of silicon oxide nano-structures was already established [46, 49, 212], a suitable material needed to be identified for spin-coating. Process compatibility with SMART texture production and LPC silicon thin-film solar cell production posed several requirements to the material, namely the possibility of spin-coating, temperature stability at temperatures above 700 °C, and a suitable refractive index  $n$  for anti-reflective properties between glass ( $n_{\text{glass}} = 1.5$  at a wavelength of 600 nm) and silicon ( $n_{\text{c-Si}} \approx 3.9$ ).

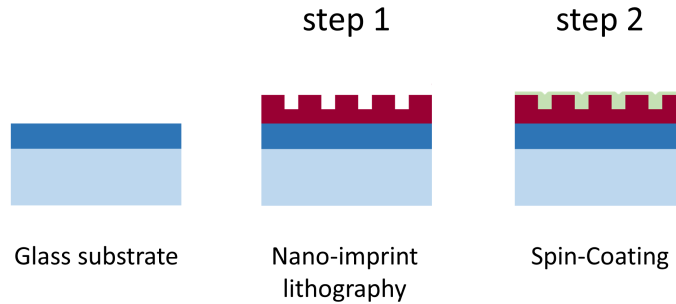


**Figure 5.1:** Schematic process of combining nano-imprint lithography (step 1) of nano-pillar arrays with spin-coating (step 2) to form a SMART texture. A detailed description of the production process is found in section 3.1.3.

The material that was identified is titanium oxide, which can be produced as a multi-crystalline material from liquid precursor solutions. The precursor consists of titanium tetraisopropoxide diluted in ethanol [162, 163]. The precursor solution was spin-coated with different spin speeds and dried for 30 min at 150 °C. Thermal annealing for 30 min at 500 °C is performed, during which a compact titanium oxide ( $\text{TiO}_x$ ) layer is formed.

Figure 5.2(a) illustrates the formation of titanium oxide measured by Raman spectroscopy. The dried sol-gel (black) only exhibits pronounced peaks assigned to the silicon substrate, indicating an amorphous titanium oxide layer. After annealing, an additional pronounced peak at  $143 \text{ cm}^{-1}$  arises, which is assigned to titanium oxide in the anatase phase [213, 214]. The  $\text{TiO}_x$  film thickness after annealing, as disclosed in Fig. 15.2(b), can be varied between 30 nm and 100 nm by changing the rotation speed  $v$  during spin coating from 3000 rpm to 500 rpm. The common function  $h = A/\sqrt{v}$  for spin-coated layers was fitted to the measured data [215] by optimizing the parameter  $A$ .

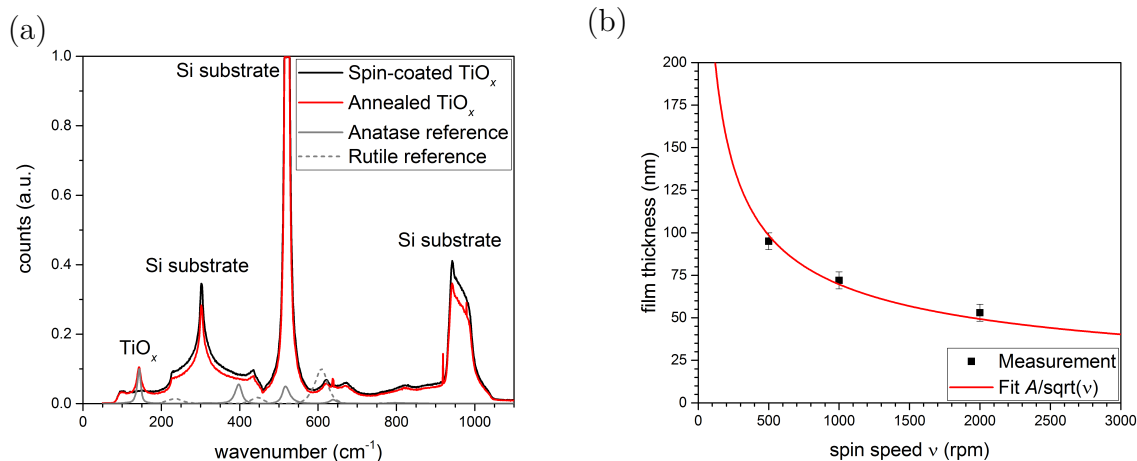


**Figure 5.2:** (a) Raman spectroscopy images of the dried sol-gel after spin-coating (black) and after thermal annealing (red). Reference spectra (grey) for titanium oxide in anatase (solid) and rutile (dashed) phase, taken from [216, 217]. (b) Dependency of the film thickness of titanium oxide sol-gel on the spin speed after thermal annealing.

The SMART texture is implemented as an optically rough texture with a smooth interface between glass and silicon. Thus, the titanium oxide filling the voids between the silicon oxide nano-pillars needs to exhibit a suitable refractive index to provide anti-reflective properties at the glass-silicon interface. Refractive indices of the employed materials are depicted in Fig. 5.3. The refractive index of titanium oxide (green curve) was measured by spectroscopic ellipsometry, while for *c*-Si (black) [76] and silicon oxide (blue) [218] literature values were taken. For reference, the optimum refractive index for a single-layer anti-reflection layer (magenta) is calculated, given by the geometric mean of the refractive indices forming the interface (see section 2.1.2). The titanium oxide layer exhibits a refractive index of 2.1 (as a reference value, the refractive index at a wavelength of 600 nm is considered), which is slightly higher than that of the state-of-the-art silicon nitride with approximately 1.9 [138]. The titanium oxide layer derived from spin-coating and thermal annealing of a sol-gel solution is therefore a suitable material to be employed in a SMART texture aimed at optimized anti-reflection at the glass-silicon interface in LPC silicon thin-film solar cells.

To confirm the smoothing properties of the spin-coated films on the nano-pillar array, SMART textures with a height of  $h = 50$  nm were produced. Figure 5.4(a) illustrates the surface of a nano-pillar array with a height of 50 nm before (left) and after (right) applying a 50 nm thick titanium oxide layer as measured by atomic force microscopy. For reference, both images are depicted using an equal height scale. After spin-coating, the height of the texture features is reduced as the titanium oxide preferentially fills the volume between the SiO<sub>x</sub> nano-pillars. The resulting surface is smooth and does not exhibit steep flanks or edges.

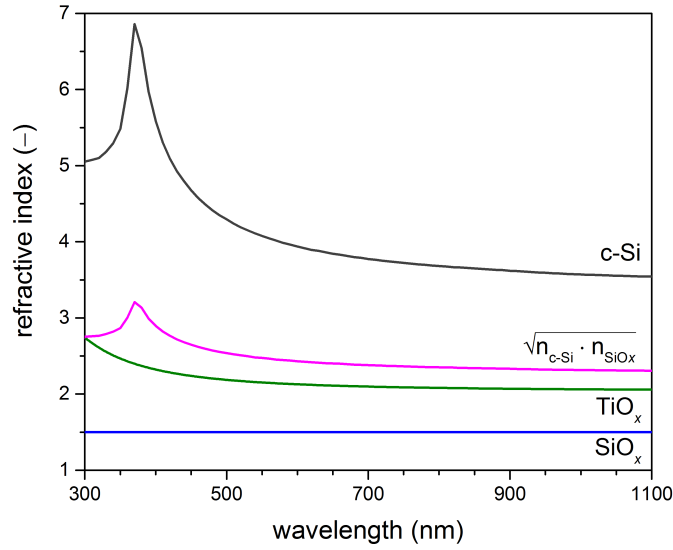


**Figure 5.3:** Refractive index of the titanium oxide ( $\text{TiO}_x$ , green) layer after thermal annealing measured by spectroscopic ellipsometry in comparison to silicon oxide ( $\text{SiO}_x$ , blue) and crystalline silicon (c-Si, black). Literature data were taken for c-Si [76] and  $\text{SiO}_x$  [218]. The optimum refractive index (magenta) for anti-reflection calculated from  $\sqrt{n_{\text{c-Si}} \cdot n_{\text{SiO}_x}}$  is included for reference.

This is further illustrated by the scanning electron microscope image in Fig. 5.4(b). A nano-pillar array with a period of 1000 nm and height of approximately 500 nm was smoothed using multiple spin coating and drying cycles. The complete stack was then annealed prior to silicon deposition. The smoothing of the spin-coated  $\text{TiO}_x$  is effective also for thicker layers, preferentially filling the areas between the silicon oxide pillars, resulting in a smooth surface.

Hence, spin-coated titanium oxide is a suitable material for the SMART texture. The spin-coating process ensures a preferential filling of the areas between the  $\text{SiO}_x$  nano-pillars. The employed titanium oxide exhibits a refractive index of 2.1 and is therefore suited as a smoothing material employed in the SMART texture, therein providing anti-reflective texture at the glass-silicon interface of LPC silicon thin-film solar cells.

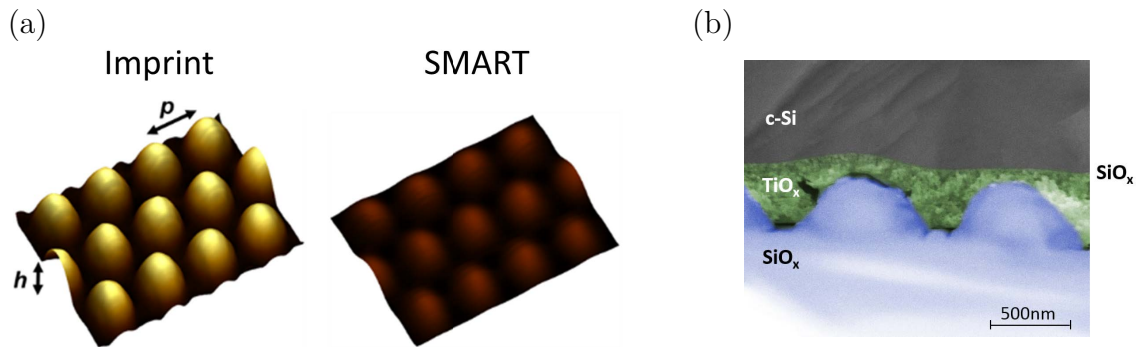


**Figure 5.4:** (a) Atomic force microscope images of a hexagonal nano-pillar array with a height  $h = 50$  nm and period  $p = 750$  nm before (left) and after (right) spin-coating. (b) Scanning electron microscope image in cross-section of an exemplary SMART texture with a period of 1000 nm and a height of  $\approx 500$  nm.

### 5.3 Optical analysis

The SMART texture was established as a three-dimensional texture that provides a refractive index contrast suitable for anti-reflection at the glass-silicon interface as well as a smooth surface. To analyze its potential as anti-reflective texture at the buried glass-silicon interface of LPC silicon thin-film solar cells on glass, its optical properties were investigated using three-dimensional simulations to identify a suitable geometrical parameter set. Based on these results, SMART textures were produced and their optical properties compared to the simulations.

#### 5.3.1 Simulations

Three-dimensional simulations using the finite element method were carried out as described in section 3.5.2. The simulations aimed at finding suitable geometry parameters to guideline an optimized experimental realization of the SMART texture. Simulations were carried out by Duote Chen and Dr. Klaus Jäger in cooperation with the author of this thesis. One unit cell of the simulated stack with a glass substrate, SMART texture and silicon absorber is depicted in Fig. 3.14. As the computational domain is limited by time and capacity, the glass and silicon layers are treated as infinitely thick using perfectly matched layers, in which all light is absorbed which reaches them. An a posteriori correction of reflection at the air-glass interface is performed to account for light scattered back at the glass-silicon interface at oblique angles [202]. The SMART texture consists of a silicon oxide nano-pillar of diameter  $d$  and height  $h$  and a titanium oxide layer filling the voids between the nano-pillars. The size of the hexagonal unit cell defines the period  $P$  of

the texture. Period and diameter influence the  $\text{SiO}_x$  filling fraction  $ff$  of the texture defined by the ratio of silicon oxide surface area to total area of the unit cell (cf. Eq. (3.4)). A 10 nm thin silicon oxide layer on top of the SMART texture is required as a passivation layer in the experimental structure and therefore also included in the simulations. Simulated absorptance values are averaged over the wavelength range 400 nm to 600 nm. For these wavelengths, the penetration depth of the incoming light is, on the one hand, small enough to exclude an influence of the rear interface which is not taken into account in the simulations. On the other hand, parasitic absorption of the glass substrate and titanium oxide is negligible (cf. section 3.4.2). This allows for a better comparability to experimental results.

In order to gain insights on suitable structural parameters for the SMART texture production, the geometric parameters of filling fraction  $ff$ , period  $P$  and height  $h$  were varied in the simulations. As a first parameter, the filling fraction was varied between 0.25, 0.5 and 0.75 for a fixed period of 750 nm. Figure 5.5(a) exhibits the mean absorptance between 400 nm and 600 nm for a hexagonal nano-pillar array with varied  $ff$ . For  $ff = 0.25$ , corresponding to a nano-pillar with small diameter and, thereby, a titanium oxide rich texture, the highest absorptance values are observed. For  $ff = 0.25$  and  $ff = 0.5$ , optimal absorptance is found for a height of 40 nm – 50 nm. For  $ff = 0.75$ , the silicon oxide-rich surface, optimum height is higher with about 60 nm – 70 nm, absolute values of absorptance, however, are lower. Fill factors below 0.25 were not investigated due to technological constraints in the production of very narrow nano-pillars. Therefore, further calculations were carried out using a  $\text{SiO}_x$  filling fraction of 0.25.

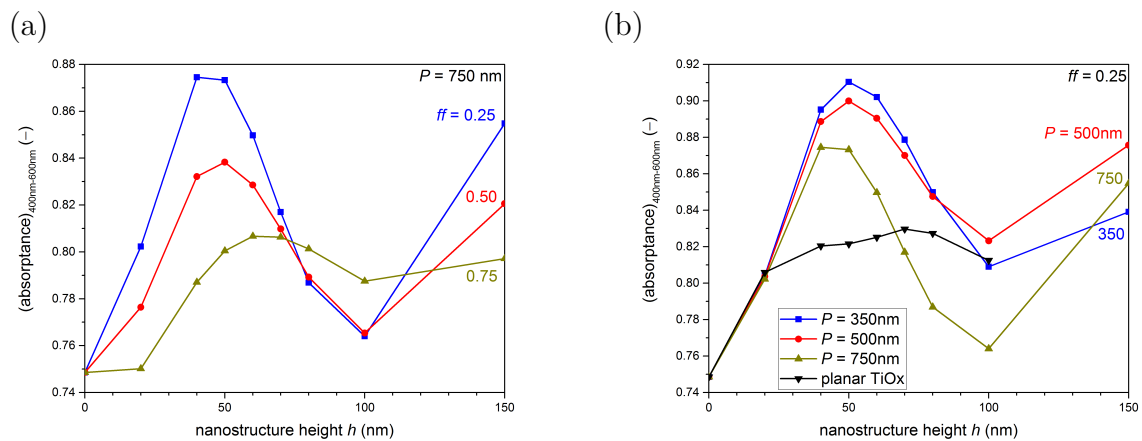


**Figure 5.5:** (a) Mean absorptance in the wavelength range 400 nm to 600 nm for varied filling fraction  $ff$  of the nano-pillar, for a fixed period of  $P = 750$  nm. (b) Mean absorptance in the wavelength range 400 nm – 600 nm for varied periods of the SMART texture, with a fixed filling fraction  $ff = 0.25$ .

As second parameter, the period of the nano-texture is varied between 350 nm and 750 nm. Mean absorptance between 400 nm and 600 nm for  $P = 350$  nm (blue), 500 nm (red), and 750 nm (yellow) is depicted in Fig. 5.5(b). To prove the effectiveness of the SMART texture, a planar titanium oxide layer (black) is included in the study. For all periods, light in-coupling at the optimal nano-structure height  $h$  of around 40 nm – 60 nm is enhanced compared to a planar  $\text{TiO}_x$  layer. While absolute differences are modest, smaller periods yield higher light in-coupling values.

To summarize, simulation results reveal that nano-pillar arrays with narrow diameters are required for efficient light in-coupling in LPC silicon thin-film solar cells. A  $\text{SiO}_x$  filling fraction of  $ff = 0.25$  was identified as a guideline to experimental SMART textures. While absolute differences were smaller than for the filling fraction variation, a lower period was determined to be beneficial for light in-coupling.

### 5.3.2 Comparison of experiment and simulations

Several SMART textures with a silicon absorber produced by solid phase crystallization (SPC) were manufactured. While SPC silicon is not suitable for solar cell applications due to its limited material quality [38], its optical properties are equivalent to LPC silicon for wavelengths up to 900 nm [169]. Therefore, it allows analyzing the optical properties of silicon absorbers with a textured interface using a facile and stable processing method. The study was restricted to a period of 750 nm despite smaller periods being superior in regards to light in-coupling as this period has proven to be more stable during LPC compared to smaller periods [49].

Based on the simulation results discussed above, three distinct SMART textures were manufactured. Their optical properties are illustrated in Fig. 5.6. The produced SMART textures differ in filling fraction and SMART texture height, namely  $ff = 0.75$  and  $h = 300$  nm (Fig. 5.6(a)),  $ff = 0.50$  and  $h = 80$  nm (Fig. 5.6(b)), and  $ff = 0.25$  and  $h = 60$  nm (Fig. 5.6(c)). Different SMART texture heights for the simulated absorptance curves are displayed. To exclude the influence of the back interface, the analysis is limited to the wavelength range from 300 nm to 600 nm, for which the penetration depth in crystalline silicon is smaller than the absorber thickness. The steep absorption increase for wavelengths  $< 400$  nm in the experimental samples stems from parasitic absorption in the glass substrate and titanium oxide layer.

For all textures, simulations replicate the main absorption features found in experiment. One peak around 560 nm in Fig. 5.6(a) is not observed in experiment. As the peak is only found for one wavelength, it is considered to be a numerical artifact from meshing (Dr. Klaus Jäger, personal communication, February 2018). The overall

absorptance, however, is higher for the experimental textures. This is attributed to differences in the modelled and real SMART texture, e.g. a residual roughness of the SMART texture surface or a complete coverage of the SMART texture with titanium oxide. Still, the general trend of the simulations follows the same course as the experimental structures for all filling fractions and heights.

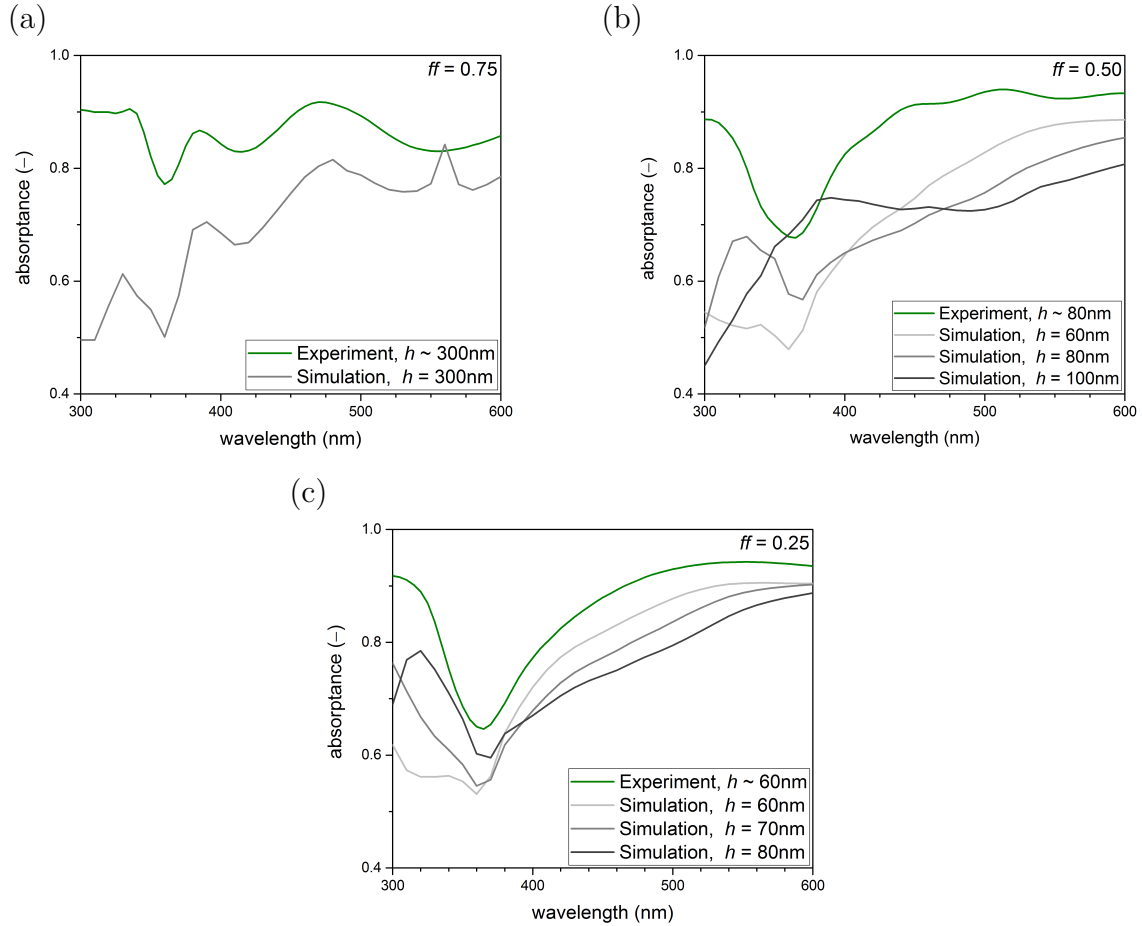


**Figure 5.6:** Comparison of simulated and experimental absorptance of a silicon absorber with a SMART texture at the glass-silicon interface. The SMART textures are characterized by (a) a filling fraction of 0.75 and a height of 300 nm, (b) filling fraction of 0.50 and a height of 80 nm, and (c) filling fraction of 0.25 and a height of 60 nm. Multiple heights of the simulated structures are added for reference.

Simulation results hence provide useful hints towards the optimal geometrical parameters for the SMART texture as an anti-reflective measure at the glass-silicon interface of LPC silicon thin-film solar cells. In consequence, the optimum parameters derived from simulations while considering technological feasibility, namely a period of 750 nm, filling fraction of 0.25 and height of 40 nm to 60 nm, were used in the experimental SMART textures.

## 5.4 Proof-of-concept solar cells

Having identified and established an optimized geometrical parameter set for SMART texture production, LPC silicon thin-film solar cells were produced on glass substrates with a SMART texture with the abovementioned parameters of  $P = 750$  nm,  $ff = 0.25$ , and  $h = 50$  nm. The devices exhibit a silicon absorber thickness of  $8\ \mu\text{m}$  and an n-type doping concentration of  $\approx 1 \times 10^{17}\ \text{cm}^{-3}$ . Figure 5.7 illustrates the optical properties of the SMART texture compared to a reference solar cell with a planar 250 nm silicon oxide/70 nm silicon nitride/10 nm silicon oxide stack processed in parallel – the best planar interlayer stack regarding optical and electronic solar cell performance at the time of the experiment. With regards to light in-coupling as measured by 1–reflectance ( $1 - R$ , solid lines in Fig. 5.7), the SMART texture reduces reflection in the wavelength range from 300 nm – 800 nm. For longer wavelengths, reflection at the silicon back-side dominates the properties and no difference between the cells is found within the measurement variability. Transmittance of the solar cells (dashed) is lower for the SMART textured absorber. Due to the texture being optically rough, the SMART texture also scatters light away from normal incidence into higher angles, leading to a longer light path in the absorber and, as a consequence, lower transmittance.

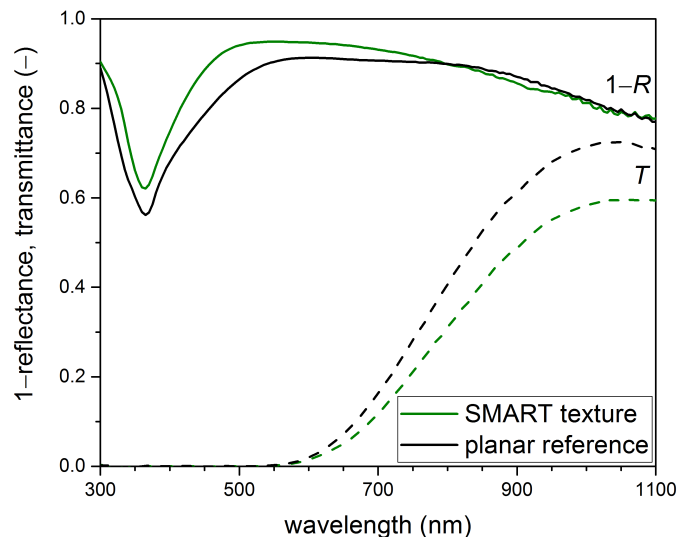


**Figure 5.7:** Optical properties, as measured by 1–reflectance ( $1 - R$ , solid) and transmittance  $T$  (dashed), of LPC silicon thin-film solar cells with a planar glass-silicon interface (black) and a SMART texture (green).

The light in-coupling properties of the SMART texture are compared to those of a sinusoidal texture with a period of 750 nm and height-to-period ratio of 0.5 in Fig. 5.8. In the wavelength range from 300 nm to 450 nm, the sinusoidal texture allows

to couple in more light, while from 450 nm to 600 nm, the SMART texture absorbs slightly more light. Overall, mean absorptance from 400 nm – 600 nm of 91.8% is slightly higher for the sinusoidal texture than for the SMART texture absorbing 90.8%. However, both textures efficiently reduce reflectance compared to the planar reference, which absorbs 84.0% of the incoming light. It is noted that 4% of the incoming light is already reflected at the sun-facing air-glass interface (dotted line in Fig. 5.8).

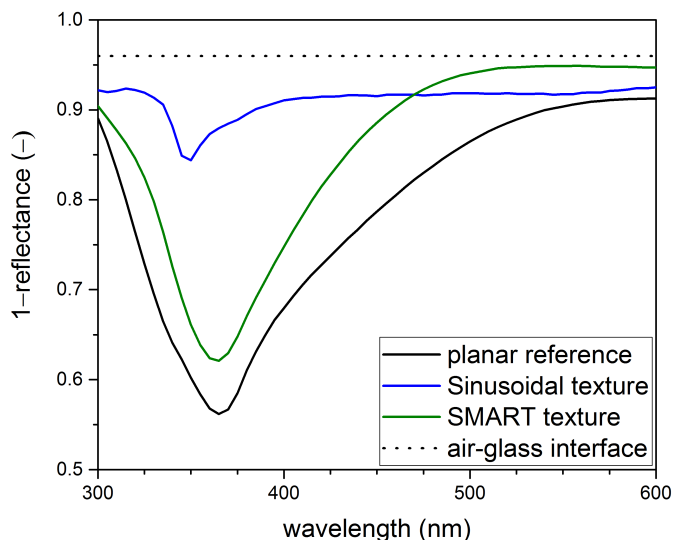


**Figure 5.8:** Light in-coupling properties, as measured by 1–reflectance, of LPC silicon thin-film solar cells with a planar glass-silicon interface (black), a SMART texture (green), and a sinusoidal texture (blue). For reference, reflectance at the sun-facing air-glass interface (dotted) is included.

As discussed in the previous chapter, absorption enhancement does not lead to increased solar cell efficiency if the texture induces defects and limits the material quality. Hence, electronic properties of the solar cells are at least equally important for device performance. Figure 5.9 depicts the mean open-circuit voltage as a measure of material quality for the five best solar cells with a SMART texture and a sinusoidal texture and their respective reference samples exhibiting a planar glass-silicon interface. Mean  $V_{oc}$  is about 20 mV higher for the reference solar cell manufactured in parallel to the SMART texture compared to the reference to the sinusoidal textured solar cell. This is attributed to different doping concentrations, absorber thicknesses, and additional process variations. If the influence of textures on the material quality is investigated, a drop in mean  $V_{oc}$  by 25 mV is observed for the sinusoidal texture. As discussed before, this is caused by an increase in recombination due to texture-induced defects [48, 49]. For the SMART texture, on the contrary, no detrimental effect on material quality is observed. Mean  $V_{oc}$  is higher by 20 mV for solar cells with a SMART texture compared to the corresponding pla-

nar reference. An open-circuit voltage gain from an enhanced short-circuit current density (cf. Fig. 5.10) was estimated to  $\Delta V_{oc} \approx 3$  mV using a one-diode model. As the doping concentration and absorber thickness is the same for the parallel processed samples, the increased  $V_{oc}$  is attributed to an improved interface passivation of the SMART texture compared to the  $\text{SiO}_x/\text{SiN}_x/\text{SiO}_x$  interlayer stack used in the planar reference. A similar passivating effect of titanium oxide has also been reported in literature [219–223], but further experiments are needed to prove this hypothesis.

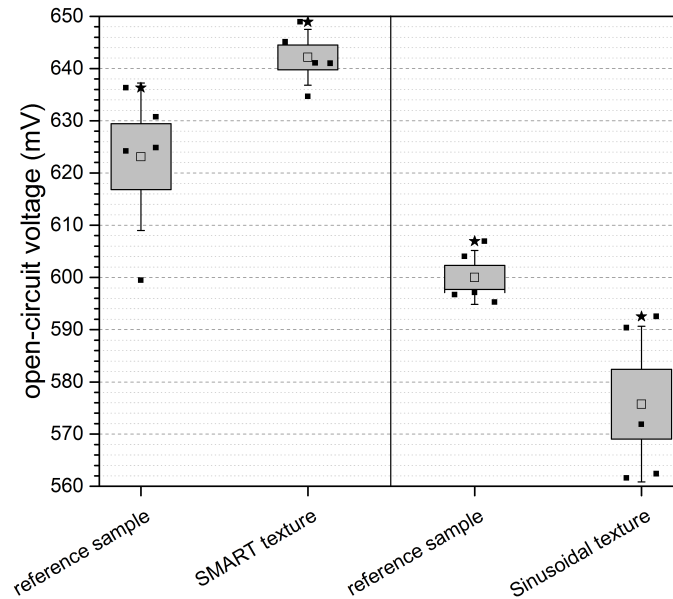


**Figure 5.9:** Open-circuit voltage measured with a Suns- $V_{oc}$  unit for the five best solar cells on SMART texture and sinusoidal texture and their respective reference samples exhibiting a planar glass-silicon interface. Mean  $V_{oc}$  is depicted by an open square, best  $V_{oc}$  with a star. The box symbolizes the standard error, the whiskers the standard deviation.

Hence, the SMART texture does not negatively influence the material quality of the LPC silicon absorber. This finding is confirmed by current-voltage characteristics of the solar cells displayed in Fig. 5.10. To investigate the influence of the lithography-free quasi cell process (cf. section 3.3), both the current-voltage characteristics measured directly and calculated from Suns- $V_{oc}$  without influence of series resistance is illustrated. For both solar cells, the relatively high series resistance of the quasi cells leads to a decreased fill factor, but short-circuit current density and open-circuit voltage is maintained (cf. section 2.3). As stated before, the open-circuit voltage of the device with a SMART texture at the glass-silicon interface is higher by about 20 mV. The more significant difference, however, is found for short-circuit current density. Introducing the SMART texture increases  $j_{sc}$  from  $19.0 \text{ mA cm}^{-2}$  for the reference sample to  $23.3 \text{ mA cm}^{-2}$  for the solar cell with a SMART texture,

a gain of  $4.3 \text{ mA cm}^{-2}$ . This can be explained by the increased light absorption due to enhanced light in-coupling and light scattering, which amounts to a gain in maximum achievable short-circuit current density  $j_{sc,max}$  of  $3.8 \text{ mA cm}^{-2}$ . The additional  $j_{sc}$  gain of  $0.5 \text{ mA cm}^{-2}$  is attributed to an enhanced carrier extraction due to the improved surface passivation and measurement uncertainties.

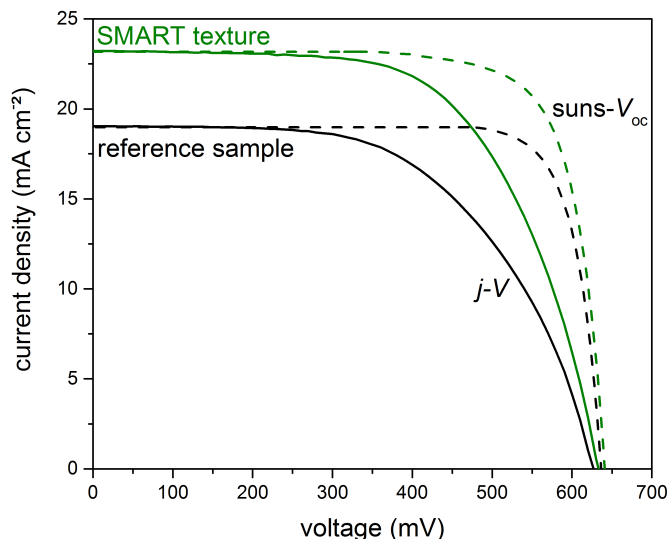


**Figure 5.10:** Current-voltage characteristics measured using a solar simulator (solid) and calculated from Suns- $V_{oc}$  (dashed) for solar cells with a planar glass-silicon interface (black) and a SMART texture (green).

To further analyze the potential of the SMART texture to increase the short-circuit current density and, thereby, efficiency of LPC silicon thin-film silicon solar cells, its external quantum efficiency is compared to a state-of-the-art solar cell with an n-type  $13 \mu\text{m}$  thick LPC absorber with a doping concentration of  $1 \times 10^{17} \text{ cm}^{-3}$  and a random pyramid back-side texture. The state-of-the-art solar cell exhibits an interdigitated back contact (IBC) system. This IBC cell design has a dead area of approximately 8% [42], by which the EQE is scaled to allow a fair comparison to the full-emitter quasi cell with a SMART texture. If additional light trapping measures at the air-glass interface are employed, this solar cell provides a power conversion efficiency of 13.2%, the record efficiency for LPC silicon solar cells at the time of the experiment [42].

Light in-coupling as measured by  $1 - \text{reflectance}$  is illustrated together with EQE in Fig. 5.11. As already discussed for the reference sample processed in parallel to the cell with a SMART texture, the introduction of the SMART texture leads to a reduction of reflectance in the short wavelength range up to about 700 nm (grey shaded area in Fig. 5.11). For longer wavelengths, the greater absorber layer thickness ( $13 \mu\text{m}$  vs.  $8 \mu\text{m}$ ) and random pyramid texture of the IBC cell dominates the

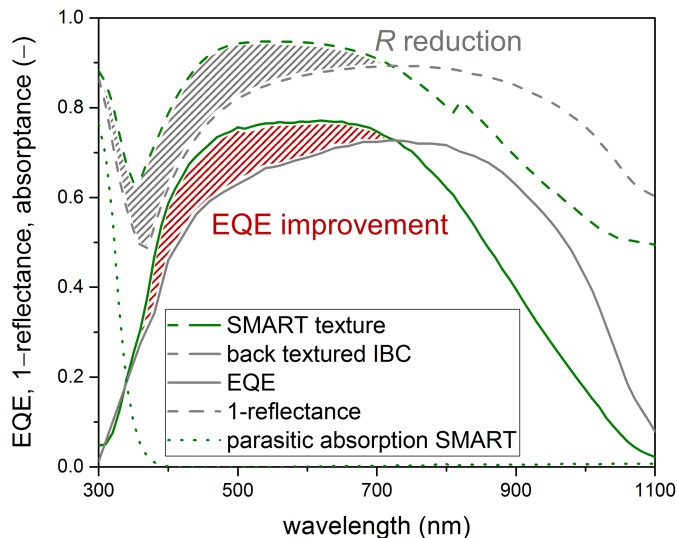


**Figure 5.11:** External quantum efficiency (EQE, solid) and light in-coupling as measured by 1–reflectance (dashed) for a solar cell with a SMART texture (green) and a state-of-the-art back textured interdigitated back contacted solar cell (black) – the record device at the time of the experiment. Parasitic absorption of the SMART texture is included for reference (dotted). Data for the back textured IBC cell was taken from [42].

optical properties and, hence, absorptance is higher than for the SMART textured cell which has a flat back-side.

The same trend is observed for the external quantum efficiency. While in the long wavelength regime, EQE is higher for the state-of-the-art cell due to the higher absorber thickness and pyramid back-side texture, in the short wavelength range the reduced reflection leads to an increase in EQE (red shaded area in Fig. 5.11). The electronic material quality of the SMART texture can therefore be considered equivalent to that of the state-of-the-art device. In particular, it can be concluded that the SMART texture does not induce defects at the glass-silicon interface, in contrast to prior texturing methods. This assumption is supported by the internal quantum efficiency (IQE) depicted in Fig. 5.12. IQE, the ratio of EQE and absorptance, is a measure for the extraction efficiency of electron-hole pairs generated in the LPC silicon absorber. It is equivalent for both the solar cell with the SMART texture (green) and the back-textured IBC cell (black) up to about 800 nm. For longer wavelengths, IQE is higher for the back-textured device. As longer wavelengths are generally absorbed closer to the rear side instead of the front interface, this is rather attributed to better back-side passivation in the more sophisticated IBC cell design than to a negative impact of the front-side texture.

Short-circuit current densities were calculated from the measured EQE. As EQE provides a spectral measurement, contributions from different wavelength ranges can be examined as opposed to  $j - V$  characteristics summing over all wavelengths.

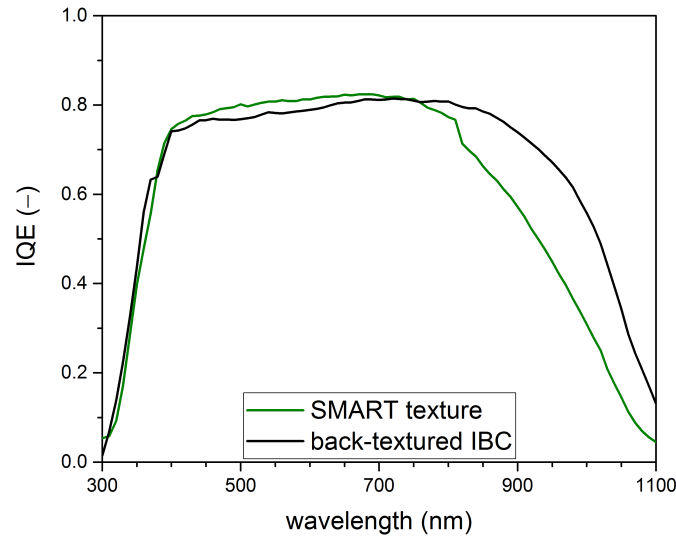


**Figure 5.12:** Internal quantum efficiency (IQE) of the solar cell with a SMART texture (green) and back-textured interdigitated back contacted (IBC) cell (black).

Table 5.2 summarizes  $j_{sc,EQE}$  calculated from EQE measurements in the wavelength range 300 – 700 nm and for the whole spectral range usable for energy conversion in silicon. For comparison, the maximum achievable short-circuit current density  $j_{sc,max}$  calculated from absorptance is included. Maximum achievable short-circuit current density from 300 nm to 700 nm of the solar cell with a SMART texture is higher than that of the back-textured IBC cell by  $1.9 \text{ mA cm}^{-2}$ . If electronic material properties are taken into account by measuring EQE, the same gain in  $j_{sc}$  is observed, from  $j_{sc,EQE}(300 \text{ nm} - 700 \text{ nm}) = 13.2 \text{ mA cm}^{-2}$  to  $15.0 \text{ mA cm}^{-2}$  for the back-textured IBC and SMART textured solar cell, respectively.

**Table 5.2:** Short-circuit current density calculated from 1–reflectance ( $j_{sc,max}$ ) and from external quantum efficiency ( $j_{sc,EQE}$ ) measurements, for the solar cell with a SMART texture and the back-textured IBC reference cell.

Solar cell	thickness $\mu\text{m}$	$j_{sc,max}$ (300 – 700 nm) $\text{mA cm}^{-2}$	$j_{sc,max}$ $\text{mA cm}^{-2}$	$j_{sc,EQE}$ (300 – 700 nm) $\text{mA cm}^{-2}$	$j_{sc,EQE}$ $\text{mA cm}^{-2}$
IBC refer- ence	13	16.9	35.3	13.2	25.6
SMART texture	8	18.8(+1.9)	34.6(–0.7)	15.0(+1.8)	24.2(–1.4)

Therefore, bulk material and interface quality of LPC silicon on a SMART texture can be considered equivalent to state-of-the-art solar cells with planar glass-silicon interface. For the complete wavelength range, both  $j_{sc,max}$  and  $j_{sc,EQE}$  of the IBC device are higher due to the back-side texturing and higher absorber thickness.

In a nutshell, the SMART texture has demonstrated to provide both, increased light in-coupling into LPC silicon thin-film solar cells and state-of-the-art material quality. Solar cells with an 8  $\mu\text{m}$  thick LPC absorber on a SMART texture exhibit an open-circuit voltage of up to 649 mV and short-circuit current density calculated from EQE of  $24.2 \text{ mA cm}^{-2}$ . Analysis of the quantum efficiency compared to a state-of-the-art solar cell reveal the potential of the SMART texture to increase the short-circuit current density of LPC silicon solar cells. In the wavelength range from 300 nm to 700 nm, an EQE enhancement equivalent to a gain in short-circuit current density of  $1.8 \text{ mA cm}^{-2}$  proves the suitability of the SMART texture to be implemented in high efficiency LPC silicon thin-film solar cells on glass.

## 5.5 SMART texture optimization

Having established the SMART texture as a suitable texture to combine improved light in-coupling with an excellent material quality of the LPC silicon thin-film absorber, measures to further optimize the SMART texture with respect to an improved yield and optical properties were taken. In order to achieve this, enhanced light in-coupling of the SMART texture at the front glass-silicon interface as well as the combination of the SMART texture with light trapping textures at the silicon back-side were investigated. Additionally, novel interlayer deposition techniques developed for planar LPC silicon thin-film silicon solar cells, there improving both optical and interface quality, were incorporated in the SMART texture manufacturing process.

### 5.5.1 Titanium oxide sol-gel annealing

The titanium oxide sol-gel was optimized with respect to light in-coupling. To realize this, a higher refractive index of the annealed  $\text{TiO}_x$  layer was targeted, which will be addressed experimentally in the latter. One-dimensional simulations were carried out to illustrate the benefit of a higher refractive index. In this preliminary simulations, the SMART texture was modelled as an effective medium of silicon oxide and titanium oxide between a glass substrate and a silicon layer (cf. section 3.5.1). The mixing ratio was chosen in line with the filling fraction of 0.25 of nano-pillars in the experimental SMART textures. For simplicity, the scattering effect of the SMART texture was neglected and the silicon thickness was assumed to be infinite. These restrictions reduce simulation accuracy, but are acceptable for this qualitative analysis. Figure 5.13 depicts the amount of light coupled into the silicon layer for

three different refractive indices of the titanium oxide layer. The result demonstrates that higher refractive indices of the layer derived from titanium oxide sol-gel are desirable to increase light in-coupling, with most of the anti-reflective effect in the wavelength range from 450 nm to 800 nm. Using lower filling fraction or planar titanium oxide films, which would further increase the effective refractive index, was not experimentally feasible due to limitations in the nano-pillar production process and a lack of compatibility with the LPC process, respectively. Improved light in-coupling can be explained by the higher refractive index of the mixed medium being closer to the optimum for anti-reflection between glass and crystalline silicon,  $\sqrt{n_{c-Si} \cdot n_{SiO_2}} \approx 2.4$  (see also Fig. 5.3).

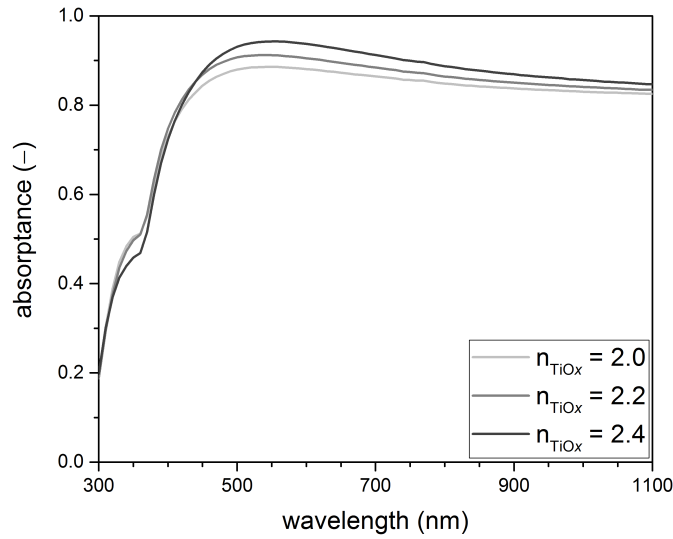


**Figure 5.13:** Simulation of absorptance of a silicon oxide/titanium oxide effective medium with varied refractive index of the titanium oxide layer. The optical thickness of the layer, the product of refractive index and physical thickness, is kept constant at 120 nm for improved comparability.

In order to realize a higher refractive index experimentally, the annealing temperature was increased from 500 °C to 800 °C. The annealing time of 30 min was kept constant. This temperature is still lower than the softening point of the glass substrate [75], whereby bending or cracking of the glass can be prevented. The temperature increase leads to a higher refractive index, as revealed by ellipsometry measurements disclosed in Fig. 5.14(a). The refractive index of the titanium oxide layer annealed at 500 °C (light blue curve) is lower than that of the  $TiO_x$  layer annealed at 800 °C (green curve) over the whole wavelength range. The refractive index at 600 nm of the  $TiO_x$  layer annealed at the higher annealing temperature of 800 °C amounts to 2.3, compared to 2.1 for an annealing at 500 °C. For the same spin speed, the resulting layer thickness is reduced from 55 nm after spin-coating to 45 nm and 36 nm for the samples annealed at 500 °C and 800 °C, respectively. As

the temperatures during liquid phase crystallization reach above 700 °C, the higher annealing temperature additionally prevents further densification during the LPC process, which might affect the interface quality negatively.

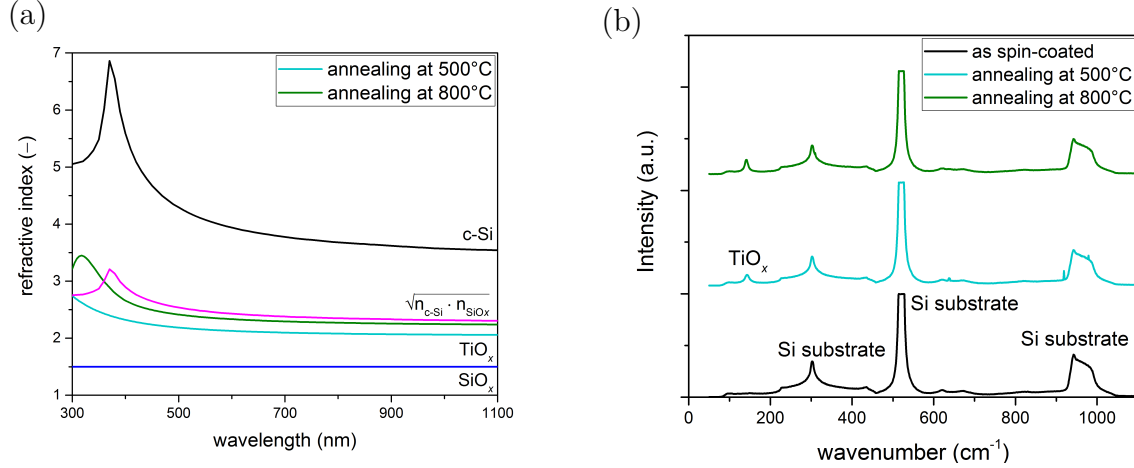


**Figure 5.14:** (a) Refractive index of the titanium oxide layers annealed at 500 °C (light blue) and at 800 °C (green) measured by ellipsometry. Literature data were taken for the refractive indices for crystalline silicon [76] and silicon oxide [218] used to calculate the optimal refractive index (magenta) for anti-reflection. (b) Raman spectroscopy of the titanium oxide layer annealed at 500 °C (light blue) and at 800 °C (green), compared to the titanium oxide layer before annealing (black). Reference spectra for titanium oxide in anatase and rutile phase are displayed in Fig. 5.2(b).

Raman spectroscopy measurements were performed as fingerprint method of changes in the micro-structure of the titanium oxide layer. Raman spectra of the samples annealed at different temperatures displayed in Fig. 5.14(b) reveal that the micro-structure of the titanium oxide film is unchanged by the increased annealing temperature, with a characteristic titanium oxide peak at approximately  $140\text{ cm}^{-1}$ . Hence, the higher refractive index and reduced layer thickness can be attributed to a denser film after annealing at 800 °C compared to 500 °C.

The optimized annealing for the titanium oxide layer was implemented in the SMART texture production process. Figure 5.15 presents the absorptance of LPC silicon thin-film solar cells with a SMART texture annealed at 500 °C (light blue) and at 800 °C (green), highlighted for the wavelength range from 300 nm to 700 nm. As a reference, reflectance at the air-glass interface amounting to 4% at normal incidence is included in the graph (dotted). The SMART thickness of 45 nm is the same for both samples. Due to the lower thickness of  $TiO_x$  layers annealed at 800 °C, the spin speed was adjusted accordingly to reach a comparable thickness of the  $TiO_x$  layer constituting the SMART texture. As a consequence, the absorptance maximum for the SMART texture annealed at 800 °C is shifted to longer wavelengths. Minimum reflectance is reduced from 6.8% (absolute) to 5.3% (absolute) due to the higher

refractive index, including 4 % already reflected at the air-glass interface. Mean absorptance in the wavelength range from 400 nm to 600 nm amounts to 90.5 % for the optimized SMART texture. With an optimized sinusoidal texture, in comparison, mean absorptance of 93.0 % could be realized (cf. section 4.3.2).

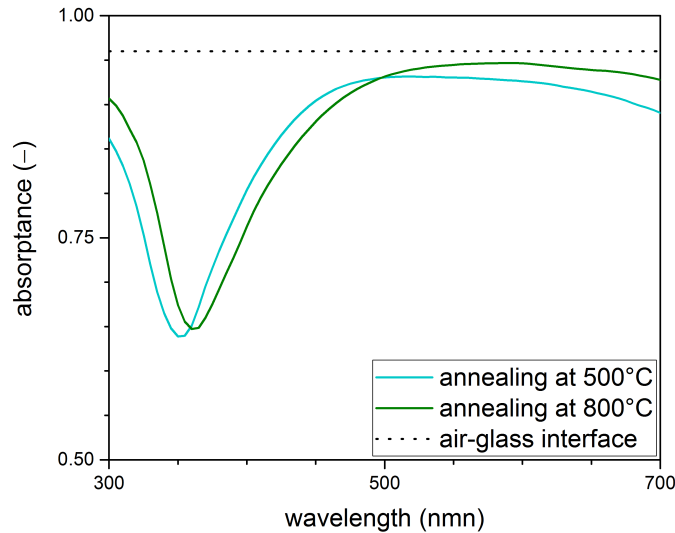


**Figure 5.15:** Absorptance in LPC silicon with a SMART texture annealed at 500 °C (light blue) and 800 °C (green). Reflectance at the air-glass interface (dotted) is included for reference.

In summary, titanium oxide films produced by optimized thermal annealing at 800 °C were demonstrated to exhibit a denser film and thereby higher refractive index. Using this high temperature annealing in the SMART texture production process allowed to further enhance the light in-coupling into LPC silicon thin-film absorbers.

### 5.5.2 Combination with light-trapping measures

The SMART texture efficiently reduces reflection at the front-side glass-silicon interface of LPC silicon thin-film solar cells. However, fully exploiting the solar spectrum usable for current generation in silicon, in particular the long wavelength range, requires the implementation of additional light trapping measures at the silicon back-side. Common approaches for LPC silicon solar cells with a planar glass-silicon interface are a random pyramid texture produced by wet-chemical etching in potassium hydroxide (KOH) for light scattering and a rear reflector to enhance the light path in the absorber. Both these measures can be combined for optimized light trapping in LPC silicon layers [209].

KOH pyramid textures and back reflectors were implemented in LPC silicon absorbers deposited on a SMART texture. Figure 5.16 discloses the absorptance of

15  $\mu\text{m}$  thick LPC silicon layers for a planar glass-silicon interface with a silicon nitride anti-reflective layer (black) and a SMART texture (green), combined with KOH pyramids (dashed) or a white paint back reflector (dotted). Absorptance of the white paint (grey) is included for reference. Implementing the rear-side light trapping textures does not alter the absorptance properties for the short wavelength range up to 600 nm, as for these wavelengths the penetration depth is smaller than the absorber thickness. The absorptance of the silicon layer with a SMART texture at the glass-silicon interface is higher than that of the sample with a planar silicon nitride anti-reflective layer over the whole wavelength range. Particularly, the long wavelength absorptance is enhanced even if no additional light trapping measures are employed. This can be attributed to the SMART texture increasing the light path in the silicon absorber due to scattering at the front side.

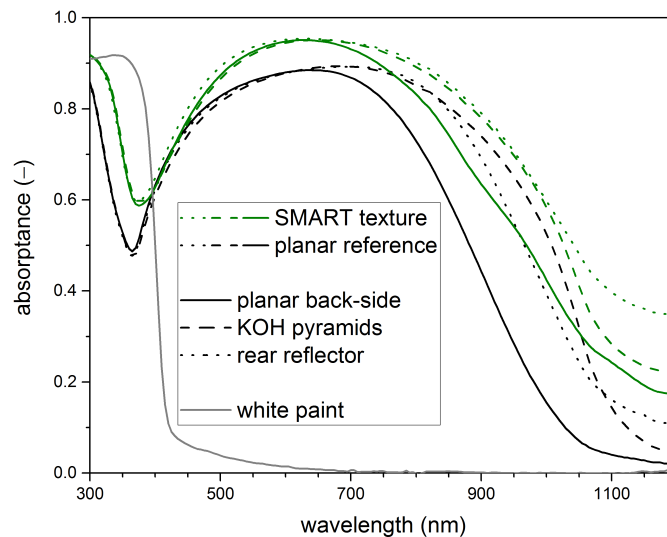


**Figure 5.16:** Absorptance of 15  $\mu\text{m}$  thick LPC silicon absorbers with a planar glass-silicon interface (black) and a SMART texture (green) with a planar back-side (solid), KOH pyramid texture (dashed) or a white paint back reflector (dotted) for light trapping at the silicon back-side. Parasitic absorption of the white paint (grey) is included for reference.

Both light trapping measures increase absorptance in the long wavelength range for the two samples. For the absorber with a planar glass-silicon interface, the implementation of KOH pyramids is more effective for absorption enhancement than a rear reflector due to the scattering increasing the light path more than the simple doubling by the white paint reflecting light back into the absorber. For the SMART texture, on the contrary, both light trapping measures are equally effective. As the SMART texture scatters a part of the incident light at the front glass-silicon interface into larger angles, the rear reflector is more effective in increasing the light path than for a planar glass-silicon interface. Parasitic absorption in the white paint

reflector can be neglected as it exhibits a parasitic absorption only for wavelengths  $< 700$  nm, which are absorbed before reaching the silicon back-side.

If both light trapping measures are combined, as illustrated in Fig. 5.17(a), absorptance can further be enhanced by combining both the scattering of the KOH pyramid texture with the back-reflectance of the white paint back reflector. While absorptance differences between planar reference and SMART texture get smaller if back-side textures are implemented, the SMART texture still absorbs a higher proportion of the incoming light for the whole wavelength range. At a wavelength of 1200 nm, for which crystalline silicon is not absorbing, parasitic absorption of 10% (absolute) for the planar reference and 33% for the SMART texture are observed. Such high absorptance values have previously been reported for textured thin-film silicon solar cells on glass substrates and have been attributed to parasitic absorption in the glass and free carrier absorption [52, 224–226].

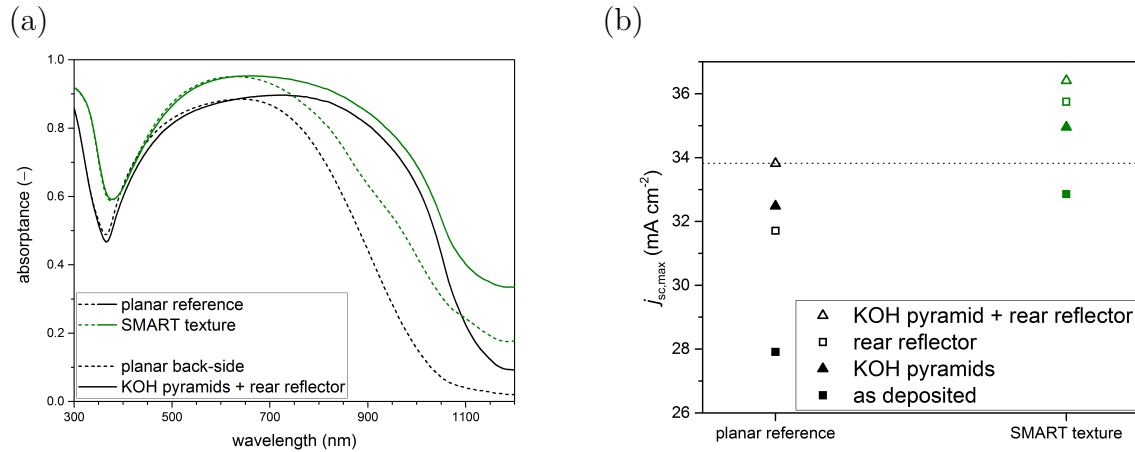


**Figure 5.17:** (a) Absorptance of 15  $\mu\text{m}$  thick LPC silicon absorbers with a planar glass-silicon interface (black) and a SMART texture (green) without back-side light management measures (dotted) and with KOH pyramids and a white paint back reflector (solid). (b) Maximum achievable short-circuit current density calculated from absorptance for 15  $\mu\text{m}$  thick LPC silicon absorber with a planar glass-silicon interface (black) and a SMART texture (green) for different light trapping measures at the silicon back-side. For reference, the highest value achieved for the sample with a planar glass-silicon interface is highlighted with a dotted line.

The optical potential of LPC silicon absorbers with a SMART texture is evaluated in terms of maximum achievable short-circuit current density in Fig. 5.17(b). Implementing a SMART texture at the glass-silicon interface increases the maximum achievable short-circuit current density from  $27.9 \text{ mA cm}^{-2}$  to  $32.9 \text{ mA cm}^{-2}$  without additional light trapping measures (filled squares). All light trapping measures increase  $j_{sc,max}$ , whereby the effectiveness of KOH texturing (filled triangles) is higher for the planar reference than for the SMART texture. If both light trapping means are introduced (open triangles), the maximum short-circuit current density is raised

to  $33.8 \text{ mA cm}^{-2}$  and  $36.4 \text{ mA cm}^{-2}$  for the reference sample and SMART texture. Hence, the SMART texture can efficiently be combined with state-of-the-art light trapping measures at the silicon back-side to improve light trapping in the LPC silicon absorber, allowing to increase maximum achievable short-circuit current density by  $2.6 \text{ mA cm}^{-2}$  compared to a planar glass-silicon interface with silicon nitride anti-reflective layer.

To sum up, the SMART texture was combined with KOH pyramid textures and white paint back reflectors at the silicon back-side of  $15 \mu\text{m}$  thick LPC silicon absorbers. These state-of-the-art light trapping measures increased absorptance in the long wavelength range for both, a reference sample and a SMART textured LPC silicon layer. Combining a SMART texture with a KOH pyramid texture and a white paint back reflector provided optimized light management, yielding a maximum achievable short-circuit current density of  $36.4 \text{ mA cm}^{-2}$ , compared to  $33.8 \text{ mA cm}^{-2}$  if these measures are implemented in an absorber with a planar glass-silicon interface with optimized silicon nitride anti-reflective layer, possibly enhancing the cell performance in future cell designs.

### 5.5.3 Implementation of novel interlayer developments

At the time this thesis was conducted, novel interlayer systems were developed to optimize the material and interface quality in planar LPC silicon solar cells (cf. section 4.3.1). The most recent advance in interlayer development was plasma-oxidation of the top  $\approx 10 \text{ nm}$  of the anti-reflective silicon nitride layer as passivation layer [43, 138]. Thus, the silicon oxide/silicon nitride/silicon oxide interlayer stack was substituted by a silicon oxide/silicon nitride/silicon oxy-nitride stack. Using this approach, a surface recombination velocity as low as  $200 \text{ cm s}^{-1}$  could be reached [43, 138]. Additionally, the higher refractive index of the silicon oxy-nitride layer compared to the previously employed silicon oxide layer reduced optical losses in the short wavelength range (see Fig. 4.7 and [43]).

In the SMART texture, the anti-reflective layer is constituted by titanium oxide instead of silicon nitride. Hence, the silicon oxide passivation layer is replaced by a silicon nitride layer. The first  $10 \text{ nm}$  of this silicon nitride layer can be then oxidized in order to implement the benefits of plasma oxidation in the SMART texture production process.

In order to identify suitable parameters for a SMART texture/silicon nitride double-layer system, one-dimensional simulations were performed. The SMART texture was modelled as a silicon oxide/titanium oxide effective medium, for which scattering is

implemented using scalar scattering theory [197, 198] as described in section 3.5.1. Of the silicon nitride layer thickness, the top 10 nm were assumed to consist of silicon oxy-nitride (Si(ON)) after plasma oxidation. The thickness of the effective medium representing the SMART texture was varied between 0 nm and 80 nm. Thicker silicon nitride layers of which only the top 10 nm are oxidized were also considered, varying the silicon nitride layer thickness between 10 nm (no residual  $\text{SiN}_x$  layer) and 90 nm (80 nm  $\text{SiN}_x$  + 10 nm Si(ON)).

Maximum achievable short-circuit current densities were calculated from these simulations, and are illustrated in Fig. 5.18 for (a) an infinitely thick silicon absorber and (b) a 15  $\mu\text{m}$  thick absorber with a KOH pyramid texture and a rear reflector at the back-side.

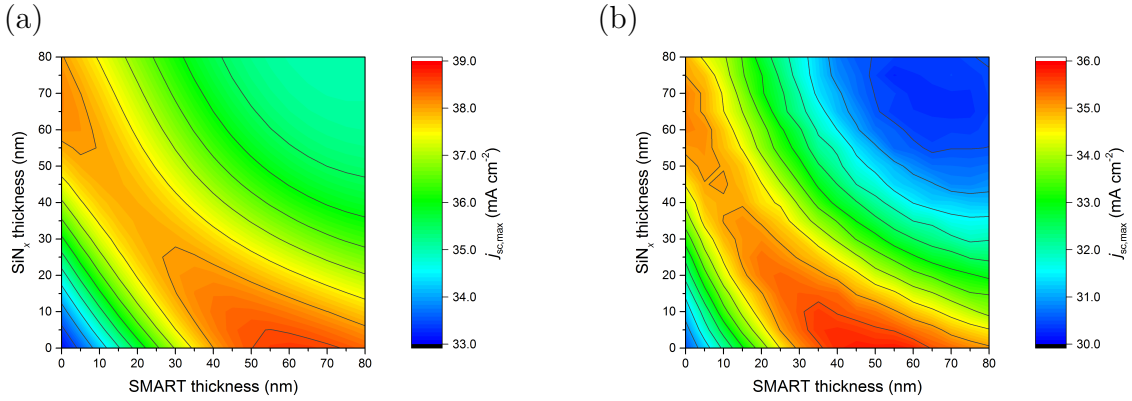


**Figure 5.18:** Maximum achievable short-circuit current density ( $j_{sc,max}$ ) as a function of varied  $\text{SiN}_x$  and SMART layer thicknesses derived from one-dimensional simulations of a SMART texture/silicon nitride/silicon oxy-nitride interlayer stack, for (a) an infinitely thick LPC silicon absorber and (b) a 15  $\mu\text{m}$  thick LPC silicon absorber with a KOH back-side texture.

For an infinitely thick absorber layer, where only light in-coupling is considered, the optimum parameters are a thickness of the effective medium between 50 nm and 60 nm and a silicon oxy-nitride thickness of 10 nm. This result is in line with three-dimensional simulations discussed in section 5.3.1, validating the use of the simple one-dimensional approach. Introducing a thicker silicon nitride layer than the 10 nm that are oxidized reduces the maximum achievable short-circuit current density. In particular,  $j_{sc,max}$  is higher for an interlayer system with a SMART texture than for a planar silicon nitride anti-reflective coating with optimized thickness. Maximum achievable short-circuit current density for a realistic silicon absorber with a thickness of 15  $\mu\text{m}$ , KOH pyramid back-side texture and rear reflector, is disclosed in Fig. 5.18(b). The parameter range that allows the highest absorptance is broader, with SMART thicknesses from 40 nm to 50 nm and silicon nitride thickness under the Si(ON) layer of 0 – 10 nm. The highest maximum achievable short-circuit current

density,  $j_{sc,max} = 35.8 \text{ mA cm}^{-2}$ , is found for a SMART thickness of 50 nm and a 10 nm thick silicon oxy-nitride layer, an increase of  $0.6 \text{ mA cm}^{-2}$  compared to an optimized silicon nitride anti-reflective layer.

To validate the simulation results, glass substrates with a SMART texture with a thickness of 45 nm and silicon nitride layers of 10 nm, 20 nm, and 30 nm were produced. The first 10 nm of the silicon nitride layers were oxidized using the plasma oxidation process. To analyze the optical potential for light in-coupling of the double-interlayer samples, 15  $\mu\text{m}$  thick silicon layers were deposited and subsequently crystallized by solid phase crystallization. Absorptance characteristics of these samples are illustrated in Fig. 5.19.

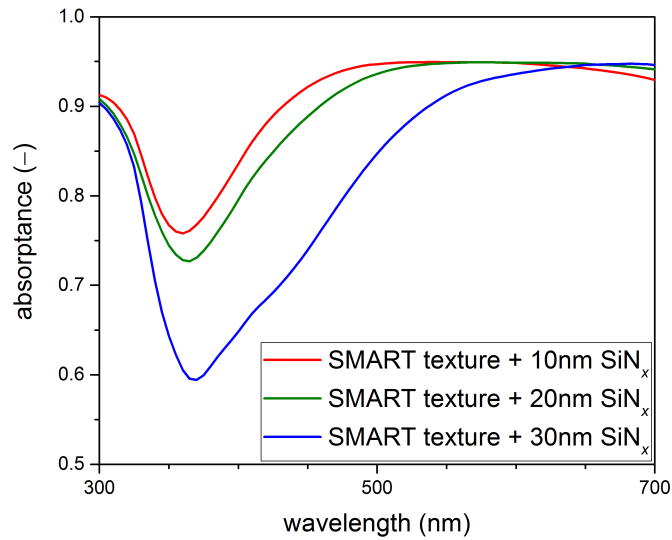


**Figure 5.19:** Absorptance of silicon absorbers with a 45 nm thick SMART texture and varied silicon nitride thickness, of which the first 10 nm are oxidized.

The trend predicted by the simulations is confirmed. The sample without residual silicon nitride layer under the 10 nm thin silicon oxy-nitride gives the highest mean absorptance, while thicker silicon nitride layers shift maximum absorptance to longer wavelengths and reduce light in-coupling for the wavelength range between 300 nm and 700 nm. For all samples, a maximum absorptance of 95% is found, whereof 4% of the light is reflected at the sun-facing air-glass interface. This proves the excellent anti-reflective properties of the SMART texture in combination with a silicon (oxy-)nitride layer.

Figure 5.20 exhibits the absorptance properties of the optimized SMART/silicon oxy-nitride interlayer stack (green, solid curve in Fig. 5.20) compared to a SMART texture with a 10 nm thick silicon oxide passivation layer (green, dashed), and the respective reference samples (black) with a silicon oxide/silicon nitride/silicon oxide ( $\text{SiO}_x$ , dashed) and a silicon oxide/silicon nitride/silicon oxy-nitride ( $\text{Si}(\text{ON})$ ,

solid) interlayer stack. For both planar and SMART textured interlayer stacks, the substitution of the passivation layer from  $\text{SiO}_x$  to  $\text{Si}(\text{ON})$  reduces reflection in the short wavelength range  $< 500$  nm, while maximum absorptance remains unchanged. In terms of mean absorptance between 400 nm and 600 nm, replacing the diffusion barrier of silicon oxide by silicon oxy-nitride leads to an increase from 90.6% to 92.9% (absolute) for the SMART texture. The optimized planar  $\text{SiO}_x/\text{SiN}_x/\text{Si}(\text{ON})$  interlayer stack provides a mean absorptance of 90.2%. This anti-reflective effect corresponds to an enhanced maximum achievable short-circuit current density gain of  $0.6 \text{ mA cm}^{-2}$  in the wavelength range from 400 nm to 600 nm, indicating an underestimated  $j_{\text{sc,max}}$  gain for the simulations with  $0.6 \text{ mA cm}^{-2}$  for the whole wavelength range. Hence, combining the SMART texture with the plasma oxidation process allows to further optimize light in-coupling in LPC silicon thin-film solar cells.

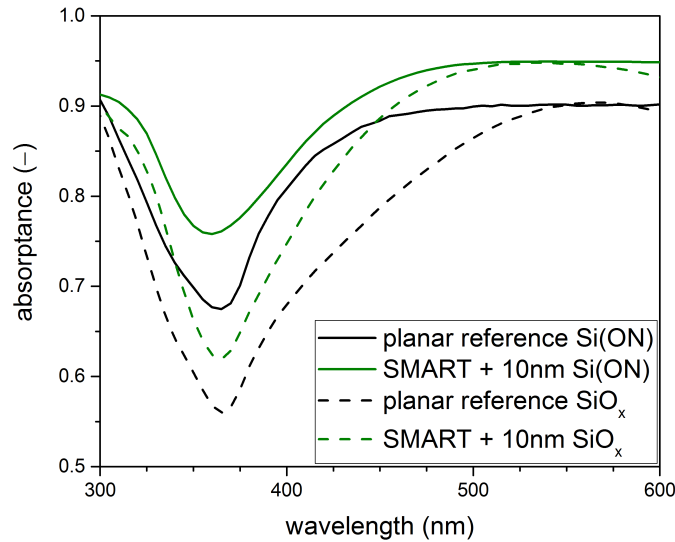


**Figure 5.20:** Absorptance of LPC silicon layers with a SMART texture (green) with a silicon oxide ( $\text{SiO}_x$ , dashed) and silicon oxy-nitride ( $\text{Si}(\text{ON})$ , solid) passivation layer, and reference samples with a planar silicon oxide/silicon nitride/silicon oxide interlayer stack ( $\text{SiO}_x$ , dashed) and with a silicon oxide/silicon nitride/silicon oxy-nitride interlayer stack ( $\text{Si}(\text{ON})$ , solid).

To summarize, multiple approaches to optimize the SMART texture were investigated. Raising the annealing temperature from  $500^\circ\text{C}$  to  $800^\circ\text{C}$  allowed to increase the refractive index of the titanium oxide layer, leading to improved anti-reflective properties at the glass-silicon interface. In addition, combinations of the SMART texture with light trapping measures at the silicon back-side, namely a random pyramid texture and a white paint rear reflector, were produced and analyzed in regards to their absorption properties. It was found that by combining the SMART texture with both light trapping techniques, a maximum achievable short-circuit current density of up to  $36.4 \text{ mA cm}^{-2}$  could be reached, an enhancement of  $2.6 \text{ mA cm}^{-2}$

compared to a planar interlayer stack with silicon nitride anti-reflective layer. Finally, the novel interlayer deposition technique of plasma oxidation of silicon nitride layers was applied to the SMART texture. Simulations were conducted to identify optimal layer thicknesses of the SMART texture/silicon nitride/silicon oxy-nitride interlayer stack. Using a 45 nm thick SMART texture in combination with a plasma-oxidized 10 nm thick silicon oxy-nitride layer, the short wavelength absorptance could be further increased, leading to a mean absorptance from 400 nm to 600 nm of 92.9% (absolute) compared to 90.6% and 90.2% for the SMART texture with silicon oxide diffusion barrier and optimized planar silicon oxide/silicon nitride/silicon oxy-nitride interlayer stack, respectively.

## 5.6 Towards solar cells on optimized SMART texture

Solar cells were produced on SMART textures with a silicon oxide and silicon oxy-nitride passivation layer and a reference sample with a planar silicon oxide/silicon nitride/silicon oxy-nitride interlayer stack. The 16  $\mu\text{m}$  thick LPC silicon absorbers were textured at the rear side with random pyramids derived from KOH etching. Figure 5.21(a) displays the external quantum efficiency (solid) and light in-coupling as measured by  $1 - \text{reflectance}$  (dashed) for the solar cells on SMART texture with  $\text{SiO}_x$  (green) and  $\text{Si}(\text{ON})$  (red) passivation layer and the reference sample (black). It is found that the liquid phase crystallization process alters the sample exhibiting a SMART texture and  $\text{Si}(\text{ON})$  passivation layer. Both the optical and electronic properties are deteriorated. Comparison to one-dimensional simulations as presented previously reveal that the light in-coupling properties correspond to a SMART texture height of 30 nm. As both samples were produced in parallel, the changed properties observed for the SMART texture with a silicon oxy-nitride layer are attributed to the interlayer stack being altered during LPC. The parallel processed samples exhibit the same SMART texture and the  $\text{Si}(\text{ON})$  passivation layer did not alter the optical properties after an SPC process, excluding these processes as an reason for the deteriorated properties. Internal quantum efficiency (IQE) for the wavelength range from 300 nm to 700 nm is disclosed in Fig. 5.21(b), for illumination from both superstrate (solid) and substrate (dashed) configuration (see Fig. 4.11(a) for a schematic of the measurement principle). If IQE is measured in substrate configuration, an equivalent IQE independent of the interlayer system is found. Thus, the bulk material quality seems not to be reduced by both SMART textures. In contrast, measurements through the glass, where most of the incoming

light is absorbed close to the glass-silicon interface, reveal a reduced carrier collection by the solar cells on SMART textures.

Internal quantum efficiency of the reference sample (black) is higher than 90% for wavelengths  $> 400$  nm. The SMART texture with silicon oxide passivation layer exhibits an IQE that is reduced by less than 10% (absolute), which is accounted for by a higher recombination caused by the  $\text{SiO}_x$  passivation layer. IQE of the SMART texture with silicon oxy-nitride passivation layer, in contrast, is limited to values below 70%. As IQE for illumination in substrate configuration was found to be equivalent, this is attributed to a deteriorated glass-silicon interface and, as a consequence, higher interface recombination velocity. In terms of short-circuit current density, the planar reference provides the highest  $j_{sc,EQE}$  of  $31.4 \text{ mA cm}^{-2}$ . The SMART texture with silicon oxide passivation layer still gives a high  $j_{sc,EQE}$  of  $29.4 \text{ mA cm}^{-2}$ , whereby the reduced interface quality of the SMART texture with a silicon oxy-nitride passivation layer limits  $j_{sc,EQE}$  to  $20.5 \text{ mA cm}^{-2}$ .

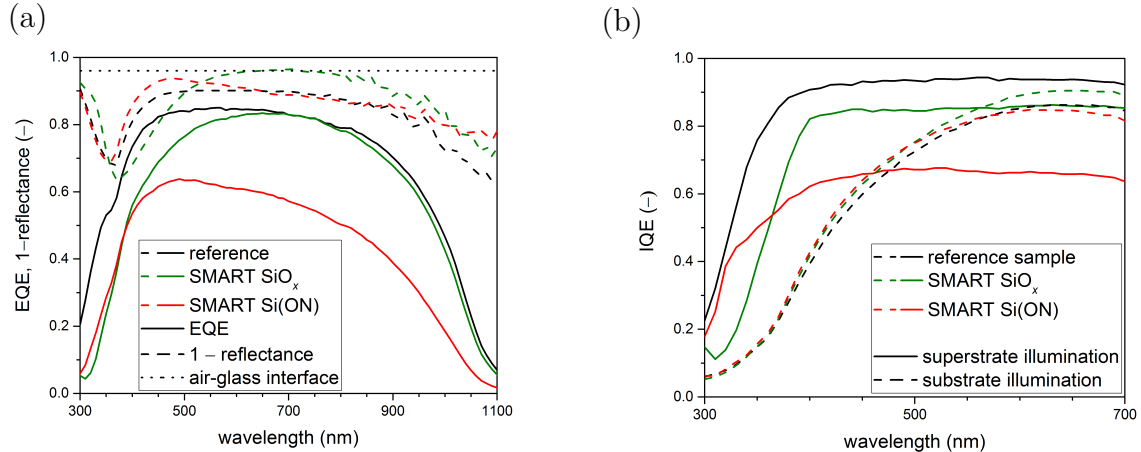


**Figure 5.21:** (a) External quantum efficiency (EQE, solid) and light in-coupling, as measured by 1-reflectance (dashed) of solar cells with a SMART texture with a silicon oxide (green) or silicon oxy-nitride (red) passivation layer and a reference sample (black). (b) Internal quantum efficiency for these solar cells, measured in superstrate (solid) and substrate (dotted) configuration.

Open-circuit voltage measurements performed using the suns- $V_{oc}$  method support the finding of higher recombination in the devices with SMART texture, as illustrated in Fig. 5.22. Spectral illumination during the  $V_{oc}$  measurements does not allow to distinguish between a primary influence of front and back interface as has been the case for the IQE measurement from both sides of the solar cells. Still, a similar trend is found for open-circuit voltages. While the solar cells on a planar glass substrate provides high  $V_{oc}$ 's well above 600 mV, the devices with a SMART texture exhibit lower  $V_{oc}$ 's indicating increased recombination. Mean  $V_{oc}$  for the SMART texture with  $\text{SiO}_x$  passivation layer is reduced by 20 mV, whereas for a Si(ON) passivation layer, mean open-circuit voltage drops by about 70 mV.

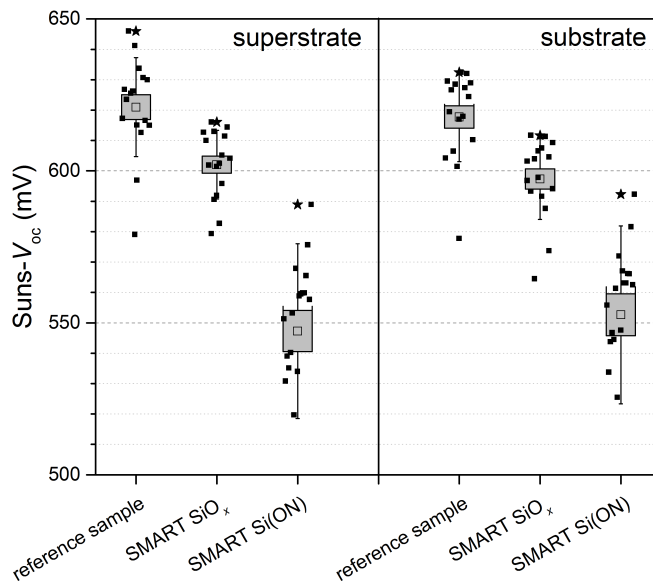


**Figure 5.22:** Open-circuit voltage measured by the suns- $V_{oc}$  method for solar cells with SMART textures with a silicon oxide ( $\text{SiO}_x$ ) and silicon oxy-nitride ( $\text{Si(ON)}$ ) passivation layer and a reference sample, in both superstrate (left) and substrate (right) configuration. Mean  $V_{oc}$  is depicted by an open square, best  $V_{oc}$  with a star. The box symbolizes the standard error, the whiskers the standard deviation.

Summarizing, it was found that the plasma oxidation process developed for LPC silicon thin-film solar cells with planar glass-silicon interface could thus far not be implemented in the SMART texture production process. While optical properties in the short wavelength range were improved as revealed on solid phase crystallized silicon absorbers, optical as well as electronic properties were deteriorated in LPC silicon thin-film solar cells. In consequence, both external quantum efficiency and open-circuit voltage were diminished for solar cells exhibiting a SMART texture and silicon oxy-nitride passivation layer.

## 5.7 Conclusion

The smooth anti-reflective three-dimensional (SMART) texture was introduced as a possible texture to overcome the trade-off between increased light in-coupling and electronic material quality at the glass-silicon interface of liquid phase crystallized silicon thin-film solar cells. A three-dimensional nano-texture that is optically rough due to the refractive index contrast of the employed materials and, at the same time, exhibits a smooth surface could be realized. To do this, nano-imprinting of silicon oxide nano-pillars was combined with spin-coating of titanium oxide. Using three-dimensional simulations, optimal geometrical parameters under consideration

of experimental feasibility of a period of 750 nm, filling fraction of 0.25, and height of 40 nm – 60 nm were identified and subsequently experimentally realized.

The SMART texture was successfully implemented in the liquid phase crystallization process, and proof-of-concept solar cells were manufactured. It could be demonstrated that the SMART texture allows to decrease reflection losses at the glass-silicon interface while preserving interface and bulk material quality. Consequently, the increased absorption lead to a higher short-circuit current density compared to reference devices with a planar glass-silicon interface and state-of-the-art cells with a comparable doping concentration. For a wavelength range from 300 nm to 700 nm, the short-circuit current density of a solar cell on a SMART texture was higher by  $1.8 \text{ mA cm}^{-2}$  than that of a solar cell with a interdigitated back contact system that provides a power conversion efficiency of 13.2% if combined with additional light management measures at the air-glass interface. Hence, the SMART texture proved to be a suitable texture to enhance light in-coupling in LPC silicon solar cells while maintaining a high material quality.

Based on these results, further optimization steps of the SMART texture were taken. First, an increase of the annealing temperature allowed to enhance the refractive index of the titanium oxide layer further, leading to increased light in-coupling. Second, the SMART texture was combined with light trapping measures at the silicon back-side. It was found that the SMART front-side texture is compatible with state-of-the-art rear-side light trapping methods, namely random pyramids produced by wet-chemical etching in KOH and a white paint back reflector. Employing both light trapping measures for a SMART texture with optimized refractive index yielded a maximum achievable short-circuit current density of  $36.4 \text{ mA cm}^{-2}$ . Finally, novel interlayer deposition methods that provided optimized interface passivation and decreased reflection for planar devices were implemented into the SMART texture production process. The silicon oxide passivation layer was replaced by a plasma-oxidized silicon nitride layer. One-dimensional simulations of these layer stacks in combination with a SMART texture yielded optimal optical properties for a SMART texture thickness of 40 nm – 50 nm and a silicon oxy-nitride layer thickness of 10 nm, without underlying non-oxidized silicon nitride. Optically, the higher refractive index of the silicon oxy-nitride layer allowed to reduce reflection in the short wavelength range, whereas the absorptance maximum remained unchanged.

Solar cells with these optimized SMART textures were produced. It was found that both the optical and electronic material quality of SMART textures with a silicon oxy-nitride passivation layer were diminished, limiting the solar cell performance compared to both a SMART texture with silicon oxide passivation layer and a reference with planar silicon oxide/silicon nitride/silicon oxy-nitride interlayers. The SMART texture with silicon oxide passivation layer provided a short-circuit current

density of  $29.4 \text{ mA cm}^{-2}$ , compared to  $31.4 \text{ mA cm}^{-2}$  measured on the reference cell. Measurements of the internal quantum efficiency in both substrate and superstrate configuration indicated that the lower material quality of devices with a SMART texture and silicon oxy-nitride passivation layer was caused by an increase of defects close to the glass-silicon interface.

The SMART texture is the most promising texture for anti-reflection at the buried glass-silicon interface developed up to now, allowing to reach interface and bulk material quality comparable to state-of-the-art devices with planar glass-silicon interface. To fully capitalize on its potential and contribute to increasing short-circuit current density of LPC silicon thin-film solar cells, optimized passivation layers in combination with the SMART texture need to be developed.

# 6 Tailor-made micro-textures for light trapping

Due to the low absorption coefficient of silicon in the long wavelength regime, light trapping structures that enhance the light path in the absorber are of utmost importance to fully exploit the solar spectrum. Thin-film solar cells particularly benefit from these measures considering the decreased thickness of the absorber layer and, hence, reduced light path. For single-crystalline silicon wafer cells, the most common light trapping measure are random pyramids derived from wet-chemical etching in a solution containing potassium hydroxide (KOH) [88, 171]. This process has been adapted to LPC silicon thin-film solar cells [42, 43, 52]. As pyramid formation is based on a grain orientation-dependent etch rate, the result for the poly-crystalline LPC silicon differs from single-crystalline silicon wafers. While the etching of a  $\{100\}$  surface leads to upright pyramids with  $\{111\}$  facets, grains with varying surface orientation give rise to tilted pyramids with a distinct tilting angle. This results in – unfavorable – varying optical properties from grain to grain and gives rise to an inhomogeneous appearance of the solar cells (cf. Figure 6.7).

This chapter presents a method that was developed to enable the production of tailor-made micro-structures for LPC silicon absorbers, independent of crystal grain orientation. A process similar to the one presented in chapter 4, using a combination of nano-imprint lithography (NIL) and reactive ion etching (RIE), allows to produce micro-structured LPC silicon surfaces with a wide range of slopes, periods and heights. The optical properties of these structures are analyzed, and solar cell results on textured absorbers are presented.

Parts of the results presented in this chapter were previously published in [227].

## 6.1 Process development and optimization

Reactive ion etching of silicon is an industrially established process, widely used in semiconductor industry and microelectromechanical systems (MEMS) [228–231].

Therefore, a variety of RIE processes were proposed for silicon etching using several gas compositions [207, 230]. In the common processes, resist materials or metals are used as rigid etching masks. This requires a high selectivity between silicon and the mask material and generally limits the etched profiles to vertical flanks. The method employed in the scope of this thesis, on the contrary, relies on nano-imprinted resist layers as three-dimensional soft etching masks in order to allow arbitrary surface textures to be replicated. Process parameters in reactive ion etching were varied and examined in order to identify a set of parameters that allows the replication of nano- and micro-textures in LPC silicon with high structural fidelity.

### 6.1.1 Variation of the gas composition

In a first step, different gas compositions were examined based on processes known from literature [207, 230], using  $\text{CHF}_3$  and  $\text{SF}_6$  as etching agents. In order to replicate structures without distortions, a combination facilitating a selectivity close to 1 : 1 needed to be identified. Figure 6.1(a) illustrates the etch rates for silicon as well as two commercially available UV-NIL resist materials, UVcur06 [157] and OrmoComp [158], for different combinations of etching gases to determine a suitable process. Gas compositions investigated include a mixture of 25 sccm Ar / 25 sccm  $\text{CHF}_3$  (process (I)), these gases with additional 1 sccm of oxygen (process (II)), a mixture without the dilution gas argon with 40 sccm  $\text{CHF}_3$  / 2 sccm  $\text{O}_2$  (process (III)) and a combination of 35 sccm  $\text{CHF}_3$  with 14 sccm  $\text{SF}_6$  (process (IV)).

For both resists, the incorporation of oxygen (cf. processes (I) and (II) in Fig. 6.1(a)) in the process leads to a step increase in etch rate due to organic compounds in the resist being quickly etched. The gas compositions without oxygen, processes (I) and (IV), both reveal similar etch rates for UVcur06 and silicon, with OrmoComp having a higher rate. Etching selectivities for LPC silicon to UVcur06 of 1.0 :  $1.7 \pm 0.3$  and 1.0 :  $1.0 \pm 0.2$  were found for processes (I) and (IV), respectively. Therefore, further investigations will be carried out using UVcur06 as resist and gas mixtures deriving from process (IV), providing close to optimum selectivity and high etch rates. UVcur06, additionally, is advantageous for the desired processes compared to OrmoComp, as it can be completely removed in an oxygen plasma [157], ensuring process compatibility with the subsequent processes in LPC silicon thin-film solar cell production.

In a second optimization step, the ratio of etching gases  $\text{CHF}_3$  and  $\text{SF}_6$  is varied from 3 : 1 to 1 : 2.5, while keeping the overall gas flow constant at 50 sccm. Etch rates measured for UVcur06 and LPC silicon are depicted in Fig. 6.1(b). Etch rates

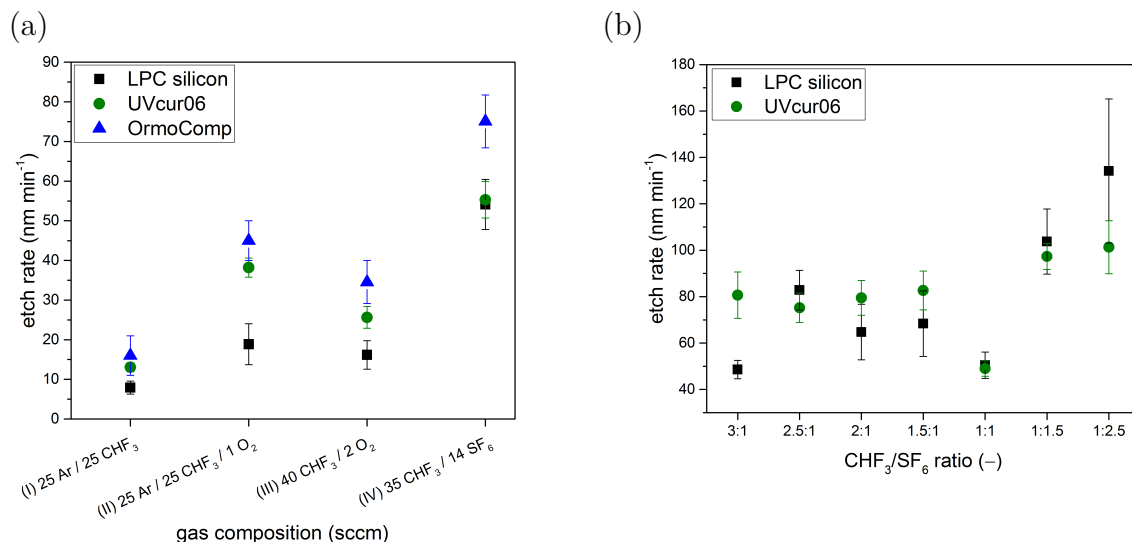


**Figure 6.1:** (a) Etch rates for LPC silicon (black squares) and the two commercial resists UVcur06 (green circles) and OrmoComp (blue triangles) for different gas compositions during reactive ion etching. (b) Etch rates for LPC silicon (black squares) and UVcur06 (green circles) for different  $\text{CHF}_3/\text{SF}_6$  ratios, based on process (IV).

providing a selectivity close to 1 : 1 were determined for gas ratios of 2.5 : 1, 1 : 1 and 1 : 1.5.

In order to assess anisotropy for the gas combinations with suitable selectivity, an inverted pyramid texture with a period of  $1.25\ \mu\text{m}$  and a pyramid base of  $1.0\ \mu\text{m}$  imprinted into UVcur06 was replicated using these gas ratios and etch rates. Possible residues of UVcur06 after RIE etching – being an organic resist – could be removed using an oxygen plasma [157]. The surfaces of these silicon structures were analyzed using atomic force microscopy in order to evaluate the process most suitable for texture replication. Surface profiles were extracted from the AFM measurements, as illustrated in Fig. 6.2. For all gas ratios, the micro-structures reveal distortions due to partly isotropic etching. That leads to a narrowing of the  $250\ \text{nm}$  wide bars between the inverted pyramids. Depending on the degree of isotropy, the height of the structures is reduced and sharp features of the textures are rounded. This was observed for the gas ratios of 1 : 1 and 1 : 1.5. For the gas ratio 2.5 : 1, partly isotropic etching lead to a narrowing, but no height reduction is found.

Hence, a gas composition of  $35.7\ \text{sccm}\ \text{CHF}_3$  and  $14.3\ \text{sccm}\ \text{SF}_6$  – corresponding to a gas ratio of 2.5 : 1 – was used in an additional optimization step aimed at further reducing isotropy, thereby enabling a texture replication with high structural fidelity.

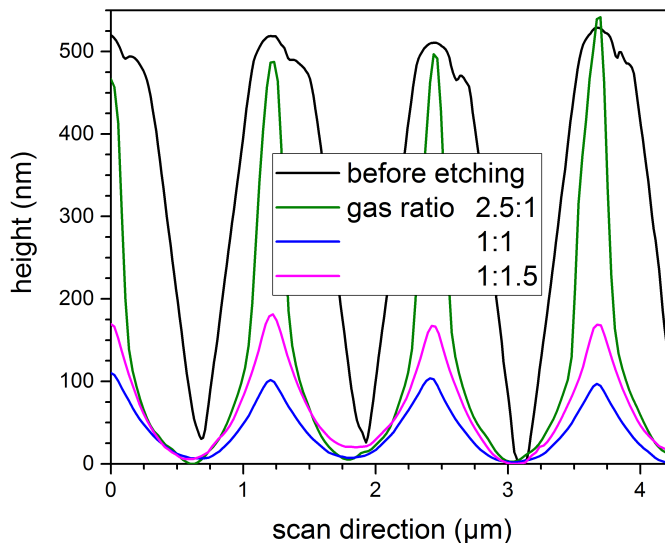


**Figure 6.2:** Surface profiles measured by AFM for the imprinted nano-structure and different gas ratios between  $\text{CHF}_3$  and  $\text{SF}_6$ .

### 6.1.2 Process parameter optimization

A suitable process for pattern replication requires high anisotropy to avoid pattern distortion during etching. Further experiments were therefore carried out to optimize the etching step. Having identified a suitable gas composition, the plasma power was varied to increase anisotropy. The utilized Oxford 80 RIE etcher is equipped with a capacitively coupled radio frequency (RF) and an inductively coupled plasma (ICP) power source, allowing to apply both a RF power  $P_{\text{RF}}$  and an ICP power  $P_{\text{ICP}}$  (also see section 3.1.2).

Figure 6.3 demonstrates the etch rate for a variety of combinations of  $P_{\text{RF}}$  and  $P_{\text{ICP}}$  for LPC silicon and UVcur06. Generally, the etch rate rises for both materials with increasing  $P_{\text{ICP}}$ . This increase is higher for silicon than for UVcur06 and, as a consequence, etch selectivity is not suitable for pattern replication with high structural fidelity.  $P_{\text{ICP}}$  should therefore be kept below 50 W to maintain an appropriate selectivity. Suitable processes are highlighted by arrows in Fig. 6.3. For these processes – labeled (I), (II) and (III), a test structure consisting of a line grating with a period of 690 nm was nano-imprinted into UVcur06 and subsequently replicated into silicon using the parameter sets determined before. SEM images in cross section, as depicted in Fig. 6.4, allow to assess the anisotropy of the structures after etching. For the non-conductive nano-imprinted UVcur06 layer, the SEM image is blurry due to charging effects. Still, the line grating pattern can be recognized and a grating height of 170 nm to 180 nm is found. Processes (I) and (II) give the same height as the imprinted structure, whereas the height of the replicated line grating for process (III) is reduced to about 130 nm.

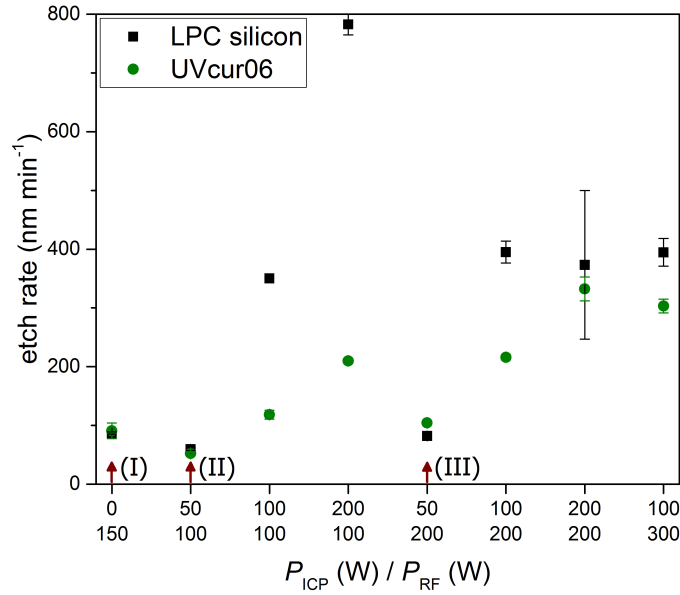


**Figure 6.3:** Etch rates of LPC silicon (black squares) and the organic resist UVcur06 (green circles) for different radio-frequency (RF) and inductively-coupled plasma (ICP) powers during RIE.

Assessing anisotropy is done using the angle of the flanks of the line grating texture, which are vertical in the master structure. Charging of the imprinted structure, however, does not allow to confidently determine the angle of the flanks. The angle of the etched samples were determined to  $16 \pm 3^\circ$  and  $10 \pm 2^\circ$  for etching processes (I) and (II), respectively. In comparison, process (III) yields an angle of  $32 \pm 7^\circ$ . Using process (II) with  $P_{\text{RF}} = 100 \text{ W}$  and  $P_{\text{ICP}} = 50 \text{ W}$  gives the highest anisotropy of the processes investigated, constituting the optimized plasma power for structure replication with high structural fidelity.

Summarizing, an optimized process for directional etching of micro- and nano-structures in LPC silicon could be identified. Using several optimization steps varying the gas composition, gas ratio and plasma power during the reactive ion etching process, a gas composition of 35.7 sccm  $\text{CHF}_3$  and 14.3 sccm with a chamber pressure of 20 mTorr, an RF power of  $P_{\text{RF}} = 100 \text{ W}$ , and an inductively coupled plasma power of  $P_{\text{ICP}} = 50 \text{ W}$  were determined as optimal parameters. Employing these parameters facilitates a selectivity of close to 1 : 1 and a pattern replication with high structural fidelity due to highly anisotropic etching.

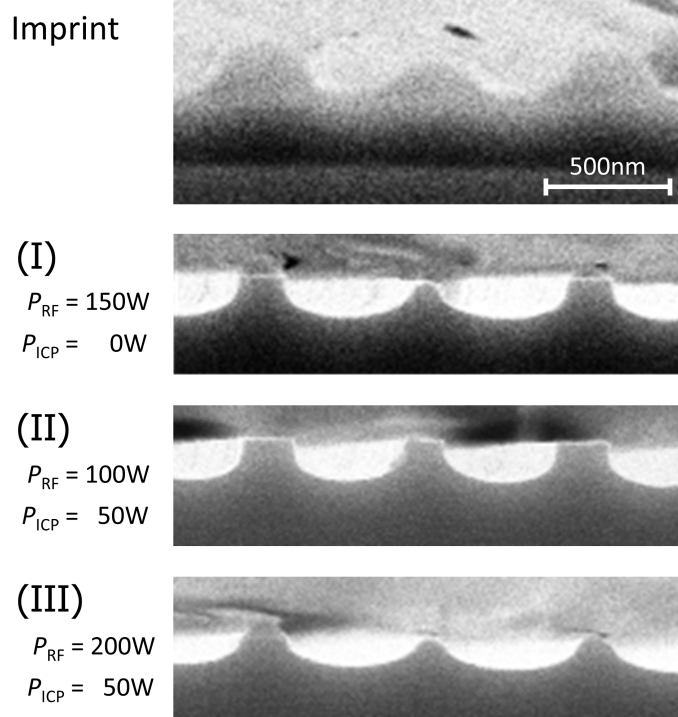


**Figure 6.4:** Cross-section SEM images of a line grating imprinted into UVcur06 and replicated into silicon for the etching conditions (I), (II) and (III). The scale bar holds for all images.

## 6.2 Structural analysis

### 6.2.1 Grain orientation dependency

Having established a RIE process that allows to replicate nano-imprinted structures into silicon, an analysis of the silicon surface for different surface orientations aims at verifying that the process is independent of grain orientation for poly-crystalline LPC silicon. For this, silicon surfaces structured with an inverted pyramid array were produced by NIL+RIE for wafers of different surface orientations, namely a  $\{100\}$ ,  $\{111\}$  and multi-crystalline surface. As a reference, wafers of the same orientation were wet-chemically etched in a commonly applied KOH-based etching solution [170]. Figure 6.5 illustrates the surfaces of wafer pieces of the three orientations examined, textured using KOH wet-chemical etching (first row) and NIL+RIE (second row). As expected for the wet-chemical etching process, the surface texture depends on grain orientation. For the  $\{100\}$  wafer, the wet-chemically etched pyramids lead to reduced direct reflection and light scattering at the surface. For the  $\{111\}$  wafer, KOH etching does not have a texturing effect, and, hence, the flat front surface causes pronounced reflection, revealing the author taking the photograph.

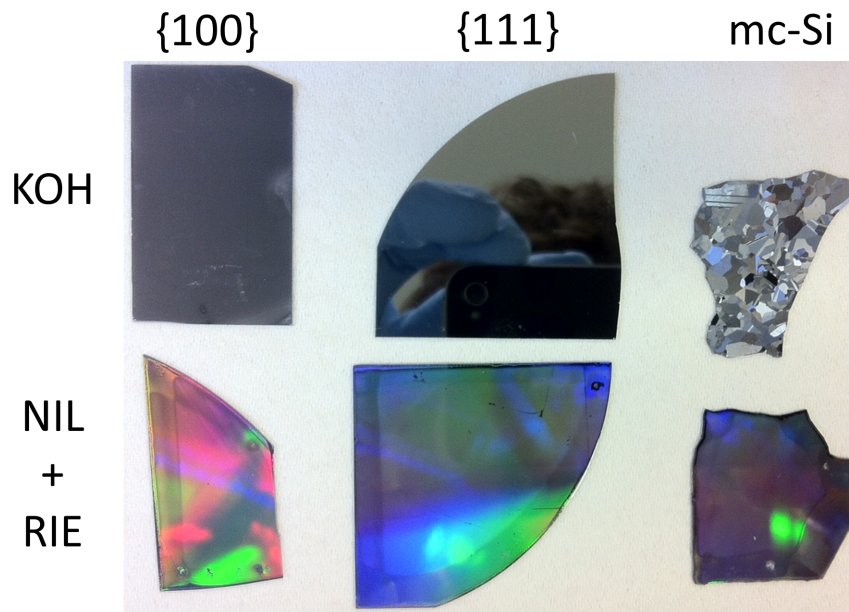


**Figure 6.5:** Wafer pieces of different silicon surface orientations, textured using a wet-chemical etching solution (KOH, first row) or a combination of nano-imprinting and reactive ion etching (NIL+RIE, second row).

The multi-crystalline silicon wafer, with multiple grains and their corresponding surface orientations, reveals different reflection properties for each grain. On the contrary, no difference in visual appearance is observed for the wafer pieces textured by NIL+RIE. In particular, individual grains of the multi-crystalline silicon wafer are not discernible. The periodic structure leads to diffraction, whereby the changing angles for the three samples cause differently colored appearance.

Laser scanning confocal microscopy images displayed in Fig. 6.6 support these findings. Again, for the samples etched in a KOH-based solution, grain orientation dependency of the resulting texture is evident. For a {100} wafer, upright pyramids form, constituting the optimal case for light trapping. For a {111} wafer, the KOH solution has no texturing effect and the wafer is flat, posing the worst case. For the multi-crystalline wafer, which represents the closest resemblance to a LPC silicon surface, the pyramids on grains of different orientations are distinctly tilted. The optical properties hence depend on the grain orientation, which explains the patchy structure observed in Fig. 6.5. For the wafer pieces textured using NIL+RIE, the inverted pyramid structure is found independent of grain orientation. In particular, the grains of the multi-crystalline silicon surface are not distinguishable.

Thus, the etch rate and structure replication during NIL+RIE does not depend on grain orientation and confirms that NIL+RIE is a suitable candidate to provide a surface-orientation independent texturing method for LPC silicon. This is further demonstrated by Fig. 6.7, showing (a) photographs of LPC silicon absorbers with

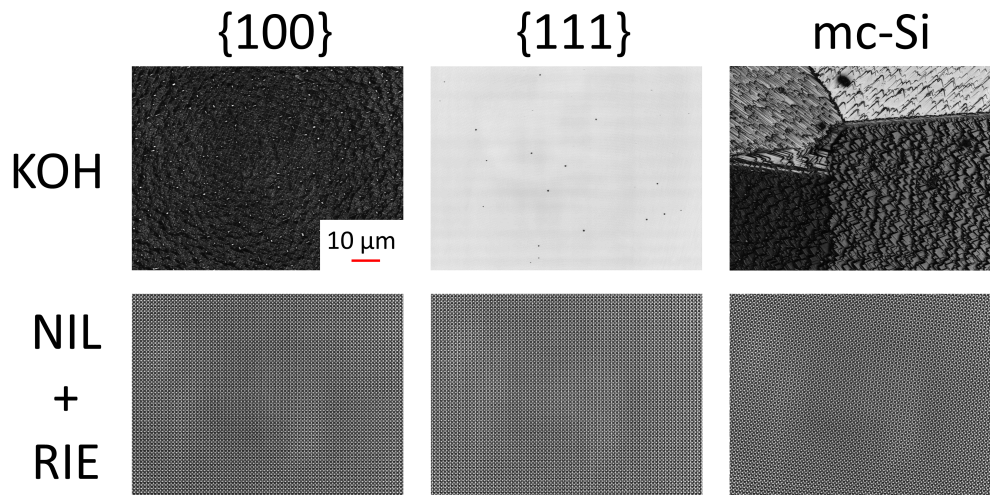


**Figure 6.6:** Laser scanning confocal microscopy images of wafer pieces of different surface orientations textured using a wet-chemical etching solution (KOH, first row) or a combination of nano-imprinting and reactive ion etching (NIL+RIE, second row). The scale bar applies to all images.

a wet-chemical random pyramid texture (KOH) and a periodic nano-texture with inverted pyramids of  $1.25\ \mu\text{m}$  period produced by NIL+RIE and (b) their respective surfaces measured using laser scanning confocal microscopy. For the LPC silicon layer with a KOH texture, the different grain orientations lead to tilted pyramids and an inhomogeneous appearance. This is not the case for the NIL+RIE texture, where the whole surface is covered with the pyramid array etched into the LPC silicon. No difference in texture is observed for different grains.

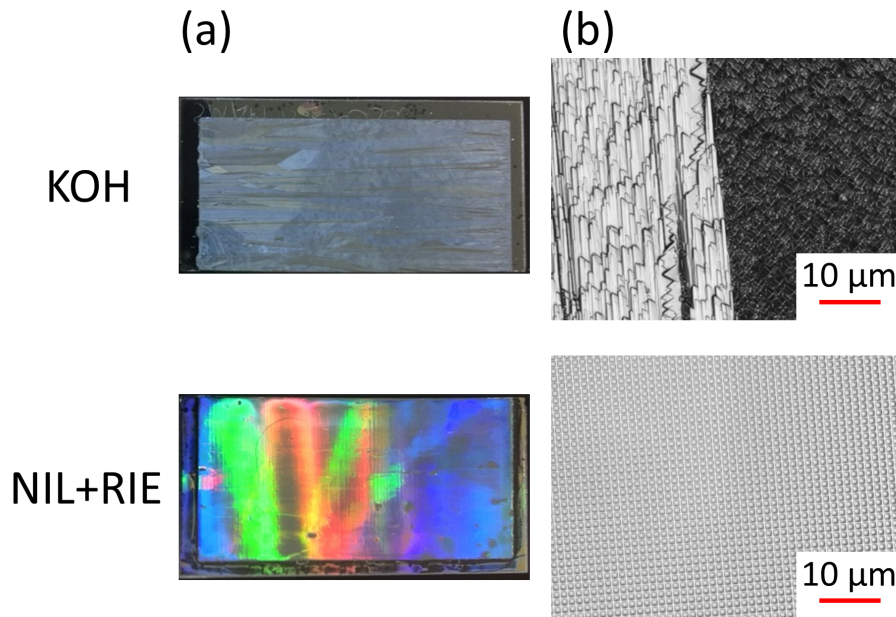
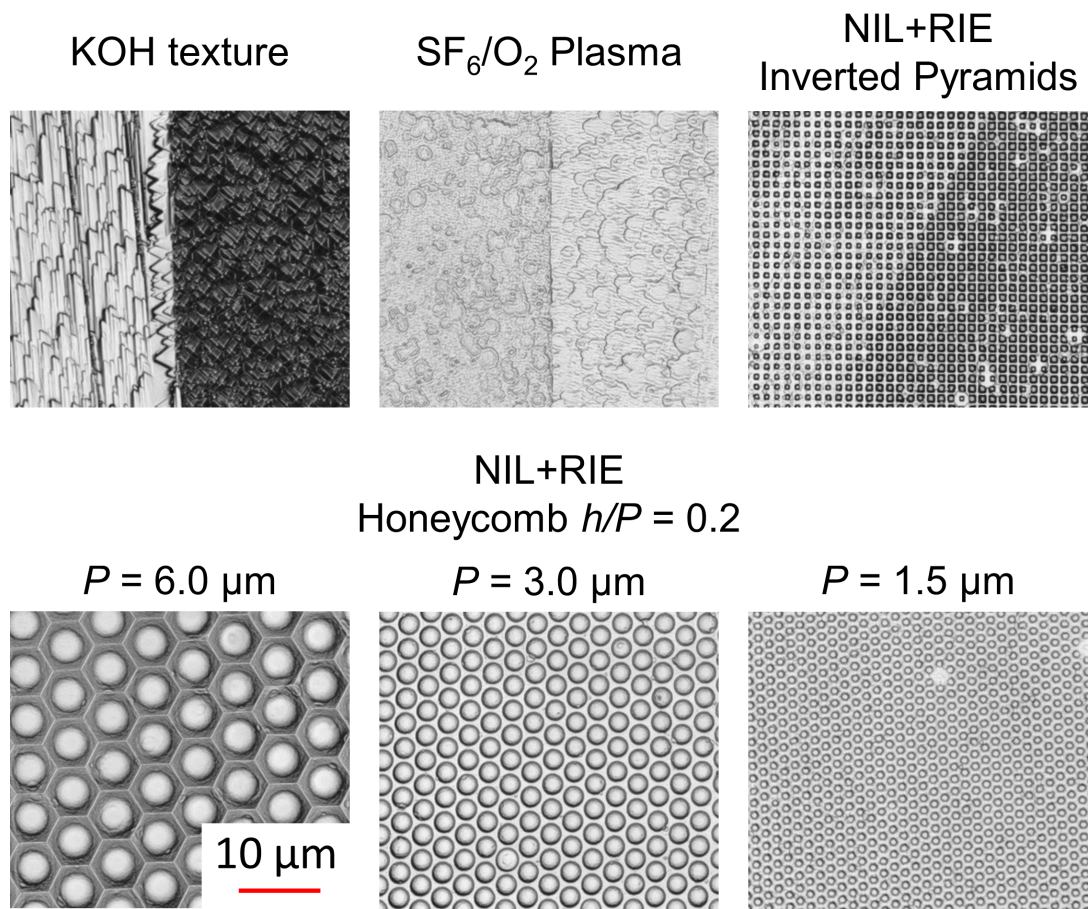


**Figure 6.7:** (a) Photographs and (b) laser scanning confocal microscope images of the LPC silicon surface after wet-chemical etching (KOH) and reactive-ion etching of nano-imprinted nano-structures (NIL+RIE).

### 6.2.2 Surface analysis

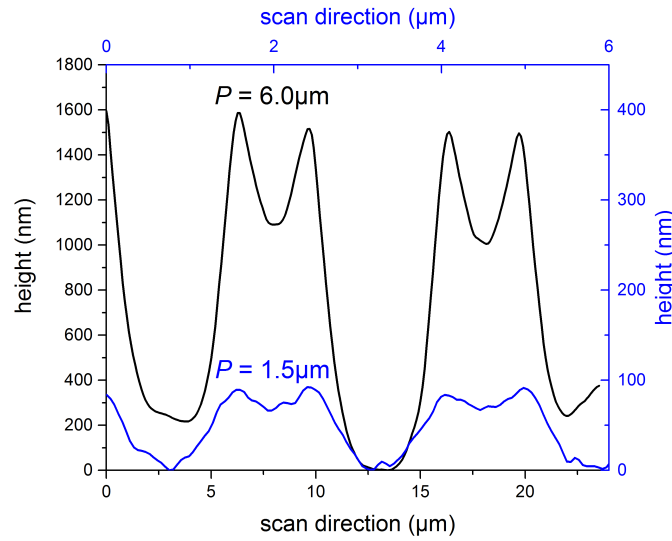
The developed method of NIL+RIE was applied to a range of micro-textures with a honeycomb pattern, which have proven to be a suitable light trapping texture in high-efficiency micro-crystalline silicon thin-film solar cells [146, 147]. Honeycomb masters with periods of 1.5  $\mu\text{m}$ , 3.0  $\mu\text{m}$  and 6.0  $\mu\text{m}$  and height-to-period ratios ranging from 0.1 to 0.3 were produced (see section 3.1.1) and replicated in LPC silicon using NIL+RIE. In addition, an inverted pyramid array with a period of 1.25  $\mu\text{m}$  and pyramid base of 1.0  $\mu\text{m}$  produced by NIL+RIE and a random micro-texturing method based on texturing in a  $\text{SF}_6/\text{O}_2$  plasma introduced by Moreno et al. [232, 233] are investigated. The resulting surface texture was examined using atomic force microscopy (AFM) and laser scanning confocal microscopy (LSCM).

Figure 6.8 exhibits the surface topography of the investigated micro-textures measured by LSCM. As discussed above, the texturing result on grains with different silicon crystal grain orientation varies for the random pyramid texture produced by wet-chemical etching in KOH. The  $\text{SF}_6/\text{O}_2$  plasma texturing leads to small random pyramid-like shapes and larger bowl-shaped features, whereby the texturing is independent of grain orientation. Both, the inverted pyramid array and different honeycomb textures with varying period could successfully be replicated, demonstrating that the NIL+RIE method is suitable for textures exhibiting smooth as well as sharp-edged features.



**Figure 6.8:** Laser scanning confocal microscope images of textured LPC silicon surfaces with different texturing methods and textures. The scale bar holds for all images.

Further analysis of the surface topography of replicated honeycomb textures was conducted using atomic force microscopy. Figure 6.9 depicts AFM profiles for two example cases of a shallow honeycomb texture with a period of  $1.5\ \mu\text{m}$  and a height of  $125\ \text{nm}$  (blue), and the most pronounced texture produced, with a period of  $6.0\ \mu\text{m}$  and a height of  $1.4\ \mu\text{m}$  (black), covering the extremes of honeycomb periods and heights produced. For better comparison of the textures despite their differing dimensions, the axes of the  $1.5\ \mu\text{m}$  period sample are stretched by a factor of four – the ratio of the periods. The characteristic honeycomb pattern is clearly observed for both samples. The height of the small period texture is slightly reduced compared to its master structure, from  $125\ \text{nm}$  to  $100\ \text{nm}$ . The larger pitched honeycomb pattern is replicated with a high structural fidelity and the height is similar to the master structure. In parts, the replicated structure is even higher than the master. Deviations from the heights of the master structured are attributed to inhomogeneities in manufacturing and characterization in both master and NIL+RIE samples.



**Figure 6.9:** Surface profiles measured using atomic force microscopy of LPC silicon surfaces textured with honeycomb patterns with a period of  $6.0\ \mu\text{m}$  (black) and  $1.5\ \mu\text{m}$  (blue) and height-to-period ratios of 0.25 and 0.1, respectively. Axes for sample with a period of  $1.5\ \mu\text{m}$  were colored in blue for clarity.

The honeycomb textures were designed for light trapping in micro-crystalline silicon thin-film solar cells in substrate configuration [148, 149]. For LPC silicon devices, the light impinges through the glass and therefore reaches the textured surface from the opposite side as for micro-crystalline silicon thin-film solar cells. In order to elucidate the influence of texture inversion, honeycomb master textures with an inverted structure were produced (see section 3.1.1) and replicated in LPC silicon using the NIL+RIE method. Due to technological constraints, the masters with a period of  $6.0\ \mu\text{m}$  could not be inverted in the scope of this thesis. Figure 6.10 discloses LPC silicon surface profiles measured by AFM of a honeycomb texture with a period of  $3.0\ \mu\text{m}$  and a height-to-period ratio of 0.2 (black) and its inverse texture (blue, solid). For better comparison, the negative of the inverted texture is shown in addition (blue, dashed).

It is evident that inverted honeycomb master textures could successfully be produced and replicated in LPC silicon. The inverse pattern has an equivalent height and morphology as the initial honeycomb texture.

Further, the homogeneity of the NIL+RIE method over large areas is analyzed. For a honeycomb texture with a period of  $3.0\ \mu\text{m}$  and a height of  $290\ \text{nm}$ , the surface of LPC silicon after etching was examined using LSCM. Figure 6.11 presents five LSCM images with a magnification of  $150\times$  that were taken in the center and four corners of the  $3 \times 3\ \text{cm}^2$  large sample. The surface profiles were analyzed via line profiles and heights were extracted and averaged over 15 periods (see insets in Fig.

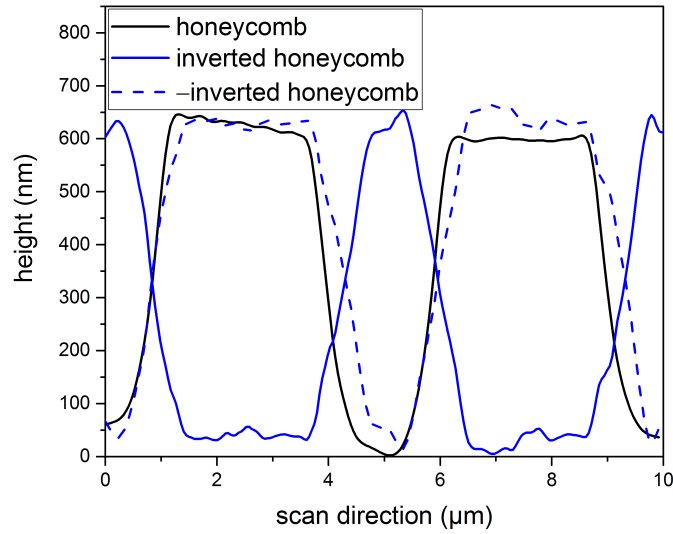


**Figure 6.10:** Comparison of surface profiles measured by AFM for LPC silicon surfaces textured with a honeycomb texture with a period of  $3.0 \mu\text{m}$  (black) and its inverse structure (blue). For clarity, the negative of the inverted structure surface is included (blue, dashed).

6.11). Structure heights ranging from 280 nm to 330 nm were measured in individual LSCM images. Comparing the mean heights of individual images, values between 290 nm and 315 nm were found. The nano-structure heights therefore vary to the same extent on both short and long range. Large-area homogeneity of less than 10% mean height deviations is thus given over the whole sample area of  $3 \times 3 \text{ cm}^2$ .

In a nutshell, the NIL+RIE method is suited to produce tailor-made micro-textures for LPC silicon thin-film absorbers. An inverted pyramid texture and honeycomb textures were replicated in silicon wafers of different surface orientations and LPC silicon. Surface analysis revealed that using NIL+RIE, texturing independent of grain orientation is feasible, in contrast to wet-chemical etching in KOH. Furthermore, the successful replication of honeycomb patterns with a wide range of periods and heights and inverted honeycomb textures with a homogeneity of more  $3 \times 3 \text{ cm}^2$  was demonstrated.

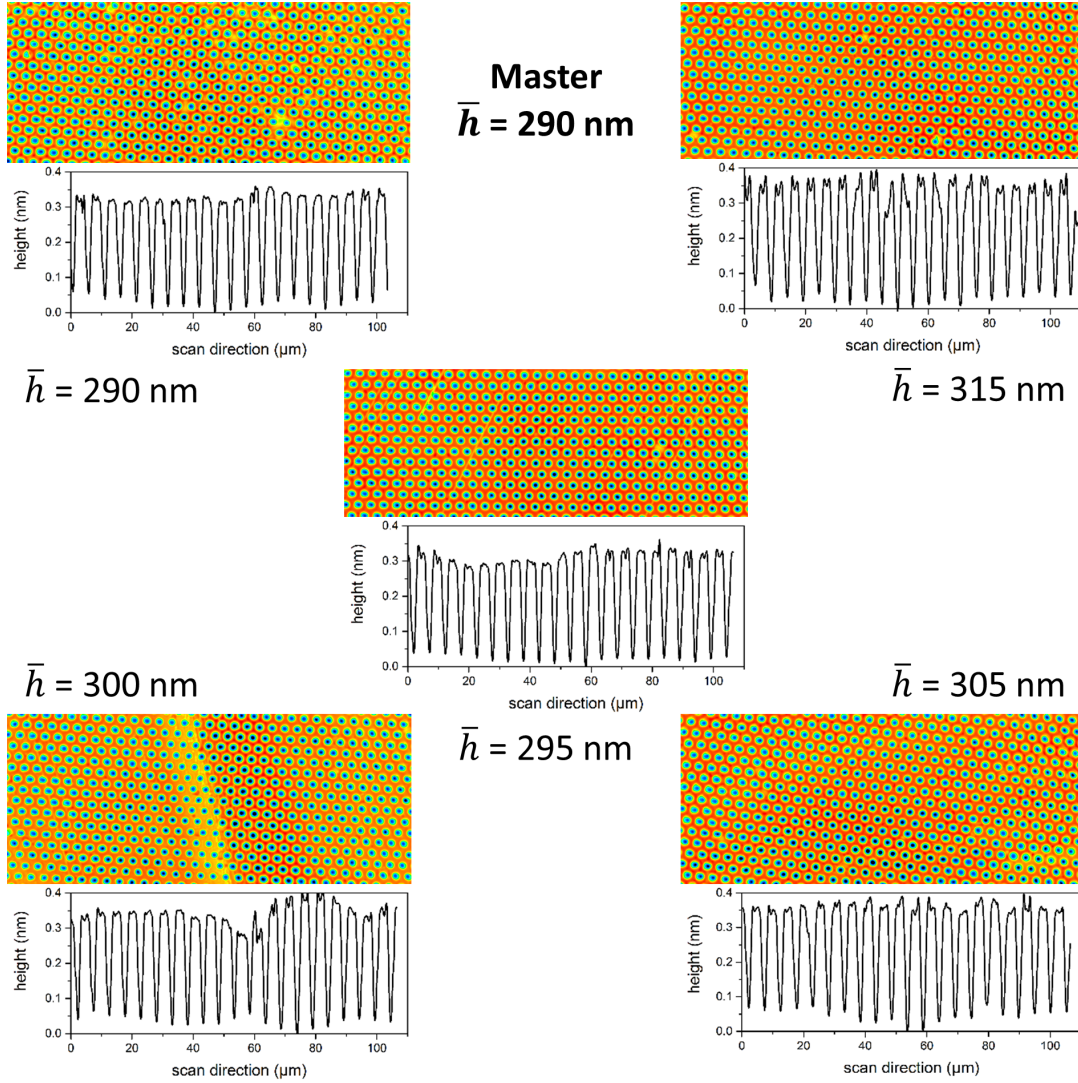


**Figure 6.11:** Laser scanning confocal microscopy images of a LPC silicon surface with a honeycomb texture with a period of  $3.0\ \mu\text{m}$  and a height of  $290\ \text{nm}$ .

## 6.3 Optical analysis

Light trapping structures for LPC silicon thin-film solar cells need to efficiently scatter light into high angles to enhance the light path in the absorber, thus increasing absorption. In the last section, grain-orientation independent replication of honeycomb textures in LPC silicon with a high degree of structural fidelity and homogeneity over  $3 \times 3\ \text{cm}^2$  was presented. This section aims at finding the most suitable honeycomb structure for light trapping and compares this texture to other texturing methods known from literature.

Figure 6.12 exhibits the absorptance of  $16\ \mu\text{m}$  thick LPC silicon absorbers with honeycomb textures with a period of (a)  $1.5\ \mu\text{m}$ , (b)  $3.0\ \mu\text{m}$  and (c)  $6.0\ \mu\text{m}$  for different height-to-period ratios. No additional rear reflector was used in this experiment.

For all periods, absorption is highest for the largest height-to-period ratio. Honeycomb textures with  $h/P \leq 0.1$  do not increase absorptance (cf. green curves in Fig. 6.12(a) and (b)), as very shallow structures do not efficiently back-scatter light at the silicon rear-side. High height-to-period ratio honeycomb textures are therefore favorable for absorption enhancement in LPC silicon thin-film solar cells.

With respect to the period of honeycomb textures, it has been shown for multicrystalline silicon thin-film solar cells that the optimal period depends on the solar cell thickness [58], with higher periods favorable for cells with a thicker absorber layer. The same trend is observed for honeycomb textures etched into the LPC silicon layers as illustrated in Fig. 6.12(d) disclosing absorptance of honeycomb textures with a height-to-period ratio of 0.2 for varying periods between 1.5  $\mu\text{m}$  and 6.0  $\mu\text{m}$ .

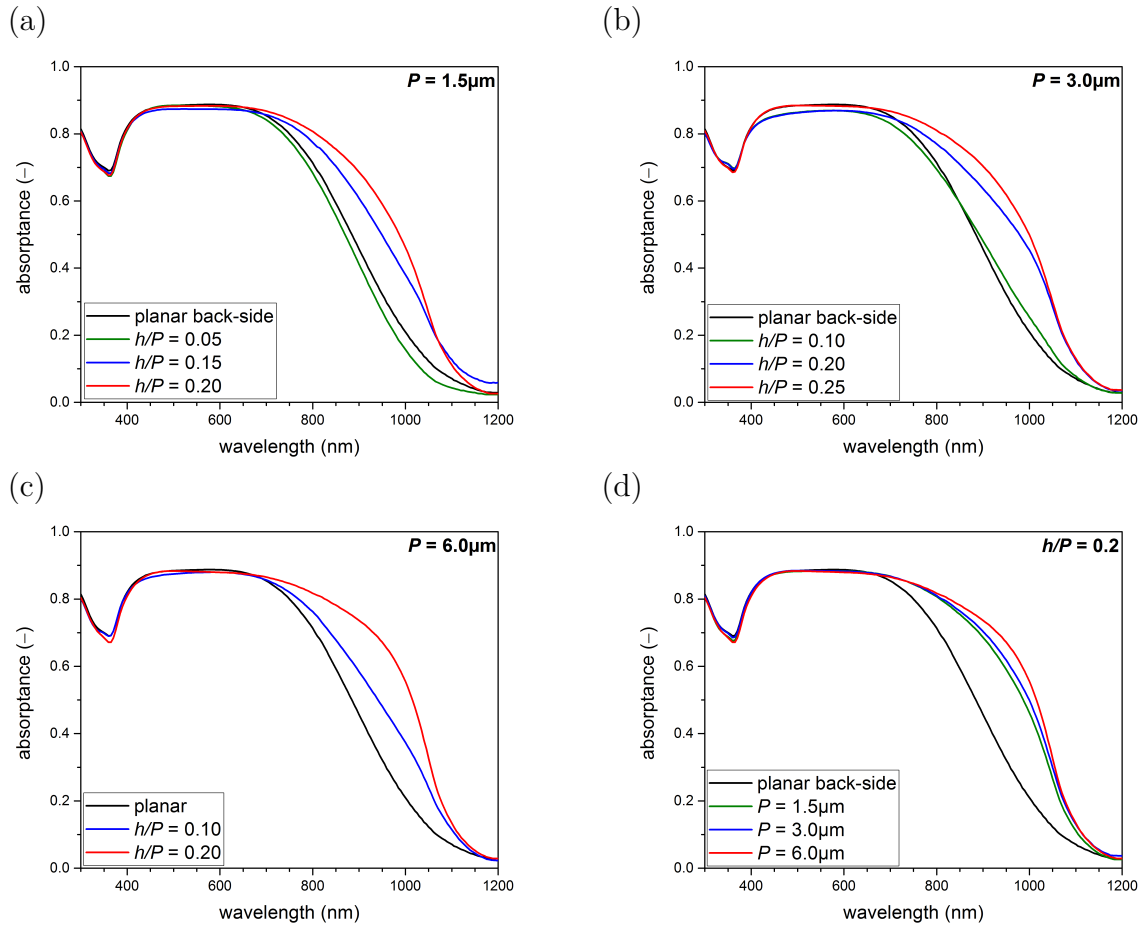


**Figure 6.12:** Absorptance of 15  $\mu\text{m}$  thick LPC silicon absorbers with honeycomb textures with a period of (a) 1.5  $\mu\text{m}$ , (b) 3.0  $\mu\text{m}$  and (c) 6.0  $\mu\text{m}$  at the silicon back-side, for different height-to-period ratios  $h/P$ . (d) Absorptance of honeycomb textures with a fixed height-to-period ratio of 0.2 for different texture periods.

Absorptance in the wavelength range from 800 nm to 1100 nm is highest for the honeycomb texture with a period of 6.0  $\mu\text{m}$ . In terms of maximum achievable short-

circuit current density, the implementation of the honeycomb textures increases  $j_{sc,max}$  by more than  $3 \text{ mA cm}^{-2}$ , from  $29.1 \text{ mA cm}^{-2}$  for a planar silicon back-side to  $32.4 \text{ mA cm}^{-2}$ ,  $32.8 \text{ mA cm}^{-2}$  and  $33.2 \text{ mA cm}^{-2}$ , for periods of  $1.5 \mu\text{m}$ ,  $3.0 \mu\text{m}$  and  $6.0 \mu\text{m}$ , respectively.

As stated before, light impinges on the honeycomb texture in LPC silicon from the opposite side as in their original design as light trapping textures for multi-crystalline silicon thin-film solar cells. Therefore, masters with honeycomb patterns were inverted (see section 3.1.1) and subsequently replicated in LPC silicon. Figure 6.13 illustrates the absorptance of a honeycomb pattern (solid) with a period of  $3.0 \mu\text{m}$  (blue) and an aspect ratio of  $h/P = 0.2$  and its inverted structure (dashed) compared to a planar back-side (black).

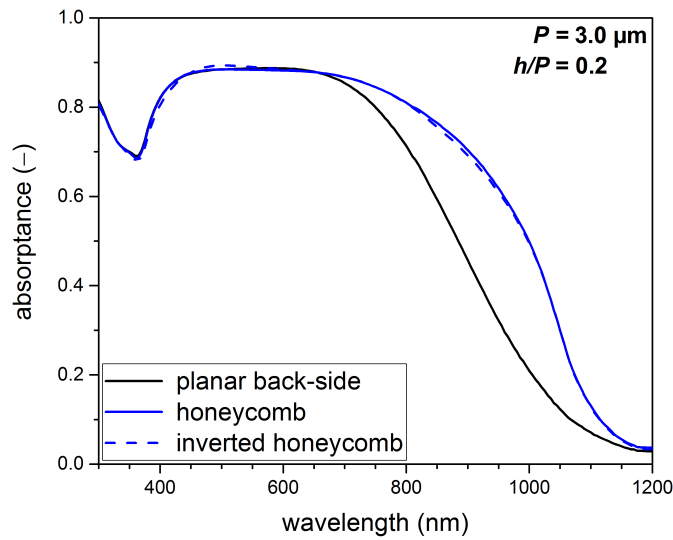


**Figure 6.13:** Absorptance of a LPC silicon absorber with a honeycomb back-side texture (blue, solid) and with an inverted honeycomb texture of the same period of height-to-period ratio (blue, dashed), compared to a planar back-side (black).

No difference in absorption between the honeycomb texture and its inverted structure is found. The texture inversion due to changed processing compared to multi-crystalline thin-film solar cells, thus, has no effect on the optical properties and can be applied for light trapping in LPC silicon thin-film solar cells.

Figure 6.14 summarizes the results obtained from absorptance measurements. As a figure-of-merit for light trapping, mean absorptance between  $800 \text{ nm}$  and  $1100 \text{ nm}$  is chosen. A clear trend to larger height-to-period ratios is observed, and for the highest structures, a larger texture period is favorable. No clear difference is found for honeycomb textures and its inverse.

Hence, the honeycomb texture providing the best light trapping for LPC silicon thin-

film solar cells on glass is a structure with a period of  $6.0\ \mu\text{m}$  and a height-to-period ratio of 0.2, corresponding to a texture height of  $1.2\ \mu\text{m}$ .

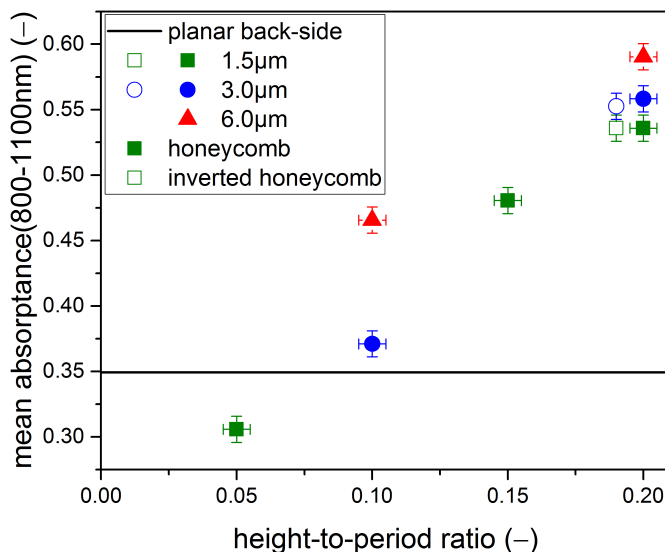


**Figure 6.14:** Mean absorbance between 800 nm and 1100 nm for LPC silicon absorbers with honeycomb textures of different periods (closed symbols) and inverted honeycomb textures (open symbols), compared to a planar silicon back-side (black line). The inverted honeycomb textures exhibit a height-to-period ratio of 0.2, and were shifted for clarity only.

The absorbance of this optimized honeycomb texture (red curve) in comparison to other textures is depicted in Fig. 6.15. All textures, including a random micro-texture (magenta) produced by a plasma-based method established by Moreno et al. [232, 233], an inverted pyramid array with a period of  $1.25\ \mu\text{m}$ , pyramid base of  $1.0\ \mu\text{m}$  and height of  $\approx 600\ \text{nm}$  produced by NIL+RIE (yellow) and the state-of-the-art random pyramid etching using KOH (solid black) enhance absorption in the LPC silicon absorber compared to a planar back-side (dashed black).

The random micro-texture and the inverted pyramid array exhibit lower light trapping than the KOH and honeycomb texture. This is also represented by the maximum achievable short-circuit current density calculated from the absorption curves, which are summarized in Table 6.1. The maximum achievable short-circuit current density of the sample with a KOH texture of  $j_{sc,max} = 33.5\ \text{mA cm}^{-2}$  is slightly higher than that of the LPC silicon absorber with a honeycomb texture providing  $j_{sc,max} = 33.2\ \text{mA cm}^{-2}$ . Thus, the KOH pyramid texture still provides the best light trapping among the textures investigated even though the pyramids are tilted depending on grain orientation in the poly-crystalline LPC silicon material.

Absorption was measured for different spots on the absorber layers in order to investigate the homogeneity of optical properties for the samples with a KOH pyramidal

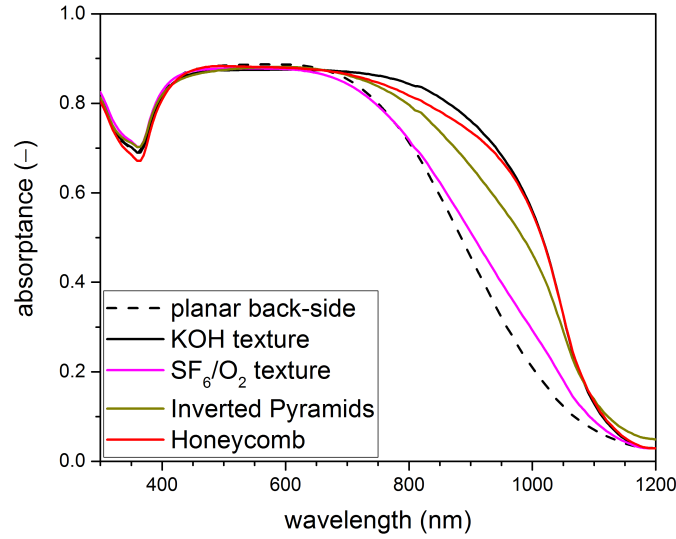


**Figure 6.15:** Absorptance of LPC silicon on glass with different back-side textures as described in the legend.

texture and the NIL+RIE honeycomb texture. The measurement results are disclosed in Fig. 6.16(a), where mean absorptance and its standard deviation for four spots on the silicon absorbers with a KOH texture (black) and honeycomb texture produced by NIL+RIE (red) are plotted. The four spots were chosen with the aim of measuring on grains with different crystal grain orientations. Absorptance values on one texture vary to the same extent as the difference between the textures. The difference in absorptance previously found is, hence, not statistically significant.

**Table 6.1:** Maximum achievable short-circuit current density  $j_{sc,max}$  of 16  $\mu\text{m}$  thick LPC silicon absorbers with different micro-textures at the back-side.

Texture	Planar back-side	Random micro-texture	Inverted pyramids	Honeycomb texture	KOH pyramids
$j_{sc,max}$ ( $\text{mA cm}^{-2}$ )	29.1	29.8	32.2	33.2	33.5

For solar cell applications, the dependency of absorptance with respect to the incident angle of the light is crucial for device performance, as irradiation varies during the day and year. Therefore, absorption characteristics of the LPC silicon absorbers with a KOH pyramid and honeycomb texture were measured in dependency of the incident angle. Figure 6.16(b) displays the mean absorptance averaged for wavelengths from 800 nm to 1100 nm for a 16  $\mu\text{m}$  thick LPC silicon absorber with a planar back-side (grey), a pyramidal KOH texture (black) and the optimized honeycomb texture (red). Both texturing methods increase the absorption in the silicon layer by more than 20% (absolute). As already observed for normal incidence, equivalent

absorption characteristics of the honeycomb texture produced by NIL+RIE and the random KOH pyramid texture are also found for oblique light incidence if statistical variations and measurement uncertainties are taken into account. Regarding the change of absorption with the angle of incidence, the same trend is observed for all samples, indicating that the sun-facing air-glass interface and glass-silicon interface dominates angle-dependent absorption properties. From an incident angle of  $10^\circ$  up to  $70^\circ$ , mean absorptance in the long wavelength range declines by less than 10% (relative). Thus, both the random pyramid texture and honeycomb texture are suitable for light trapping up to high angles of incidence of  $70^\circ$ .

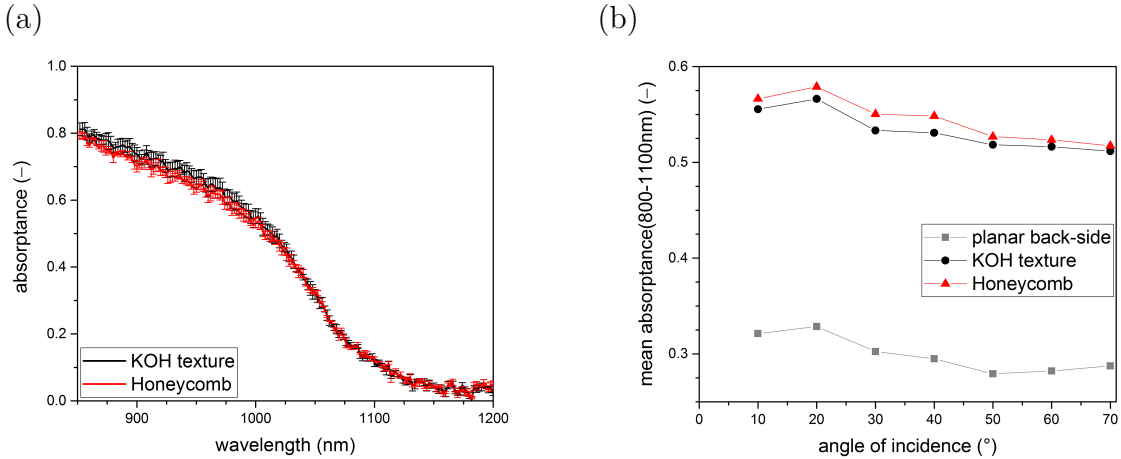


**Figure 6.16:** (a) Mean absorptance and standard deviation for four spots on different grains of LPC silicon absorbers with a KOH pyramid texture (black) and Honeycomb texture (red). (b) Mean absorptance between 800 nm and 1100 nm of LPC silicon absorbers with planar back-side (grey squares), textured with a KOH-based solution (black circles) and with a honeycomb texture produced by NIL+RIE (red triangles), in dependency of the incident angle.

In summary, the absorption characteristics of  $15\ \mu\text{m}$  thick LPC silicon absorbers with different back-side textures were investigated. In particular, honeycomb textures with periods between  $1.5\ \mu\text{m}$  and  $6.0\ \mu\text{m}$  and height-to-period ratios between 0.1 and 0.3 were analyzed. An optimum honeycomb texture for light trapping was identified exhibiting a period of  $6.0\ \mu\text{m}$  and a height of  $1.2\ \mu\text{m}$ . This honeycomb texture revealed absorption characteristics equivalent to the state-of-the-art random pyramid texture produced by wet-chemical etching in KOH, both for normal incidence and for oblique angles of incidence.

## 6.4 Solar cell results

Solar cells were produced on the back-side textured LPC silicon absorber according to the device design described in section 3.3. To confirm that the NIL+RIE method

does not alter the material quality of the LPC absorber or interface passivation, measurements of the external quantum efficiency (EQE) were performed. Figure 6.17 depicts EQE (solid lines) and absorptance (dashed) of LPC silicon thin-film solar cells with a textured back-side, either a random pyramid texture produced by wet-chemical etching in KOH (black) or a honeycomb texture produced by NIL+RIE (red).

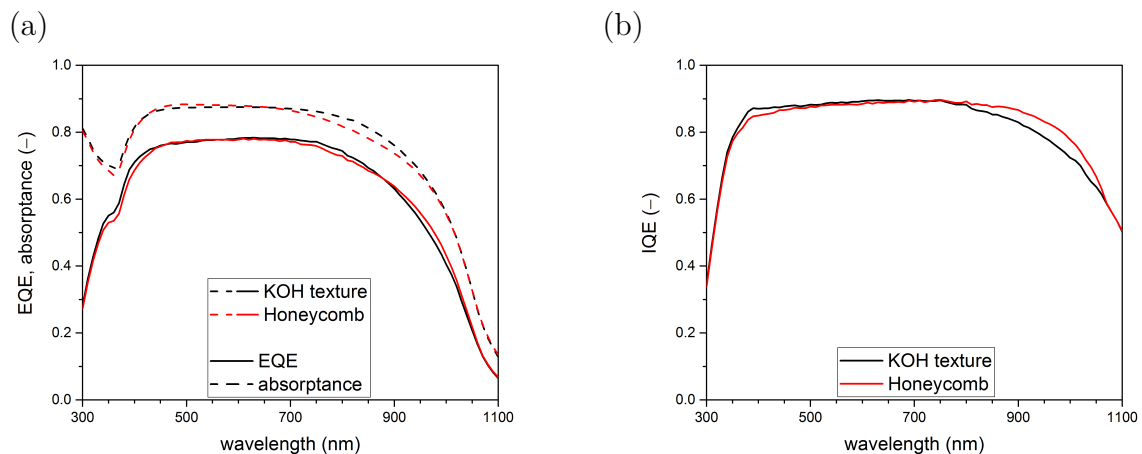


**Figure 6.17:** (a) External quantum efficiency (EQE, solid) and absorptance (dashed) and (b) internal quantum efficiency (IQE) of LPC silicon thin-film solar cells with a random pyramid texture produced by wet-chemical etching in KOH (black) and a honeycomb texture produced by NIL+RIE (red).

As EQE is a measure of the current extracted from the solar cell depending on the wavelength of the incoming radiation, it comprises both optical losses and electronic losses. The absorption characteristics of both textures, as discussed before, is comparable within statistical fluctuations. To evaluate the electronic losses independently, internal quantum efficiency (IQE) is calculated from EQE and absorptance and displayed in Fig. 6.17(b). Small differences in the short wavelength range around 400 nm are attributed to inhomogeneities from the interlayer production process. The IQE gain for longer wavelengths, from 800 nm to 1050 nm, stems from a relatively low absorptance measured for the honeycomb texture (cf. section 6.3) and is considered negligible. Total IQE values over 0.9 indicate an excellent electronic material quality for both textures. In particular, the reactive ion etching process employed to replicate the honeycomb texture in LPC silicon does not negatively affect the external quantum efficiency, indicating a comparable interface and material quality. Short-circuit current densities calculated from EQE amount to  $28.8 \text{ mA cm}^{-2}$  and  $28.7 \text{ mA cm}^{-2}$  for the KOH and NIL+RIE texture, respectively. This is confirmed by measurements of the open-circuit voltage, as disclosed in Fig. 6.18.  $V_{oc}$  values above 630 mV were determined for solar cells with every back-side texture. Overall,  $V_{oc}$  of the solar cells with a planar back-side is higher by

about 20 mV. This could be explained by a lower surface area and, hence, better passivation properties. Between the textured solar cells, no significant difference is found. Mean  $V_{oc}$  values of 643 mV, 630 mV and 619 mV were determined for the cells with planar back-side, random pyramid texture produced by wet-chemical etching in KOH and honeycomb texture, respectively.

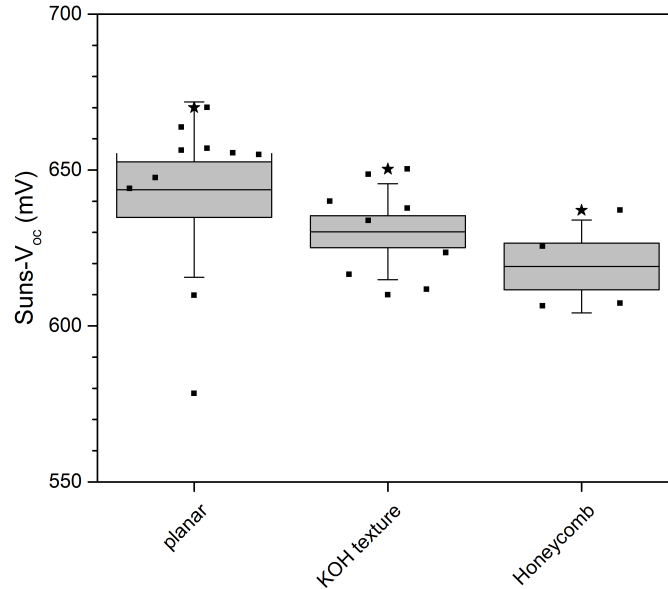


**Figure 6.18:** Open-circuit voltage ( $V_{oc}$ ) measured by the Suns- $V_{oc}$  method, for LPC silicon solar cells with planar and textured back-sides. Mean  $V_{oc}$  is depicted by an open square, best  $V_{oc}$  with a star. The box symbolizes the standard error, the whiskers the standard deviation.

To summarize, liquid phase crystallized silicon thin-film solar cells with different back-side textures were investigated with respect to the performance of solar cells manufactured on the textured back-sides. Both the internal quantum efficiency and open-circuit voltage reveal that the micro-textures produced by NIL+RIE can be implemented into LPC silicon thin-film solar cells without reducing external quantum efficiency or open-circuit voltage. In particular, the ion bombardment during RIE seems not to negatively influence the absorber's material quality. Both bulk and interface quality of the solar cell with a honeycomb texture was equivalent to solar cells with a planar or KOH-textured back-side. Hence, the NIL+RIE method is applicable as a back-side texturing method for LPC silicon thin-film solar cells on glass.

## 6.5 Conclusion

The NIL+RIE method for the production of tailor-made light trapping textures in liquid phase crystallized silicon thin-film solar cells on glass was introduced. This technology is based on replicating nano-imprinted structures into the underlying LPC silicon layer by reactive ion etching. By optimizing the process parameters during RIE and a proper choice of nano-imprint resist, pattern replication with high structural fidelity could be reached.

Honeycomb textures developed for light trapping in micro-crystalline silicon thin-film solar cells [146, 147] with periods between  $1.5\ \mu\text{m}$  and  $6.0\ \mu\text{m}$  and height-to-period ratios from 0.1 to 0.3 were produced as master textures for nano-imprint lithography. Honeycomb textures with heights ranging from  $125\ \text{nm}$  to  $1.4\ \mu\text{m}$  as well as an inverted pyramid texture with a period of  $1.25\ \mu\text{m}$  were successfully replicated in LPC silicon, proving the variability of the NIL+RIE process. Analysis of back-textured surfaces yielded that the NIL+RIE process is homogenous over an area of  $3 \times 3\ \text{cm}^2$  and, in contrast to the state-of-the-art random pyramid texture produced by wet-chemical etching in KOH solutions [41–43, 51, 52], independent of the grain orientation of the poly-crystalline silicon material.

Optical properties of  $16\ \mu\text{m}$  thick LPC silicon absorber layers with honeycomb back-side textures were analyzed with respect to their light trapping ability. It was found that higher height-to-period ratios and larger periods for equivalent height-to-period ratios are beneficial. Thus, optimized geometrical parameters for light trapping in LPC silicon absorber with a honeycomb texture were found for a period of  $6.0\ \mu\text{m}$  and a height-to-period ratio of 0.2. The optimized honeycomb texture was compared to other back-side textures known from literature [41–43, 51, 52, 232, 233] and found to provide equivalent light trapping abilities to the state-of-the-art random pyramid texture produced by wet-chemical etching in KOH, both at normal and oblique incidence.

Solar cells on textured liquid phase crystallized silicon absorbers revealed that introducing the honeycomb texture by means of the NIL+RIE method does not negatively affect material and interface quality of the LPC silicon absorber layer. A short-circuit current density of  $28.7\ \text{mA cm}^{-2}$  and a mean open-circuit voltage of  $619\ \text{mV} \pm 15\ \text{mV}$  were measured on devices with a NIL+RIE honeycomb texture, compared to  $28.8\ \text{mA cm}^{-2}$  and  $630\ \text{mV} \pm 15\ \text{mV}$  for the state-of-the-art KOH texture.

In order to improve light trapping and, in consequence, the short-circuit current density and power conversion efficiency in LPC silicon thin-film solar cells on glass, different textures might be examined. One approach is to further increase the pe-

riods or height-to-period ratios of the honeycomb textures. This, however, would require to find new processes for honeycomb texture production (Hitoshi Sai, personal communication, March 2017). Another route for improved light trapping is texturing using sharp-edges textures. The honeycomb texture was designed as a light trapping texture that, at the same time, allows to grow micro-crystalline silicon on the texture without deteriorating material quality. This trade-off – while being crucial and widely discussed in other chapters of this thesis – does not restrict texture choice for back-side textures taking place after the absorber deposition and crystallization. Hence, textures with edges and steep flanks could be advantageous for light trapping. Thirdly, a combination of front-side textures with the NIL+RIE back-side structures could be employed for improved light trapping. If a tailor-made texture at the back-side of the silicon absorber is appropriately chosen, it could affect light trapping and, hence, solar cell performance positively [103].

# 7 Discussion

Throughout this thesis, three approaches to improve light management in liquid phase crystallized silicon thin-film solar cells on glass were presented. Sinusoidal nano-textures (Chapter 4) and smooth anti-reflective three-dimensional (SMART) textures (Chapter 5) implemented at the glass-silicon interface primarily aimed at optimizing light in-coupling into the devices, while the NIL+RIE method for the replication of micro-textures at the silicon back-side (Chapter 6) focused on light trapping of long wavelength light.

This chapter sets these approaches into context and gives a general outline to light management in LPC silicon thin-film solar cells on glass (section 7.1). For this, the Tiedje-Yablonovitch limit is introduced as a benchmark for optimized light absorption in a 15  $\mu\text{m}$  thin silicon layer (section 7.1.1). The optical losses of state-of-the-art planar LPC solar cells are analyzed with respect to the Tiedje-Yablonovitch limit (section 7.1.2) and compared to cells with light management techniques developed in the scope of this thesis being employed (section 7.1.3). From these, conclusions for future cell designs are drawn.

Finally, potential applications of the methods developed in this thesis for improving other solar cell types, namely perovskite-silicon tandem devices, are discussed (section 7.2).

Parts of section 7.2 were previously published in [234].

## 7.1 Optical loss analysis

### 7.1.1 The Tiedje-Yablonovitch limit for silicon thin-film solar cells

The mean solar photon flux at the earth surface corresponds to a maximum short-circuit current density for silicon solar cells of  $43.9 \text{ mA cm}^{-2}$  (see section 2.1). However, silicon has a low absorption coefficient in the near infrared due to its indirect

bandgap, causing inherent optical losses due to non-absorption. Optimized absorption under the assumption of a Lambertian scatterer was calculated by Tiedje et al. (cf. section 2.1.2 and [44]). Figure 7.1 illustrates the absorptance of a  $15\ \mu\text{m}$  thick silicon layer assuming no front reflection and a single path through the absorber (black), two paths due to a perfect rear reflector (blue) and the Tiedje-Yablonovitch limit (red) calculated according to Eq. (2.18).

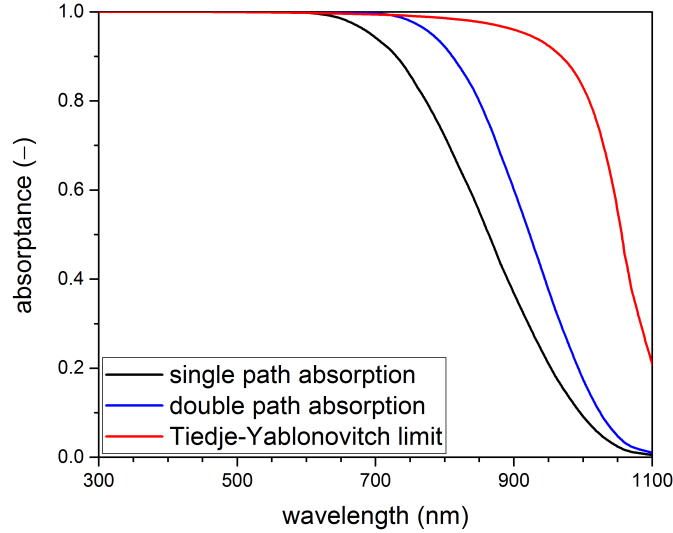


**Figure 7.1:** Absorptance of a  $15\ \mu\text{m}$  thick silicon layer with a single path through the absorber (black), double path due to a perfect back-reflector (blue) and in the Tiedje-Yablonovitch limit (red) calculated from Eq. (2.18).

For a single and double light path, absorptance is reduced for wavelengths  $> 600\ \text{nm}$  and  $> 700\ \text{nm}$ , respectively, limiting the maximum achievable short-circuit current density to  $30.8\ \text{mA cm}^{-2}$  and  $34.2\ \text{mA cm}^{-2}$ , respectively. The low absorption coefficient of silicon in the near infrared limits absorptance in this wavelength range. For a Lambertian scatterer, the light path enhancement leads to higher absorptance, and losses are mainly limited to the wavelength range from  $900\ \text{nm}$  to  $1100\ \text{nm}$ . In total, a maximum achievable short-circuit current density of  $40.5\ \text{mA cm}^{-2}$  is found for a  $15\ \mu\text{m}$  thick silicon layer. Silicon thin-film solar cells with a thickness of  $15\ \mu\text{m}$  therefore inherently lose a short-circuit current density of  $3.4\ \text{mA cm}^{-2}$  due to non-absorption of long wavelength light. The Tiedje-Yablonovitch limit is used as benchmark for light management in the following, where losses at different interfaces play a role in addition to the trapping of long wavelength light.

### 7.1.2 Losses in state-of-the-art planar devices

In order to analyze the optical losses in LPC silicon thin-film solar cells with planar glass-silicon interface, their absorptance characteristics were measured as well as calculated using one-dimensional simulations. Figure 7.2(a) exhibits the measured absorptance of 15  $\mu\text{m}$  thick LPC silicon absorber with  $\text{SiO}_x/\text{SiN}_x/\text{SiO}_x$  (light grey) and  $\text{SiO}_x/\text{SiN}_x/\text{Si}(\text{ON})$  interlayers, for which a planar back-side (grey) and a back-side with additional light trapping measures (black) is depicted, in particular a random pyramid texture and white paint rear reflector. The Tiedje-Yablonovitch limit is included for reference. As already discussed in section 5.5.3, changing the passivation layer from  $\text{SiO}_x$  to  $\text{Si}(\text{ON})$  leads to enhanced light in-coupling in the short wavelength range up to 600 nm, while leaving the absorptance maximum unchanged. For longer wavelength light, implementing light trapping measures is inevitable to facilitate high absorptance.

To analyze their optical properties further, the difference in maximum achievable short-circuit current density of the three samples to the Tiedje-Yablonovitch limit is illustrated in Fig. 7.2(b). This representation on the one hand weights absorptance with the solar spectrum to take changes of photon flux into account. On the other hand, the benchmark of maximum absorptance given by the Tiedje-Yablonovitch limit is considered. This cumulative  $j_{\text{sc, TY}}$  loss hence visualizes the part of the solar spectrum that cannot be utilized for energy conversion up to the respective wavelength due to the employed device design.

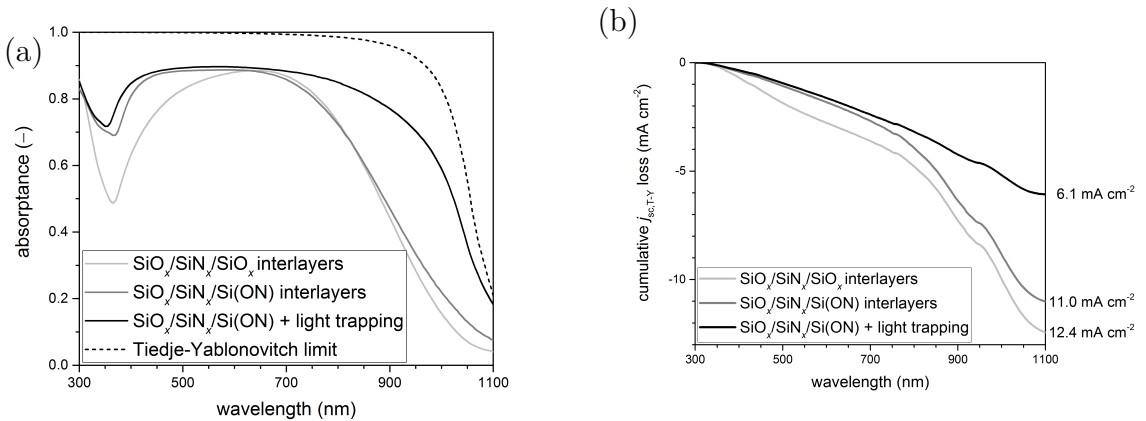


**Figure 7.2:** (a) Absorptance of a 15  $\mu\text{m}$  thick LPC silicon absorber with a  $\text{SiO}_x/\text{SiN}_x/\text{SiO}_x$  interlayer stack with a planar back-side (light grey) and  $\text{SiO}_x/\text{SiN}_x/\text{Si}(\text{ON})$  interlayers with a planar back-side (grey) and additional KOH texture and white paint rear reflector (black). The Tiedje-Yablonovitch limit (dashed) for a 15  $\mu\text{m}$  thick silicon layer is included for reference. (b) Cumulative short-circuit current density loss compared to the Tiedje-Yablonovitch limit  $j_{\text{sc, TY}}$  for the three samples.

Comparing the interlayer stacks of silicon oxide/silicon nitride/silicon oxide (light grey) to the silicon oxide/silicon nitride/silicon oxy-nitride (grey) reveals decreased losses due to the higher refractive index of the passivation layer. Consequently, maximum achievable short-circuit current density losses are reduced by  $1.4 \text{ mA cm}^{-2}$  if utilizing a Si(ON) passivation layer. The main loss occurs for wavelengths  $> 700 \text{ nm}$ , where the penetration depth of the incoming light becomes larger than the absorber thickness. Hence, a random pyramid texture produced by wet-chemical etching in KOH and back reflectors are employed to improve light trapping (black curves in Fig. 7.2). Implementing these measures reduces the losses in the long wavelength range between  $700 \text{ nm}$  and  $1100 \text{ nm}$  by  $4.9 \text{ mA cm}^{-2}$ , leading to a total  $j_{sc, \text{TY}}$  loss of  $6.1 \text{ mA cm}^{-2}$ .

One-dimensional simulations were performed to further resolve losses at the interfaces of LPC silicon thin-film solar cells with a state-of-the-art  $\text{SiO}_x/\text{SiN}_x/\text{Si(ON)}$  interlayer stack and a random pyramid texture and white paint rear reflector at the silicon back-side for light trapping. Simulations allow to change the structure of the solar cell such that losses at individual interfaces can be calculated, and are disclosed as (a) absorptance and (b) cumulative  $j_{sc, \text{TY}}$  loss in Fig. 7.3. The first loss takes place at the sun-facing air-glass interface, where, for normal incidence, 4% of the incoming light are reflected (cf. Eq. (2.16)) due to the difference in refractive indices (grey area in Fig. 7.3(a)). This corresponds to a maximum achievable short-circuit current density loss of  $1.8 \text{ mA cm}^{-2}$  (grey area in Fig. 7.3(b)). This loss has been addressed in record LPC silicon devices by attaching a light trapping foil with millimeter-sized pyramids [235]. However, the foil is not suitable for device applications as it is only modularly attached to the cell and would suffer from severe soiling in outdoor applications.

Losses at the glass-silicon interface (light blue areas in Fig. 7.3) are calculated by utilizing an infinitely thick silicon absorber. In this configuration, absorptance equals the proportion of light coupled into the silicon absorber as the rear-side is “switched off”. As apparent from Fig. 7.3(a), reflectance at the glass-silicon interface depends on the wavelength of the incoming light due to wavelength-dependent refractive indices of the materials and anti-reflective properties of the  $60 \text{ nm}$  thin  $\text{SiN}_x$  layer. Optimized anti-reflective properties of the interlayer stack for a wavelength of  $550 \text{ nm}$  allow to minimize optical losses in this wavelength range. In total, the glass-silicon interface amounts to a  $j_{sc, \text{TY}}$  loss of  $4.5 \text{ mA cm}^{-2}$ .

The loss at the silicon back-side (brown areas in Fig. 7.3) is calculated for a optimized LPC silicon absorber with a  $\text{SiO}_x/\text{SiN}_x/\text{Si(ON)}$  interlayer stack, absorber thickness of  $15 \mu\text{m}$ , random KOH pyramid texture, and back reflector. The loss at this interface is calculated by subtracting the absorptance of this realistic stack from

the one with a Lambertian scatterer at the back-side (yellow area in Fig. 7.3(a)), which causes inherent losses of  $3.4 \text{ mA cm}^{-2}$  (see section 7.1.1). Due to the absorber thickness being larger than the penetration depth of the incoming light up to approximately 700 nm, losses at the silicon back-side only come forth in the long wavelength range. As the absorption coefficient in this wavelength range is very low for silicon, absorptance becomes as low as 10% for a wavelength of 1100 nm and most of the light is reflected back after passing through the absorber at least twice. Losses due to the rear interface amount to  $0.9 \text{ mA cm}^{-2}$ . In comparison, the front glass-silicon interface induces a loss of  $2.6 \text{ mA cm}^{-2}$  in the same wavelength range (700 nm – 1100 nm).

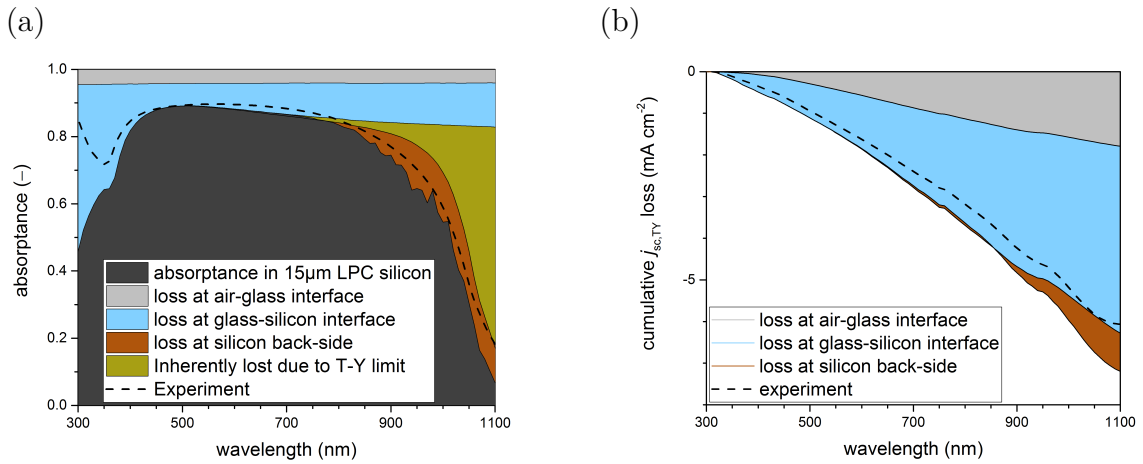


**Figure 7.3:** One-dimensional simulations of losses at different interfaces in a 15  $\mu\text{m}$  thick LPC silicon absorber with  $\text{SiO}_x/\text{SiN}_x/\text{Si}(\text{ON})$  interlayers, illustrated as (a) absorptance and (b) cumulative short-circuit current density loss compared to the Tiedje-Yablonovitch limit  $j_{\text{sc,TY}}$ . The experimental absorptance and cumulative  $j_{\text{sc,TY}}$  loss (dashed) are enclosed for comparison.

Moreover, the cumulative  $j_{\text{sc,TY}}$  loss simulated for the realistic structure is compared to the experimental sample (dashed). The total loss for the simulated structure is slightly higher than in experiment, whereby the difference is gradually increasing with wavelength up to a  $j_{\text{sc,TY}}$  loss difference of  $1.1 \text{ mA cm}^{-2}$ . This is attributed to deviations in film thicknesses and refractive indices of the experimental and numerical structure, and parasitic absorption in the experiment. It is therefore assumed that results from the numerical analysis of losses at different interfaces provide meaningful insights for the experimental structure.

To sum up, an analysis of losses in state-of-the-art LPC silicon thin-film solar cells by experiment and one-dimensional simulations was presented. It was found that the state-of-the-art structure with a  $\text{SiO}_x/\text{SiN}_x/\text{Si}(\text{ON})$  interlayer stack and light trapping measures of KOH pyramid texture and white paint rear reflector exhibits short-circuit current density losses compared to the Tiedje-Yablonovitch limit of

$j_{sc,TY} = 6.1 \text{ mA cm}^{-2}$ , whereby about two thirds of the loss occurs in the wavelength range from 700 nm to 1100 nm. For the same structure, one-dimensional simulations yielded losses of  $j_{sc,TY} = 7.2 \text{ mA cm}^{-2}$ . The simulations allowed to discriminate between losses at different interfaces, revealing that the glass-silicon interface dominates the losses with  $4.5 \text{ mA cm}^{-2}$ . The air-glass interface and silicon back-side cause additional losses of  $1.8 \text{ mA cm}^{-2}$  and  $0.9 \text{ mA cm}^{-2}$ , respectively.

### 7.1.3 Loss analysis for textured LPC silicon thin-film solar cells

As discussed in the previous section, optical losses emanate from both the front glass-silicon interface and the silicon back-side of LPC silicon thin-film solar cells, whereby the glass-silicon interface is the most important loss factor. In the scope of this thesis, several techniques were employed to mitigate these losses. The double-sided sinusoidal texture (Chapter 4) allows to engage in reducing both loss mechanisms, namely light in-coupling at the glass-silicon interface and insufficient light trapping, while the SMART texture (Chapter 5) and honeycomb textures (Chapter 6) produced by a method combining nano-imprint lithography (NIL) and reactive ion etching (RIE) mainly consider losses at the front and back interface, respectively. Figure 7.4 presents (a) absorptance and (b) short-circuit current density losses of  $15 \mu\text{m}$  thick LPC silicon absorbers with a  $\text{SiO}_x/\text{SiN}_x/\text{Si}(\text{ON})$  interlayer stack and a random pyramid back-side (black) and honeycomb texture produced by NIL+RIE (blue) at the back-side.

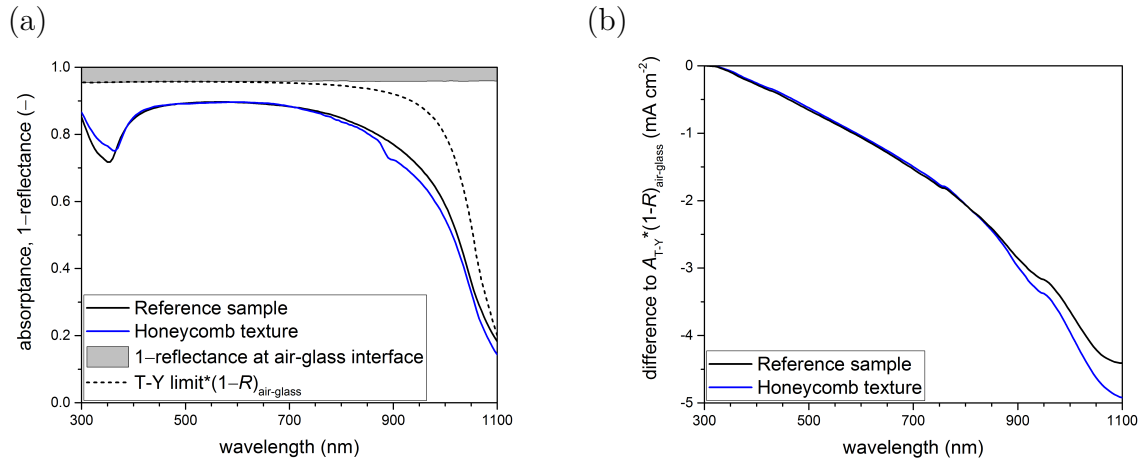


**Figure 7.4:** (a) Absorptance and (b) cumulative short-circuit current density loss compared to the Tiedje-Yablonovitch limit after glass reflectance,  $A_{T-Y} \cdot (1 - R_{air-glass})$ , of  $15 \mu\text{m}$  thick LPC silicon absorber with back-side light trapping textures.

$j_{sc}$  losses are represented compared to the Tiedje-Yablonovitch limit after glass reflectance,  $A_{T-Y} \cdot (1 - R_{air-glass})$ , constituting the maximum absorptance that may be reached with glass-silicon interface and back-side texturing.

Reflectance  $R$  at the air-glass interface, as represented by  $1 - R_{air-glass}$  (grey areas in Fig. 7.4), and the Tiedje-Yablonovitch limit (black, dashed) after air-glass reflectance is included for reference in Fig. 7.4(a). The honeycomb texture produced by NIL+RIE does not enhance light trapping properties compared to the reference sample. It was already shown that the material quality of the honeycomb texture and reference sample are identical (see section 6.4). Still, the advantages of the NIL+RIE method presented in Chapter 6, namely the feasibility of tailoring back-side textures and being independent of crystal grain orientation, may facilitate further improvement to the state-of-the-art KOH texturing.

Figure 7.5 discloses (a) absorptance and (b) cumulative  $A_{T-Y} \cdot (1 - R_{air-glass})$  losses of 15  $\mu\text{m}$  thick LPC silicon absorbers with a sinusoidal texture (blue) and SMART textures (green) implemented at the glass-silicon interface, compared to a reference sample with state-of-the-art planar  $\text{SiO}_x/\text{SiN}_x/\text{Si}(\text{ON})$  interlayers (black).

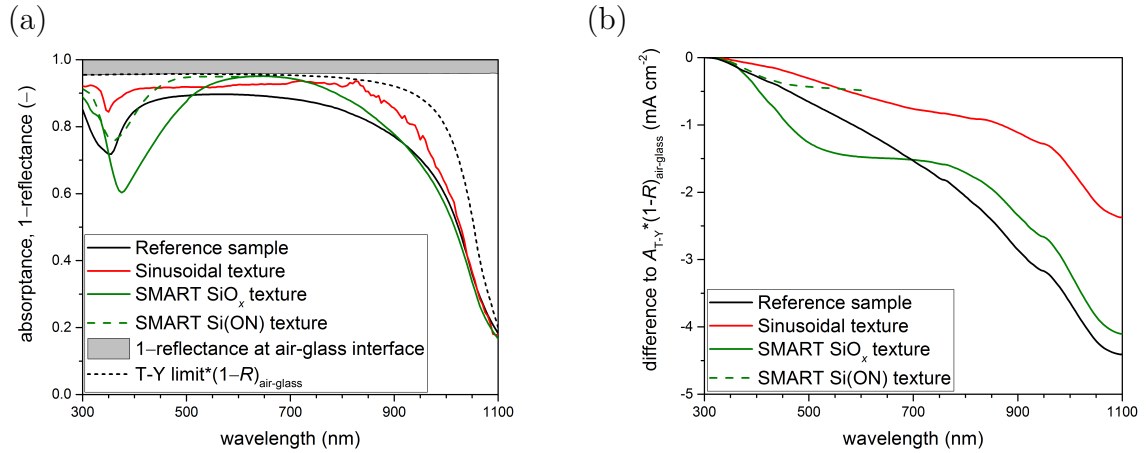


**Figure 7.5:** (a) Absorptance and (b) cumulative short-circuit current density loss compared to the Tiedje-Yablonovitch limit after glass reflectance,  $A_{T-Y} \cdot (1 - R_{air-glass})$ , of 15  $\mu\text{m}$  thick LPC silicon absorber with different textures implemented at the glass-silicon interface.

The sinusoidal texture enhances absorptance over the whole wavelength range (red curve in Fig. 7.5(a)), minimizing short-circuit current density losses compared to the  $A_{T-Y} \cdot (1 - R_{air-glass})$  limit to  $2.4 \text{ mA cm}^{-2}$ , of which  $1.6 \text{ mA cm}^{-2}$  originate from the wavelength range from 700 nm to 1100 nm. From 300 nm to 700 nm, only  $0.8 \text{ mA cm}^{-2}$  are lost for energy conversion. The sinusoidal texture is thereby the most effective texture to optimize light management in LPC silicon thin-film solar cells. Material quality, however, was found to be deteriorated by the sinusoidal texture (see section 4.4). Hence, the enhanced absorptance could not be utilized

for increased current generation due to a decreased internal quantum efficiency, and short-circuit current density was limited.

For the SMART texture, a successful liquid phase crystallization was thus far only achieved with a 10 nm thick silicon oxide passivation layer (SMART SiO<sub>x</sub>, solid). Hence, reflectance in the short wavelength range is higher due to the lower refractive index of the passivation layer compared to the other samples. For a 10 nm thick silicon oxy-nitride passivation layer (SMART Si(ON), dashed), only solid phase crystallization was feasible (see section 5.6). Consequently, the analysis for this sample is restricted to wavelengths up to 600 nm to exclude the influence of the silicon back-side as it does not exhibit a back-side texture. With a silicon oxy-nitride passivation layer, a higher absorptance is observed, corresponding to a short-circuit current density loss at the glass-silicon interface (reflectance at the air-glass interface was subtracted) of 0.5 mA cm<sup>-2</sup> compared to 1.5 mA cm<sup>-2</sup> for the SMART texture with a silicon oxide passivation layer up to 600 nm. In the wavelength range from 500 nm to 700 nm, the SMART texture with a SiO<sub>x</sub> passivation layer exhibits the highest absorptance of all samples. Overall, short-circuit current density losses compared to the Tiedje-Yablonovitch limit after air-glass reflectance  $A_{T-Y} \cdot (1 - R_{\text{air-glass}})$  for the SMART texture with SiO<sub>x</sub> passivation layer amount to 4.1 mA cm<sup>-2</sup>. With a silicon oxy-nitride passivation layer, the expected loss is reduced to 3.1 mA cm<sup>-2</sup>. In comparison, the state-of-the-art device design with planar glass-silicon interface exhibits losses of 4.5 mA cm<sup>-2</sup>. It could be shown that LPC silicon thin-film solar cells on SMART texture evince a material and interface quality comparable to that of solar cells with a planar glass-silicon interface (see section 5.4). As a consequence, enhanced light management may be utilized to achieve an increased short-circuit current density.

To summarize, optical losses of 15 μm thick textured LPC silicon absorbers were analyzed. The sinusoidal texture and SMART texture reduced losses compared to the planar reference device. In terms of maximum achievable short-circuit current density loss compared to the Tiedje-Yablonovitch limit after air-glass reflectance,  $A_{T-Y} \cdot (1 - R)_{\text{air-glass}}$ , losses were reduced from 4.5 mA cm<sup>-2</sup> for the reference sample to 2.4 mA cm<sup>-2</sup> and 4.1 mA cm<sup>-2</sup>, respectively. The future implementation of the silicon oxy-nitride passivation layer will allow to lower losses for the SMART texture to 3.1 mA cm<sup>-2</sup>.

### 7.1.4 Conclusion

Having analyzed the losses in state-of-the-art planar LPC silicon thin-film solar cells and presented potential gains by the implementation of the texturing methods and textures developed in the scope of this thesis, this section summarizes their potential and indicates the most promising device designs for increased power conversion efficiencies of LPC silicon solar cells. Table 7.1 recapitulates the strengths and weaknesses of the three textures discussed in the thesis and demonstrates opportunities expected from their application. Based on these considerations, recommendations for further research are given.

Addressing the losses for state-of-the-art devices with a planar glass-silicon interface to reach higher short-circuit current densities requires the implementation of light management measures. Tailor-made light management measures need to be employed at the glass-silicon interface. Of the textures investigated thus far, the SMART texture is the most promising approach as it already could prove its suitability for high-efficiency solar cells by exceeding reference devices with a planar glass-silicon interface in terms of short-circuit current density. While the sinusoidal texture gave better optical properties, no interlayer system studied achieved a sufficient surface passivation of the sinusoidally textured glass-silicon interface, resulting in degraded electronic properties. To fully exploit the potential of the SMART texture and improve short-circuit current density in LPC silicon thin-film solar cells, the passivation layers at the glass-silicon interface of SMART textured devices need to be further optimized. Further optimization of the SMART texture encompasses varied texture geometries, e.g. conical silicon oxide structures to exploit an additional graded index effect.

The NIL+RIE method established in the scope of the thesis allows to produce tailored micro-structures for light trapping at the LPC silicon back-side. The method was applied for honeycomb textures which were originally designed for light trapping in micro-crystalline silicon thin-film solar cells. In this cell type, all layers were deposited after texturing, which restricted the usable textures to those allowing defect-free growth [147]. This restriction does not apply for the back-side of LPC silicon solar cells. Hence, textures with steep flanks like (inverted) pyramids should be examined systematically to optimize light trapping. In the scope of this thesis, one inverted pyramid texture with a period of  $1.25\ \mu\text{m}$  was studied, proving the suitability of the NIL+RIE method also for textures with steep flanks, but the systematic variation of texture parameters was limited to honeycomb textures.

Furthermore, the combination of tailor-made back-side textures with textures at the glass-silicon interface may give rise to synergistic effects if texture periods and light scattering properties are properly chosen [32, 103, 236]. To elucidate the effect of a

combination of front and back-side texture on light trapping and identify textures that allow optimized light management in LPC silicon thin-film solar cells, three-dimensional simulations of the full device need to be established. Based on these simulation results, optimized textures may be integrated in the LPC silicon thin-film solar cell process employing the methods developed in the scope of this thesis.

**Table 7.1:** Strength and weaknesses, opportunities and recommendations for further research of the textures discussed in the scope of this thesis.

Texture	strengths & weaknesses	opportunities	recommendations
Sinusoidal texture	<i>s</i> Best optical properties	• Optimal light management in LPC silicon solar cells	• Analyze growth defects to definitely decide suitability for LPC silicon solar cells
	<i>s</i> Double-sided texture feasible		
	<i>w</i> Reduced electronic material properties		
SMART texture	<i>s</i> Separation of optical and electronic interface	• Improved light coupling in high efficiency LPC silicon solar cells	• Optimization of passivation layer to exploit full potential
	<i>s</i> Proved capability to outperform reference samples		
	<i>w</i> Passivation not yet optimized		
Honeycomb texture by NIL+RIE	<i>s</i> Versatile production method for tailor-made textures	• Improved light trapping in LPC silicon solar cells	• Investigation of additional light trapping textures for LPC silicon
	<i>s</i> Texturing independent of crystal grain orientation	• Application to other solar cell types	• Employ texturing method to perovskite/silicon tandem devices
	<i>w</i> So far no enhanced light trapping compared to KOH etched pyramids		

front-side textures

back-side texture

Liquid phase crystallized silicon thin-film solar cells may benefit from SMART textures at the front and tailor-made micro-textures produced by NIL+RIE at the back-side of the device if the processes are further optimized. If the crystallization of SMART textures with a silicon oxy-nitride passivation layer can be established, a maximum achievable short-circuit current density gain of  $1.4 \text{ mA cm}^{-2}$  compared to the state-of-the-art planar  $\text{SiO}_x/\text{SiN}_x/\text{Si(ON)}$  interlayer stack is to be expected. The random pyramid texture produced by wet-chemical etching in KOH already provides light trapping properties close to the Tiedje-Yablonovitch limit with losses of  $0.9 \text{ mA cm}^{-2}$ . Optimizing tailor-made micro textures produced by NIL+RIE further might enable to mitigate this loss.

Additionally, reflectance at the air-glass interface causing losses of  $1.8 \text{ mA cm}^{-2}$  needs to be addressed as it is the most accessible loss. Alternatives to the modularly attached anti-reflective foil employed in record LPC silicon thin-film solar cells thus far are a planar anti-reflective coating or a sub-wavelength nano-texture, e.g. a moth eye texture [80, 237]. A moth-eye film on the air-glass interface allows to reduce the reflectance from 4% to less than 1% [238]. Hence, a short-circuit current density gain of  $1.4 \text{ mA cm}^{-2}$  is expected from its usage in LPC silicon thin-film solar cells. Implementing all of these measures, a total gain in maximum achievable short-circuit current density of  $2.8 \text{ mA cm}^{-2}$  from improved light management is feasible using only methods that demonstrated not to affect material quality negatively, increasing  $j_{\text{sc,max}}$  from  $34.4 \text{ mA cm}^{-2}$  to  $37.2 \text{ mA cm}^{-2}$ . Assuming an internal quantum efficiency of 90%, which has already been shown in state-of-the-art devices (cf. Fig. 6.17(b)), a short-circuit current density of  $j_{\text{sc}} = 33.4 \text{ mA cm}^{-2}$  can be expected. If this short-circuit current density can be reached with a fill factor of 79% [123] and open-circuit voltages of 670 mV (see Fig. 6.18) as already reached for individual cells, a power conversion efficiency of up to 18% is feasible for textured liquid phase crystallized silicon thin-film solar cells on glass.

## 7.2 Potential applications for other solar cell types

While this thesis was conducted, substantial effort in the photovoltaics community was put in the development of high-efficiency perovskite/silicon tandem solar cell. In order to reach high efficiencies using two-terminal devices, the short-circuit current density of both sub-cells need to be matched [89]. In a planar device, light corresponding to a short-circuit current density of  $\approx 7.0 \text{ mA cm}^{-2}$  are lost due to reflection [239]. Texturing the interface between the sub-cells can efficiently reduce

these losses [234]. However, standard device processing for perovskite solar cells employing spin-coating and subsequent anti-solvent crystallization [240] limits the textures applicable. In particular, a random pyramid texture with feature sizes of  $> 1 \mu\text{m}$  produced by wet-chemical etching in KOH is not appropriate as spin-coating of  $\approx 500 \text{ nm}$  thick perovskite layers is not feasible on pronounced textures [241, 242]. To overcome this, the NIL+RIE method presented in Chapter 6 might be applied to replicate smooth textures in the silicon wafer prior to cell processing. This way, the optical gain from texturing can be combined with the capability of spin-coating and facile processing of the perovskite top cell. To prove the feasibility of this concept, sinusoidal nano-textures with periods of 500 nm and 750 nm and heights of 80 nm and 200 nm were produced on glass. Subsequently, perovskite layers were spin-coated and crystallized on the textured glass substrates. Cross-section SEM images as depicted in Fig. 7.6 prove that successful spin-coating of dense perovskite films is achieved on sinusoidally textured glass substrates. The top surface of the perovskite layers is not altered by the textured substrate, posing no restrictions to further cell processing.

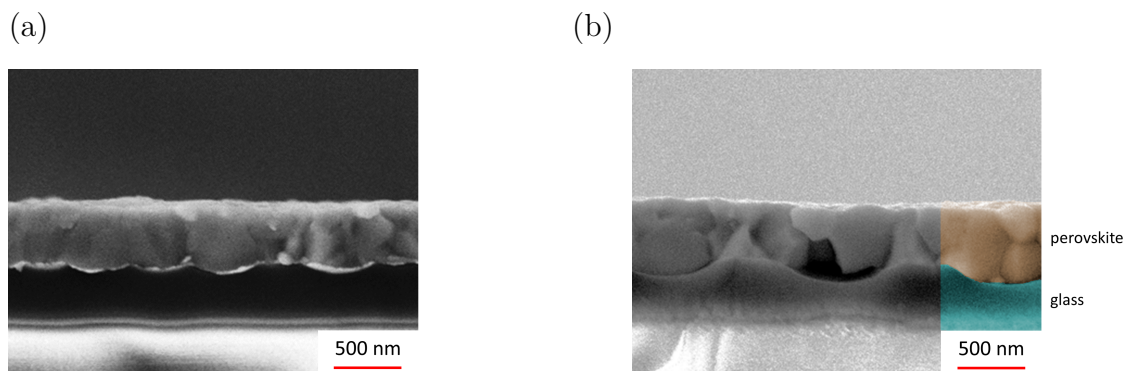


**Figure 7.6:** Scanning electron microscope images of perovskite layers on sinusoidally textured glass substrates with (a) a period of  $P = 500 \text{ nm}$  and (b)  $P = 750 \text{ nm}$ . Images adapted from [234].

Future experiments on silicon wafers patterned by the NIL+RIE method need to be conducted based on these promising preliminary results to further investigate the benefit of nano-textured silicon wafers for perovskite-silicon tandem solar cell applications.



## 8 Summary and Outlook

Liquid phase crystallization (LPC) of 10 – 20  $\mu\text{m}$  thick silicon layers on glass is a promising technology for thin-film solar cells, as it provides excellent material quality using a thin-film approach. To reach efficiencies close to wafer-based devices, efficient light management measures are required, aiming at improved light in-coupling at the buried glass-silicon interface and enhanced light trapping at the silicon rear-side.

Three light management textures were developed and implemented in liquid phase crystallized silicon thin-film solar cells on glass. Sinusoidal nano-textures with height-to-period ratios of 0.5 and smooth anti-reflective three-dimensional (SMART) textures were developed for light in-coupling at the buried glass-silicon interface. Different textures, in particular honeycomb patterns with varying texture period and height-to-period ratio, were examined with respect to their light trapping properties at the back-side of LPC silicon thin-film solar cells.

Sinusoidal nano-textures previously studied by Köppel et al. [48] were optimized with respect to light in-coupling and combined with novel interlayer deposition technologies developed for LPC silicon thin-film solar cells on planar glass substrates. A novel production method employing nano-imprint lithography (NIL) of an organic resist in combination with reactive ion etching (RIE) was developed, allowing to produce sinusoidal textures with a height-to-period ratios of 0.5, compared to 0.3 for the previously employed method relying on high-temperature stable sol-gels. Optical properties could be optimized using sinusoidal textures produced by this method. However, sinusoidally textured solar cells exhibited a reduced external quantum efficiency, indicating texture-induced defects at the glass-silicon interface and in the bulk. It was therefore concluded that the sinusoidal texture in combination with current interlayer stacks is not ideally suited as light in-coupling texture in LPC silicon thin-film solar cells.

The SMART texture was developed to meet all constraints for interlayers during fabrication of textured LPC silicon thin-film solar cells, namely a high temperature stability, anti-reflective properties, and passivation and wetting at the buried glass-silicon interface. For the production of SMART textures, nano-imprinting of

silicon oxide nano-pillars was combined with spin-coating of titanium oxide. This procedure on the one hand allowed to form a structure that is optically rough and on the other hand exhibited a smooth surface. LPC silicon thin-film solar cells with a SMART texture reached open-circuit voltages up to 649 mV and an enhanced external quantum efficiency compared to a state-of-the-art LPC silicon solar cell at the time of the experiment. Further optimizations including a combination of the SMART texture with back-side textures were carried out, leading to a maximum achievable short-circuit current density of  $36.4 \text{ mA cm}^{-2}$ . A passivation method based on plasma-oxidation of silicon nitride was employed for the SMART texture. While optical properties could further be enhanced, so far no successful liquid phase crystallization could be achieved. Solar cells with a SMART texture with a previously employed silicon oxide passivation layer provided a short-circuit current density of  $29.4 \text{ mA cm}^{-2}$ , compared to  $31.4 \text{ mA cm}^{-2}$  for a reference sample with optimized planar interlayers exhibiting a silicon oxy-nitride passivation layer. The SMART texture allowed to combine optical properties of textured interfaces with an interface and material quality of planar interfaces. Thus, open-circuit voltages and short-circuit current densities close to wafer-based record devices could be reached. However, further research of passivation layers is required to incorporate recent advances in LPC technology for planar substrates.

A method for the replication of micro-textures at the back-side of LPC silicon was developed and applied to a range of textures. This texturing method is based on an approach combining nano-imprint lithography of organic resists with subsequent reactive ion etching to transfer the texture into LPC silicon, allowing to produce tailor-made structures independent of the silicon crystal grain orientation. The method was applied to honeycomb textures of varying periods and height-to-period ratios. Light trapping properties of the honeycomb texture with optimized geometry were found to be equivalent to that of a solar cell with a state-of-the-art random pyramid texture produced by wet-chemical etching. LPC silicon solar cells with an optimized honeycomb texture and KOH pyramid texture at the back-side provided equivalent external quantum efficiencies and short-circuit current densities of  $28.7 \text{ mA cm}^{-2}$  and  $28.8 \text{ mA cm}^{-2}$ , respectively. This indicates a comparable interface quality between a state-of-the-art random pyramid textures and a honeycomb texture produced by replicating the nano-imprinted texture in LPC silicon using reactive ion etching. Thus, the NIL+RIE method was established as a method for the implementation of tailor-made micro-textures at the back-side of LPC silicon solar cells independent of crystal grain orientation.

Optical losses of current state-of-the-art LPC silicon thin-film solar cells on glass were analyzed by experiment and one-dimensional simulations. It was found that

the current device design exhibits losses compared to the Tiedje-Yablonoitch limit of  $6.1 \text{ mA cm}^{-2}$  derived from experiment and  $7.2 \text{ mA cm}^{-2}$  calculated from one-dimensional simulations. Thereof, losses of  $4.5 \text{ mA cm}^{-2}$  could be attributed to reflection at the buried glass-silicon interface, constituting the main loss.

The potential of the textures introduced and discussed in this thesis to mitigate these losses was investigated. Losses at the glass-silicon interface were determined to be reduced to  $2.4 \text{ mA cm}^{-2}$  and  $4.1 \text{ mA cm}^{-2}$  for the sinusoidal texture and SMART texture with silicon oxide passivation layer, respectively. For the SMART texture with silicon oxy-nitride passivation layer, a loss of  $3.1 \text{ mA cm}^{-2}$  was estimated.

Finally, possible short-circuit current density gains from implementing interface textures were used to derive an efficiency potential of 18% for LPC silicon thin-film solar cells on glass and indicate the route towards reaching it.

First experiments to investigate the capability of applying the NIL+RIE method for texturing silicon wafers as bottom cell in monolithic two-terminal perovskite-silicon tandem solar cells were presented. As a proof of concept, the feasibility of perovskite spin-coating on sinusoidally textured glass substrates was demonstrated.

Future LPC silicon solar cell designs may benefit from implementing nano-structures at the glass-silicon interface. Hereby, the SMART texture is the most promising approach developed so far. It already demonstrated an excellent material quality in combination with improved anti-reflective properties. To fully exploit the potential gains in short-circuit current density, a passivation layer compatible with the SMART texture providing equivalent passivation properties to state-of-the-art planar interlayer stacks needs to be identified.

Back-side texturing using nano-imprint lithography and reactive ion etching may be implemented to facilitate a structuring independent of silicon crystal grain orientation. Further textures need to be investigated to identify a texture enhancing light trapping and, in consequence, short-circuit current density.

In addition, the developed method of nano-imprinting and subsequent pattern replication by reactive ion etching shall be examined as texturing method to be employed in two-terminal monolithic silicon-perovskite tandem solar cells.



# List of Figures

## Chapter 1

1.1	Schematic device structure and absorptance of LPC silicon . . . . .	3
1.2	Schematic device structures of textured LPC silicon . . . . .	5

## Chapter 2

2.1	AM1.5g irradiance and photon flux spectrum . . . . .	10
2.2	Absorption depth in crystalline silicon . . . . .	11
2.3	Reflection and refraction at the interface of two media . . . . .	13
2.4	Reflection, absorption, and transmission in a three-layer stack . . .	15
2.5	Equivalent circuit of a solar cell and influence of $R_s$ . . . . .	23
2.6	$j - V$ and $P - V$ curve of a solar cell . . . . .	24

## Chapter 3

3.1	Schematic of honeycomb master production . . . . .	28
3.2	Schematic of the inversion of honeycomb master structures . . . . .	29
3.3	Schematic of the nano-imprint lithography process . . . . .	31
3.4	Schematic of further processing after nano-imprint lithography . . .	32
3.5	Schematic of the reactive ion etching chamber. . . . .	33
3.6	Schematic SMART texture production process . . . . .	35
3.7	Schematic back-side texture production processes . . . . .	38
3.8	Schematic solar cell production process . . . . .	39
3.9	Example of an atomic force microscope image . . . . .	40
3.10	Example of a laser scanning confocal microscope image . . . . .	41
3.11	Example of a scanning electron microscope image . . . . .	42
3.12	UV/Vis/NIR measurement set-up and example spectrum . . . . .	44
3.13	Model of a textured LPC silicon layer for 1-dimensional simulations	49
3.14	Unit cell of SMART texture employed in 3-dimensional simulations	50

## Chapter 4

4.1	Mean absorptance depending on height-to-period ratio . . . . .	52
4.2	Etch rates for $\text{SiO}_x$ and resists . . . . .	54
4.3	AFM profiles of imprinted and replicated surfaces . . . . .	55
4.4	AFM surface images of imprinted and replicated surfaces . . . . .	55
4.5	AFM profiles of sinusoidal nano-textures . . . . .	56
4.6	AFM surface images of sinusoidal nano-textures . . . . .	57
4.7	Absorptance of planar and textured substrates for different interlayers	58

## List of Figures

4.8	Mean $A$ of planar and textured substrates for different interlayers . . .	60
4.9	Absorptance of sinusoidal textures for different height-to-period ratios	61
4.10	EQE of sinusoidal textures for different height-to-period ratios . . .	62
4.11	IQE of sinusoidal textures for different height-to-period ratios . . .	63

## Chapter 5

5.1	Schematic of the SMART texture production process . . . . .	69
5.2	Structural properties of spin-coated titanium oxide sol-gel . . . . .	70
5.3	Refractive index of spin-coated titanium oxide layers . . . . .	71
5.4	AFM and SEM surface analysis of the SMART texture . . . . .	72
5.5	Mean absorptance for varied $ff$ and varied $P$ . . . . .	73
5.6	Comparison of simulated and experimental absorptance . . . . .	75
5.7	Optical properties of LPC silicon solar cells with SMART texture . .	76
5.8	Light in-coupling of a SMART texture and sinusoidal texture . . . .	77
5.9	Open-circuit voltage of solar cells with a SMART texture . . . . .	78
5.10	Current-voltage characteristics of solar cells with a SMART texture	79
5.11	EQE of solar cells with a SMART texture . . . . .	80
5.12	IQE of solar cells with a SMART texture . . . . .	81
5.13	Simulated absorptance with varied refractive indices of $\text{TiO}_x$ . . . .	83
5.14	Structural properties of the $\text{TiO}_x$ sol-gel with 800 °C annealing . . .	84
5.15	Light in-coupling of the $\text{TiO}_x$ sol-gel with 800 °C annealing . . . . .	85
5.16	Absorptance of SMART texture with light trapping measures . . . .	86
5.17	Absorptance of SMART texture with combined light trapping measures	87
5.18	Simulations for SMART texture / $\text{SiN}_x$ / $\text{Si(ON)}$ multi-layer stacks	89
5.19	Absorptance of SMART textures with varying $\text{SiN}_x$ layer thickness	90
5.20	Comparison of $A$ for SMART textures with different passivation . .	91
5.21	EQE and IQE of solar cells exhibiting a SMART texture . . . . .	93
5.22	$V_{oc}$ of solar cells with SMART texture and $\text{Si(ON)}$ passivation layer	94

## Chapter 6

6.1	RIE etch rates for silicon and resists for different gas compositions .	99
6.2	AFM surface profiles in silicon for different $\text{CHF}_3/\text{SF}_6$ ratios . . . .	100
6.3	RIE etch rates for silicon and UVcur06 for different plasma powers .	101
6.4	REM cross-sections of nano-textures for different plasma powers . .	102
6.5	Grain orientation dependency for KOH and NIL+RIE texturing . .	103
6.6	LSCM images of wafer surfaces after KOH and NIL+RIE texturing	104
6.7	Grain orientation dependency in LPC silicon texturing . . . . .	105
6.8	LSCM surface images of investigated back-textures in LPC silicon .	106
6.9	AFM surface profiles of distinct honeycomb patterns . . . . .	107
6.10	AFM surface profiles of a honeycomb pattern and its inverse . . . .	108
6.11	LSCM analysis of homogeneity of honeycomb pattern replication . .	109
6.12	Absorptance of honeycombs with varied height-to-period ratio . . .	110
6.13	Absorptance of honeycomb patterns and its inverse . . . . .	111
6.14	Mean absorptance of different honeycomb patterns . . . . .	112
6.15	Absorptance of LPC silicon with different back-side textures . . . .	113

6.16	Mean and angular absorptance of back-textured LPC silicon . . . .	114
6.17	EQE and IQE of LPC silicon with KOH and honeycomb back-side .	115
6.18	$V_{oc}$ of LPC silicon with KOH and honeycomb back-side texture . .	116
<b>Chapter 7</b>		
7.1	Tiedje-Yablonovitch limit of thin-film silicon . . . . .	120
7.2	Experimental loss analysis of state-of-the-art planar devices . . . . .	121
7.3	Simulated loss analysis of state-of-the-art planar devices . . . . .	123
7.4	Absorptance and cumulative $j_{sc,T-Y}$ loss of back-textured solar cells	124
7.5	Absorptance and cumulative $j_{sc,T-Y}$ loss of front-textured solar cells	125
7.6	SEM image of perovskite on sinusoidal nano-textures . . . . .	131

# List of Tables

## Chapter 1

- 1.1 Solar cell parameters short-circuit current density  $j_{sc}$ , open-circuit voltage  $V_{oc}$ , fill factor  $FF$  and power conversion efficiency  $\eta$  of the record cells for LPC silicon [43] compared to high performance multi-crystalline (mc-Si) wafer-based devices [5]. . . . . 2

## Chapter 3

- 3.1 Hole diameter in photolithography and etchant dilution in de-ionized water used in honeycomb master production. . . . . 29
- 3.2 Overview of layer stacks and production processes for different sample types manufactured in this thesis. . . . . 36

## Chapter 5

- 5.1 Comparison of changes in maximum achievable short-circuit current density  $j_{sc,max}$  derived from absorptance and short-circuit current density  $j_{sc,EQE}$  calculated from external quantum efficiency (EQE) for LPC silicon thin-film solar cells with different textures at the glass-silicon interface, compared to their respective reference samples with planar glass-silicon interface. . . . . 68
- 5.2 Short-circuit current density calculated from 1–reflectance ( $j_{sc,max}$ ) and from external quantum efficiency ( $j_{sc,EQE}$ ) measurements, for the solar cell with a SMART texture and the back-textured IBC reference cell. . . . . 81

## Chapter 6

- 6.1 Maximum achievable short-circuit current density  $j_{sc,max}$  of 16  $\mu\text{m}$  thick LPC silicon absorbers with different micro-textures at the back-side. . . . . 113
- 7.1 Strength and weaknesses, opportunities and recommendations for further research of the textures discussed in the scope of this thesis. . . . 129

## Chapter 7

# Bibliography

- [1] Agora Energiewende and Sandbag. *The European Power Sector in 2017. State of Affairs and Review of Current Developments*. 2018. URL: [https://www.agora-energiewende.de/fileadmin/Projekte/2018/EU\\_Jahresrueckblick\\_2017/Agora\\_EU-report-2017\\_WEB.pdf](https://www.agora-energiewende.de/fileadmin/Projekte/2018/EU_Jahresrueckblick_2017/Agora_EU-report-2017_WEB.pdf) (accessed 1. Feb. 2018).
- [2] ITRPV. *International Technology Roadmap for Photovoltaic*. 2017. URL: <http://www.itrpv.net/.cm4all/mediadb/ITRPVEighthEdition2017.pdf> (accessed 18. Jan. 2018).
- [3] K. Yoshikawa, H. Kawasaki, W. Yoshida, T. Irie, K. Konishi, K. Nakano, T. Uto, D. Adachi, M. Kanematsu, H. Uzu, and K. Yamamoto. “Silicon heterojunction solar cell with interdigitated back contacts for a photoconversion efficiency over 26%”. *Nat. Energy* **2** (2017), p. 17032.
- [4] M. A. Green, Y. Hishikawa, E. D. Dunlop, D. H. Levi, J. Hohl-Ebinger, and A. W. Ho-Baillie. “Solar cell efficiency tables (version 51)”. *Prog. Photovoltaics Res. Appl.* **26** (2018), pp. 3–12.
- [5] J. Benick, R. Müller, F. Schindler, A. Richter, H. Hauser, F. Feldmann, P. Krenckel, S. Riepe, M. C. Schubert, M. Hermle, and S. W. Glunz. “Approaching 22% Efficiency With Multicrystalline N-Type Silicon Solar Cells”. *33rd Eur. PV Sol. Energy Conf. Exhib.* (2017), pp. 460–464.
- [6] M. Kerr, P. Campbell, and A. Cuevas. “Lifetime and efficiency limits of crystalline silicon solar cells”. *Conf. Rec. Twenty-Ninth IEEE Photovolt. Spec. Conf. - 2002.* **3** (2002), pp. 438–441.
- [7] A. Richter, M. Hermle, and S. Glunz. “Reassessment of the Limiting Efficiency for Crystalline Silicon Solar Cells”. *IEEE J. Photovoltaics* **3** (2013), pp. 1184–1191.
- [8] J. Poortmans and V. Arkhipov, eds. *Thin Film Solar Cells: Fabrication, Characterization and Applications*. 1st edition. John Wiley & Sons, Ltd, 2006.

- [9] I. Gordon, F. Dross, V. Depauw, A. Masolin, Y. Qiu, J. Vaes, D. Van Gestel, and J. Poortmans. “Three novel ways of making thin-film crystalline-silicon layers on glass for solar cell applications”. *Sol. Energy Mater. Sol. Cells* **95** (2011), S2–S7.
- [10] K. V. Nieuwenhuysen, F. Duerinckx, I. Kuzma, D. Van Gestel, G. Beaucarne, and J. Poortmans. “Progress in epitaxial deposition on low-cost substrates for thin-film crystalline silicon solar cells at IMEC”. *J. Cryst. Growth* **287** (2006), pp. 438–441.
- [11] I. Kuzma-Filipek, K. V. Nieuwenhuysen, J. V. Hoeymissen, M. R. Payo, E. V. Kerschaver, J. Poortmans, R. Martens, G. Beaucarne, E. Schmich, S. Lindkugel, and S. Reber. “Efficiency (>15%) for thin-film epitaxial silicon solar cells on 70 cm<sup>2</sup> area offspec silicon substrate using porous silicon segmented mirrors”. *Prog. Photovoltaics Res. Appl.* **18** (2010), pp. 137–143.
- [12] E. Kobayashi, Y. Watabe, R. Hao, and T. S. Ravi. “High efficiency heterojunction solar cells on n-type kerfless mono crystalline silicon wafers by epitaxial growth”. *Appl. Phys. Lett.* **106** (2015), pp. 223504-1 – 223504-4.
- [13] R. Cariou, W. Chen, I. Cosme-Bolanos, J.-L. Maurice, M. Foldyna, V. Depauw, G. Patriarche, A. Gaucher, A. Cattoni, I. Massiot, S. Collin, E. Cadel, P. Pareige, and P. Roca i Cabarrocas. “Ultrathin PECVD epitaxial Si solar cells on glass via low-temperature transfer process”. *Prog. Photovoltaics Res. Appl.* **24** (2016), pp. 1075–1084.
- [14] J. Van Hoeymissen, V. Depauw, I. Kuzma-Filipek, K. Van Nieuwenhuysen, M. R. Payo, Y. Qiu, I. Gordon, and J. Poortmans. “The use of porous silicon layers in thin-film silicon solar cells”. *Phys. Status Solidi A* **208** (2011), pp. 1433–1439.
- [15] V. Depauw, Y. Qiu, K. Van Nieuwenhuysen, I. Gordon, and J. Poortmans. “Epitaxy-free monocrystalline silicon thin film: first steps beyond proof-of-concept solar cells”. *Prog. Photovoltaics Res. Appl.* **19** (2011), pp. 844–850.
- [16] V. Depauw, X. Meng, O. El Daif, G. Gomard, L. Lalouat, E. Drouard, C. Trompoukis, A. Fave, C. Seassal, and I. Gordon. “Micrometer-thin crystalline-silicon solar cells integrating numerically optimized 2-D photonic crystals”. *IEEE J. Photovoltaics* **4** (2014), pp. 215–223.
- [17] M. A. Green, P. A. Basore, N. Chang, D. Clugston, R. Egan, R. Evans, D. Hogg, S. Jarnason, M. Keevers, P. Lasswell, J. O’Sullivan, U. Schubert, A. Turner, S. R. Wenham, and T. Young. “Crystalline silicon on glass (CSG) thin-film solar cell modules”. *Sol. Energy* **77** (2004), pp. 857–863.

- [18] M. A. Green. “Polycrystalline silicon on glass for thin-film solar cells”. *Appl. Phys. A* **96** (2009), pp. 153–159.
- [19] R. Brendel. *Thin-Film Crystalline Silicon Solar Cells: Physics and Technology*. 1st edition. Wiley-VCH Verlag GmbH, 2003.
- [20] S. Mokkaapati and K. R. Catchpole. “Nanophotonic light trapping in solar cells”. *J. Appl. Phys.* **112** (2012), pp. 101101-1 – 101101-19.
- [21] S. Fahr, T. Kirchartz, C. Rockstuhl, and F. Lederer. “Approaching the Lambertian limit in randomly textured thin-film solar cells”. *Opt. Express* **19** (2011), A865–A874.
- [22] C. Battaglia, C. M. Hsu, K. Söderström, J. Escarré, F. J. Haug, M. Charrière, M. Boccard, M. Despeisse, D. T. Alexander, M. Cantoni, Y. Cui, and C. Ballif. “Light trapping in solar cells: Can periodic beat random?” *ACS Nano* **6** (2012), pp. 2790–2797.
- [23] D. Zhou and R. Biswas. “Photonic crystal enhanced light-trapping in thin film solar cells”. *J. Appl. Phys.* **103** (2008), pp. 093102-1 – 093102-5.
- [24] S. B. Mallick, M. Agrawal, and P. Peumans. “Optimal light trapping in ultra-thin photonic crystal crystalline silicon solar cells”. *Opt. Express* **18** (2010), pp. 5691–5706.
- [25] H. A. Atwater and A. Polman. “Plasmonics for improved photovoltaic devices”. *Nat. Mater.* **9** (2010), pp. 205–213.
- [26] H. Tan, R. Santbergen, A. H. M. Smets, and M. Zeman. “Plasmonic Light Trapping in Thin-film Silicon Solar Cells with Improved Self-Assembled Silver Nanoparticles”. *Nano Lett.* **12** (2012), p. 4070.
- [27] E. Garnett and P. Yang. “Light trapping in silicon nanowire solar cells”. *Nano Lett.* **10** (2010), pp. 1082–1087.
- [28] K.-Q. Peng and S.-T. Lee. “Silicon Nanowires for Photovoltaic Solar Energy Conversion”. *Adv. Mater.* **23** (2011), pp. 198–215.
- [29] S. E. Han and G. Chen. “Optical Absorption Enhancement in Silicon Nanohole Arrays for Solar Photovoltaics”. *Nano Lett.* **10** (2010), pp. 1012–1015.
- [30] K.-Q. Peng, X. Wang, L. Li, X.-L. Wu, and S.-T. Lee. “High-Performance Silicon Nanohole Solar Cells”. *J. Am. Chem. Soc.* **132** (2010), pp. 6872–6873.

- [31] C. Trompoukis, I. Abdo, R. Cariou, I. Cosme, W. Chen, O. Deparis, A. Dmitriev, E. Drouard, M. Foldyna, E. G. Caurel, I. Gordon, B. Heidari, A. Herman, L. Lalouat, K.-D. Lee, J. Liu, K. Lodewijks, F. Mandorlo, I. Massiot, A. Mayer, V. Mijkovic, J. Muller, R. Orobtcouk, G. Poulain, P. Prod'Homme, P. R. i. Cabarrocas, C. Seassal, J. Poortmans, R. Mertens, O. E. Daif, and V. Depauw. “Photonic nanostructures for advanced light trapping in thin crystalline silicon solar cells”. *Phys. Status Solidi A* **212** (2015), pp. 140–155.
- [32] K. X. Wang, Z. Yu, V. Liu, Y. Cui, and S. Fan. “Absorption Enhancement in Ultrathin Crystalline Silicon Solar Cells with Antireflection and Light-Trapping Nanocone Gratings”. *Nano Lett.* **12** (2012), pp. 1616–1619.
- [33] J. Zhu, C. M. Hsu, Z. Yu, S. Fan, and Y. Cui. “Nanodome solar cells with efficient light management and self-cleaning”. *Nano Lett.* **10** (2010), pp. 1979–1984.
- [34] M. J. Keevers, T. L. Young, U. Schubert, and M. A. Green. “10% efficient CSG minimodules”. In: *Proceedings of the 22nd European Photovoltaic Solar Energy Conference*. 2007, pp. 1783–1790.
- [35] D. Amkreutz, J. Müller, M. Schmidt, T. Hänel, and T. F. Schulze. “Electron-beam crystallized large grained silicon solar cell on glass substrate”. *Prog. Photovoltaics Res. Appl.* **19** (2011), pp. 937–945.
- [36] J. Dore, R. Evans, U. Schubert, B. D. Eggleston, D. Ong, K. Kim, J. Huang, O. Kunz, M. Keevers, R. Egan, S. Varlamov, and M. A. Green. “Thin-film polycrystalline silicon solar cells formed by diode laser crystallisation”. *Prog. Photovoltaics Res. Appl.* **21** (2013), pp. 1377–1383.
- [37] S. Varlamov, J. Dore, R. Evans, D. Ong, B. Eggleston, O. Kunz, U. Schubert, T. Young, J. Huang, T. Soderstrom, K. Omaki, K. Kim, A. Teal, M. Jung, J. Yun, Z. M. Pakhuruddin, R. Egan, and M. A. Green. “Polycrystalline silicon on glass thin-film solar cells: A transition from solid-phase to liquid-phase crystallised silicon”. *Sol. Energy Mater. Sol. Cells* **119** (2013), pp. 246–255.
- [38] C. Becker, D. Amkreutz, T. Sontheimer, V. Preidel, D. Lockau, J. Haschke, L. Jogschies, C. Klimm, J. J. Merkel, P. Plocica, S. Steffens, and B. Rech. “Polycrystalline silicon thin-film solar cells: Status and perspectives”. *Sol. Energy Mater. Sol. Cells* **119** (2013), pp. 112–123.
- [39] J. Haschke, D. Amkreutz, L. Korte, F. Ruske, and B. Rech. “Towards wafer quality crystalline silicon thin-film solar cells on glass”. *Sol. Energy Mater. Sol. Cells* **128** (2014), pp. 190–197.

- [40] D. Amkreutz, J. Haschke, S. Kühnapfel, P. Sonntag, and B. Rech. “Silicon thin-film solar cells on glass with open-circuit voltages above 620 mV formed by liquid-phase crystallization”. *IEEE J. Photovoltaics* **4** (2014), pp. 1496–1501.
- [41] T. Frijnts, S. Kühnapfel, S. Ring, O. Gabriel, S. Calnan, J. Haschke, B. Stanowski, B. Rech, and R. Schlatmann. “Analysis of photo-current potentials and losses in thin film crystalline silicon solar cells”. *Sol. Energy Mater. Sol. Cells* **143** (2015), pp. 457–466.
- [42] P. Sonntag, N. Preissler, M. Bokalič, M. Trahms, J. Haschke, R. Schlatmann, M. Topič, B. Rech, and D. Amkreutz. “Silicon Solar Cells on Glass with Power Conversion Efficiency above 13% at Thickness below 15 Micrometer”. *Sci. Rep.* **7** (2017), p. 873.
- [43] C. Thi Trinh, N. Preissler, P. Sonntag, M. Muske, K. Jäger, M. Trahms, R. Schlatmann, B. Rech, and D. Amkreutz. “Potential of interdigitated back-contact silicon heterojunction solar cells for liquid phase crystallized silicon on glass with efficiency above 14%”. *Sol. Energy Mater. Sol. Cells* **174** (2018), pp. 187–195.
- [44] T. Tiedje, E. Yablonovitch, G. Cody, and B. Brooks. “Limiting efficiency of silicon solar cells”. *IEEE Trans. Electron Devices* **31** (1984), pp. 711–716.
- [45] V. Preidel, D. Amkreutz, J. Haschke, M. Wollgarten, B. Rech, and C. Becker. “Balance of optical, structural, and electrical properties of textured liquid phase crystallized Si solar cells”. *J. Appl. Phys.* **117** (2015), p. 225306.
- [46] V. Preidel. “Kristalline Silizium-Dünnschichten auf nanoimprintstrukturiertem Glas”. Doctoral Thesis. Technische Universität Berlin, 2015.
- [47] C. Becker, V. Preidel, D. Amkreutz, J. Haschke, and B. Rech. “Double-side textured liquid phase crystallized silicon thin-film solar cells on imprinted glass”. *Sol. Energy Mater. Sol. Cells* **135** (2015), pp. 2–7.
- [48] G. Köppel, B. Rech, and C. Becker. “Sinusoidal nanotextures for light management in silicon thin-film solar cells”. *Nanoscale* **8** (2016), pp. 8722–8728.
- [49] G. Köppel. “Liquid phase crystallized silicon on sinusoidal textured glass substrates”. Doctoral Thesis. Technische Universität Berlin, 2017.
- [50] G. Köppel, D. Amkreutz, P. Sonntag, G. Yang, R. Van Swaaij, O. Isabella, M. Zeman, B. Rech, and C. Becker. “Periodic and Random Substrate Textures for Liquid-Phase Crystallized Silicon Thin-Film Solar Cells”. *IEEE J. Photovoltaics* **7** (2017), pp. 85–90.

- [51] M. Z. Pakhuruddin, J. Dore, J. Huang, and S. Varlamov. “Effects of front and rear texturing on absorption enhancement in laser-crystallized silicon thin-films on glass”. *Jpn. J. Appl. Phys.* **54** (2015), 08KB04.
- [52] M. Z. Pakhuruddin, J. Huang, J. Dore, and S. Varlamov. “Light Absorption Enhancement in Laser-Crystallized Silicon Thin Films on Textured Glass”. *IEEE J. Photovoltaics* **60** (2016), pp. 159–165.
- [53] D. Song, D. Inns, A. Straub, M. L. Terry, P. Campbell, and A. G. Aberle. “Solid phase crystallized polycrystalline thin-films on glass from evaporated silicon for photovoltaic applications”. *Thin Solid Films* **513** (2006), pp. 356–363.
- [54] H. Cui, P. R. Campbell, and M. A. Green. “Compatibility of glass textures with E-beam evaporated polycrystalline silicon thin-film solar cells”. *Appl. Phys. A* **111** (2013), pp. 935–942.
- [55] M. Python, O. Madani, D. Dominé, F. Meillaud, E. Vallat-Sauvain, and C. Ballif. “Influence of the substrate geometrical parameters on microcrystalline silicon growth for thin-film solar cells”. *Sol. Energy Mater. Sol. Cells* **93** (2009), pp. 1714–1720.
- [56] D. Kim, R. Santbergen, K. Jäger, M. Sever, J. Krč, M. Topič, S. Hänni, C. Zhang, A. Heidt, M. Meier, R. van Swaaij, and M. Zeman. “Effect of substrate morphology slope distributions on light scattering, nc-Si:H film growth, and solar cell performance”. *ACS Appl. Mater. Interfaces* **6** (2014), pp. 22061–22068.
- [57] M. Sever, J. Krč, and M. Topič. “Prediction of defective regions in optimisation of surface textures in thin-film silicon solar cells using combined model of layer growth”. *Thin Solid Films* **573** (2014), pp. 176–184.
- [58] A. Tamang, H. Sai, V. Jovanov, S. I. Bali, K. Matsubara, and D. Knipp. “On the interplay of interface morphology and microstructure of high-efficiency microcrystalline silicon solar cells”. *Sol. Energy Mater. Sol. Cells* **151** (2016), pp. 81–88.
- [59] H. Sai, Y. Kanamori, and M. Kondo. “Flattened light-scattering substrate in thin film silicon solar cells for improved infrared response”. *Appl. Phys. Lett.* **98** (2011), p. 113502.
- [60] K. Söderström, G. Bugnon, R. Biron, C. Pahud, F. Meillaud, F.-J. Haug, and C. Ballif. “Thin-film silicon triple-junction solar cell with 12.5% stable efficiency on innovative flat light-scattering substrate”. *J. Appl. Phys.* **112** (2012), p. 114503.

- [61] K. Söderström, G. Bugnon, F.-J. Haug, S. Nicolay, and C. Ballif. “Experimental study of flat light-scattering substrates in thin-film silicon solar cells”. *Sol. Energy Mater. Sol. Cells* **101** (2012), pp. 193–199.
- [62] O. Isabella, H. Sai, M. Kondo, and M. Zeman. “Full-wave optoelectrical modeling of optimized flattened light-scattering substrate for high efficiency thin-film silicon solar cells”. *Prog. Photovoltaics Res. Appl.* **22** (2014), pp. 671–689.
- [63] Y. D. Kim, K.-S. Han, J.-H. Shin, J.-Y. Cho, C. Im, and H. Lee. “Novel patterned layer to enhance conversion efficiency of amorphous silicon thin-film solar cells”. *Phys. Status Solidi A* **211** (2014), pp. 1493–1498.
- [64] National Renewable Energy Laboratory (NREL). *Reference Solar Spectral Irradiance: Air Mass 1.5*. URL: <http://rredc.nrel.gov/solar/spectra/am1.5/> (accessed 18. Jan. 2018).
- [65] M. A. Green. *Solar Cells - Operating Principles, Technology and System Application*. 1st edition. University of NSW, 1992.
- [66] H.-G. Wagemann and H. Eschrich. *Photovoltaik*. 2nd edition. Vieweg+Teubner Verlag, 2010.
- [67] S. M. Sze and K. K. Ng. *Physics of Semiconductor Devices*. 3rd edition. Wiley-Interscience, 2006.
- [68] J. I. Pankove. *Optical Processes in Semiconductors*. 1st edition. Dover Publications, 1971.
- [69] A. H. M. Smets, K. Jäger, O. Isabella, R. A. C. M. M. Van Swaaij, and M. Zeman. *Solar Energy: The physics and engineering of photovoltaic conversion, technologies and systems*. 1st edition. UIT Cambridge, 2016.
- [70] H. Ibach and H. Lüth. *Solid-State Physics*. 4th edition. Springer-Verlag Berlin Heidelberg, 2009.
- [71] P. Y. Yu and M. Cardona. *Fundamentals of Semiconductors*. 4th edition. Springer-Verlag Berlin Heidelberg, 2010.
- [72] E. Hecht. *Optics*. 5th edition. Pearson, 2016.
- [73] W. Demtröder. *Experimentalphysik 3*. 4th edition. Springer-Verlag Berlin Heidelberg, 2010.
- [74] C. Kittel. *Introduction to Solid State Physics*. 8th revised edition. John Wiley & Sons, Ltd, 2005.

- [75] Corning Display Technologies. *EAGLE XG (R) Slim Glass Product Information Sheet*. 2013. URL: <https://www.corning.com/media/worldwide/cdt/documents/EAGLE%20XG%20C2%AE%20Slim%20Glass.pdf> (accessed 21. Feb. 2018).
- [76] M. A. Green. “Self-consistent optical parameters of intrinsic silicon at 300 K including temperature coefficients”. *Sol. Energy Mater. Sol. Cells* **92** (2008), pp. 1305–1310.
- [77] A. N. Sprafke and R. B. Wehrspohn. “Current Concepts for Optical Path Enhancement In Solar Cells”. *Photon Management in Solar Cells*. Ed. by R. B. Wehrspohn, U. Rau, and A. Gombert. 1st edition. Wiley-VCH Verlag GmbH, 2015. Chap. 1.
- [78] W. H. Southwell. “Gradient-index antireflection coatings”. *Opt. Lett.* **8** (1983), pp. 584–586.
- [79] J. Q. Xi, M. F. Schubert, J. K. Kim, E. F. Schubert, M. Chen, S. Y. Lin, W. Liu, and J. A. Smart. “Optical thin-film materials with low refractive index for broadband elimination of Fresnel reflection”. *Nat. Photonics* **1** (2007), pp. 176–179.
- [80] H. K. Raut, V. A. Ganesh, A. S. Nair, and S. Ramakrishna. “Anti-reflective coatings: A critical, in-depth review”. *Energy Environ. Sci.* **4** (2011), pp. 3779–3804.
- [81] U. Schulz. “Review of modern techniques to generate antireflective properties on thermoplastic polymers.” *Appl. Opt.* **45** (2006), pp. 1608–1618.
- [82] S. Chhajed, M. F. Schubert, J. K. Kim, and E. F. Schubert. “Nanostructured multilayer graded-index antireflection coating for Si solar cells with broadband and omnidirectional characteristics”. *Appl. Phys. Lett.* **93** (2008), pp. 1–4.
- [83] J. Moghal, J. Kobler, J. Sauer, J. Best, M. Gardener, A. A. Watt, and G. Wakefield. “High-performance, single-layer antireflective optical coatings comprising mesoporous silica nanoparticles”. *ACS Appl. Mater. Interfaces* **4** (2012), pp. 854–859.
- [84] T. C. Choy. *Effective Medium Theory*. 2nd edition. Oxford University Press, 2015.

- [85] C. Battaglia, K. Söderström, J. Escarré, F.-J. Haug, D. Dominé, P. Cuony, M. Boccard, G. Bugnon, C. Denizot, M. Despeisse, A. Feltrin, and C. Ballif. “Efficient light management scheme for thin film silicon solar cells via transparent random nanostructures fabricated by nanoimprinting”. *Appl. Phys. Lett.* **96** (2010), pp. 8–11.
- [86] X. Liu, P. R. Coxon, M. Peters, B. Hoex, J. M. Cole, and D. J. Fray. “Black silicon: fabrication methods, properties and solar energy applications”. *Energy Environ. Sci.* **7** (2014), pp. 3223–3263.
- [87] M. A. Green. “Lambertian light trapping in textured solar cells and light-emitting diodes: Analytical solutions”. *Prog. Photovoltaics Res. Appl.* **10** (2002), pp. 235–241.
- [88] J. D. Hylton, A. R. Burgers, and W. C. Sinke. “Alkaline Etching for Reflectance Reduction in Multicrystalline Silicon Solar Cells”. *J. Electrochem. Soc.* **151** (2004), G408–G427.
- [89] A. Luque and S. Hegedus. *Handbook of Photovoltaic Science and Engineering*. 2nd edition. John Wiley & Sons, Ltd, 2001.
- [90] A. Torre. *Linear Ray and Wave Optics in Phase Space*. 1st edition. Elsevier, 2005.
- [91] F.-J. Haug, M. Bräuninger, and C. Ballif. “Fourier light scattering model for treating textures deeper than the wavelength”. *Opt. Express* **25** (2017), pp. 14–22.
- [92] A. Shah, P. Torres, R. Tscharnner, N. Wyrsh, and H. Keppner. “Photovoltaic Technology: The Case for Thin-Film Solar Cells”. *Science* **285** (2000), pp. 692–699.
- [93] A. V. Shah, H. Schade, M. Vanecek, J. Meier, E. Vallat-Sauvain, N. Wyrsh, U. Kroll, C. Droz, and J. Bailat. “Thin-film silicon solar cell technology”. *Prog. Photovoltaics Res. Appl.* **12** (2004), pp. 113–142.
- [94] J. Müller, B. Rech, J. Springer, and M. Vanecek. “TCO and light trapping in silicon thin film solar cells”. *Sol. Energy* **77** (2004), pp. 917–930.
- [95] R. Dewan, I. Vasilev, V. Jovanov, and D. Knipp. “Optical enhancement and losses of pyramid textured thin-film silicon solar cells”. *J. Appl. Phys.* **110** (2011), pp. 013101-1 – 013101-10.
- [96] M. van Lare, F. Lenzmann, and A. Polman. “Dielectric back scattering patterns for light trapping in thin-film Si solar cells”. *Opt. Express* **21** (2013), pp. 20738–20746.

- [97] A. Ingenito, O. Isabella, and M. Zeman. “Experimental Demonstration of  $4n^2$  Classical Absorption Limit in Nanotextured Ultrathin Solar Cells with Dielectric Omnidirectional Back Reflector”. *ACS Photonics* **1** (2014), pp. 270–278.
- [98] B. Bläsi, H. Hauser, and A. J. Wolf. “Photon Management Structures for Solar Cells”. *Proc. SPIE* **8428** (2012), 8438Q-10 – 8438Q-12.
- [99] C. P. Murcia, R. Hao, C. Leitz, A. Lochtefeld, and A. Barnett. “Thin crystalline silicon solar cells with metallic back reflector”. In: *37th IEEE Photovoltaic Specialists Conference*. IEEE, 2011, pp. 661–664.
- [100] L. V. Mercaldo, I. Usatii, E. M. Esposito, P. D. Veneri, J.-W. Schüttauf, E. Moulin, F.-J. Haug, C. Zhang, and M. Meier. “Metal versus dielectric back reflector for thin-film Si solar cells with impact of front electrode surface texture”. *Prog. Photovoltaics Res. Appl.* **24** (2016), pp. 968–977.
- [101] E. Yablonovitch. “Statistical ray optics”. *J. Opt. Soc. Am.* **72** (1982), pp. 899–907.
- [102] J. Zhao, A. Wang, M. A. Green, and F. Ferrazza. “19.8% efficient "honeycomb" textured multicrystalline and 24.4% monocrystalline silicon solar cells”. *Appl. Phys. Lett.* **73** (1998), pp. 1991–1993.
- [103] P. Campbell and M. A. Green. “Light trapping properties of pyramidally textured surfaces”. *J. Appl. Phys.* **62** (1987), pp. 243–249.
- [104] H. Nussbaumer, G. Willeke, and E. Bucher. “Optical behavior of textured silicon”. *J. Appl. Phys.* **75** (1994), pp. 2202–2209.
- [105] S. C. Baker-Finch and K. R. McIntosh. “Reflection of normally incident light from silicon solar cells with pyramidal texture”. *Prog. Photovoltaics Res. Appl.* **19** (2011), pp. 406–416.
- [106] Z. Yu, A. Raman, and S. Fan. “Fundamental limit of nanophotonic light trapping in solar cells”. *Proc. Natl. Acad. Sci.* **107** (2010), pp. 17491–17496.
- [107] A. Polman and H. A. Atwater. “Photonic design principles for ultrahigh-efficiency photovoltaics”. *Nat. Mater.* **11** (2012), pp. 174–177.
- [108] D. M. Callahan, J. N. Munday, and H. A. Atwater. “Solar cell light trapping beyond the ray optic limit”. *Nano Lett.* **12** (2012), pp. 214–218.
- [109] T. Markvart. “Beyond the Yablonovitch limit: Trapping light by frequency shift”. *Appl. Phys. Lett.* **98** (2011), pp. 8–10.
- [110] H. J. Queisser. “Defects in Semiconductors: Some Fatal, Some Vital”. *Science* **281** (1998), pp. 945–950.

- [111] R. C. Newman. “Defects in silicon”. *Reports Prog. Phys.* **45** (2000), pp. 1163–1210.
- [112] C. A. J. Ammerlaan, A. Chantre, and P. Wagner. *Science and Technology of Defects in Silicon*. 1st edition. Elsevier, 2014.
- [113] N. M. Johnson, D. K. Biegelsen, and M. D. Moyer. “Deuterium passivation of grain-boundary dangling bonds in silicon thin films”. *Appl. Phys. Lett.* **40** (1982), pp. 882–884.
- [114] P. M. Fahey, P. B. Griffin, and J. D. Plummer. “Point defects and dopant diffusion in silicon”. *Rev. Mod. Phys.* **61** (1989), pp. 289–384.
- [115] K. Lips, P. Kanschä, and W. Fuhs. “Defects and recombination in microcrystalline silicon”. *Sol. Energy Mater. Sol. Cells* **78** (2003), pp. 513–541.
- [116] S. Steffens, C. Becker, D. Amkreutz, A. Klossek, M. Kittler, Y. Y. Chen, A. Schnegg, M. Klingsporn, D. Abou-Ras, K. Lips, and B. Rech. “Impact of dislocations and dangling bond defects on the electrical performance of crystalline silicon thin films”. *Appl. Phys. Lett.* **105** (2014), pp. 022108-1 – 022108-5.
- [117] W. Shockley and W. T. Read. “Statistics of the Recombination of Holes and Electrons”. *Phys. Rev.* **87** (1952), pp. 835–842.
- [118] J. Nelson. *The Physics of Solar Cells*. 1st edition. Imperial College Press, 2003.
- [119] P. Würfel. *Physics of Solar Cells*. 3rd edition. Wiley-VCH Verlag, 2016.
- [120] R. N. Hall. “Electron-hole recombination in Germanium”. *Phys. Rev.* **87** (1952), p. 381.
- [121] A. Richter, S. W. Glunz, F. Werner, J. Schmidt, and A. Cuevas. “Improved quantitative description of Auger recombination in crystalline silicon”. *Phys. Rev. B* **86** (2012), pp. 1–14.
- [122] P. Sonntag, M. Bokalič, M. Filipic, T. Frijnts, D. Amkreutz, M. Topič, and B. Rech. “Analysis of Local Minority Carrier Diffusion Lengths in Liquid-Phase Crystallized Silicon Thin-Film Solar Cells”. *IEEE J. Photovoltaics* **7** (2017), pp. 32–36.
- [123] C. Thi Trinh, R. Schlatmann, B. Rech, and D. Amkreutz. “Progress in and potential of liquid phase crystallized silicon solar cells”. *Sol. Energy* (2018), in press.
- [124] D. K. Schroder. “Carrier Lifetimes in Silicon”. *IEEE Trans. Electron Devices* **44** (1997), pp. 160–170.

- [125] G. W. Neudeck and R. F. Pierret, eds. *Advanced Semiconductor Fundamentals*. 2nd edition. Pearson Education, Inc., 2002.
- [126] A. Luque and S. Hegedus, eds. *Handbook of Photovoltaic Science and Engineering*. 2nd edition. Wiley-VCH Verlag, 2010.
- [127] J. L. Benton, C. J. Doherty, S. D. Ferris, D. L. Flamm, L. C. Kimerling, and H. J. Leamy. “Hydrogen passivation of point defects in silicon”. *Appl. Phys. Lett.* **36** (1980), pp. 670–671.
- [128] N. H. Nickel, N. M. Johnson, and W. B. Jackson. “Hydrogen passivation of grain boundary defects in polycrystalline silicon thin films”. *Appl. Phys. Lett.* **62** (1993), pp. 3285–3287.
- [129] S. Martinuzzi, I. Périchaud, and F. Warchol. “Hydrogen passivation of defects in multicrystalline silicon solar cells”. *Sol. Energy Mater. Sol. Cells* **80** (2003), pp. 343–353.
- [130] B. Gorka, B. Rau, P. Dogan, C. Becker, F. Ruske, S. Gall, and B. Rech. “Influence of hydrogen plasma on the defect passivation of polycrystalline Si thin film solar cells”. *Plasma Process. Polym.* **6** (2009), pp. 36–40.
- [131] J. R. Elmiger and M. Kunst. “Investigation of charge carrier injection in silicon nitride/silicon junctions”. *Appl. Phys. Lett.* **69** (1996), pp. 517–519.
- [132] S. W. Glunz, D. Biro, S. Rein, and W. Warta. “Field-effect passivation of the SiO<sub>2</sub>-Si interface”. *J. Appl. Phys.* **86** (1999), pp. 683–691.
- [133] B. Hoex, J. J. Gielis, M. C. Van De Sanden, and W. M. Kessels. “On the c-Si surface passivation mechanism by the negative-charge-dielectric Al<sub>2</sub>O<sub>3</sub>”. *J. Appl. Phys.* **104** (2008), pp. 113703-1 – 113703-7.
- [134] R. S. Bonilla and P. R. Wilshaw. “A technique for field effect surface passivation for silicon solar cells”. *Appl. Phys. Lett.* **104** (2014), p. 232903.
- [135] A. D. Mallorquí, E. Alarcón-Lladó, I. C. Mundet, A. Kiani, B. Demaurex, S. De Wolf, A. Menzel, M. Zacharias, and A. Fontcuberta i Morral. “Field-effect passivation on silicon nanowire solar cells”. *Nano Res.* **8** (2015), pp. 673–681.
- [136] D. Amkreutz, W. D. Barker, S. Kühnapfel, P. Sonntag, O. Gabriel, S. Gall, U. Bloeck, J. Schmidt, J. Haschke, and B. Rech. “Liquid-Phase Crystallized Silicon Solar Cells on Glass: Increasing the Open-Circuit Voltage by Optimized Interlayers for n- and p-Type Absorbers”. *IEEE J. Photovoltaics* **5** (2015), pp. 1757–1761.

- [137] N. Preissler, J. A. Töfflinger, O. Gabriel, P. Sonntag, D. Amkreutz, B. Stanowski, B. Rech, and R. Schlatmann. “Passivation at the interface between liquid-phase crystallized silicon and silicon oxynitride in thin film solar cells”. *Prog. Photovoltaics Res. Appl.* **25** (2017), pp. 515–524.
- [138] N. Preissler, C. Thi Trinh, M. Trahms, P. Sonntag, D. Abou-Ras, H. Kirmse, R. Schlatmann, B. Rech, and D. Amkreutz. “Impact of Dielectric Layers on Liquid-Phase Crystallized Silicon Solar Cells”. *IEEE J. Photovoltaics* **8** (2018), pp. 30–37.
- [139] J. Haschke, D. Amkreutz, T. Frijnts, S. Kühnapfel, T. Hänel, and B. Rech. “Influence of Barrier and Doping Type on the Open-Circuit Voltage of Liquid Phase-Crystallized Silicon Thin-Film Solar Cells on Glass”. *IEEE J. Photovoltaics* **5** (2015), pp. 1001–1005.
- [140] S. W. Glunz, A. B. Sproul, W. Warta, and W. Wetzling. “Injection-level-dependent recombination velocities at the Si-SiO<sub>2</sub> interface for various dopant concentrations”. *J. Appl. Phys.* **75** (1994), pp. 1611–1615.
- [141] T. Markvart and L. Castañer. “Principles of Solar Cell Operation”. *Pract. Handb. Photovoltaics*. 2nd edition. Elsevier, 2012, pp. 7–31.
- [142] D. Chan and J. Phang. “Analytical methods for the extraction of solar-cell single- and double-diode model parameters from I-V characteristics”. *IEEE Trans. Electron Devices* **34** (1987), pp. 286–293.
- [143] A. Hovinen. “Fitting of the solar cell IV-curve to the two diode model”. *Phys. Scr.* **1994** (1994), pp. 175–176.
- [144] D. Eisenhauer, G. Köppel, C. Becker, and B. Rech. *Lichtdurchlässiger Träger für einen halbleitenden Dünnschichtaufbau sowie Verfahren zur Herstellung und Anwendung des lichtdurchlässigen Trägers*. 2016.
- [145] L. J. Guo. “Nanoimprint lithography: methods and material requirements”. *Adv. Mater.* **19** (2007), pp. 495–513.
- [146] H. Sai, K. Saito, and M. Kondo. “Enhanced photocurrent and conversion efficiency in thin-film microcrystalline silicon solar cells using periodically textured back reflectors with hexagonal dimple arrays”. *Appl. Phys. Lett.* **101** (2012), pp. 173901-1 – 173901-6.
- [147] H. Sai, K. Saito, and M. Kondo. “Investigation of textured back reflectors with periodic honeycomb patterns in thin-film silicon solar cells for improved photovoltaic performance”. *IEEE J. Photovoltaics* **3** (2013), pp. 5–10.

- [148] H. Sai, K. Saito, N. Hozuki, and M. Kondo. “Relationship between the cell thickness and the optimum period of textured back reflectors in thin-film microcrystalline silicon solar cells”. *Appl. Phys. Lett.* **102** (2013), pp. 053509-1 – 053509-6.
- [149] H. Sai, T. Matsui, K. Matsubara, M. Kondo, and I. Yoshida. “11.0%-Efficient thin-film microcrystalline silicon solar cells with honeycomb textured substrates”. *IEEE J. Photovoltaics* **4** (2014), pp. 1349–1353.
- [150] H. Sai, K. Maejima, T. Matsui, T. Koida, M. Kondo, S. Nakao, Y. Takeuchi, H. Katayama, and I. Yoshida. “High-efficiency microcrystalline silicon solar cells on honeycomb textured substrates grown with high-rate VHF plasma-enhanced chemical vapor deposition”. *Jpn. J. Appl. Phys.* **54** (2015), 08KB05-1 – 08KB05-6.
- [151] Micro Resist Technologies. *Processing Guidelines - OrmoStamp*. 2012. URL: <https://www.nanotech.ucsb.edu/wiki/images/1/19/OrmoStamp-NIL-Lithography-UV-Soft-RevA.pdf> (accessed 29. Jan. 2018).
- [152] A. P. Amalathas and M. M. Alkaisi. “Periodic upright nanopillar fabricated by ultraviolet curable nanoimprint lithography for thin film solar cells”. *Int. J. Nanotechnol.* **14** (2017), pp. 3–14.
- [153] S. Y. Chou, P. R. Krauss, and P. J. Renstrom. “Nanoimprint lithography”. *J. Vac. Sci. Technol. B* **14** (1996), pp. 4129–4133.
- [154] J. Escarré, C. Battaglia, K. Söderström, C. Pahud, R. Biron, O. Cubero, F.-J. Haug, and C. Ballif. “UV imprinting for thin film solar cell application”. *J. Opt.* **14** (2012), p. 024009.
- [155] E. A. Costner, M. W. Lin, W.-L. Jen, and C. G. Willson. “Nanoimprint Lithography Materials Development for Semiconductor Device Fabrication”. *Annu. Rev. Mater. Res.* **39** (2009), pp. 155–180.
- [156] M. Verschuuren and H. Van Sprang. “3D Photonic Structures by Sol-Gel Imprint Lithography”. In: *MRS Spring Meeting*. Vol. 1002. 2007, N03–05.
- [157] Micro Resist Technologies. *Processing Guidelines - UVcur06*. 2018. URL: [http://www.microresist.de/sites/default/files/download/PI\\_mr\\_uvcur21\\_2017.pdf](http://www.microresist.de/sites/default/files/download/PI_mr_uvcur21_2017.pdf) (accessed 19. Feb. 2018).
- [158] Micro Resist Technologies. *Processing Guidelines - OrmoComp*. 2018. URL: [http://www.microchem.com/PDFs\\_MRT/OrmocompOverview.pdf](http://www.microchem.com/PDFs_MRT/OrmocompOverview.pdf) (accessed 19. Feb. 2018).
- [159] N. G. Einspruch and D. M. Brown. *Plasma Processing for VLSI*. 8th edition. Academic Press, 2014.

- [160] I. W. Rangelow and P. Hudek. “Lithography and Reactive Ion Etching in Microfabrication”. *Photons and Local Probes*. Ed. by O. Marti and R. Möller. 300th edication. Springer, 1995, pp. 325–344.
- [161] K. Nojiri. *Dry Etching Technology for Semiconductors*. 1st edition. Springer, 2015.
- [162] P. Docampo, J. M. Ball, M. Darwich, G. E. Eperon, and H. J. Snaith. “Efficient organometal trihalide perovskite planar-heterojunction solar cells on flexible polymer substrates”. *Nat. Commun.* **4** (2013), p. 2761.
- [163] G. E. Eperon, V. M. Burlakov, A. Goriely, and H. J. Snaith. “Neutral Color Semitransparent Microstructured Perovskite Solar Cells”. *ACS Nano* **8** (2014), pp. 591–598.
- [164] J. Dore, D. Ong, S. Varlamov, R. Egan, and M. A. Green. “Progress in Laser-Crystallized Thin-Film Polycrystalline Silicon Solar Cells: Intermediate Layers, Light Trapping, and Metallization”. *IEEE J. Photovoltaics* **4** (2014), pp. 33–39.
- [165] N. Preissler, J. A. Töfflinger, I. Shutsko, O. Gabriel, S. Calnan, B. Stannowski, B. Rech, and R. Schlatmann. “Interface passivation of liquid-phase crystallized silicon on glass studied with high-frequency capacitance-voltage measurements”. *Phys. Status Solidi A* (2016), pp. 1–8.
- [166] D. Amkreutz, N. Preissler, C. Thi Trinh, M. Trahms, P. Sonntag, R. Schlatmann, and B. Rech. “Influence of the precursor layer composition and deposition processes on the electronic quality of liquid phase crystallized silicon absorbers”. *Prog. Photovoltaics Res. Appl.* (2017).
- [167] S. Schiller, U. Heisig, and S. Panzer. *Electron Beam Technology*. 1st edition. John Wiley & Sons, Ltd, 1982.
- [168] O. Gabriel, T. Frijnts, N. Preissler, D. Amkreutz, S. Calnan, S. Ring, B. Stannowski, B. Rech, and R. Schlatmann. “Crystalline silicon on glass - interface passivation and absorber material quality”. *Prog. Photovoltaics Res. Appl.* **15** (2015), pp. 659–676.
- [169] D. Lockau, T. Sontheimer, C. Becker, E. Rudigier-Voigt, F. Schmidt, and B. Rech. “Nanophotonic light trapping in 3-dimensional thin-film silicon architectures”. *Opt. Express* **21** (2013), A42–A52.
- [170] GP Solar GmbH. *GP Alka-Tex additive to improve the IPA-free texturing of monocrystalline Si-wafers*. URL: <http://www.gpsolar.de/en/materials/chemicals/alka-tex/> (accessed 15. Jan. 2018).

- [171] Y. Wang, R. Luo, J. Ma, and S.-Q. Man. “Fabrication of the pyramidal microstructure on silicon substrate using KOH solution”. In: *Proceedings of the 2015 International Conference on Advanced Engineering Materials and Technology*. 2015, pp. 302–307.
- [172] S. Kühnappel, S. Gall, B. Rech, and D. Amkreutz. “Towards monocrystalline silicon thin films grown on glass by liquid phase crystallization”. *Sol. Energy Mater. Sol. Cells* **140** (2015), pp. 86–91.
- [173] W. Kern. “The Evolution of Silicon Wafer Cleaning Technology”. *J. Electrochem. Soc.* **137** (1990), pp. 1887–1892.
- [174] G. Binnig and C. F. Quate. “Atomic Force Microscope”. *Phys. Rev. Lett.* **56** (1986), pp. 930–933.
- [175] P. Eaton and P. West. *Atomic force microscopy*. 1st edition. Oxford University Press, 2010.
- [176] B. Cappella and G. Dietler. “Force-distance curves by atomic force microscopy”. *Surf. Sci. Rep.* **34** (1999), pp. 1–104.
- [177] L. Reimer. *Scanning Electron Microscopy*. 2nd edition. Springer, 1998.
- [178] R. Reichelt. “Scanning Electron Microscopy”. *Science of Microscopy*. Ed. by P. W. Hawkes and J. C. H. Spence. 1st edition. Springer, 2007.
- [179] D. J. Gardiner and P. R. Graves. *Practical Raman Spectroscopy*. 1st edition. Springer-Verlag Berlin Heidelberg, 1989.
- [180] H. G. Tompkins, E. A. Irene, C. Hill, and N. Carolina. *Handbook of Ellipsometry*. 1st edition. 2005.
- [181] SENTECH Instruments GmbH. *Spectroscopic ellipsometry software SpectraRay/4*.
- [182] G. E. Jellison and F. A. Modine. “Parameterization of the optical functions of amorphous materials in the interband region”. *Appl. Phys. Lett.* **69** (1996), pp. 371–373.
- [183] G. E. Jellison and F. A. Modine. “Erratum: “Parameterization of the optical functions of amorphous materials in the interband region””. *Appl. Phys. Lett.* **69** (1996), p. 2137.
- [184] J. M. Palmer and B. G. Grant. *The Art of Radiometry*. 1st edition. SPIE Press, 2009.
- [185] M. A. Green, K. Emery, Y. Hishikawa, W. Warta, E. D. Dunlop, D. H. Levi, and A. W. Y. Ho-Baillie. “Solar cell efficiency tables (version 50)”. *Prog. Photovoltaics Res. Appl.* **25** (2017), pp. 668–676.

- [186] M. O'Donnell and R. Zadoyan. "How to minimize measurements errors in solar cell testing". *Sol. Ind.* **4** (2011), pp. 38–42.
- [187] H. J. Snaith. "The perils of solar cell efficiency measurements". *Nat. Photonics* **6** (2012), pp. 337–340.
- [188] R. Sinton, A. Cuevas, and M. Stuckings. "Quasi-steady-state photoconductance, a new method for solar cell material and device characterization". *Conf. Rec. Twenty Fifth IEEE Photovolt. Spec. Conf. - 1996* (1996), pp. 457–460.
- [189] R. A. Sinton and A. Cuevas. "A quasi-steady-state open-circuit voltage method for solar cell characterization". In: *16th European Photovoltaic Solar Energy Conference*. Glasgow, UK, 2000.
- [190] M. J. Kerr and A. Cuevas. "Generalized analysis of the illumination intensity vs. open-circuit voltage of solar cells". *Sol. Energy* **76** (2004), pp. 263–267.
- [191] S. Bowden, V. Yelundur, and A. Rohatgi. "Implied-Voc and Suns-Voc measurements in multicrystalline solar cells". *Conf. Rec. Twenty-Ninth IEEE Photovolt. Spec. Conf. - 2002.* **3** (2002), pp. 371–374.
- [192] A. V. Lavrinenko, J. Laegsgaard, N. Gregersen, F. Schmidt, and T. Sondergaard. *Numerical Methods in Photonics*. 1st edition. CRC Press, 2014.
- [193] R. Santbergen and R. J. C. van Zolingen. "The absorption factor of crystalline silicon PV cells: A numerical and experimental study". *Sol. Energy Mater. Sol. Cells* **92** (2008), pp. 432–444.
- [194] R. Santbergen, A. H. Smets, and M. Zeman. "Optical model for multilayer structures with coherent, partly coherent and incoherent layers". *Opt. Express* **21** (2013), A262–A267.
- [195] D. Thorp and S. R. Wenham. "Ray-tracing of arbitrary surface textures for light-trapping in thin silicon solar cells". *Sol. Energy Mater. Sol. Cells* **48** (1997), pp. 295–301.
- [196] T. Yagi, Y. Uraoka, and T. Fuyuki. "Ray-trace simulation of light trapping in silicon solar cell with texture structures". *Sol. Energy Mater. Sol. Cells* **90** (2006), pp. 2647–2656.
- [197] K. Jäger. "On the Scalar Scattering Theory for Thin-Film Solar Cells". Doctoral Thesis. Delft University of Technology, 2012.
- [198] K. Jäger, M. Fischer, R. A. C. M. M. Van Swaaij, and M. Zeman. "A scattering model for nano-textured interfaces and its application in optoelectrical simulations of thin-film silicon solar cells". *J. Appl. Phys.* **111** (2012), p. 083108.

- [199] O. Levy and D. Stroud. “Maxwell Garnett theory for mixtures of anisotropic inclusions: Application to conducting polymers”. *Phys. Rev. B* **56** (1997), pp. 8035–8046.
- [200] J. Pomplun, S. Burger, L. Zschiedrich, and F. Schmidt. “Adaptive finite element method for simulation of optical nano structures”. *Phys. Status Solidi B* **244** (2007), pp. 3419–3434.
- [201] S. Burger, L. Zschiedrich, J. Pomplun, and F. Schmidt. “JCMsuite: An Adaptive FEM Solver for Precise Simulations in Nano-Optics”. In: *Integrated Photonics and Nanophotonics Research and Applications 2008*. Optical Society of America, 2008, ITuE4.
- [202] K. Jäger, M. Hammerschmidt, G. Köppel, S. Burger, and C. Becker. “On Accurate Simulations of Thin-Film Solar Cells With a Thick Glass Superstrate”. *Opt. Express* **26** (2018), A99–A107.
- [203] D. Eisenhauer, G. Köppel, B. Rech, and C. Becker. “Improved light management in crystalline silicon thin-film solar cells by advanced nano-texture fabrication”. In: *Light, Energy and the Environment*. Optical Society of America, 2017, PW2A.4.
- [204] D. Lockau, M. Hammerschmidt, J. Haschke, M. Blome, F. Ruske, F. Schmidt, and B. Rech. “A comparison of scattering and non-scattering anti-reflection designs for back contacted polycrystalline thin film silicon solar cells in superstrate configuration”. *Proc. SPIE* **9140** (2014), p. 914006.
- [205] K. Jäger, C. Barth, M. Hammerschmidt, S. Herrmann, S. Burger, F. Schmidt, and C. Becker. “Simulations of sinusoidal nanotextures for coupling light into c-Si thin-film solar cells”. *Opt. Express* **24** (2016), A569.
- [206] A. J. Wolf, H. Hauser, V. Kübler, C. Walk, O. Höhn, and B. Bläsi. “Origination of nano- and microstructures on large areas by interference lithography”. *Microelectron. Eng.* **98** (2012), pp. 293–296.
- [207] S. M. Sze and M.-K. Lee. *Semiconductor Devices: Physics and Technology*. 3rd edition. John Wiley & Sons, Ltd., 2012.
- [208] D. Eisenhauer, G. Köppel, K. Jäger, D. Chen, O. Shargaieva, P. Sonntag, D. Amkreutz, B. Rech, and C. Becker. “Smooth anti-reflective three-dimensional textures for liquid phase crystallized silicon thin-film solar cells on glass”. *Sci. Rep.* **7** (2017), p. 2658.
- [209] G. Köppel, D. Eisenhauer, B. Rech, and C. Becker. “Combining tailor-made textures for light in-coupling and light trapping in liquid phase crystallized silicon thin-film solar cells”. *Opt. Express* **25** (2017), A467–A472.

- [210] D. Eisenhauer, K. Jäger, G. Köppel, B. Rech, and C. Becker. “Optical Properties of Smooth Anti-reflective Three-dimensional Textures for Silicon Thin-film Solar Cells”. *Energy Procedia* **102** (2016), pp. 27–35.
- [211] M. Z. Pakhuruddin, J. Huang, S. Kühnapfel, J. Dore, S. Gall, and S. Varlamov. “Properties of laser-crystallised silicon thin-film solar cells on textured glass”. *J. Mater. Sci. Mater. Electron.* **28** (2017), pp. 10391–10399.
- [212] C. Becker, P. Wyss, D. Eisenhauer, J. Probst, V. Preidel, M. Hammerschmidt, and S. Burger. “5 x 5 cm<sup>2</sup> silicon photonic crystal slabs on glass and plastic foil exhibiting broadband absorption and high-intensity near-fields”. *Sci. Rep.* **4** (2014), p. 5886.
- [213] U. Balachandran and N. Eror. “Raman spectra of titanium dioxide”. *J. Solid State Chem.* **42** (1982), pp. 276–282.
- [214] O. Frank, M. Zikalova, B. Laskova, J. Kürti, J. Koltai, and L. Kavan. “Raman spectra of titanium dioxide (anatase, rutile) with identified oxygen isotopes (16, 17, 18)”. *Phys. Chem. Chem. Phys.* **14** (2012), pp. 14567–14572.
- [215] D. B. Hall, P. Underhill, and J. M. Torkelson. “Spin coating of thin and ultrathin polymer films”. *Polym. Eng. Sci.* **38** (1998), pp. 2039–2045.
- [216] RRUFF. *Raman spectra for Anatase Titanium Oxide*. URL: <http://rruff.info/anatase/R060277> (accessed 20. Feb. 2018).
- [217] RRUFF. *Raman spectra for Rutile Titanium Oxide*. URL: <http://rruff.info/rutile/display=default/R110109> (accessed 20. Feb. 2018).
- [218] M. Polyanskiy. *Optical constants of SiO<sub>2</sub>*. URL: <https://refractiveindex.info/?shelf=main&book=SiO2&page=Gao> (accessed 21. Feb. 2018).
- [219] B. S. Richards, J. E. Cotter, and C. B. Honsberg. “Enhancing the surface passivation of TiO<sub>2</sub> coated silicon wafers”. *Appl. Phys. Lett.* **80** (2002), pp. 1123–1125.
- [220] J. Barbé, A. F. Thomson, E.-C. Wang, K. McIntosh, and K. Catchpole. “Nanoimprinted TiO<sub>2</sub> sol-gel passivating diffraction gratings for solar cell applications”. *Prog. Photovoltaics Res. Appl.* **20** (2012), pp. 143–148.
- [221] A. F. Thomson and K. R. McIntosh. “Light-enhanced surface passivation of TiO<sub>2</sub>-coated silicon”. *Prog. Photovoltaics Res. Appl.* **20** (2012), pp. 343–349.
- [222] B. Liao, B. Hoex, A. G. Aberle, D. Chi, and C. S. Bhatia. “Excellent c-Si surface passivation by low-temperature atomic layer deposited titanium oxide”. *Appl. Phys. Lett.* **104** (2014), pp. 253903-1 – 253903-4.

- [223] B. Liao, B. Hoex, K. D. Shetty, P. K. Basu, and C. S. Bhatia. “Passivation of Boron-Doped Industrial Silicon Emitters by Thermal Atomic Layer Deposited Titanium Oxide”. *IEEE J. Photovoltaics* **5** (2015), pp. 1062–1066.
- [224] Q. Wang, T. Soderstrom, K. Omaki, A. Lennon, and S. Varlamov. “Etch-back silicon texturing for light-trapping in electron beam evaporated thin-film polycrystalline silicon solar cells”. *Energy Procedia* **15** (2012), pp. 220–228.
- [225] T. Soderstrom, Q. Wang, K. Omaki, O. Kunz, D. Ong, and S. Varlamov. “Light confinement in e-beam evaporated thin film polycrystalline silicon solar cells”. *Phys. Status Solidi RRL* **5** (2011), pp. 181–183.
- [226] G. Jin, P. I. Widenborg, P. Campbell, and S. Varlamov. “Lambertian matched absorption enhancement in PECVD poly-Si thin film on aluminum induced textured glass superstrates for solar cell applications”. *Prog. Photovoltaics Res. Appl.* **18** (2010), pp. 582–589.
- [227] D. Eisenhauer, H. Sai, T. Matsui, G. Köppel, B. Rech, and C. Becker. “Honeycomb micro-textures for light trapping in multi-crystalline silicon thin-film solar cells”. *Opt. Express* **26** (2018), A498–A507.
- [228] G. C. Schwartz. “Reactive ion etching of silicon”. *J. Vac. Sci. Technol.* **16** (1979), pp. 410–413.
- [229] R. Legtenberg. “Anisotropic Reactive Ion Etching of Silicon Using SF<sub>6</sub>/O<sub>2</sub>/CHF<sub>3</sub> Gas Mixtures”. *J. Electrochem. Soc.* **142** (1995), pp. 2020–2028.
- [230] H. Jansen, H. Gardeniers, M. De Boer, M. Elwenspoek, and J. Fluitman. “A survey on the reactive ion etching of silicon in microtechnology”. *J. Micromechanics Microengineering* **6** (1996), pp. 14–28.
- [231] F. Marty, L. Rousseau, B. Saadany, B. Mercier, O. Français, Y. Mita, and T. Bourouina. “Advanced etching of silicon based on deep reactive ion etching for silicon high aspect ratio microstructures and three-dimensional micro- and nanostructures”. *Microelectronics J.* **36** (2005), pp. 673–677.
- [232] M. Moreno, D. Daineka, and P. Roca i Cabarrocas. “Plasma texturing for silicon solar cells: From pyramids to inverted pyramids-like structures”. *Sol. Energy Mater. Sol. Cells* **94** (2010), pp. 733–737.
- [233] M. Moreno, D. Murias, J. Martínez, C. Reyes-Betanzo, A. Torres, R. Ambrosio, P. Rosales, P. Roca i Cabarrocas, and M. Escobar. “A comparative study of wet and dry texturing processes of c-Si wafers for the fabrication of solar cells”. *Sol. Energy* **101** (2014), pp. 182–191.

- [234] D. Chen, P. Manley, P. Tockhorn, D. Eisenhauer, G. Köppel, M. Hammer-schmidt, S. Burger, S. Albrecht, B. Rech, and C. Becker. “Nanophotonic Light Management for Perovskite-Silicon Tandem Solar Cells”. *J. Photonics Energy* **8** (2018), pp. 022601-1 – 022601-13.
- [235] C. Ulbrich, A. Gerber, K. Hermans, A. Lambertz, and U. Rau. “Analysis of short circuit current gains by an anti-reflective textured cover on silicon thin film solar cells”. *Prog. Photovoltaics Res. Appl.* **21** (2013), pp. 1672–1681.
- [236] O. Isabella, R. Vismara, D. N. Linssen, K. X. Wang, S. Fan, and M. Zeman. “Advanced light trapping scheme in decoupled front and rear textured thin-film silicon solar cells”. *Sol. Energy* **162** (2018), pp. 344–356.
- [237] S. A. Boden and D. M. Bagnall. “Optimization of moth-eye antireflection schemes for silicon solar cells”. *Prog. Photovoltaics Res. Appl.* **18** (2010), pp. 195–203.
- [238] temicon GmbH. *HT-AR-02 High Performance Antireflective Molds HT-AR-02*. URL: [https://www.temicon.com/fileadmin/downloads/product-sheets/2016/temicon\\_db\\_HT-AR-02\\_16\\_08.pdf](https://www.temicon.com/fileadmin/downloads/product-sheets/2016/temicon_db_HT-AR-02_16_08.pdf) (accessed 24. Jan. 2018).
- [239] K. Jäger, L. Korte, B. Rech, and S. Albrecht. “Numerical optical optimization of monolithic planar perovskite-silicon tandem solar cells with regular and inverted device architectures”. *Opt. Express* **25** (2017), A473–A482.
- [240] M. Saliba, T. Matsui, J.-Y. Seo, K. Domanski, J.-P. Correa-Baena, M. K. Nazeeruddin, S. M. Zakeeruddin, W. Tress, A. Abate, A. Hagfeldt, and M. Grätzel. “Cesium-containing triple cation perovskite solar cells: improved stability, reproducibility and high efficiency”. *Energy Environ. Sci.* **9** (2016), pp. 1989–1997.
- [241] M. Saliba, S. M. Wood, J. B. Patel, P. K. Nayak, J. Huang, J. A. Alexander-Webber, B. Wenger, S. D. Stranks, M. T. Hörantner, J. T. W. Wang, R. J. Nicholas, L. M. Herz, M. B. Johnston, S. M. Morris, H. J. Snaith, and M. K. Riede. “Structured Organic-Inorganic Perovskite toward a Distributed Feedback Laser”. *Adv. Mater.* **28** (2016), pp. 923–929.
- [242] S. Albrecht, M. Saliba, J. P. Correa Baena, F. Lang, L. Kegelmann, M. Mews, L. Steier, A. Abate, J. Rappich, L. Korte, R. Schlatmann, M. K. Nazeeruddin, A. Hagfeldt, M. Grätzel, and B. Rech. “Monolithic perovskite/silicon-heterojunction tandem solar cells processed at low temperature”. *Energy Environ. Sci.* **9** (2016), pp. 81–88.



# Appendices



# A Scientific Contributions

## Patent Application

- Deutsches Patentamt 10 2016 107 877.8, “Lichtdurchlässiger Träger für einen halbleitenden Dünnschichtaufbau sowie Verfahren zur Herstellung und Anwendung des lichtdurchlässigen Trägers”, filed: 28.04.2016, Helmholtz-Zentrum Berlin für Materialien und Energie, Inventors: **David Eisenhauer**, Grit Köppel, Christiane Becker, Bernd Rech.

## Peer-Reviewed Publications

- **David Eisenhauer**, Grit Köppel, Klaus Jäger, Duote Chen, Oleksandra Shargaieva, Paul Sonntag, Daniel Amkreutz, Bernd Rech, and Christiane Becker. “Smooth anti-reflective three-dimensional textures for liquid phase crystallized silicon thin-film solar cells on glass”. *Scientific Reports* **7** (2017), 2658.
- **David Eisenhauer**, Klaus Jäger, Grit Köppel, Bernd Rech, and Christiane Becker. “Optical properties of smooth anti-reflective three-dimensional textures for silicon thin-film solar cells”. *Energy Procedia* **102** (2016), 27-35.
- **David Eisenhauer**, Hitoshi Sai, Takuya Matsui, Grit Köppel, Bernd Rech, and Christiane Becker. “Honeycomb micro-textures for light trapping in multi-crystalline silicon thin-film solar cells”. *Optics Express* **26** (2018), A498–A507.
- Grit Köppel, **David Eisenhauer**, Bernd Rech, and Christiane Becker. “Combining tailor-made textures for light in-coupling and light trapping in liquid phase crystallized silicon thin-film solar cells”. *Optics Express* **25** (2017), A467–A472.
- Grit Köppel, **David Eisenhauer**, Bernd Rech, and Christiane Becker. “Tailoring Nano-Textures for Optimized Light In-Coupling in Liquid Phase Crystallized Silicon Thin-Film Solar Cells”. *Physica status solidi C* **14** (2017), 170017.

## CHAPTER A Scientific Contributions

- Duote Chen, Phillip Manley, Philipp Tockhorn, **David Eisenhauer**, Grit Köppel, Martin Hammerschmidt, Sven Burger, Steve Albrecht, Christiane Becker, and Klaus Jäger. “Nanophotonic Light Management for Perovskite-Silicon Tandem Solar Cells”. *Journal of Photonics for Energy* **8** (2018), 022601-1–022601-13.
- Steffen Braunger, Laura Mundt, Christian Wolff, Mathias Mews, Carolin Rehermann, Marko Jost, Alvaro Tejada, **David Eisenhauer**, Christiane Becker, Jorde Andres Guerra, Eva Unger, Lars Korte, Dieter Neher, Martin Schubert, Bernd Rech, and Steve Albrecht. “On the Appearance of Wrinkled Morphology for  $\text{Cs}_{0.17}\text{FA}_{0.83}\text{Pb}(\text{I}_{0.83}\text{Br}_{0.17})_3$  Perovskites and the Impact on Solar Cell Performance”. *Journal of Physical Chemistry Letters* **122** (2018), 17123–17135.

### Conference Contributions

- **David Eisenhauer**, Grit Köppel, Bernd Rech, and Christiane Becker. “Angle resolved reflectivity analysis of textured substrates for liquid-phase crystallized silicon thin-film solar cells”. In: *Light, Energy and the Environment*, page JW4A.35. Optical Society of America, OSA Technical Digest (online), 10.1364/FTS.2016.JW4A.35, 2016.
- **David Eisenhauer**, Grit Köppel, Klaus Jäger, Bernd Rech, and Christiane Becker. “Imprinted Nanostructures for Light Management in Crystalline Silicon Thin-Film Solar Cells on Glass”. In: *Light, Energy and the Environment*, page PM2B.5. Optical Society of America, OSA Technical Digest (online), 10.1364/PV.2016.PM2B.5, 2016.
- **David Eisenhauer**, Grit Köppel, Bernd Rech, and Christiane Becker. “Improved Light Management in Crystalline Silicon Thin-Film Solar Cells by Advanced Nano-Texture Fabrication”. In: *Light, Energy and the Environment*, page PW2A.4. Optical Society of America, OSA Technical Digest (online), 10.1364/PV.2017.PW2A.4, 2017.
- Klaus Jäger, Grit Köppel, **David Eisenhauer**, Duote Chen, Martin Hammerschmidt, Sven Burger, and Christiane Becker. “Optical simulations of advanced light management for liquid-phase crystallized silicon thin-film solar cells”. In: *Proc. SPIE*, volume 10356, 2017.
- **David Eisenhauer**, Bernd Rech, and Christiane Becker. “Mitigating Optical Losses in Crystalline Silicon Thin-Film Solar Cells on Glass”. In: Proceedings of the 2018 WCPEC-7, 2018. Accepted manuscript.

- Pushendra Kumar, **David Eisenhauer**, Moataz M. K. Yousef, Qi Shi, Ahmed S. G. Khalil, Christiane Becker, Tonu Pullerits, and Khadga Jung Karki. “Photoimpedance Spectroscopy Analysis of Planar and Nano-textured Thin-film Silicon Solar Cells”. In ICUOA 2018: 20th International Conference on Ultrafast Optics and Applications.



# B Acknowledgement

Many individuals have made either direct or indirect contributions to this work and for that I am extremely grateful.

First and foremost, I would like to thank Prof. Dr. Bernd Rech and Prof. Dr. Christiane Becker who gave me the opportunity to work at HZB, provided me with the appealing research topic, supported me in all aspects and agreed to review my thesis. I would also like to thank Prof. Dr. Olindo Isabella and RNDr. Antonín Fejfar, CSc., for their precious time and efforts evaluating this thesis.

Deepest gratitude is owed to Prof. Dr. Christiane Becker and all members of her young investigator group. Prof. Dr. Christiane Becker gave me all the freedom to pursue my research and provided guidance whenever necessary. Dr. Klaus Jäger and Duote Chen are acknowledged for developing and conducting optical simulations. I thank Dr. Klaus Jäger for proof-reading parts of the thesis. Special thanks go to Dr. Grit Köppel, Martin Krüger, Sebastian Roder and Johannes Sutter who have been cheerful roommates, helpful co-workers and have become good friends. Thank you all for work-related support and, more importantly, making every day a joy.

I am indebted to Dr. Veit Preidel and Dr. Grit Köppel. Upon their legacy and fruitful discussions much of this work is built. I hope this thesis will be worthy to share a shelf with theirs. Especially, I thank Dr. Grit Köppel for supporting me during our mutual time at HZB and beyond.

Dr. Paul Sonntag, Dr. Cham Thi Trinh, Dr. Natalie Preissler, Martina Trahms, and Dr. Daniel Amkreutz are acknowledged for bringing the LPC technology forward, only thereby enabling many of the results obtained in this thesis.

I thank Dr. Takuya Matsui, Dr. Hitoshi Sai, Dr. Hiroshi Umishio and Dr. Koji Matsubara for their hospitality and sacrificing their time to assist me during my research stay at AIST in Japan. Helmholtz-Zentrum Berlin, in particular Dr. Gabriele Lampert, is acknowledged for financial support in the PhD student research abroad program. Once more, Prof. Dr. Bernd Rech and Prof. Dr. Christiane Becker are acknowledged for encouraging and supporting this stay abroad.

This work is built onto a foundation of hard working scientists, technicians and staff from HZB, PVcomB, and BeSSY who keep everything running. For that I am extremely grateful. Marion Krusche, Antonia Tallarek, Martin Krüger, Holger Rhein,

## CHAPTER B Acknowledgement

Erhard Conrad, Carola Klimm, Daniel Amkreutz, Martin Muske, Mona Wittig, Kerstin Jacob, Thomas Lußky, Andreas von Kozierowski, Tobias Hänel, Karolina Mack, and Ivo Rudolph deserve special thanks.

I also thank the “Mensa-Gang” for their help and friendship. It is a pleasure to be able to rely on our 11:30 date.

I whole heartedly thank my family for their unconditional support and love. Finally, I’m infinitely grateful to Laura, who makes me a happier and better person every day.

# C Declaration

Hiermit versichere ich, dass ich diese Arbeit selbstständig verfasst und keine anderen als die angegebenen Hilfsmittel und Quellen benutzt habe.

Berlin, 28.02.2018

David Eisenhauer